The Dissertation Committee for Frederick Todd Davidson certifies that this is the approved version of the following dissertation:

An Experimental Study of Film Cooling, Thermal Barrier Coatings and Contaminant Deposition on an Internally Cooled Turbine Airfoil Model

Committee:

David G. Bogard, Supervisor

Thomas M. Kiehne

Atul Kohli

Ofodike A. Ezekoye

Michael E. Webber

An Experimental Study of Film Cooling, Thermal Barrier Coatings and Contaminant Deposition on an Internally Cooled Turbine Airfoil Model

by

Frederick Todd Davidson, B.S.; M.S.E.

Dissertation

Presented to the Faculty of the Graduate School of

The University of Texas at Austin

in Partial Fulfillment

of the Requirements

for the Degree of

Doctor of Philosophy

The University of Texas at Austin

May 2012

Dedication

To my loving wife, Audrey.

Acknowledgements

I would like to thank the U.S. Department of Energy's National Energy Technology Laboratory which provided the majority of the funding for this research through the University Turbine Systems Research program. The U.S. Department of Defense's Office of Naval Research also provided funding through the Electric Ship Research and Development Consortium.

My deepest gratitude is expressed to Dr. David G. Bogard. His guidance and teaching over the past four years have been instrumental in my development as an engineer. I would also like to thank the members of my committee, Dr. Thomas Kiehne, Dr. Atul Kohli, Dr. Ofodike Ezekoye, and Dr. Michael Webber.

A thank you is also in order for all of my lab mates who I have worked with in the Turbulence and Turbine Cooling Research Laboratory who helped in one way or another in completing this research: Dr. Jason Dees, Dr. Jason Albert, Tom Dyson, Emily Boyd, Marc Nathan, David Kistenmacher, and John McClintic.

I would also like to thank my friends and family outside of the workplace that made graduate school so memorable.

And finally: Audrey, thank you for everything.

An Experimental Study of Film Cooling, Thermal Barrier Coatings and Contaminant Deposition on an Internally Cooled Turbine Airfoil Model

Frederick Todd Davidson, Ph.D.
The University of Texas at Austin, 2012

Supervisor: David G. Bogard

Approximately 10% of all energy consumed in the United States is derived from high temperature gas turbine engines. As a result, a 1% increase in engine efficiency would yield enough energy to satisfy the demands of approximately 1 million homes and savings of over $800 million in fuel costs per year. Efficiency of gas turbine engines can be improved by increasing the combustor temperature. Modern engines now operate at temperatures that far exceed the material limitations of the metals they are comprised of in the pursuit of increased thermal efficiency. Various techniques to thermally protect the turbine components are used to allow for safe operation of the engines despite the extreme environments: film cooling, internal convective cooling, and thermal barrier coatings. Historically, these thermal protection techniques have been studied separately without account for any conjugate effects. The end goal of this work is to provide a greater understanding of how the conjugate effects might alter the predictions of thermal behavior and consequently improve engine designs to pursue increased efficiency.

The primary focus of this study was to complete the first open literature, high resolution experiments of a modeled first stage turbine vane with both active film cooling

and a simulated thermal barrier coating (TBC). This was accomplished by scaling the thermal behavior of a real engine component to the model vane using the matched Biot number method. Various film cooling configurations were tested on both the suction and pressure side of the model vane including: round holes, craters, traditional trenches and a novel modified trench. IR thermography and ribbon thermocouples were used to measure the surface temperature of the TBC and the temperature at the interface of the TBC and vane wall, respectively. This work found that the presence of a TBC significantly dampens the effect of altering film cooling conditions when measuring the TBC interface temperature. This work also found that in certain conditions adiabatic effectiveness does not provide an accurate assessment of how a film cooling design may perform in a real engine.

An additional focus of this work was to understand how contaminant deposition alters the cooling performance of a vane with a TBC. This work focused on quantifying the detrimental effects of active deposition by seeding the mainstream flow of the test facility with simulated molten coal ash. It was found that in most cases, except for round holes operating at relatively high blowing ratios, the performance of film cooling was negatively altered by the presence of contaminant deposition. However, the cooling performance at the interface of the TBC and vane wall actually improved with deposition due to the additional thermal resistance that was added to the exterior surface of the model vane.

Table of Contents

List of Tables

List of Figures

Nomenclature

A	area
Aug	augmentation, defined as $(\phi_{TBC} - \phi_{No\ TBC})/(1 - \phi_{No\ TBC})$
Bi	Biot number, defined as ht/k
C	airfoil chord length (linear distance from the stagnation point to the trailing tip)
C_d	discharge coefficient
d	diameter
DR	density ratio, defined as ρ_c/ρ_∞
H	vane span height
h	heat transfer coefficient
I	momentum flux ratio, defined as $\rho_c U_c^2/\rho_\infty U_\infty^2$; current
k	thermal conductivity
L	length of film cooling hole
l	arbitrary length scale
M	blowing ratio, defined as $\rho_c U_c/\rho_\infty U_\infty$
$\dot{m}$	mass flow rate
N	number
p	pitch (e.g. the distance between adjacent film cooling holes in a single row)
P	pressure; volumetric porosity
PS	pressure side of the vane
q''	heat flux
R	gas constant; resistance
R''	contact resistance
Ra	average centerline roughness
Re	Reynolds number, defined as $\rho Ul/\mu$
s	streamwise distance along vane surface where $s = 0$ is the stagnation point
SS	suction side of the vane
Stk	Stokes number, defined as $\tau/(l_{char}/U_{char})$
T	temperature
t	thickness; depth
Tu	turbulence intensity
U	velocity
V	voltage
w	width
x	arbitrary streamwise distance, where $x = 0$ is often the edge of the film cooling design
z	spanwise distance

Greek

α	inclination angle; angle of attack
α	correction for internal convective driving temperature

β	ratio of orifice diameter to pipe diameter
β	non-dimensional expression for additional thermal resistance beyond that of the vane
χ	warming factor from inlet of vane to exit of film cooling hole
Δ	difference; change
δ	uncertainty
ε	emissivity
ϕ	overall effectiveness, defined as $(T_\infty - T_{w,e})/(T_\infty - T_{c,vane\ inlet})$
η	adiabatic effectiveness, defined as $(T_\infty - T_{aw})/(T_\infty - T_{c,hole\ exit})$
Λ_f	integral length scale
μ	dynamic viscosity
ρ	density
σ	Stefan-Boltzmann constant
τ	external TBC condition, defined as $(T_\infty - T_{TBC})/(T_\infty - T_{c,vane\ inlet})$; flow field time constant

Subscripts

avg	average
aw	adiabatic wall
Bond	bond coat
c	coolant
c,hole exit	coolant at the exit of a film cooling hole
c,vane inlet	coolant at the vane inlet
char	characteristic (e.g. characteristic length scale)
conv	convection (e.g. convective driving temperature)
dyn	dynamic (e.g. dynamic pressure)
e	external
f	film cooling
foil	heat flux foil
g	gas
h	film cooling hole
h_i	data obtained during the test in which ϕ_i was measured allowing for estimation of h_i
i	internal
∞	mainstream; hot gas path
min	minimum
o	no film cooling
p	particle
pred	prediction
r	radial passage
rad	radiation
req	requirement (e.g. requirement for the maximum safe operating temperature)
res	resistor
SH	showerhead

TBC	thermal barrier coating
U	U-bend passage
Uin	inlet of U-bend passage
Uout	outlet of U-bend passage
w	vane wall

Superscript

$\bar{}$	lateral average

Chapter 1

1. INTRODUCTION

This section will provide an overview of gas turbine engines and the key components which are of interest for this study. In particular, the concepts of turbine vane film cooling and thermal barrier coatings will be discussed in detail. A discussion of other relevant studies is also provided. Finally, the specific objectives for this body of work are outlined focusing on various aspects of experimentally measuring the thermal behavior of an actively cooled turbine vane with a thermal barrier coating.

1.1. Overview of Gas Turbine Engines

1.1.1. Brayton Cycle

Modern day gas turbine engines are used for a wide array of applications such as jet propulsion, marine power plants, and electricity generation. These engines are the product of design efforts from individuals like George Brayton (1830-1892) and Frank Whittle (1907-1992). Their designs have come to influence people's lives on a daily basis. To put this in perspective, over 500 million barrels of oil were used in 2009 for jet fuel according to the U.S. Energy Information Administration's Annual Energy Review (2009). This amounted to roughly 3 quadrillion BTU's, or quads, of energy consumed. Furthermore, approximately 7 quads of electricity were produced from natural gas in 2009. This means that in 2009 over 10% of all the energy consumed in the U.S. resulted from burning either natural gas or jet fuel in a high temperature gas turbine engine. Consequently, only a 1% improvement in the efficiency of all domestic gas turbines would result in fuel savings of approximately $500MM in oil and $200MM in natural

gas. These numbers assume $100 per barrel of oil and $3 per MMBTU of natural gas. Alternatively, the energy savings from increasing domestic gas turbine efficiency by 1% would be enough to meet the demands of 1 million homes for an entire year. Integrated gasification combined cycle (IGCC) plants may soon start to replace coal fired steam turbine systems in order to alleviate ever growing environmental concerns associated with traditional coal power plants. This transition could lead to an even higher fraction of high temperature turbine systems in the domestic electric power grid.

George Brayton's efforts in the late nineteenth century were pivotal in the design of gas turbine engines. He is credited with inventing a heat engine cycle that is defined by isentropic compression, constant pressure heat addition, isentropic expansion, and constant pressure heat rejection. This is now known as the Brayton Cycle and is shown in Figure 1.1. This cycle is the backbone of all modern gas turbine engines. During the 1920's, significant progress was made developing a functioning engine utilizing the Brayton Cycle. Whittle was one of two engineers that independently designed an engine characterized by three primary components: a compressor, a combustor, and a turbine. These open cycle engines allowed for the development of jet propulsion for the first time. Figure 1.2 provides a diagram of a generic system used for propulsion as well as a photograph of a first stage turbine blade. Alternate applications of the engine led to closed loop systems which generate electricity. Simple schematics of an open and closed loop system are shown in Figure 1.3.

1.1.2. The Effect of Turbine Inlet Temperature

Modern designers of gas turbine engines strive to improve cyclic efficiency by driving up the combustor temperature. This may be understood by recognizing that the thermal efficiency of a gas turbine engine is

$$\eta_{th} = 1 - \left(\frac{1}{r_p}\right)^{\frac{k-1}{k}} \tag{1.1}$$

where k is the ratio of specific heats and r_p is the pressure ratio across the compressor. Assuming that the engine operates under the ideal conditions of the Brayton Cycle and that the pressure ratio across the turbine is the same as that of the compressor, the engine efficiency simplifies to

$$\eta_{th} = 1 - \frac{T_4}{T_3} \tag{1.2}$$

since it may be shown that

$$\frac{T_3}{T_4} = r_p^{\left(\frac{k-1}{k}\right)} \tag{1.3}$$

where T_3 and T_4 are the temperatures at the inlet and outlet of the turbine, respectively. Further details concerning this derivation are discussed by Dusinberre and Lester (1962).

Equation (1.2) supports the claim that in order to increase the engine efficiency a designer may simply drive up the combustor exit temperature which will increase the temperature at the inlet of the turbine. Unfortunately, significant increases in the combustor temperature can expose engine components to conditions that exceed their material limitations jeopardizing the safety tolerances of the design. Modern gas turbine engines counteract this by employing sophisticated cooling techniques to thermally

protect the components. These techniques include actively cooling the components with relatively cooler air as well as passively protecting the system by improving the material durability of the components. The first-stage turbine vanes and blades are the focus of much of the effort to thermally protect the engine because the first stage components are exposed to some of the highest temperatures in the engine. Thermal protection techniques, if implemented correctly, allow for an increase in the combustor temperature and an improvement in the overall efficiency of the engine. The result has been an increase in combustor temperature from approximately 900°C (1650°F) in the early 1950's to temperatures now approaching 2000°C (3630°F) with aviation engines such as Pratt and Whitney's J57 and F135, respectively. The aforementioned advances in turbine inlet temperature are discussed by Soechting (1999) and Langston (2007).

Improved thermal protection of turbine components can also lead to significant improvements in engine life. According to Soechting (1999), a 13°C (25°F) increase in metal temperature of a first-stage turbine vane will result in a two-fold (2x) reduction in airfoil durability. Reduced component life increases maintenance costs for engine operators and directly affects system profitability. This is particularly true for power generation facilities that are designed to operate continuously without prolonged down time that would allow for replacement of turbine components. Consequently, a detailed understanding of the interactive effects of both active and passive thermal protection techniques is required to optimize thermal efficiency, minimize operating costs, and maximize the life span of modern gas turbine engines.

1.1.3. Thermal Protection Techniques

As previously mentioned, gas turbine engines employ various cooling techniques to protect components that are exposed to the most extreme thermal environments. One thermal protection technique is to convectively cool internal passages within the engine components with relatively cooler air, or 'coolant', bled off of the compressor upstream of the combustor. The internal coolant can also be utilized in another thermal protection technique called film cooling. Film cooling uses small discrete holes in the wall of an engine component to emit internal coolant onto the components external surface. This additional layer of relatively cooler fluid creates a larger temperature drop between the hot gas path and the component surfaces. A diagram of a typical film cooled turbine airfoil is shown in Figure 1.4. Distinct film cooling holes can be seen in the right hand image of this figure. Figure 1.5 provides a generic picture of how coolant emits from film cooling holes and covers the surface of a turbine component. Bogard and Thole (2006) provide a thorough review of the physics and general characteristics of film cooling.

Gas turbine engines can also be passively protected by improving the durability of the metal used for the engine components. As discussed by Soechting (1999), significant research was focused on this effort from 1960 to 1985 resulting in a 100°C improvement in the operating temperature of turbine blades. This improvement allowed the nickel-based components to approach temperatures of 1100°C. Modern systems are now exceeding metal operating temperatures of 1200°C which is approximately 150°C below the melting temperature of the materials, according to Perepezko (2009). Langston

(2007) reported that the melting temperature of some super alloys may be in excess of 1400°C. Utilization of new materials such as molybdenum (Mo) and niobium (Nb) alloyed with silicon (Si) may push the operating temperature of the metals even higher.

The material durability of the engine can be further improved by covering the surface of the components with a thin layer of material that is able to protect the underlying metal from harsh high temperature environments. Thermal barrier coatings (TBC's) are comprised of a layer of high temperature resistant ceramic material with a low thermal conductivity as well as an oxidation resistant bond coat that attaches the TBC to the surface of the turbine component. According to Meier and Gupta (1994), TBC's can provide a 150°C reduction in the metal temperature of the component during engine operation. State-of-the-art TBC's can be expected to provide an even larger temperature drop. Padture *et al.* (2002) provided an overview of gas turbine TBC's and discussed metal temperature reductions of 300°C due to the presence of TBC. Figure 1.6 shows the cross-section of a scanning electron micrograph (SEM) of an electron-beam physical-vapor deposited (EB-PVD) TBC on the surface of a turbine blade.

1.2. Modeling Turbine Systems

Historically, designers of turbine components must balance the extremely high costs of full scale rig tests with the uncertainty inherent to smaller, more simplistic experiments. The smaller experiments have required simplifications of the complicated fluid dynamic and heat transfer physics that exist in an operating gas turbine engine. The simplifications have led to the practice of decoupling the effects of internal cooling from the effects of film cooling with the use of an adiabatic wall condition. An adiabatic wall

means that there is no heat transfer across the wall of the engine component. This is accomplished by assuming that the wall of a turbine component has a thermal conductivity of zero. This prevents any thermal interaction between the external film cooling and the internal convective cooling. This strategy has been used by experimentalist in order to simplify the system and isolate the effects of external film cooling. In reality, turbine components are not adiabatic, and as a result, the adiabatic wall condition does not account for the conjugate effects that occur in a real engine (i.e. the combination of internal convection, external film cooling, 3-D wall conduction, etc). This can have a profound effect on the perceived performance of a given design as shown by Dees (2010) and the results that will be presented herein.

Adiabatic effectiveness, η, is defined as

$$\eta = \frac{T_\infty - T_{aw}}{T_\infty - T_{c,hole\ exit}} \tag{1.4}$$

where T_∞ is the temperature of the hot gas path, T_{aw} is the surface temperature of the adiabatic wall, and $T_{c,hole\ exit}$ is the temperature of the coolant at the exit of the film cooling hole. Ideal film cooling would mean that the surface temperature of the wall was the same temperature as the coolant, resulting in an adiabatic effectiveness value of η = 1.0. The performance of a given film cooling design is also dependent upon how it affects the local convective heat transfer. This is important because the presence of film cooling can actually increase the convective heat transfer coefficient. The convective heat transfer coefficients h_f and h_o are measured in order to quantify the change in

convective heat transfer coefficient with and without film cooling, respectively. The ratio of these coefficients is the heat transfer augmentation which is defined as

$$\frac{h_f}{h_o} = \frac{\left(\frac{q"}{T_{aw} - T_{w,e}}\right)_{\text{with film cooling}}}{\left(\frac{q"}{T_{\infty} - T_{w,e}}\right)_{\text{no film cooling}}} \tag{1.5}$$

where q" is the heat flux on the external surface of the turbine component and $T_{w,e}$ is the external surface temperature of the component wall. Notice that the driving temperature in the case with film cooling is defined as the adiabatic wall temperature, T_{aw}. Once determined, the adiabatic effectiveness and heat transfer augmentation are often used to describe some of the boundary conditions for a computational solution of a realistic turbine component. However, adiabatic effectiveness does not account for conjugate heat transfer effects. Consequently, the use of adiabatic effectiveness as a boundary condition may not yield the correct computational solution for the operating metal temperature of the turbine component. The metal surface temperature of a conducting (i.e. not adiabatic) turbine component can be non-dimensionalized and expressed as the overall effectiveness, ϕ, which is defined as

$$\phi = \frac{T_{\infty} - T_{w,e}}{T_{\infty} - T_{c,vane\ inlet}} \tag{1.6}$$

where T_{∞} is the temperature of the hot gas path and $T_{c,vane\ inlet}$ is the temperature of the coolant at the inlet of the turbine vane. It is most appropriate to define the coolant temperature at the inlet of the turbine vane. This is due to the fact that the ideal cooling performance of a conducting vane with internal convective cooling would be for the

external wall temperature to be equal to the temperature at the inlet of the vane (i.e. $T_{w,e} = T_{c,vane\ inlet} \rightarrow \phi = 1.0$). Of course, ideal cooling with $\phi = 1.0$ is not possible in a realistic system. If the coolant temperature were defined at the exit of the film cooling hole, similar to the adiabatic case, it would be possible to have an overall effectiveness of $\phi > 1.0$ due to the internal convective cooling.

As mentioned above, the adiabatic wall assumption does not capture the complete behavior of a turbine component. As a result, the practice of using adiabatic effectiveness and heat transfer coefficient augmentation to determine the final operating temperature of a turbine component has limitations. As shown by Harrison and Bogard (2008) and Dees *et al.* (2011), conjugate heat transfer effects may have noticeable effects on the true boundary condition. For instance, the adiabatic wall temperature determined via measurement of the adiabatic effectiveness has often been assumed to be the driving temperature for convective heat transfer on a film cooled model. Harrison and Bogard (2008) and Dees *et al.* (2011) found that this is not always the appropriate driving temperature if conjugate effects are accounted for. Consequently, renewed interest in modeling a conducting airfoil (i.e. one that is NOT adiabatic) has risen over the past few years in an effort to provide more accurate boundary conditions for computational codes. However, simply matching the thermal conductivity of a scaled-up model to that of the components in the engine will not necessarily provide the appropriate thermal behavior. It is worthwhile to complete a simplified 1-D analysis of the heat transfer through a turbine vane wall in order to more fully understand this. The heat flux across the wall can be expressed as

$$q" = q"_{external} = q"_{wall} = q"_{internal} \tag{1.7}$$

Solving for the convective heat transfer at the internal and external surfaces of the vane as well as the conduction through the wall according to Fourier's Law it can be shown that 1-D energy balance is

$$q" = h_e\left(T_{aw} - T_{w,e}\right) = \frac{k}{t}\left(T_{w,e} - T_{w,i}\right) = h_i\left(T_{w,i} - T_{i,conv}\right) \tag{1.8}$$

where h_e and h_i are the external and internal convective heat transfer coefficients, respectively while k and t are the thermal conductivity and thickness of the vane wall. This assumes that the driving temperature for external convective heat transfer is the adiabatic wall temperature, T_{aw}, for a film cooled configuration in order to simplify the analysis. This analysis also neglects radiation. This assumption will be discussed in greater detail later in this chapter as well as in Chapter 3. The driving temperature for internal convection is defined by $T_{i,conv}$. Equation (1.8) can be rewritten as

$$q" = \frac{\left(T_{aw} - T_{i,conv}\right)}{{}^{1}/_{h_e} + {}^{t}/_{k} + {}^{1}/_{h_i}} \tag{1.9}$$

and

$$q" = \frac{\left(T_{aw} - T_{w,e}\right)}{{}^{1}/_{h_e}} \tag{1.10}$$

Combining Equations (1.9) and (1.10) and multiplying through by h_e results in

$$\left(T_{aw} - T_{w,e}\right) = \frac{\left(T_{aw} - T_{i,conv}\right)}{1 + Bi_w + {h_e}/{h_i}} \tag{1.11}$$

where Bi_w is the Biot number of the vane wall, which is defined as

$$Bi_w = \frac{h_e t}{k} \tag{1.12}$$

The Biot number is a ratio of the conductive to convective resistances and thus allows for the relative effect of conduction and convection to be scaled from one device to another. Equation (1.4) can be reorganized to be

$$T_{aw} = T_\infty - \eta\left(T_\infty - T_{c,hole\ exit}\right) \tag{1.13}$$

Combining Equations (1.11) and (1.13) yields

$$\left[T_\infty - \eta\left(T_\infty - T_{c,hole\ exit}\right) - T_{w,e}\right] = \frac{\left[T_\infty - \eta\left(T_\infty - T_{c,hole\ exit}\right) - T_{i,conv}\right]}{1 + Bi_w + {h_e}/{h_i}} \tag{1.14}$$

A similar analytical procedure has been followed by previous researchers such as Dees (2010) and Albert (2011). These previous works assumed that the coolant temperature for adiabatic effectiveness, the driving temperature for convection, and the coolant temperature for overall effectiveness are equal such that

$$T_c = T_{c,hole\ exit} = T_{i,conv} = T_{c,vane\ inlet} \tag{1.15}$$

This assumption is inherently flawed. Improvements to this assumption and improvements to the general analytical procedure are presented in Chapter 3. If Equation (1.15) is assumed to be correct then Equation (1.14) can be rewritten as

$$\phi = \frac{\left(T_\infty - T_{w,e}\right)}{\left(T_\infty - T_{c,vane\ inlet}\right)} = \frac{(1-\eta)}{1 + Bi_w + {h_e}/{h_i}} + \eta \tag{1.16}$$

which is the form presented by Dees (2010) and Albert (2011). The overall effectiveness, ϕ, can now be expressed as a function of the adiabatic effectiveness, η, the Biot number of the wall, Bi_w, and the ratio of the external to internal convective heat transfer coefficients. If a model vane matches these parameters then it should scale the thermal behavior of the system to yield overall effectiveness measurements that are equivalent to what are found in a real engine. This is the fundamental basis for why a "matched Biot number model" will accurately represent the thermal behavior of a real engine turbine vane. For the purposes of this analysis, the description of a "matched Biot number model" implies that the model matches all three of the necessary parameters, η, Bi_w, and h_e/h_i, not just the Biot number of the wall. It should be recognized that the Biot number will vary across the surface of the turbine vane due to changes in local heat transfer coefficient and will vary due to differences between engines. Consequently, properly scaling the model vane to a real turbine vane requires that a range of Biot numbers be matched. This analysis can be extended to 3-D showing that proper scaling of the thermal behavior of the turbine component is still dependent on the same three parameters as discussed by Nathan *et al.* (2012). Consequently, despite the fact that Equation (1.16) is a simplified 1-D model, it still outlines the appropriate constraints to properly design the model vane. A thorough description of the vane model used in this study is provided in Chapter 2 to show how the system was designed to represent the

non-dimensional temperature behavior of a turbine vane in a real engine. Improvements to this model are shown in Chapter 3, including the effect of thermal barrier coatings.

1.2.1. Active Cooling

Historically, film cooling performance has been measured by creating a simplified model of the heat transfer behavior of a turbine component by setting an adiabatic condition for the wall of the turbine component, as previously discussed. The theory behind doing this was to isolate the distinct behavior of the film cooling jets from the contributions of changing internal and external convective heat transfer characteristics. Adiabatic wall conditions have dominated much of the literature due to the simplified nature of the experiment. Unfortunately, using an adiabatic wall condition does not account for the conjugate effects that are present in a real engine that may alter the perceived performance of a given design. This will become evident in discussions below concerning the effects of a conducting wall as found in the literature as well as some of the results presented in Chapter 4 and Chapter 5.

Ideal film cooling can be achieved with a two-dimensional slot that emits the coolant tangentially onto the surface of the turbine component. A two-dimensional slot, which will herein be referred to as an ideal slot, has been studied by Bittlinger *et al.* (1994). A similar design attempting tangential emission was also studied by Rastogi and Whitelaw (1973) and Blair (1974). Unfortunately, such designs are impractical in real engines, except in specific locations such as the endwall, since a continuous slot in the wall of a turbine vane would jeopardize the structural integrity of the system. Consequently, engine designers have primarily resorted to using discrete designs such as

cylindrical or shaped holes, as discussed by Bogard and Thole (2006). There are numerous factors that contribute to the performance of such discrete designs. For example, the diameter of the holes, d, the pitch between holes, p, the angle of the hole with respect to the component surface, α, the length of the hole, L, etc. All of these factors have been studied in great detail assuming an adiabatic wall condition.

One of the most important factors in determining relative film cooling performance is to understand how a given design performs with changes in mass flow rate of the coolant. This factor is often characterized by calculation of the blowing ratio, M, which is defined as

$$M = \frac{\rho_c U_c}{\rho_\infty U_\infty} \tag{1.17}$$

The blowing ratio is a measure of the relative mass flux of the coolant emitted from the holes in comparison to the local mainstream flow. The coolant velocity, U_c, is taken as an average bulk velocity based on the metering hole diameter, d. The coolant flow rate may also be characterized by the momentum flux ratio, I, which is defined as

$$I = \frac{\rho_c {U_c}^2}{\rho_\infty {U_\infty}^2} \tag{1.18}$$

The momentum flux ratio is preferable for scaling the film coolant flow rate when coolant jet separation is a concern. Greater detail concerning coolant jet separation is provided in the following paragraph.

Film cooling designs often exhibit distinct coolant jet behavior dependent upon the blowing ratio or momentum flux that the system is operated at. For instance, as the

momentum flux increases it becomes more likely that the coolant jet will separate from the surface of the turbine vane. This is a result of the coolant jet momentum being sufficient enough to overcome the local momentum of the boundary layer. Consequently, instead of being turned onto the surface of the vane, the coolant jets blow off the surface for high blowing ratios. This results in significantly reduced adiabatic effectiveness and should thus be avoided. Round holes will generally exhibit initial signs of this behavior at a momentum flux ratio of approximately $I = 0.4$. Further discussion concerning this behavior can be found in Bogard and Thole (2006). One of the primary benefits of shaped holes is that they can operate at relatively high blowing ratios without causing jet separation. This is due to the inherent nature of the shaped hole design in which the exit of the hole is formed by a diffuser that decreases the momentum of the jet allowing it to more readily lie down on the surface of the turbine component. Bunker (2005) completed a detailed review of shaped holes reviewing the superior performance of the design over that of round holes. Figure 1.7 provides a comparison of typical round holes and two different shaped hole designs.

It is vital that the use of the coolant be optimized considering that any coolant that is bled off of the compressor leads to less air passing through the combustor. Consequently, over-utilization of film coolant results in less oxidizer to burn with the fuel. As a result, suboptimal use of coolant can actually result in a reduction of the engine efficiency. For this reason engineers have been searching for film cooling designs that can come close to replicating the performance of ideal slots while still meeting the necessary structural requirements for the system. One possible design that may meet

these design requirements is trenched film cooling. Trenched film cooling was first introduced by the work of Bunker (2002) as a method to increase the effectiveness of cylindrical holes. The original proposal by Bunker described the trench as being a transverse slot on the body of the turbine airfoil within which cylindrical holes were situated. Bunker discussed that this design could be created by masking the spanwise region over a row of cylindrical holes, applying TBC to the surface of the airfoil and then removing the mask. This would leave behind a slot with the desired embedded cylindrical holes.

Waye and Bogard (2006) and Dorrington *et al.* (2007) provided extensive studies of the trench design and found that it could provide significant improvement to adiabatic film cooling effectiveness as compared to conventional cylindrical holes without a trench. The improvement in performance was attributed to the coolant jets impinging on the downstream wall of the trench spreading the coolant laterally before the coolant exited the trench. This lateral spreading allowed for a more uniform distribution of coolant on the surface of the vane downstream of the trench which provided more effective thermal protection of the surface as compared to the discrete nature of individual coolant jets. The impinging nature of the jets also allowed for much higher blowing ratios to be used without the detrimental effects of jet separation. It was found that the ideal trench was one in which the downstream wall was placed adjacent to the breakout of the round holes and maintained a minimum trench depth of $t/d = 0.75$, where t was the trench depth and d was the diameter of the embedded cooling holes.

Hylton *et al.* (1983) completed some of the first empirical modeling of a conducting airfoil which led to a better understanding of the thermal characteristics of a cooled airfoil component. Follow on studies by Turner *et al.* (1985) and Hylton *et al.* (1988) improved the model configuration to incorporate more realistic film cooling designs. As previously mentioned, it is required to match both the Biot number as well as the ratio of the internal to external heat transfer coefficients in order to properly model the thermal fields of an engine component. This was not done by Hylton *et al.* (1983, 1988) and Turner *et al.* (1985); however, these studies provided relatively simple designs that have acted as benchmarks for a wide range of additional empirical and computational work.

Dees *et al.* (2009, 2010, and 2011) expanded on the idea of a conducting model by designing and testing a 12x scale first stage turbine vane with internal cooling and active film cooling. The vane chosen for that study was the C3X that was used in the aforementioned work completed by Hylton *et al.* (1983). However, the internal coolant passages of the vane used by Dees *et al.* (2009) were very different than the design used by Hylton *et al.* (1983). Dees *et al.* (2009) manufactured the vane with an epoxy with the appropriate thermal conductivity such that the vane was a matched Biot number model. That work allowed for the first thorough collection of suction side film cooling data on a matched Biot number model vane and will be used as a baseline for comparison to some of the data collected in this study.

Albert (2011) also completed a thorough assessment of film cooling with a matched Biot number vane. Albert's work focused on the effects of round hole and

trench film cooling on the pressure side of the vane with an active showerhead. The use of the word "showerhead" in this context refers to a dense array of film cooling holes in the stagnation region of the vane. In this case, the showerhead was comprised of three rows of round holes. Albert found that the trench outperformed the round holes due to the superior spreading of the coolant as well as reduced separation. That work also simulated the effects of active contaminant deposition which will be discussed in greater detail in Section 1.3. Albert's work will also be used as a baseline for comparison to pressure side film cooling results.

Harrison and Bogard (2008) completed a computational study investigating how using the matched Biot number method to directly measure the non-dimensional surface temperature as compared to coupling adiabatic effectiveness and heat transfer augmentation can result in different boundary conditions. This work was vital in understanding the importance of using the matched Biot number method to ensure that the proper boundary conditions are being used in future computational work. Shih *et al.* (2010) completed a computational study investigating the validity of the matched Biot number method in properly modeling the thermal behavior of a real engine component. That work further supported the claim that by matching the Biot number and the ratio of heat transfer coefficients the model will accurately reflect the non-dimensional surface temperatures of a real engine.

It is of particular importance that the value of ϕ is well understood across the entire airfoil in order for engine designers to improve modern engines. A general rule of thumb in the design of gas turbine airfoils is that a 20°C (~70°F) increase of the

maximum surface temperature will lead to a 50% reduction in the airfoils oxidation life as reported by Albert (2011). Soechting (1999) reported even tighter tolerances. For a typical gas turbine engine, the temperature of the combustor gas entering the first stage of the turbine may be near T_∞ = 1500°C (2730°F) while the temperature of the cooling air is roughly T_c = 540°C (1000°F). This means that a variation of $\Delta\phi$ = 0.05 is equivalent to a change of approximately 50°C (120°F). This magnitude of change on the surface of the airfoil would jeopardize the oxidation life of the part. Consequently, it is of vital importance that the surface temperature of the vane is accurately and precisely measured in order to provide the best possible understanding of the airfoils thermal behavior for future computational fluid dynamics studies and full-scale engine testing. Matched Biot number models are one way of providing increased accuracy in determining how an engine component will behave thermally.

1.2.2. Thermal Barrier Coatings

Another technique for providing thermal protection is to apply a thermal barrier coating (TBC) to the external surface of critical engine components. TBC materials, such as yttria stabilized zirconia, provide a thin layer of low conducting material to create a large temperature drop between the hot gas path and the component walls. The majority of work concerning thermal barrier coatings has been focused on improvements in material properties, such as thermal conductivity and oxidation resistance. Meier and Gupta (1994) provided an overview of the evolution of TBC materials. The primary focus of this classic study was to emphasize the importance of understanding the cyclic

thermal spallation life of different TBC materials and application methodologies. The study also highlighted the benefits of electron beam-physical vapor deposited (EB-PVD) coating methods over other application methodologies. According to Meier and Gupta, the application of TBC can reduce the temperature at the interface of the TBC and the turbine vane wall by approximately 170°C (340°F). This interface temperature will herein be described as the 'metal' temperature unless otherwise specified. Bose and DeMasi-Marcin (1997) reviewed the experiences of Pratt & Whitney in developing successful TBC's for gas turbine applications. A primary focus of this work was to review TBC durability issues. Schlichting *et al.* (2003) also studied durability issues by focusing on the failure mechanisms of plasma-sprayed TBC's and the expected cyclic life of the coatings. They reported that TBC's can reduce the metal temperature by 100 – 300°C.

Feuerstein *et al.* (2008) reviewed the benefits and disadvantages of multiple TBC coating methodologies in terms of their thermal protection results and economic demands. Depending on the coating methodology, Feuerstein *et al.* (2008) reported that yttria stabilized zirconia, a typical material used for TBC application, could have a conductivity between $k = 0.83 – 1.71$ W/mK. The higher end of this range was reported to be for the application method of EB-PVD which has typical been used in the most advanced engines due to its cyclic durability. EB-PVD, however, does require higher capital requirements as compared to other application methods. Boyle (2006) discussed many different benefits of relying on TBC's in the design process. One benefit is the fact that by eliminating external film cooling, and relying solely on internal cooling and TBC,

the surface boundary layer remains laminar over a larger portion of the vane surface. This benefit is particularly applicable to smaller turbines in which the Reynolds number of the vane passage is lower than that of larger scale engines. Tan *et al.* (2010) developed a method to embed thermocouples within a realistic TBC. This allowed for detailed measurements of thermal conductivity and quantification of sintering effects under various thermal conditions.

Few studies have combined the effects of TBC and film cooling effectiveness. Na *et al.* (2007) completed a computational analysis of the effects of conjugate heat transfer with TBC on a flat plate with cylindrical holes at $M = 0.3$ and 0.5. This work showed that the inclusion of TBC creates more discrete film coolant jets in terms of temperature on the exterior surface, i.e the surface of the TBC, as would be expected. It also showed that the TBC improved the cooling performance at the interface of the TBC and vane wall. Changes in the blowing ratio from $M = 0.3$ to 0.5 did little to alter the temperature distribution within the simulated super alloy. The only high resolution empirical film cooling study found in the literature for a matched Biot number model with TBC was the work completed by Maikell *et al.* (2009). This work was completed on two leading edge models with varying coolant hole configurations. The first configuration had one row of cylindrical coolant holes on the stagnation line. The second configuration had three rows of coolant holes where one row was on the stagnation line and the other two were located 25° off the stagnation line opposing each other. The dimensions and properties of the simulated TBC were chosen to properly scale the thickness and conductivity ratios of the blade model and TBC materials in an actual engine. As would be expected the TBC

contributed significantly to increasing the overall effectiveness at the interface of the simulated TBC and leading edge while the surface temperature of the TBC approached that of the mainstream. It was also found that the TBC allowed the leading edge to maintain relatively high cooling performance levels even with increasing angles of attack, up to $\alpha = \pm 5°$. Davidson *et al.* (2011) and Davidson *et al.* (2012) also reported on the effects of TBC on film cooling performance with a matched Biot number model. The results of these papers are expressed within this document.

It is not surprising that there is limited film cooling data available that studies the effect of TBC. This may be explained by recognizing that most work that has been completed in the past has been with adiabatic models. Placing a low thermal conductivity TBC on top of an adiabatic model will not facilitate greater knowledge of the conjugate interaction of TBC and film cooling. There have been a few high temperature turbine rigs that have allowed for a study of film cooling on a conducting airfoil with TBC. The results from most of these studies are limited significantly by the difficulty of imaging the high temperature rotating surface. Furthermore, the spatial resolution of these studies is also limited considering that the turbine components are not scaled-up.

1.3. Deposition

Throughout the life of a gas turbine engine the system undergoes deposition, erosion, and corrosion (DEC) that detrimentally affects the performance of the engine. Contaminants in the gas path of the engine are a primary cause of the DEC. These contaminants may be derived from the ingested inlet air, such as sand or other debris, as

well as the impurities and ash particles that are a byproduct of combusted fuel. DEC levels can be significant for most gas turbine engines due to their large mass flow rates and operating lives which are often between 50 – 500 kg/s and 10,000 – 100,000 hours, respectively. The resulting effect of DEC is most commonly observed as a roughening of the turbine airfoil surface which is often due to buildup of contaminants or spallation of the thermal barrier coating. The roughing of the surface leads to decreased aerodynamic efficiency of the airfoil, increased heat transfer to the surface, and decreased film cooling performance.

Deposition is one of the primary causes for decreased cooling performance of the turbine airfoil. This is most acute on the high pressure turbine vanes and blades immediately downstream of the combustor. This is, in part, due to the fact that this is the highest temperature region of the turbine. Consequently, the contaminant particles remain molten in this region which allows them to adhere more easily to the surface of turbine components rather than bouncing off as they do once they cool and harden. Figure 1.9 and Figure 1.10 provide an understanding of how contaminant depositions both roughen the surface of a turbine airfoil and interact with the presence of film cooling holes. Figure 1.9 shows the resulting deposition after an airplane inadvertently flew through a volcanic ash plume. This figure shows explicitly how depositions can dramatically alter the surface characteristics of turbine components leading to a detrimental shift from the intended design conditions. Looking closely at this picture one may observe that the deposition is heaviest on every other vane as well as in proximity of the rows of film cooling holes. This behavior suggests that the deposition behavior is

dependent on the engine design upstream of the turbine inlet as well as the unique film cooling pattern of the turbine component in question. Figure 1.10 provides a more detailed look at deposits near a film cooling hole. The accumulation of deposits at the exit of the cooling hole will lead to alterations in the behavior of the coolant exiting the hole. This will, once again, lead to a shift away from the behavior that was originally designed for the cooling holes and thus a decrease in thermal protection of the turbine component.

Coal ash deposition on turbine components has been a major motivator for research in the field due to the consequential performance decrease of the engine. Walsh *et al.* (1990) developed an analytical model for estimating deposition levels and growth for coal ash on a steam-cooled furnace tube. Walsh generated experimental data to calibrate the analytical model with the use of two separate coal specimens with varying iron content and grind qualities. Cross-section images of the deposits were obtained which showed increased distortion, or splattering, of high iron content particulates as compared to the spheroidal appearance of lower iron particulates. They found that one of the primary drivers for depositions is whether or not the contaminant in question is molten which may increase the number of particles that adhere rather than rebound from a surface when they make contact. The analytical model included two other deposition characteristics that are important in understanding the longer term deposition results. The first of these is that the surface of the deposits begins to approach the temperature of the hot gas path with increasing deposition thickness due to the increased thermal resistance from the surface of the airfoil. This increased surface temperature leads to a greater

number of molten particles adjacent to the surface and thus an increased rate of deposition. The second important characteristic is that the growth in thickness of the deposits is eventually offset by increased erosion of the particles from the surface. This characteristic is described as a "self-regulating" behavior of the deposits and leads to a steady-state thickness of the deposits once the engine has operated for an extended period.

Wenglarz and Fox (1990) generated empirical data of coal ash depositions rates on turbine components as a function of time. This study found that the deposition rates increased significantly with gas temperature and component surface temperature. It was speculated that this was a result of a larger number of molten particles near the surface of the turbine components. It was also found that higher gas stream velocities were more likely to deliver molten particles to the surface of the turbine vane. Wenglarz and Fox (1990) discussed the fact that deposition may be increased for fuels with higher carbon fractions due to the presence of unburned hydrocarbons in the gas path. Increased deposition rates for high carbon fraction fuels were attributed to increased particulate size and particulate temperature if the particle continues to burn. The review paper by Hamed *et al.* (2006) describes the numerous studies that have been completed in order to understand erosion and deposition in turbomachinery components.

More recently, experimental work has been completed to model deposition on gas turbine components under engine-representative temperature and Mach number conditions. Much of this work has been completed at the Turbine Accelerated Deposition Facility (TADF) developed by Bons and colleagues at Brigham Young University and

more recently at The Ohio State University (Bons *et al.* (2005), Ai *et al.* (2008), Crosby *et al.* (2008), Lewis *et al.* (2011)). The strength of the TADF studies has been the fact that the contaminants are deposited under engine-representative environments. However, the set-up at the TADF does not accurately represent the flow field of a film cooled turbine which may be of utmost importance to properly model the deposition physics. The TADF forces the hot mainstream gas, laden with contaminants, past a small flat test coupon oriented at a relatively high angle with respect to the impinging mainstream as shown in Figure 1.11. This angle is typically 45° and presents a noticeably different flow field than engine conditions in which the mainstream flow through a vane passage is essentially parallel to the film cooled surface of the airfoil. Figure 1.11 also shows how this difference may have a direct effect on the behavior of the film coolant jets. As may be seen, the film coolant jets diverge as they progress downstream. According to the literature one should expect these identical coolant holes to have parallel coolant jets if they were on the body of a turbine vane. This supports the fact that the TADF does not properly model the important flow field characteristics that would be expected for a vane passage.

Never-the-less, the studies completed at the TADF are still a valuable source of information for the current work. Bons *et al.* (2005) studied the variations in deposition chemistry and physics for four different synthetic fuels. Bons *et al.* (2005) also varied particle loading by adjusting the amount of contaminant that was introduced into the mainstream flow. They found that the thickness of the deposits, which ranged from 1-4 mm for coal ash, varied linearly with respect to the particle loading tested. The coal ash

deposits revealed an isotropic, porous structure. Evidence was obtained showing penetration of the deposits into the cracks of the TBC applied to the test coupon.

Ai *et al.* (2008) focused on deposition characteristics of coal-derived syngas contaminants adjacent to film cooling holes at the TADF. They obtained results with and without thermal barrier coatings for both round and shaped film cooling holes. The deposits typically formed upstream of the film cooling hole breakout as well as between the film coolant jets. No significant deposits formed downstream of the shaped film cooling holes. Ai *et al.* (2008) found that the deposition patterns became more defined on the coupons with TBC as blowing ratio increased. The capture efficiency, or the ratio of the amount of deposited contaminants to the amount of contaminant added to the mainstream, was nearly an order of magnitude higher from the test coupons with TBC as compared to those without. This was attributed to the higher surface temperature of the TBC as compared to the exposed metal coupons. In all cases, the total amount of deposition was reduced with increasing blowing ratio. Crosby *et al.* (2008) also completed a study at the TADF investigating the effects of temperature and particle size on deposition behavior. This work showed increasing deposition rates with increased particle size. It also found that the contaminants began to deposit when the coupon surface was above the threshold temperature of 960°C (1760°F).

Another TADF study was completed by Lewis *et al.* (2011). This was follow-on work from Ai *et al.* (2008) that mapped the deposition geometries and created stereolithography models of the deposition on a film cooled flat plate. This allowed for measurement and comparison of both adiabatic effectiveness and heat transfer

augmentation of a clean surface to that of realistic deposition geometries. Lewis *et al.* (2011) found that large deposits immediately upstream of the film cooling hole breakout led to a decrease in area-averaged heat flux. This was attributed to the fact that the upstream roughness acted as an "effective ramp" forcing the mainstream flow to generate a separation cavity within which the film coolant could reside. Lewis also found that since the deposits typically form between the coolant jets they create what are essentially channels for the coolant. This allows for higher local effectiveness within the channels.

Webb *et al.* (2011) recently completed a high temperature study which focused on the deposition behavior of four different coal ash samples on realistically cooled nozzle guide vanes. This work was completed in the Turbine Reacting Flow Rig (TuRFR) at The Ohio State University. This was a second generation rig improving upon the design of the aforementioned TADF. The strength of the TuRFR is that the contaminants deposit on the surface of vanes as compared to the flat coupon in the TADF. The result is that the flow behavior should more accurately model what happens in a real engine. Webb *et al.* (2011) incorporated discrete film cooling holes in the surface of the vane in order to determine how the film cooling altered deposition behavior. Film cooling was found to have a significant effect on deposition behavior for the test case using bituminous fly ash. This was attributed to the film cooling lowering the surface temperature of the vane significantly below the melting point of the bituminous fly ash which reduced the tendency for the particles to adhere to the vane surface. It was also found that deposits tended to accumulate within film cooling holes near the leading edge.

Spallation of larger deposits was observed during testing explained by increased aerodynamic drag that overcame adhesion forces.

Somawardhana and Bogard (2007) studied how the performance of the trench could be affected by the presence of surface roughness on the vane and near-hole obstructions. The roughness and obstructions were intended to be representative of realistic engine component degradation resulting from deposition, erosion, and corrosion (DEC). This study found that the adiabatic film cooling effectiveness of the trench design was relatively insensitive to the presence of the various surface roughness conditions as compared to more conventional cylindrical holes. However, the surface roughness modeling was simplified by using materials such as sand paper to represent the surface degradation and thus may not accurately model how a trench would perform under active deposition from contaminants in the mainstream.

Simulations of deposition on a simulated turbine blade leading edge were completed by Albert *et al.* (2009) using a molten wax sprayer that was designed to generate particles that match the Stokes number for typical engine conditions. The idea behind using the wax was to match the semi-molten nature of the contaminant particles in a real engine. This work found a self-regulating behavior in the deposition thickness similar to the previously discussed findings of Walsh *et al.* (1990). A similar molten wax spray technique was used by Lawson and Thole (2010) to study deposition on turbine endwall surfaces. Their measurements showed deposits causing a decrease in adiabatic film effectiveness for a range of blowing ratios. A later study by Albert and Bogard (2011) used the molten wax method to study deposition effects on the pressure side of a

matched Biot number film cooled turbine vane model. The film effectiveness values for standard round holes and a shallow trench configuration were measured with and without deposition on the surface. Results from these measurements showed no significant effect due to these depositions. However, the deposit thickness was quite small, referred to by Albert and Bogard (2011) as being "very thin" amounts of deposition. The film effectiveness may be more greatly affected under heavier deposition. This study also found that the deposition thickness was strongly influenced by the temperature of the vane surface. Albert (2011) provided a complete review of the deposition work with no TBC that was completed at The University of Texas at Austin prior to the current study. Davidson *et al.* (2011) discussed the majority of the deposition data that will be presented herein for a film cooled model with a TBC.

1.4. Objectives for the Current Study

The intention of this body of work was to provide the first open literature experimental assessment of the thermal behavior of a modeled first-stage turbine vane with active film cooling and a thermal barrier coating, including the effects of deposition. This work builds on previous efforts conducted at The University of Texas at Austin by researchers such as Dees (2010) and Albert (2011) but extends that work to consider the effects of thermal barrier coatings. The specific goals and motivations are summarized as follows:

1.) Determine how round hole film cooling and internal convective cooling affect the cooling performance of a vane with a thermal barrier coating.

Historically, studies have focused almost exclusively on adiabatic effectiveness as a measure of film cooling performance. It is vital to determine if the film cooling performance as understood by adiabatic effectiveness measurements is applicable to systems with TBC's. The necessity for this can be understood by recognizing that recent increases in combustor temperatures now require that turbine components utilize TBC's in order to operate safely. This was not necessarily true for the engines of yesteryear which operated at lower combustor temperatures reducing the importance of incorporating a reliable TBC. The results from this study are the first open literature data showing the cooling performance of a conducting vane with a TBC in comparison to the expectations predicted by adiabatic effectiveness measurements.

2.) Determine how the cooling performance of a vane with a TBC is altered due to changes in the film cooling configuration.

Various cooling designs were studied including round holes, craters, and trenches. The performance of the trench design is of great interest since it has shown superior adiabatic effectiveness. The trench design was originally proposed to be formed with the use of TBC overlying a conducting metal wall. The measurements from this study are the first open literature results showing the performance of a trench formed with a TBC.

3.) Compare the cooling performance of an ideal and realistic trench.

The trench design can be made to be "ideal" based upon the findings of previous adiabatic effectiveness studies. However, the designs of the previous studies did not necessarily account for manufacturing constraints that will exist in a real engine. Consequently, a "realistic" trench design is proposed and tested to compare the cooling performance to that of the ideal trench.

4.) Provide detailed temperature measurements at the interface of the TBC and vane wall as well as on the external surface of the TBC.

The temperature at the interface of the TBC and vane wall is of paramount importance since the vane metal cannot exceed specific temperature requirements in order to maintain system integrity. These measurements are the first of their kind in the open literature.

5.) Develop an analytical model for predicting the thermal behavior of a film cooled vane with a TBC.

A simplified analytical model provides great physical insight into the cooling performance of an engine component with a TBC as compared to previous studies that did not incorporate a TBC.

6.) *Develop a molten wax deposition method that simulates heavy loading of contaminants in the hot gas path of an engine.*

Recent efforts to utilize higher combustor temperatures along with coal-derived syngas may produce increased contaminant concentrations in the gas path of future engines. Contaminant deposition on the surface of turbine components can significantly damage the ability for the engine to operate safely and efficiently. This can be well understood by the extreme contaminant case and aftermath of the 2010 eruption of Eyjafjallajökull in Iceland that caused the worst peacetime air travel disruption in history due to the ash cloud over the northern Atlantic. The weeklong halt in flights cost airlines hundreds of millions of dollars. The importance of the simplified testing method employed in this study can be understood by recognizing that verification testing of an engine with active contaminant deposition can ruin a $10MM dollar machine according to Wenglarz (2004). Improved proof-of-concept testing of deposition can significantly reduce the risk associated with full-scale engine operation.

7.) *Determine how active contaminant deposition alters the thermal behavior of a film cooled vane with a TBC.*

The work completed in this study is the first high resolution open literature assessment of how heavy contaminant depositions alter the cooling performance of a realistic turbine vane with a TBC. This study includes the first open literature data quantifying how contaminant deposition affects the temperature at the interface of the TBC and vane wall.

8.) Identify a film cooling configuration that is capable of mitigating the growth of deposition on the surface of the turbine component.

Mitigating contaminant deposition growth may allow for engine designs that are significantly more robust when subject to high loadings of contaminants in the hot gas path.

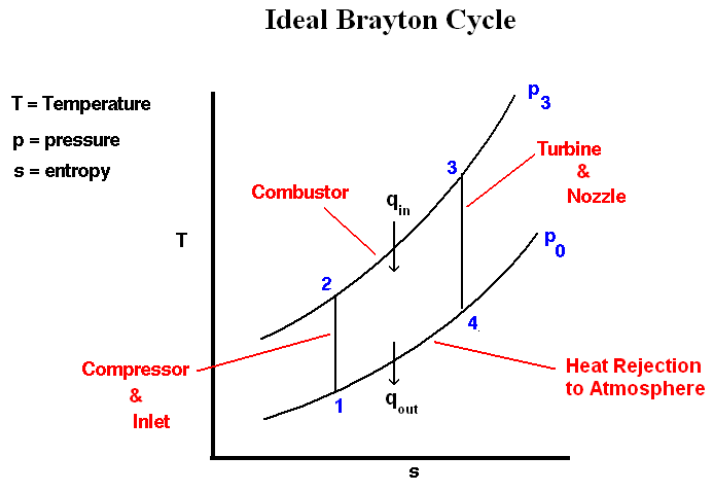

Figure 1.1: T-S Diagram of Ideal Brayton Cycle (web.mit.edu).

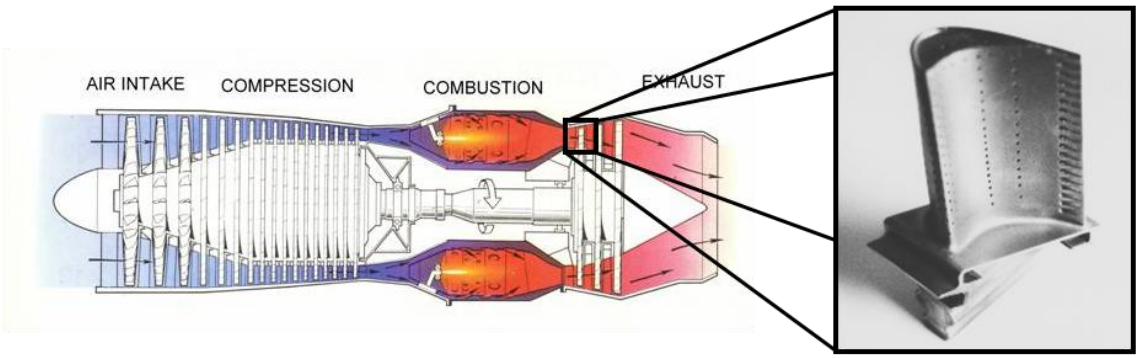

Figure 1.2: A gas turbine engine used for propulsion and a photograph of a first stage turbine blade.

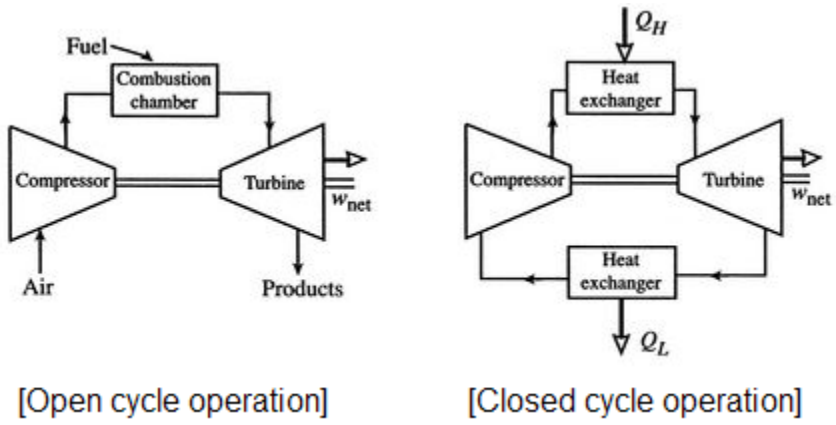

Figure 1.3: Open vs Closed cycle operation of a gas turbine engine (web.mit.edu).

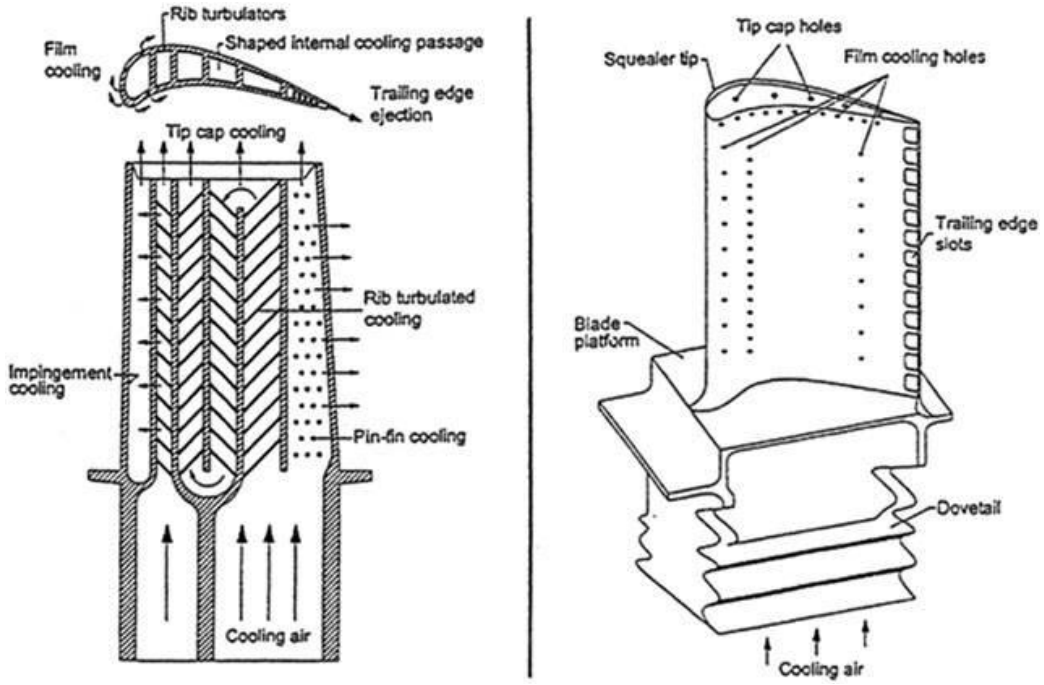

Figure 1.4: Schematic of a typical film cooled turbine blade (from Han et al., 2000).

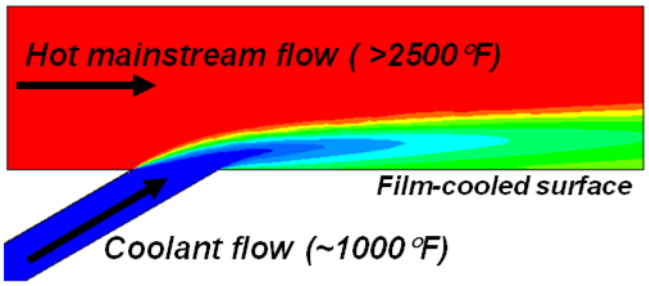

Figure 1.5: Representation of film cooling in a gas turbine engine (from Albert (2011)).

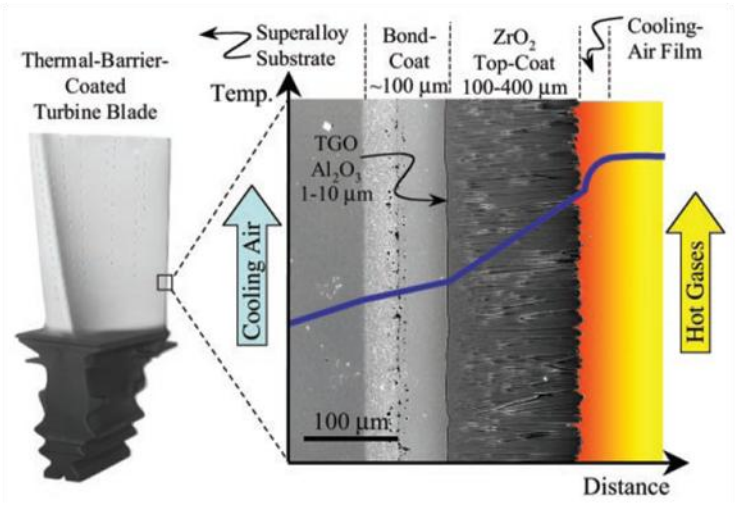

Figure 1.6: Diagram of the top-coat and bond-coat of a TBC on a turbine blade (from Padture *et al.* (2002), used with permission from AAAS).

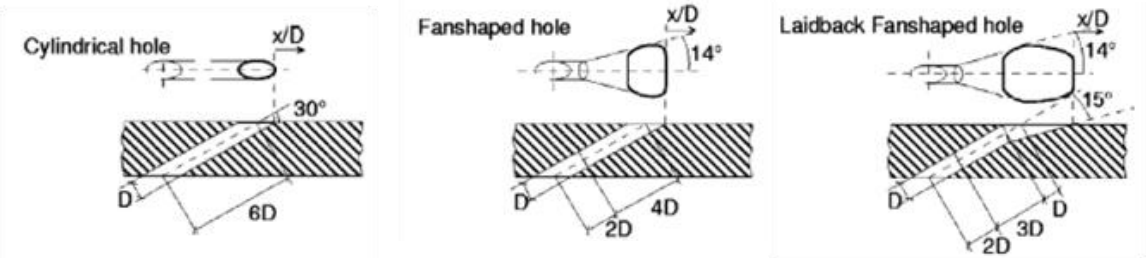

Figure 1.7: Comparison of round holes and different shaped hole designs (modified from Saumweber et al. (2003)).

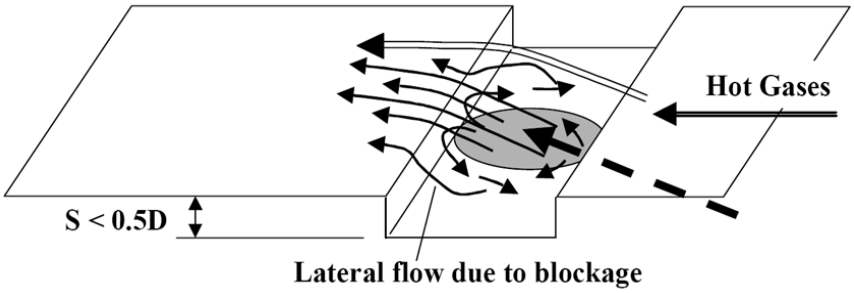

Figure 1.8: Sketch of shallow trench with embedded cylindrical hole and interaction of coolant and mainstream flow (from Bunker (2002)).

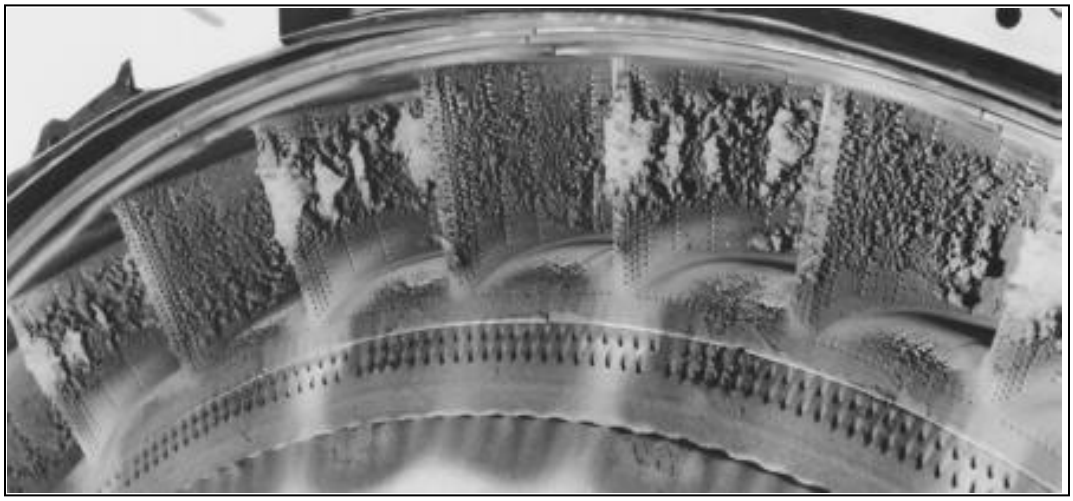

Figure 1.9: Volcanic ash deposits on first stage turbine vane (from Hamed *et al.* (2006)).

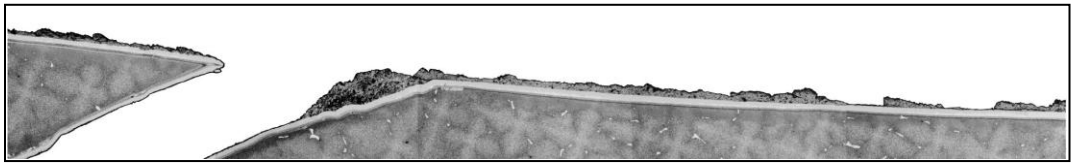

Figure 1.10: Surface contaminant deposition near film cooling hole (from Bogard *et al.* (1996)).

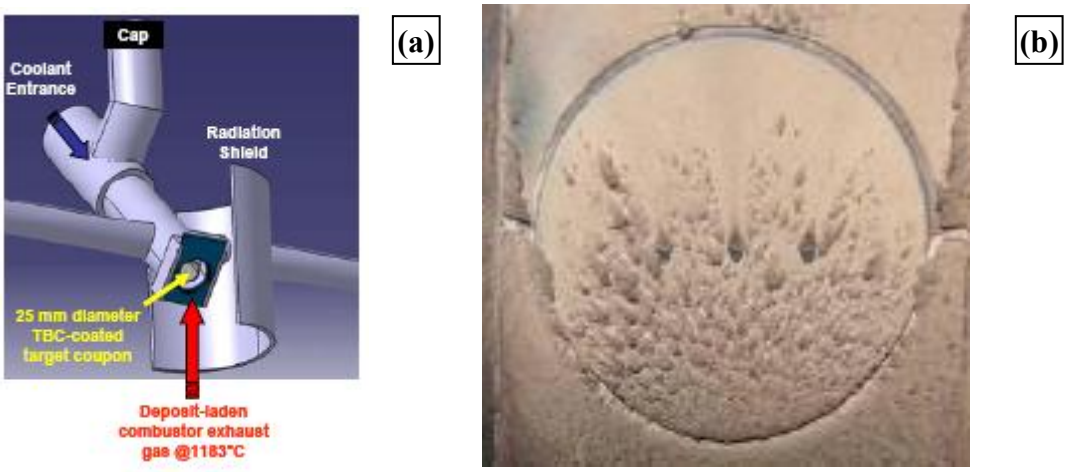

Figure 1.11: Turbine Accelerated Deposition Facility (TADF): (a) test section schematic (from Ai *et al.* (2008)) and (b) sample deposition topology of a film cooled coupon (from Lewis *et al.* (2011)).

Chapter 2

2. EXPERIMENTAL FACILITIES AND PROCEDURES

2.1. Experimental Facilities

2.1.1. Wind Tunnel

Experiments for this study were conducted at the Turbulence and Turbine Cooling Research Laboratory (TTCRL) at the University of Texas at Austin. The primary wind tunnel at this facility is a closed loop system driven by a 50 hp variable speed fan. One of the corners of the tunnel has been modified to accommodate a test section comprised of a three vane, two passage linear cascade. The center vane in the cascade is a model of a C3X airfoil scaled up by a factor of approximately 10. This airfoil was chosen to match the geometry of the airfoil used in the study by Hylton *et al.* (1983), as discussed by Dees (2010). A schematic of the corner test section is shown in Figure 2.1. The inlet velocity to the test section was set to $U_\infty = 5.8 \pm 0.05$ m/s. The center test vane has a chord length of $C = 531$ mm, defined as the distance from the stagnation point to the trailing edge. These conditions generate a Reynolds number on the order of 1×10^5 for a mainstream temperature of approximately $T_\infty = 301$ K. The Reynolds number at the inlet of the test section is similar to the inlet of a typical first-stage turbine vane. The geometric parameters defining the test section and the standard operating conditions are provided in Table 2.1.

Two different mainstream turbulence intensities were used during this study. The conditions were characterized by the turbulence intensity at the inlet of the linear cascade. The turbulence intensity was controlled by either installing or removing the turbulence

generator positioned 0.5 meters upstream of the linear cascade as shown in Figure 2.1. The generator grid consisted of 12 vertical rods 38 mm in diameter spaced 85 mm apart. The turbulence intensity of the mainstream was Tu = 0.5% with the grid removed. With the grid installed, an isotropic turbulence level of Tu = 21 ± 1% was generated across a width of ±0.4P, where P is the pitch between airfoils. The integral length scale was Λ_f = 4 cm for the higher turbulence condition. These measurements were taken at x/C = 0.27 in front of the leading edge of the center test vane. These results were obtained with the use of hot-wire anemometry and LDV as discussed by Albert (2011) and Ethridge *et al.* (2000).

Table 2.1: Test section parameters and operating conditions.

Parameter	Value	Units
Chord Length (*C*)	531	mm
Vane Span (*H*)	549	mm
Vane Pitch (*P*)	457	mm
Turning Angle	72	degrees
Mainstream Velocity (U_∞)	5.8 ± 0.05	m/s
Mainstream Temperature (T_∞)	301 ± 0.5	K
Density Ratio (*DR*)	1.2 ± 0.01	-
Inlet Reynolds Number	0.19×10^6	-

The pressure distribution around the vane could be altered with the use of adjustable walls built into the corner test section as shown in Figure 2.1. The goal of adjusting the walls was to ensure that the pressure distribution across the center test vane matched a CFD prediction for the pressure distribution in an infinite cascade. The CFD prediction was completed at GE Global Research Center, as discussed by Dees (2010).

This was accomplished by iterating on the wall location while actively measuring the pressure distribution across the vane with numerous embedded static pressure taps at the mid-span of the vane. During this iteration process, tufts were placed in the stagnation region of each vane in the cascade and were observed in order to ensure that the stagnation points were properly set for the cascade. Figure 2.2 provides a comparison of the measured pressure distribution and the CFD prediction for vane in an infinite cascade.

The wind tunnel facility at the TTCRL has a secondary flow loop in order to provide relatively cold air to the center test vane to simulate the coolant in a real engine. The parameter density ratio, *DR*, is regularly used to quantify the density difference between the hot gas path and the coolant. The density ratio is defined as

$$DR = \frac{\rho_c}{\rho_\infty} \tag{2.1}$$

where ρ_c and ρ_∞ are the density of the coolant and the mainstream, respectively. Typical engine conditions operate at density ratios near $DR = 2.0$. The current study operated at $DR = 1.2$. Bogard and Thole (2006) discussed the fact that in many instances film cooling performance is relatively insensitive to density ratio. The current study achieved a density ratio of $DR = 1.2$ by utilizing a coolant at approximately $T_c = 250$ K. This was accomplished with the secondary flow loop. The secondary loop functions by first drawing air off the mainstream flow upstream of the tunnel fan with the use of an in-line 7.5 hp radial blower as shown in Figure 2.3. The majority of air in the secondary loop is then forced through a heat exchanger cooled via liquid nitrogen. The colder air is then routed through two separate supply lines to feed the internal passages of the center test

vane. The flow rate of coolant is controlled by three separate gate valves. The flow rate through the coolant lines is measured with the use of orifice plates that were calibrated against a laminar flow element as discussed by Albert (2011).

It is vital to keep the relative humidity of the mainstream air within the tunnel as low as possible. The reason for this is to reduce the likelihood of frost formation on the external surface of the test vane as well as within the secondary flow loop and internal coolant passages of the vane. Excessive frost formation can significantly alter coolant behavior and thus detrimentally affect the accuracy of experiments. Two methods were used to reduce the humidity within the tunnel. The first of these methods was to purge the tunnel with 175 liters of liquid nitrogen. In general, this brought the relative humidity down to approximately 10%. The second method was to place desiccant packs in the tunnel once purge was completed. The presence of desiccant packs as well as operation of the nitrogen heat exchanger in the secondary flow loop often brought the relative humidity below 5% before testing began. This condition allowed for experiments to last for over 12 hours at $DR = 1.2$ without sign of frost growth on the surface of the vane model.

2.1.2. Vane Model

The center test vane was previously designed and constructed by Dees (2010) with recent improvement and modifications by Albert (2011). The vane was originally constructed from a pourable epoxy resin while more recently constructed vanes have been machined from DuPont Corian®. Both of these materials had a thermal conductivity of approximately $k = 1.0 \pm 0.1$ W/m-K. These materials were chosen in

order to properly match the Biot number of the model to that of the materials found in a real engine. As previously discussed, the model vane should match the non-dimensional thermal behavior of a real engine component if the Biot number, ratio of heat transfer coefficients, and adiabatic effectiveness are all properly matched. Figure 2.4 shows how the most recent test vane was designed with removable hatches. This allows for interchangeable film cooling configurations on the surface of the airfoil. This is a vital aspect for future work since it allows the single vane to have different film cooling configurations depending on the hatch that is used. Figure 2.5 provides a schematic of the vane with hatches in place as well as the general locations of vane feature in terms of *s/d*, where *s/d* = 0 is defined as the stagnation point. The vane design incorporated two internal coolant passages which can be seen in Figure 2.6. The forward passage was a U-bend channel with a fore and aft passage that directed the coolant into and out of the forward part of the vane, respectively. The rearmost passage was a straight channel described as the radial passage. All of the film cooling configurations were fed by the U-bend passage. Consequently, less coolant exited the U-bend as compared to the amount that entered the U-bend when active film cooling was utilized. The differential in mass flow rate between the inlet and exit of the U-bend was used to determine the mass flow rate of film coolant and consequently, the blowing ratio, *M*.

The flow rates, and hence Reynolds numbers, of the U-bend and Radial passages were altered to determine the effect of varying the internal convection. The internal Reynolds number was based on the bulk velocity of the coolant and the hydraulic diameter of the given passage. The maximum Reynolds number through the U-bend

passage was limited to Re_U = 40,000 due to the maximum output of the blower driving the secondary loop. The Reynolds number through the U-bend and Radial passage was set to $Re_U = Re_R$ = 20,000 for all cases with active film cooling. The various Reynolds number conditions are shown in Table 2.2.

Table 2.2: Summary of internal passage Reynolds Number conditions for the different experiments in this study.

Internal Passage Reynolds Number		Re_U=10,000 Re_R=10,000	Re_U=20,000 Re_R=20,000	Re_U=40,000 Re_R=20,000	*Tu*=0.5%	*Tu*=20%
t/d = 0.55 TBC	No Film	✓	✓	✓	✓	✓
	Active Film		✓		✓	✓
t/d = 1.2 TBC	No Film	✓	✓			✓
	Active Film		✓			✓

The current study incorporated a layer of cork to simulate the effects of a thermal barrier coating on a matched Biot number vane with active film cooling. Cork was chosen due to the readily available thicknesses, pliable nature, and appropriate thermal conductivity in order to properly scale the thermal behavior of the model to that of a real engine component. This was accomplished by scaling the ratios of the thickness and thermal conductivity between the TBC and vane model to that of real engine components. Numerous references were used to determine the expected range of parameters for the real engine vane. These values are reported in Table 2.3. The thermal conductivity of the cork was independently measured by setting a constant heat flux boundary condition while measuring the temperature drop across a known thickness. The experimental setup was designed to minimize heat loss by insulating all surfaces underneath and around the heat flux foil that was placed underneath the test material being studied. Temperature

measurements of the insulation surfaces found that the losses amounted to less than 4% of the heat flux from the heat flux foil. These losses were accounted for in the calculation of the thermal conductivity of the cork which was found to be $k_{cork} = 0.065 \pm 0.004$ W/m-K. Two cork thicknesses were tested in this study, $t/d = 0.55$ ($t = 2.3$ mm) and $t/d = 1.2$ ($t = 5.0$ mm). The inclusion of cork on the surface of the vane resulted in a 2% and 4% reduction in the area of the passages in comparison to the case with no TBC for the $t/d = 0.55$ and $t/d = 1.2$ TBC, respectively. This resulted in fractionally higher flow velocity through the passages when the cork was placed on the surface. The two different cork thicknesses were studied in order to assess the effect of increasing the thermal resistance of the simulated TBC. Table 2.3 shows that the parameters defining the models fall within the expected ranges for a real engine component.

Table 2.3: Comparison of vane and TBC matertial properties.

Parameter	Real Vane	*t/d* = 0.55 TBC Model Vane	*t/d* = 1.2 TBC Model Vane	Units
Vane Thickness	1.5 - 3.0 (Bunker, 2009)	12.7	12.7	mm
TBC Thickness	0.1 - 0.7 (Bunker, 2009) (Feuerstein, 2008) (Padture, 2002) (Soechting, 1999)	2.3	5.0	mm
Vane Conductivity	20 – 25 (Inconel X-750)	1.0	1.0	W/m-K
TBC Conductivity	0.8 - 1.7 (Feuerstein, 2008) (Padture, 2002)	0.065	0.065	W/m-K
Heat Transfer Coeff.	1000 – 10000 (Bunker, 2009)	25 – 90 (Dees, 2009)	25 – 90 (Dees, 2009)	W/m^2-K
TBC/Vane Thickness	0.05 – 0.5	0.18	0.39	-
TBC/Vane Conductivity	0.04 – 0.08	0.06	0.06	-
Vane *Bi*	0.1 – 1.5	0.3 – 1.1	0.3 – 1.1	-

The cork chosen for the experiments was purchased from Hobby Lobby in Austin, TX. The rolled material came in two separate reported thicknesses, 3/32" and 5/32" with dimensions of 24"x96" and 24"x48", respectively. The actual thickness of the cork was often slightly different than what it was labeled as. The thickness of the TBC was a combination of the thickness of the adhesive layer, the cork, and the primer and paint that were used to finish the exterior surface. The thickness of the t/d = 0.55 TBC was recorded as being 2.3 mm which was only the thickness of the cork not including the additional thickness of the adhesive layer and paint. This was a mistake that was recognized afterwards. Consequently, the final thickness may have been different than the thickness reported in Table 2.3 for the thinner TBC. Unfortunately, the final thickness of the thinner TBC was not recorded prior to it being destroyed. However, it can be estimated by recognizing that the thickness of the double sided tape was approximately 0.2 mm. The thickness of the primer and paint used for the thinner TBC was estimated to be 0.1 mm. Consequently, the thinner of the simulated TBC's may have been up to 0.3 mm thicker than the reported value. The thermal conductivities of the paint and tape were likely significantly higher than the conductivity of cork. This can be supported by recognizing that many plastics have a thermal conductivity between 0.1 – 0.5 W/m-K. The additional thickness due to the paint and tape will alter the thermal resistance of the TBC by approximately 4% assuming a conductivity for the paint and tape of 0.2 W/m-K. Since this effect is relatively small the original reported thickness of t/d = 0.55 was still used to define the thinner TBC. The reported thickness of the t/d = 1.2 TBC, t = 5.0 mm, included the thickness of the adhesive layer as well as the thickness

of the primer and paint. The thickness of the primer and paint used for the t/d = 1.2 TBC was approximately 0.7 mm. This was much thicker than the paint used for the t/d = 0.55 TBC. The additional layers of paint were utilized in order to ensure that the external surface of the cork was sealed. This was important since the t/d = 1.2 TBC was used in tests with active deposition.

The average surface roughness of the cork was Ra = 4.7 μm after it was primed and painted. This was measured with a contact profilometer. The roughness of as deposited TBC's in a real engine can vary from Ra = 1.4 to over 5.0 μm. The final surface roughness of a TBC is reduced below Ra = 0.75 μm with surface finish improvements according to Rigney *et al.* (1997). Consequently, the surface roughness of the simulated TBC was slightly too smooth considering that the model vane is approximately 10x scale of a real engine vane. The small difference in scaled surface roughness was not thought to have a significant effect on the thermal behavior of the vane. This conclusion was drawn based on the fact that the heat transfer and fluid dynamic behavior on the surface of the vane will likely be dominated by the presence of film cooling jets and high mainstream turbulence levels. Consequently, despite the fact that the cork was slightly too smooth, it was still thought to be the best option due to its appropriate thermal conductivity, pliability, and readily available thicknesses.

The cork was attached to the surface of the test vane with either double sided tape or spray adhesive. The double sided tape was used to attach the 3/32" thick cork to the test vane for the first experiments with a simulated TBC. The double sided tape used was 3M's 410M double sided tape. The 5/32" cork did not allow for use of the double sided

tape because it did not have sufficient adhesion to overcome the elastic memory of the material after it had been rolled up for an extended period. Instead, a spray adhesive was used to attach the 5/32" cork. The spray adhesive was Duro® All-Purpose Spray Adhesive made by Henkel Consumer Adhesives, Inc.

Various film cooling configurations were tested on both the suction side and pressure side of the vane. The suction side film cooling was exclusive to the $t/d = 0.55$ TBC and utilized the pourable epoxy model utilized by Dees (2010). The suction side film cooling was fed by a single row of 24, 4.2 mm diameter round holes inclined at 42° to the surface with a pitch of $p/d = 3$. This row of holes was located at $s/d = 31$ for the t/d = 0.55 TBC model. The curvature of the vane at this location was approximately $2r/d = 18$, where r is the radius of curvature and a smaller number implies a more curved surface. The location of the suction side holes was reported as being slightly different than what is presented in the diagram in Figure 2.5. This is because Figure 2.5 does not represent a vane with a TBC. The inclination angle of the cooling holes results in a slight different hole location when a TBC is incorporated. Holes were cut by hand through the overlying layer of simulated TBC. The hand cut holes aligned with the round holes that were machine drilled through the wall of the model vane. The suction side film cooling tests measured the performance of a transverse trench as well as the round holes. The trench was formed by cutting away the cork that overlaid the underlying round holes, leaving a shallow trench with parallel edges that ran the full length of the suction side row of holes. The trench had a depth of $t/d = 0.55$ and a width of $w/d = 1.5$. The edges of the trench lip were cut smooth approximating a 90° corner. The parallel walls of the

trench were coincident with the upstream and downstream edges of the embedded round holes. Photographs of the round holes and trench configurations on the suction side of the vane are shown in Figure 2.7. The major and minor tick marks in the scale are 1 and 1/10 inch, respectively. Various blowing ratios were tested with the suction side film cooling configurations. The blowing ratios varied from M = 0.5 up to M = 1.30. Two different mainstream turbulence intensity conditions were also tested, Tu = 0.5% and Tu = 20%. The specific blowing ratios tested for the round holes and trench configurations are shown in Table 2.4.

Table 2.4: Summary of blowing ratios tested for each suction side cooling configuration with t/d = 0.55 TBC at Tu = 0.5% and Tu = 20% with DR = 1.2.

	Blowing Ratio, *M*							
Configuration	**0**	**0.5**	**0.64**	**0.80**	**0.95**	**1.30**	***Tu*=0.5%**	***Tu*=20%**
No Film	✓						✓	✓
SS Round Holes	N/A	✓	✓		✓	✓	✓	✓
SS Trench	N/A	✓	✓	✓	✓	✓	✓	✓

The pressure side film cooling was only tested with the t/d = 1.2 TBC by utilizing the Dupont Corian® vane constructed by Albert (2011). The pressure side film cooling was fed by 24, 4.2 mm diameter round holes inclined at 30° to the surface with a pitch of p/d = 3. This row of holes was located at s/d = -32. The curvature at this location was approximately $2r/d$ = 270. The pressure side row of holes was reconfigured by manipulating the shape of the overlying TBC. This allowed for various cooling configurations to be tested all of which are shown in Figure 2.8. The first design was simply round holes as previously described. The cork near each of the discrete round

holes was then carved away with the use of a Dremel® rotary tool to form cylindrical depressions. These depressions are herein referred to as craters and were proposed by Fric and Campbell (2002). After testing the crater design, the overlying cork was further modified with the Dremel® tool. This resulted in a film cooling design that blended the discrete nature of the craters with some aspects of the trench. This design is described as a modified trench. The "tongues" of the modified trench were then removed for the next film cooling configuration, the ideal trench. This trench was described as being "ideal" since the depth exceeded $t/d = 0.75$ and the walls of the trench were coincident with the upstream and downstream edges of the embedded round holes. This was based on the findings of Dorrington *et al.* (2007) who showed that the adiabatic effectiveness achieved by a trench was maximized when the depth was at least 0.75d and the walls were adjacent to the exit of the film cooling holes. In practice, such a trench is not practical due to machining tolerances. Consequently, a final more realistic trench was tested which expanded the width of the trench. The corners of the trench walls were also rounded off to simulate a more realistic product. All of the relative dimensions of the various designs are shown in Figure 2.8. The simple round hole configuration was also tested with three rows of 18, 4.2 mm diameter round holes located in the stagnation region of the vane at s/d = -1.7, 1.7, and 5.0. These holes were inclined at an angle of 25° and spaced with a pitch of $p/d = 5.6$. The high density of holes in the stagnation region is referred to as showerhead film cooling. Figure 2.9 provides a photograph looking down the pressure side of the test vane while identifying the general location of the showerhead and pressure side film cooling holes. The blowing ratios used for each of the configurations

are shown in Table 2.5. It should be noted that for the round holes with an active showerhead the blowing ratios listed in Table 2.5 are the set point for the pressure side holes. The blowing ratio for the three rows in the showerhead was taken as an average of the total flow from the three rows of holes. For a pressure side blowing ratio of M = 1.0, 1.5, 2.0 and 3.0 the average blowing ratio for the showerhead was M_{SH} = 0.8, 1.5, 2.0, and 3.2, respectively. The blowing ratio in the showerhead was referenced to the approach velocity as opposed to the local velocity which is the method for determining the blowing ratio of the suction side and pressure side holes. An analytical solution was required to determine the blowing ratio for the system when the showerhead was active. This was a result of the fact that the blowing ratio was generally measured directly based on the difference in mass flow rate entering and exiting the vane. However, when the showerhead was active it was unclear if the coolant was exiting from the showerhead or from the pressure side row of holes. To get around this issue, Albert (2011) measured the discharge coefficient for the different cooling rows and identified the pressure ratios across the holes for a variety of internal flow conditions. This allowed for the following equation from Gritsch *et al.* (2001) to be used to determine the mass flow rate from an individual row of holes.

$$\dot{m}_{film} = C_d A_{film} P_{t,c} \left(\frac{P_{\infty,local}}{P_{t,c}}\right)^{\frac{\gamma+1}{2\gamma}} \sqrt{\frac{2\gamma}{(\gamma-1)RT_{t,c}}\left[\left(\frac{P_{t,c}}{P_{\infty,local}}\right)^{\frac{\gamma-1}{\gamma}} - 1\right]} \tag{2.2}$$

Additional discussion concerning this method can be found in Albert (2011). Unless otherwise stated, all blowing ratios listed in the results are for the pressure side row of

holes. All of the pressure side film cooling results were obtained at a turbulence intensity level of Tu = 20%.

Table 2.5: Summary of blowing ratios tested for each pressure side cooling configuration with t/d = 1.2 TBC at Tu = 20%.

	Blowing Ratio, *M*								
Configuration	**0**	**0.5**	**0.7**	**1.0**	**1.5**	**2.0**	**3.0**	**5.0**	***Tu*=20%**
No Film	✓								✓
PS Round Holes + SH	N/A			✓	✓	✓	✓		✓
PS Round Holes	N/A	✓	✓	✓		✓			✓
PS Craters	N/A			✓		✓	✓	✓	✓
PS Ideal Trench	N/A	✓		✓		✓	✓	✓	✓
PS Modified Trench	N/A	✓		✓		✓	✓	✓	✓
PS Realistic Trench	N/A	✓		✓		✓	✓	✓	✓

2.1.3. Deposition

Contaminants in the hot gas path of a gas turbine engine can have significant detrimental effects by causing deposition, erosion, and corrosion (DEC) to the engine components. They can also cause a catastrophic shutdown of the engine in the most extreme scenarios, for example significant ingestion of particulates from a volcanic ash cloud. The primary goal of this work was to simulate coal ash particles that will likely be present in future integrated gasification combined cycle plants that utilize coal to generate a combustible syngas. A greater understanding of deposition behavior may allow for better turbine designs that mitigate the detrimental effects. The contaminants in a real engine were simulated with the use of molten wax particles that were sprayed into the mainstream flow. The idea behind using wax was to simulate the molten nature of the contaminants in a real engine. The slightly molten nature of the simulated contaminant

allowed it to remain "sticky" and adhere to the surface of the vane after making contact. The wax was introduced into the mainstream flow of the wind tunnel with the use of a sprayer system that was constructed by Albert (2011). A schematic of this sprayer is shown in Figure 2.10. The nozzle used in the sprayer was a pneumatically-actuated, air atomizing spray nozzle (Spray Systems Co. 63067-1/8JJAUCO). The sprayer had a 0.016" diameter nozzle cap and shut-off/clean-out needle assembly. This nozzle diameter was larger than the diameter used by Albert (2011) which facilitated higher mass flow rates of molten wax. The nozzle was attached to a wax supply line, a hot air line, and a pneumatic control line. All of these lines, as well as the nozzle, were housed in an insulated PVC cylinder with the same form factor as the turbulence grid bars. Consequently, the sprayer housing was used to replace the center turbulence bar. The sprayer housing protruded from the top of the test section which allowed the rest of the sprayer system to be located outside of tunnel. The wax supply line was fed by a reservoir of molten wax heated by an electrically resistive wrap. The hot air line was heated by an in-line electrically resistive pipe. The air for this system was supplied by the facilities compressed air feed. All heating elements were controlled by variable power supplies to keep the air supply line, wax reservoir, and sprayer nozzle at 325 ± 1K. The specific wax used to simulate deposition in this study was RT31 supplied by Rubitherm Technologies GmbH. The wax was selected based upon its nominal solidification temperature of $T_{wax,\ solid}$ = 304 K. This was done to ensure that the droplets would be partially molten when impacting the surface of the vane after being sprayed from a nozzle at 325 K with a mainstream temperature of T_{∞} = 301 K.

As mentioned, the sprayer nozzle was placed in a cylindrical housing that replaced the center turbulence bar. This placed the nozzle slightly to the pressure side of the stagnation streamline and in-line with the mid-span of the vane as shown in Figure 2.1. Spray testing showed that the nozzle location and orientation provided full depositional coverage over the pressure side of the vane and beyond the stagnation line towards the suction side. This provided evidence that despite the single location of the sprayer the deposition results should be representative of a hot gas path with contaminants uniformly distributed. During testing, it was found that the nozzle sprayed wax at an average of 44 g/min for 3 minutes. Albert (2011) argued that the velocity profile of the approach flow is not altered significantly due to operation of the sprayer nozzle. This conclusion was based on hot-wire measurements in an alternate facility at the TTCRL as well as the fact that the high mainstream turbulence levels should break down any differences in the jet plume.

The size of the wax particles was selected based upon a Stokes number analysis to scale the behavior of the particles in the wind tunnel to the expected behavior of contaminants in a real engine. As implied, the Stokes number relates the time a particle takes to react to a change in a flow field to the time scale of the flow. The Stokes number for a spherical particle in fluid flow can be defined as

$$Stk = \frac{\tau}{l_{char}/U_{char}} = \frac{\rho_p d_p^2 U_{char}}{18 l_{char} \mu_g} \tag{2.3}$$

as shown by Hinds (1999) where the subscripts p and g refer to the particle and fluid gas, respectively. The Stokes number can be used to specify how well a particle will follow changes in the fluid flow path. A Stokes number of Stk >> 1 implies that the particle will not follow changes in the flow field well. Larger particles may fall in this regime resulting in the particle impacting the surface of the vane before changing direction due to changes in the flow field. This is intuitive if one thinks about the trajectory of a larger particle carrying significant momentum and how the trajectory would be relatively unaffected by minor changes in the surrounding flow field. A Stokes number of $Stk << 1$ means that the particle will closely follow changes in the surrounding flow field. A particle in this regime would rarely impact the surface of a vane due to inertia. The variables l_{char} and U_{char} should be selected based on the region of interest over which particles may be traveling. For the purposes of this study, the characteristic length, l_{char}, was set as the diameter of a cooling hole. Therefore the characteristic length for a real engine may vary from $l_{char} = 0.3 – 0.6$ mm. The hole diameter was used since a primary question of this study is to determine how contaminants deposit near film cooling holes and thus is a logical choice for the characteristic length. The characteristic velocity, U_{char}, was taken to be the velocity at the inlet of the cascade which is approximately $U_{char} = 250$ m/s in a real engine for an inlet Mach number of $M = 0.3$. There are other logical choices for l_{char} and U_{char}. However, as long as the analysis is done consistently for the real engine case as compared to the setup in the wind tunnel the comparison should be valid. The diameter of the contaminant particles in the engine were obtained from Bons *et al.* (2005) who stated that the size of coal ash in a typical engine is in the range of $d_p =$

1 – 10 μm with a density of ρ_p = 1980 kg/m^3. The viscosity of the gas in a real engine was assumed to be dominated by air at temperatures ranging from approximately 1300 - 1800°C. This resulted in a range of dynamic viscosity of μ_g = 5.5 – 6.5x10^{-5} Pa-s (kg/m-s) using the Sutherland equation for viscosity as presented by Munson *et al.* (2006).

The Stokes number of the wax particles can be altered by setting the diameter of the particles to a desired value. The target diameter can be determined by adjusting Equation (2.3) yielding

$$d_p = \sqrt{\frac{18Stk\, l_{char}\mu_g}{\rho_p U_{char}}} \tag{2.4}$$

Using this expression a target diameter for the wax particles can be determined knowing the expected range of Stokes numbers in a real engine. Table 2.6 details the parameter values for the Stokes number calculations as well as the resulting calculation for the target particle diameters. The expected Stokes number for particles in a real engine ranges from *Stk* = 0.34 – 120. The wax particles in the modeled system must then have a diameter of d_p = 10 – 200 μm in order to match the expected range of Stokes numbers. Figure 2.11 provides detailed images of the wax particles after being sprayed onto a test coupon. These images show that the wax particles cover the desired range of d_p = 10 – 200 μm. Consequently, the wax particles sprayed into the mainstream flow of the wind tunnel should scale to match the behavior of contaminant particles in a real engine.

Table 2.6: Calculations of expected Stokes number in a real engine and the necessary wax particle diameter to match the Stokes number range.

Stokes Number in a Real Engine			
Parameter	**Low Est.**	**High Est.**	**Source**
Particle Density, ρ_p (kg/m3)	1900	2000	Bons *et al.* (2005)
Particle Diameter, d_p (μm)	1.0	10.0	Bons *et al.* (2005)
Characteristic Velocity, U_{char} (m/s)	210	250	Albert (2011)
Characteristic Length, l_{char} (mm)	1.0	0.40	Bunker (2009)
Dynamic Viscosity of Gas, μ_g (Pa-s)	6.5x10-5	6.0x10-5	Munson *et al.* (2006)
Expected Stokes Number, *Stk*	**0.34**	**120**	
Target Diameter for Wax Particles			
Expected Stokes Number, *Stk*	0.34	120	
Particle Density, ρ_p (kg/m3)	760	760	Rubitherm (2009)
Characteristic Velocity, U_{char} (m/s)	5.8	5.8	
Characteristic Length, l_{char} (mm)	4.2	4.2	
Dynamic Viscosity of Gas, μ_g (Pa-s)	1.86x10-5	1.86x10-5	Munson *et al.* (2006)
Target Wax Particle Diameter, d_p (μm)	**10**	**200**	

2.2. Instrumentation for Sampling ϕ and τ

The cooling performance for this study is presented in two forms, the overall effectiveness, ϕ, and the external TBC condition, τ. The overall effectiveness is the non-dimensional temperature of the vane wall, as previously discussed. This means that it is a measurement of the interface cooling performance when a TBC is incorporated. The external TBC condition can be defined as

$$\tau = \frac{T_\infty - T_{TBC,e}}{T_\infty - T_{c,vane\ inlet}} \tag{2.5}$$

where $T_{TBC,e}$ is the external surface temperature of the TBC. Figure 2.12 provides a diagram for where the respective measures of performance are taken for a vane wall with

a TBC. It is worth noting that the system used in this study did not incorporate a bond coat. The bond coat was assumed to be of similar thermal conductivity as the vane wall and relatively thin. Consequently, the presence of a bond coat is not expected to dominate the heat transfer behavior of the system.

The vane wall was heavily instrumented with Type E ribbon thermocouples before the simulated TBC was applied to the surface. The thermocouples measured roughly 1.5 mm x 1.5 mm x 0.1 mm in dimension. The ribbon design was used to improve the measurement accuracy by reducing conduction losses through the thermocouple lead wires. The test vanes were individually instrumented for the two different TBC thicknesses that were studied. In both cases a 4x3 array was placed downstream of either the suction side or pressure side row of cooling holes. The arrays were similar in design such that the three columns were located 3*d*, 6*d*, and 15*d*, respectively, from the downstream edge of the round holes located at either $s/d = 31$ or $s/d = -32$. The rows of the thermocouples alternated between being in-line with the mid-pitch and centerline of the round holes. The arrays were used to provide greater measurement resolution in locations of the vanes which were expected to have larger thermal gradients. Elsewhere on the vane, the thermocouples were located at the mid-span spaced roughly 10 - 20*d* apart. Closer spacing was used in regions of interest such as the showerhead. Figure 2.13 and Figure 2.14 provide photographs of the instrumented surfaces of the vanes before the simulated TBC was applied.

All of the thermocouples placed at the interface of the $t/d = 1.2$ TBC and vane wall were calibrated. This was accomplished by submerging each of the thermocouples

in a bath of known temperature such as ice water or boiling nitrogen. All of the thermocouples were calibrated using the same input channel as was used for experimental measurements. The mainstream and coolant thermocouples were also calibrated. Figure 2.15 – Figure 2.18 compare the behavior of the thermocouples over a wide range of temperatures. It should be recognized that the calibrations of the thermocouples showed that the indicated measurement from each of the thermocouples was always biased above the actual reference temperature being measured for temperatures below 320 K. Some of the thermocouples accurately measured 320 K without significant bias.

Surface temperatures were measured with IR thermography. A FLIR Systems ThermaCam® P25 IR camera was used to take measurements of the vane surface. All measurements of τ were obtained with the use of the IR camera. The camera had a resolution of 1 - 2 pixels/mm depending on where the camera was located and a useable field of view of 260x240 pixels. The camera viewed the surface of the test vane through a NaCl window. The temperature measurements taken by the IR camera were calibrated against two thermocouples on the surface of the vane. The IR calibration accounted for any errors resulting from the fact that the NaCl window attenuates the IR signature of the vane surface. A typical IR calibration curve is shown in Figure 2.19.

2.3. Sample Results and Presentation Methodology

In order to interpret the results from this study it is important to understand how the results are being presented. The majority of the results for this study are presented in terms of the variable of interest plotted as a function of either *x/d* or *s/d*. The use of *s/d* is more common for the results presented herein, where $s = 0$ is the stagnation point of the

vane. The use of *x/d* was generally reserved for external surface film cooling data in which $x = 0$ is defined as the downstream edge of the film cooling geometry (e.g. the downstream lip of a trench). Figure 2.20 provides a sample data set presented in a typical format, albeit with some additions to provide greater understanding of how the figure relates to the vane design. In this case the variations in external convective heat transfer coefficient are shown. The more important matter though is recognizing how the surface of the 3-D vane has been laid flat on the 2-D plot. Therefore, $s/d < 0$ represents the pressure side of the vane while $s/d > 0$ represents the suction side of the vane. The location of the internal coolant passages are also identified showing where the coolant enters and exits the body of the vane. The coolant behavior within the U-bend passage is also shown. The solid gray rectangles in the figure represent internal walls that extend the complete spanwise distance of the vane. The empty gray rectangles represent the internal U-bend wall which only extended 71% of the vane span height. The top of the U-bend was located at 91% of the span height meaning that the gap through which the coolant passed from the inlet to to outlet of the U-bend was 20% of the span height. It is important to recognize that the U-bend outlet passage and the radial passage are single passages despite the fact that Figure 2.20 shows each of these passages twice, in two separate locations. This is a result of taking the 3-D surface and unraveling it onto a 2-D plot. The U-bend inlet and outlet may at times be referred to as the fore and aft channels of the U-bend passage, respectively.

2.4. Uncertainty Analysis

A detailed uncertainty analysis was completed for the variables of greatest interest, ϕ, τ, and M. The assessment of the uncertainty in these parameters allowed for a determination of the uncertainty in other variables as well, such as the mainstream velocity. The uncertainty analysis was completed with either the method proposed by Kline and McClintock (1953) or by using the sequential perturbation method described by Moffatt (1988). All uncertainties were calculated to 95% confidence.

2.4.1. Uncertainty of Overall Effectiveness, ϕ

The measurement of overall effectiveness with a TBC is a function of three independent thermocouple measurements, the mainstream temperature, T_∞, the vane inlet temperature, $T_{c,vane\ inlet}$, and the exterior vane wall temperature at the TBC interface, $T_{w,e}$. All of these thermocouples were calibrated for the t/d = 1.2 TBC experiments to reduce bias uncertainty, as previously discussed. The uncertainty in the calibrated thermocouples could then be determined by perturbing the individual data points of the calibration to determine how it affected the calibration coefficients. The data points were perturbed by ½ the resolution of the thermometer used to calibrate the thermocouples resulting in a perturbation of δT = ±0.25. This method resulted in an uncertainty of approximately δT = ±0.21 and ±0.25 K at T = 273 and 77.3 K, respectively. The uncertainty of the calibrated interface thermocouples was estimated to be $\delta T_{w,e} = \delta T_{c,vane\ inlet}$ = ±0.5 K while also accounting for the precision error of the thermocouples of $\delta T_{prec.}$ = ±0.05 K. This is higher than the previously reported values of δT = ±0.21 and ±0.25 K. This is a result of the fact that additional calibration data was obtained with the

thermocouples after completion of this study. Those experiments have provided results suggesting that the calibrated thermocouples have uncertainties higher than δT = ±0.21 and ±0.25 K. Current efforts are underway to improve the accuracy of the calibrations and the uncertainty of the thermocouples measurements. The precision uncertainty of the thermocouples was determined by observing the variation in the measurement output for a constant temperature condition. The precision uncertainty was reduced by sampling the measurement at 1000 Hz for 2 seconds. The uncertainty of the thermocouple calibrations likely produced more accurate results than δT = ±0.5 K in the range of T = 250 – 273 K. However, no calibration data points were taken over this range and thus the calibrated value is dependent upon interpolating between the calibrated points of ice water (273.2 K) and boiling nitrogen (77.3 K). For this reason the uncertainty of the interface thermocouples was estimated to be δT = ±0.5 K. The uncertainty of the thermocouple calibrations could be improved if more data points could be taken. Of particular interest is to obtain calibration data points in the range of 200 – 250 K. The uncertainty of the mainstream temperature measurement was estimate to be δT_∞ = ±0.3 K. Using Equation (1.6), the uncertainty in ϕ can be described as

$$\delta\phi^2 = \left(\delta T_\infty \frac{\partial \phi}{\partial T_\infty}\right)^2 + \left(\delta T_{w,e} \frac{\partial \phi}{\partial T_{w,e}}\right)^2 + \left(\delta T_{c,vane\ inlet} \frac{\partial \phi}{\partial T_{c,vane\ inlet}}\right)^2 + \left(\delta M \frac{\partial \phi}{\partial M}\right)^2 \qquad (2.6)$$

This resulted in an uncertainty for overall effectiveness of $\delta\phi$ = ±0.012. For the purposes of this analysis the uncertainty of ϕ due to variations in blowing ratio, M was assumed to be negligible. This is because ϕ is a weak function of blowing ratio when a TBC is

utilized. The behavior of ϕ with changes in blowing ratio will be discussed in greater detail in Chapter 4.

2.4.2. Uncertainty of External TBC Condition, τ

The uncertainty in the external TBC condition, τ, is a function of the uncertainty in measuring the mainstream temperature, coolant temperature, and the external TBC surface temperature, $T_{TBC,e}$. The uncertainty of the external TBC surface temperature is a result of the uncertainty in the calibration used to reduce the IR thermography data. As previously discussed, the IR calibration is obtained by comparing the perceived temperature of a thermocouple on the surface of the vane to the temperature being measured by the thermocouple. This provides a means for correcting the measurements of the IR camera by referencing it to known temperature values. The uncertainty in the IR calibration is then primarily a function of the uncertainty in the thermocouple measurement. This uncertainty of the thermocouples was reduced by calibrating them prior to completing the IR calibration. The uncertainty of the thermocouple measurements was found to be δT = ±0.5 K. The uncertainty in the IR calibration generated an uncertainty in the measurement of TBC surface temperature of approximately $\delta T_{TBC,e}$ = ±1.0 K. Albert (2011) reported the uncertainty of the surface temperature measurement as being δT_{surf} = ±1.3 K. The uncertainty in the measurement of τ can be expressed as

$$\delta\tau^2 = \left(\delta T_\infty \frac{\partial \tau}{\partial T_\infty}\right)^2 + \left(\delta T_{TBC,e} \frac{\partial \tau}{\partial T_{TBC,e}}\right)^2 + \left(\delta T_{c,vane\ inlet} \frac{\partial \tau}{\partial T_{c,vane\ inlet}}\right)^2 + \left(\delta M \frac{\partial \tau}{\partial M}\right)^2 \qquad (2.7)$$

This resulted in an uncertainty for the external TBC condition of $\delta\tau = \pm 0.027$ and $\delta\tau = \pm 0.021$ for a blowing ratio of M = 0.5 and 5.0, respectively. This was based on determining a function that described the dependence of τ on changes in blowing ratio. Specifically, this was accomplished using data from an ideal trench on the pressure side of the vane and spatially averaging τ over an area of $20d$ downstream of the holes in order to determine how the blowing ratio affected τ. The uncertainty in τ increased at lower blowing ratios due to the fact that the uncertainty in the blowing ratio became a larger percentage of the blowing ratio as the mass flux was decreased.

The presence of deposited wax on the surface of the modeled vane altered the emissivity of the surface. Consequently, all results for τ post-deposition must be observed with the recognition that the measurement of temperature has greater uncertainty. IR images were obtained for a constant temperature body with and without wax deposition in order to quantify this bias error. It was found that the presence of the wax increased the perceived temperature by less than 1ºC when the reference temperature of a flat black body was at approximately 12ºC. This was accomplished by cold soaking a cork coupon that was painted flat black and partially covered with wax deposition. The observed variation showed that the external TBC condition measurement with deposits will be biased down by approximately $\Delta\tau = 0.03$ at a condition of $\tau = 0.3$. This difference increases the uncertainty in the IR thermography of the TBC surface with deposition. However, the difference is small enough that reasonable comparisons with

and without deposition can still be made to determine the effect of deposition on the film cooling performance of the various cooling designs.

2.4.3. Uncertainty of Blowing Ratio, M

The uncertainty in the measurement of blowing ratio, M, is dependent on the uncertainty in the density and velocity of the coolant and local mainstream. This is expressed by Equation (1.17) as

$$M = \frac{\rho_c U_c}{\rho_\infty U_\infty} \tag{1.17}$$

The measurement of the density for the coolant and mainstream was determined with the use of the ideal gas law

$$\rho = \frac{P}{RT} \tag{2.8}$$

The uncertainty in pressure and temperature measurement were, δP = ±1000 Pa and δT = ±0.5 K, respectively. The velocity of the mainstream flow, U_∞, was determined with a pitot static probe. Consequently, the measurement of velocity can be expressed as

$$U_\infty = \sqrt{\frac{2P_{dyn}}{\rho_\infty}} \tag{2.9}$$

The uncertainty in the measurement of dynamic pressure is a function of the curve used to calibrate the pressure transducer. The uncertainty in this calibration was approximately δP_{dyn} = ±0.5 Pa = ±0.002 in_{H2O}, as reported by Albert (2011). The bulk velocity of the film coolant flow, U_c, is a function of the mass flow rate of film coolant,

$\dot{m}_c$, the density of the film coolant, ρ_c, and the area of the film cooling holes, A_h. This can be expressed as

$$U_c = \frac{\dot{m}_c}{\rho_c A_h} \tag{2.10}$$

The mass flow rate of film coolant is equivalent to the difference in coolant flow rate between the entrance and exit of the U-bend. The measurement of coolant flow rate is based on two different orifice plates that are located upstream and downstream of the entrance and exit of the U-bend, respectively. The orifice plates were calibrated with the use of a laminar flow element and monometer, as discussed by Albert (2011). The mass flow rate of coolant can then be expressed as

$$\dot{m}_c = \dot{m}_{c,vane\ inlet} - \dot{m}_{c,vane\ exit} = \left(\rho_{c,orifice} A_{orifice} \frac{C_d}{\sqrt{1-\beta^4}} \sqrt{2 \frac{\Delta P_{orifice}}{\rho_{c,orifice}}} \right) \Bigg|_{inlet-outlet} \tag{2.11}$$

Where $\beta = d_{orifice}/d_{pipe}$. Plugging Equations (2.10) and (2.11) into Equation (1.17) and simplifying yields

$$M = \frac{\sqrt{2} A_{orifice}}{\rho_\infty U_\infty A_h \sqrt{1-\beta^4}} \left(C_d \sqrt{\rho_{c,orifice} \Delta P_{orifice}} \right) \Bigg|_{inlet-outlet} \tag{2.12}$$

Further simplification of this equation and substitution for density and mainstream velocity using Equations (2.8) and (2.9) results in the expression

$$M = \frac{d_{orifice}^2 T_\infty^{0.5}}{P_\infty^{0.5} P_{dyn}^{0.5} N_h d_h^2 \left(1 - {d_{orifice}^4}/{d_{pipe}^4}\right)^{0.5}} \left[C_d \left(\frac{(P_{c,orifice,gage} + P_\infty)\Delta P_{orifice}}{T_{c,orifice}} \right)^{0.5} \right] \Bigg|_{inlet-outlet} \quad (2.13)$$

Equation (2.13) provides the solution for the blowing ratio in terms of the underlying measurements. The sequential perturbation method was then used to determine the uncertainty in blowing ratio, δM, for a generic film cooling geometry with N_h = 24 cooling holes at two different blowing ratios, M = 0.5 and 2.0. The blowing ratio uncertainty was calculated to be δM = ±0.10 and ±0.16 at M = 0.5 and 2.0, respectively, with 95% confidence. The elemental uncertainties for these calculations are shown in Table 2.7 and Table 2.8. The elemental uncertainties for the orifice plate pressure drops and discharge coefficients were determined by perturbing the data points in the respective calibrations and determining the effect on the calibration coefficients. It may be seen that the uncertainty in the blowing ratio calculation was influenced greatly by the uncertainty in pressure measurements. At a blowing ratio of M = 2.0, the uncertainty in the exit area of the coolant holes becomes very important. This is shown by the contribution the cooling hole diameter has on the uncertainty of M in Table 2.8.

An additional source of uncertainty in the blowing ratio measurement was the drift in zero for the orifice plate pressure transducers. This drift can have large effects on the calculated coolant mass flow rates, particularly at lower coolant flow rates. This source of error was mitigated by re-zeroing the voltage reading from the pressure transducers at various times throughout a single test.

Table 2.7: Elemental uncertainties in calculation of blowing ratio for $M = 0.5$.

Measurement Variable	**Nominal Value**	**Measurement Uncertainty**	**Elemental Uncertainty of *M***
Orifice Plate Diameter, $d_{orifice}$ (m)	0.0533	± 0.0001	0.004
Coolant Pipe Diameter, d_{pipe} (m)	0.0621	± 0.001	0.02
Coolant Hole Diameter, d_h (m)	0.0042	± 0.0001	0.02
Mainstream Temperature, T_∞ (K)	301	± 0.5	0.0004
Inlet Orifice Temperature, $T_{o,in}$ (K)	250	± 1	0.03
Outlet Orifice Temperature, $T_{o,out}$ (K)	258	± 1	0.02
Mainstream Pressure, P_∞ (Pa)	101300	± 1000	0.002
Mainstream Dynamic Pressure, P_{dyn} (Pa)	19.7	± 0.5	0.006
Inlet Orifice Pressure, $P_{o,in}$ (Pa, gauge)	4200	± 500	0.03
Outlet Orifice Pressure, $P_{o,out}$ (Pa, gauge)	500	± 500	0.03
Pressure Drop Across Inlet Orifice, $\Delta P_{o,in}$ (Pa)	52.0	± 0.3	0.04
Pressure Drop Across Outlet Orifice, $\Delta P_{o,out}$ (Pa)	47.0	± 0.3	0.04
Inlet Orifice Discharge Coefficient, $C_{d,in}$	0.715	± 0.002	0.04
Outlet Orifice Discharge Coefficient, $C_{d,out}$	0.748	± 0.002	0.03
Calculated *M* (using Eq. (2.13))	**0.50**	**δM =**	**± 0.10**
		$\delta M / M$ =	**± 20%**

Table 2.8: Elemental uncertainties in calculation of blowing ratio for $M = 2.0$.

Measurement Variable	**Nominal Value**	**Measurement Uncertainty**	**Elemental Uncertainty of *M***
Orifice Plate Diameter, $d_{orifice}$ (m)	0.0533	± 0.0001	0.02
Coolant Pipe Diameter, d_{pipe} (m)	0.0621	± 0.001	0.08
Coolant Hole Diameter, d_h (m)	0.0042	± 0.0001	0.1
Mainstream Temperature, T_∞ (K)	301	± 0.5	0.002
Inlet Orifice Temperature, $T_{o,in}$ (K)	249	± 1	0.03
Outlet Orifice Temperature, $T_{o,out}$ (K)	258	± 1	0.02
Mainstream Pressure, P_∞ (Pa)	101300	± 1000	0.002
Mainstream Dynamic Pressure, P_{dyn} (Pa)	19.7	± 0.5	0.03
Inlet Orifice Pressure, $P_{o,in}$ (Pa, gauge)	4200	± 500	0.03
Outlet Orifice Pressure, $P_{o,out}$ (Pa, gauge)	500	± 500	0.03
Pressure Drop Across Inlet Orifice, $\Delta P_{o,in}$ (Pa)	61.8	± 0.3	0.03
Pressure Drop Across Outlet Orifice, $\Delta P_{o,out}$ (Pa)	43.7	± 0.3	0.04
Inlet Orifice Discharge Coefficient, $C_{d,in}$	0.709	± 0.002	0.04
Outlet Orifice Discharge Coefficient, $C_{d,out}$	0.749	± 0.002	0.03
Calculated *M* (using Eq. (2.13))	**2.00**	**δM =**	**± 0.16**
		$\delta M / M$ =	**± 8%**

2.4.4. Repeatability

Repeatability measurements were taken for a wide range of experiments in order to assess in-test and test-to-test repeatability. In-test repeatability measurements were taken during all experiments. This was accomplished by measuring τ and ϕ for a specific condition, generally $M = 2.0$ and $Re_{Ubend} = Re_{Radial} = 20{,}000$, at the beginning and end of an experiment. The experimental data was thrown out if the repeatability measurements did not agree. Test-to-test repeatability measurements were also completed in order to determine how well results could be replicated from one day to the next. Figure 2.21 – Figure 2.23 provide comparisons for in-test and test-to-test repeatability measurements for both ϕ and τ. The repeatability measurements showed results that were comparable to the previously reported uncertainties for ϕ and τ at a 95% confidence level.

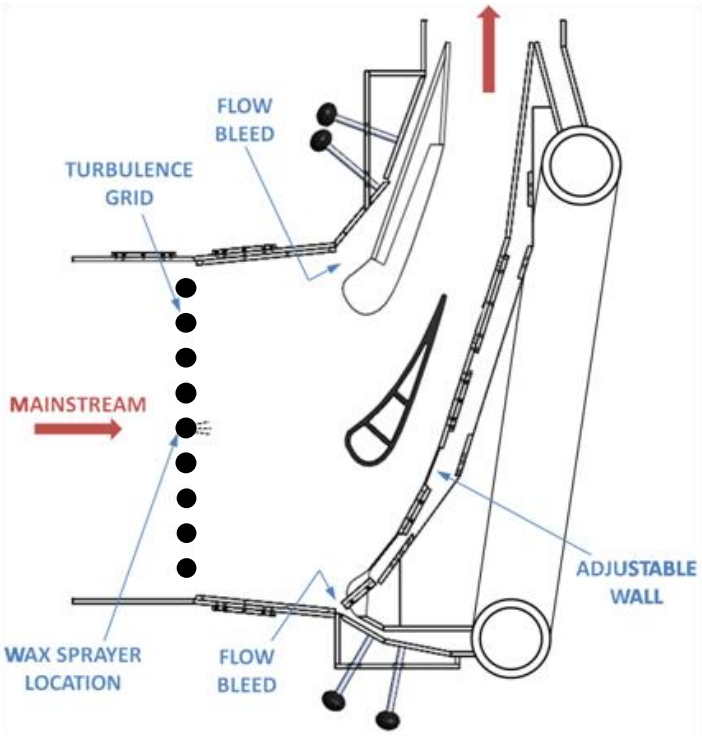

Figure 2.1: Corner test section with center test vane.

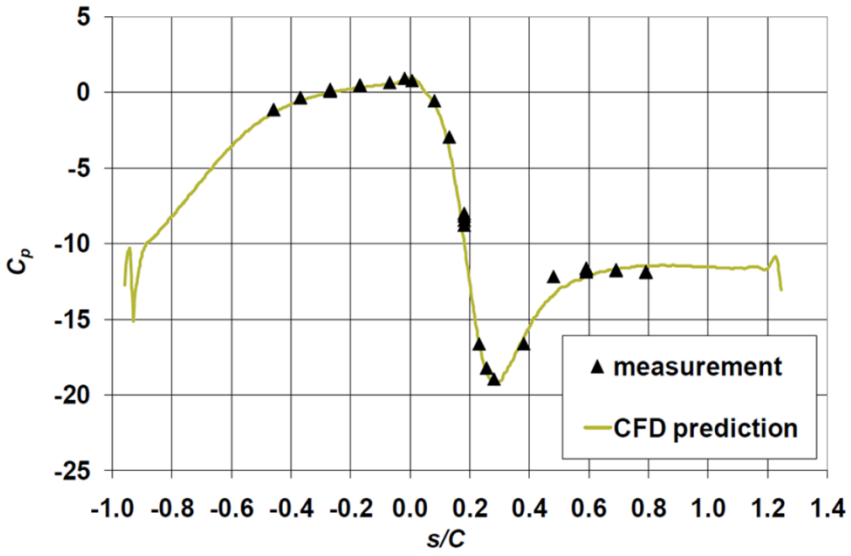

Figure 2.2: Pressure distribution across center test vane compared to CFD prediction for an infinite cascade.

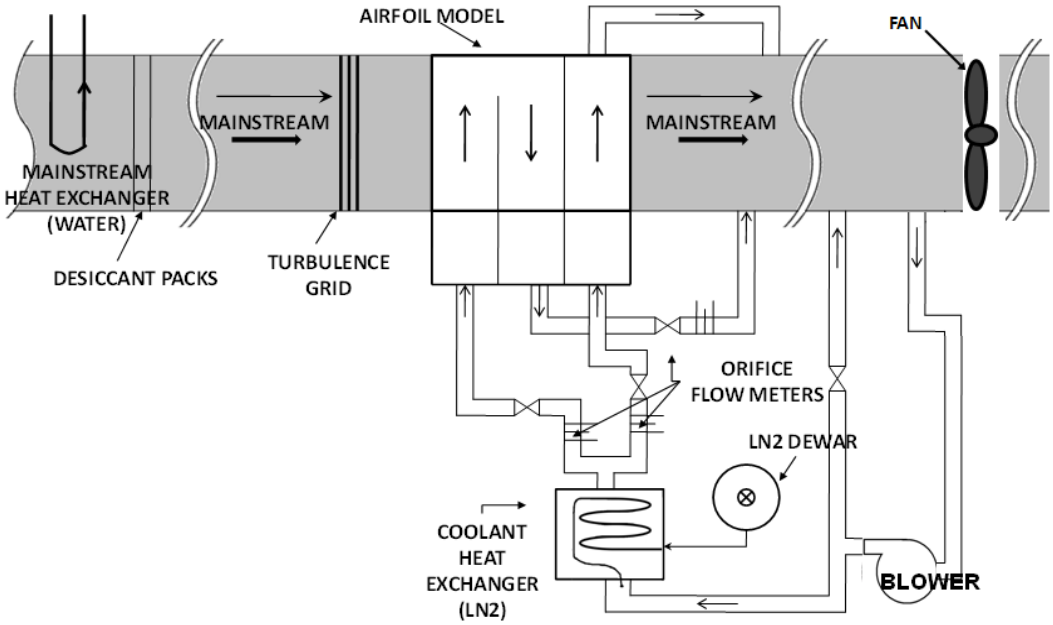

Figure 2.3: Schematic of wind tunnel components and secondary flow loop.

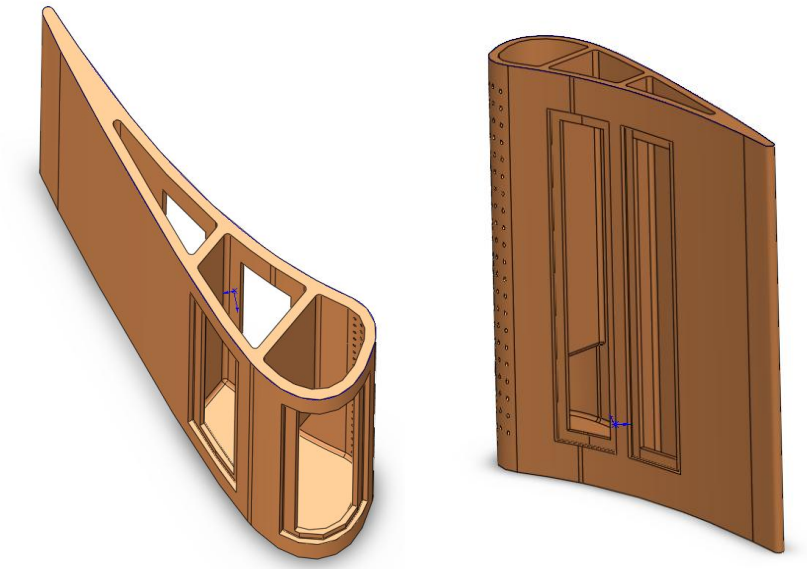

Figure 2.4: Corian test vane with hatches removed.

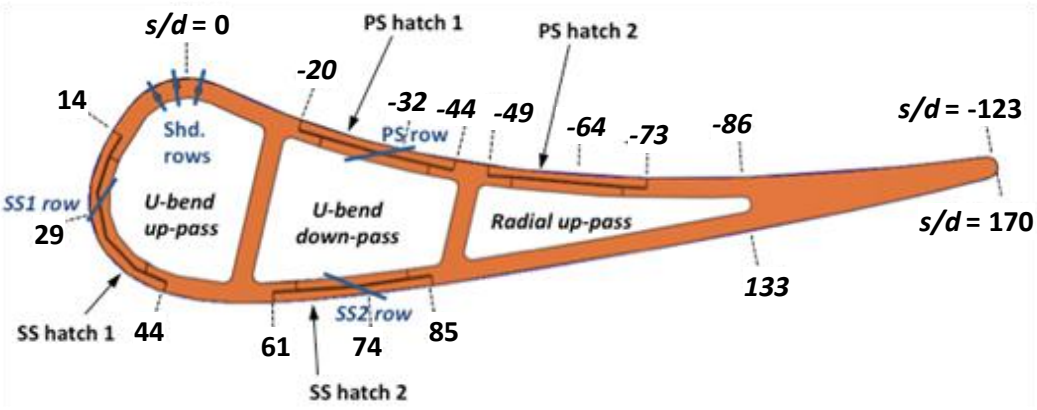

Figure 2.5: Vane cross section and s/d locations.

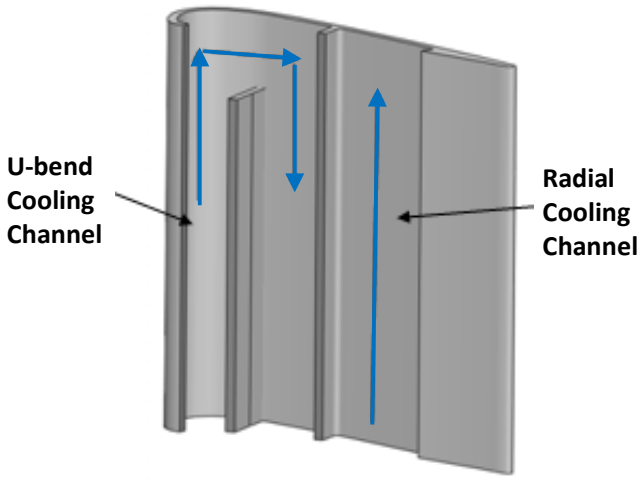

Figure 2.6: Internal flow paths of test vane.

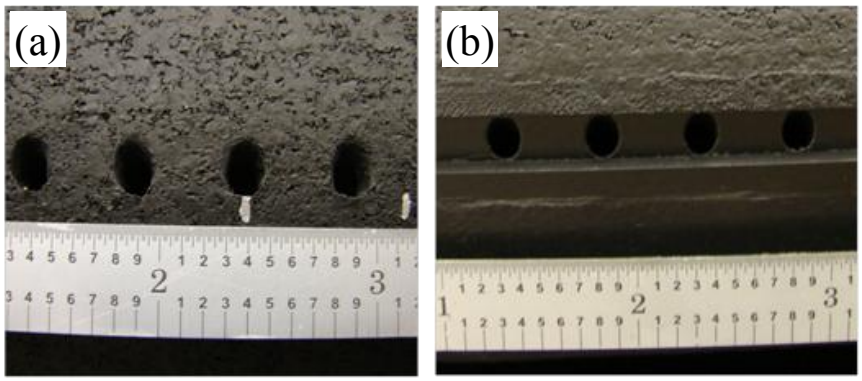

Figure 2.7: Comparison of suction side film cooling geometries with t/d = 0.55 TBC: (a) round holes and (b) trench.

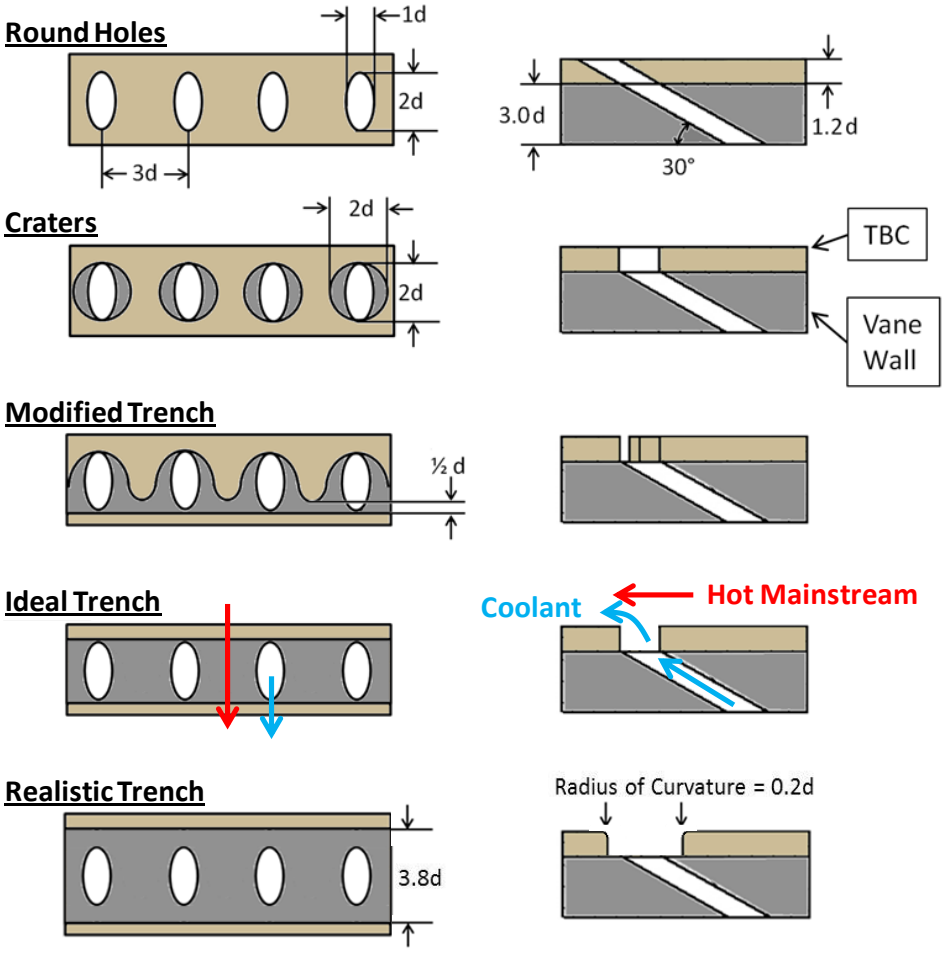

Figure 2.8: Schematic of various pressure side cooling hole designs with a t/d = 1.2 TBC.

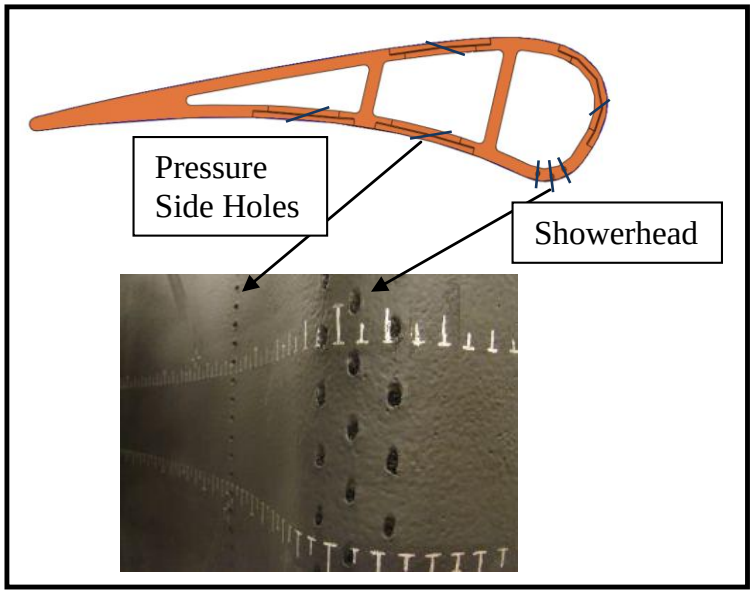

Figure 2.9: Location of showerhead and pressure side film cooling holes for the *t/d* =1.2 model in relation to vane cross-section.

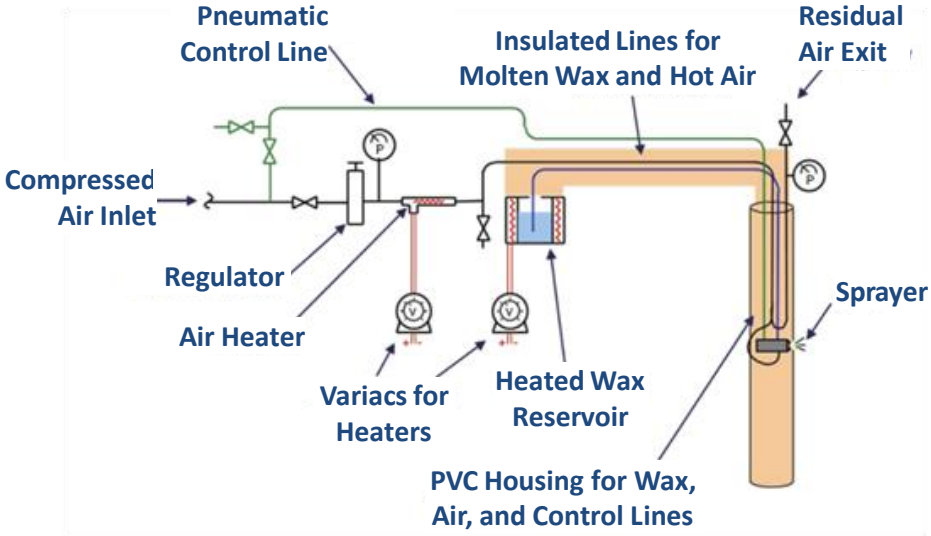

Figure 2.10: Wax sprayer schematic.

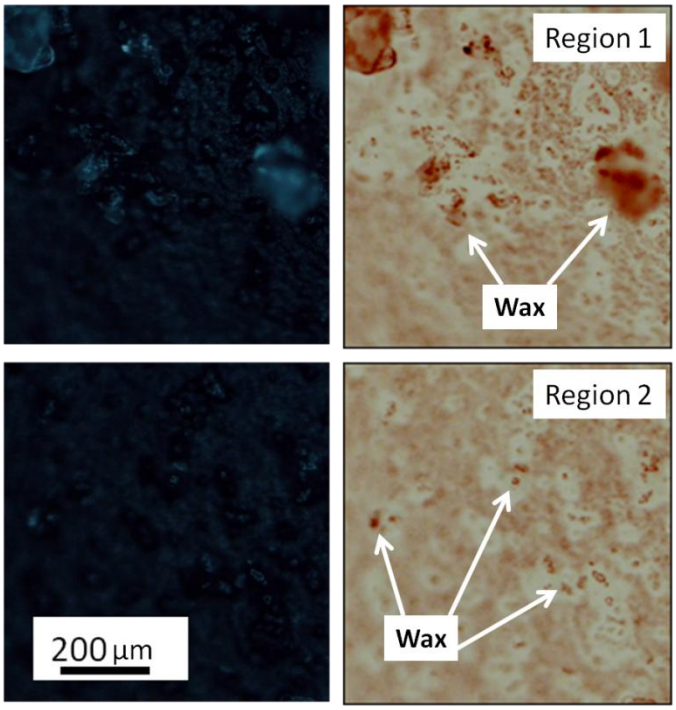

Figure 2.11: Wax particle sizing micrograph with (right) and without (left) image filtering.

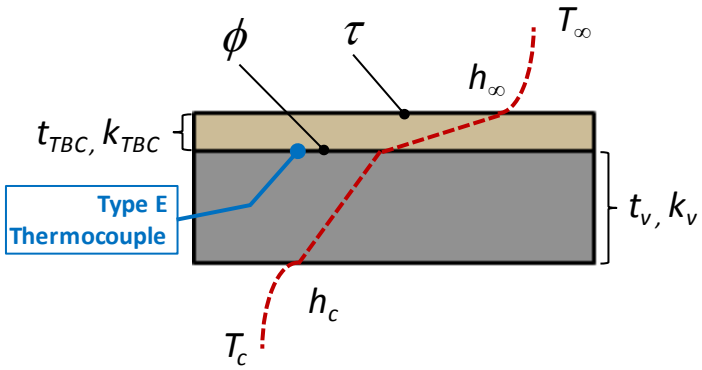

Figure 2.12: Vane wall cross-section with a TBC and relative location of measurements of interest.

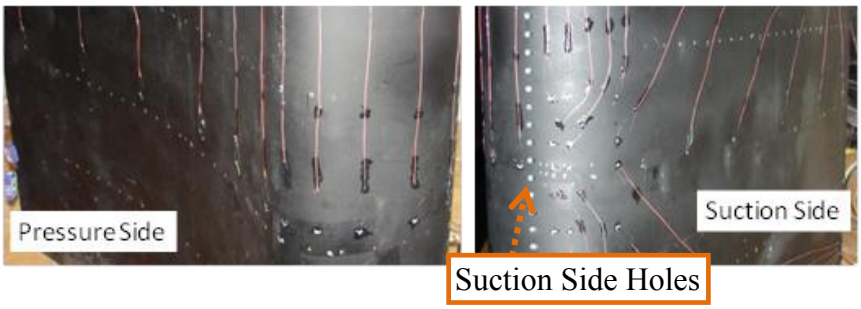

Figure 2.13: Photographs of interface thermocouples prior to applying *t/d* = 0.55 TBC to the vane surface.

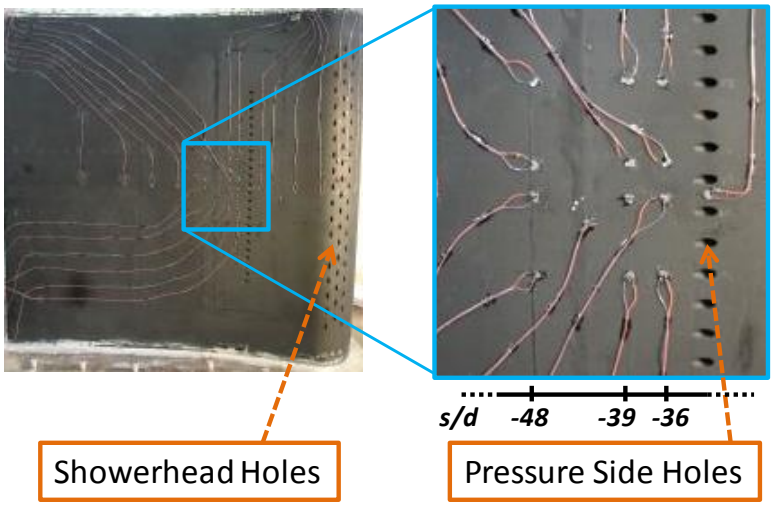

Figure 2.14: Photographs of interface thermocouples prior to applying *t/d* = 1.2 TBC to the vane surface.

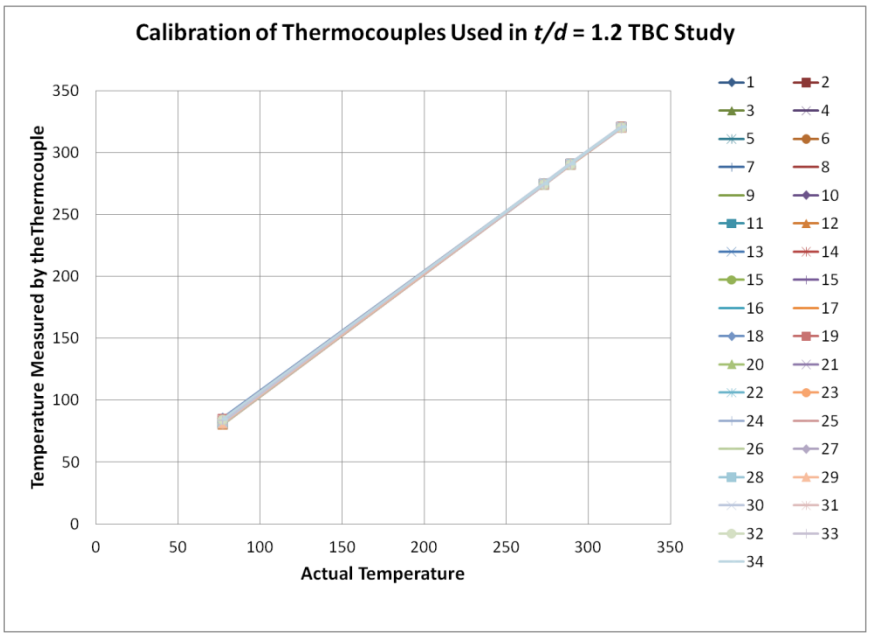

Figure 2.15: Comparison of the calibration curves used for all of the t/d = 1.2 TBC interface thermocouples over the entire temperature range.

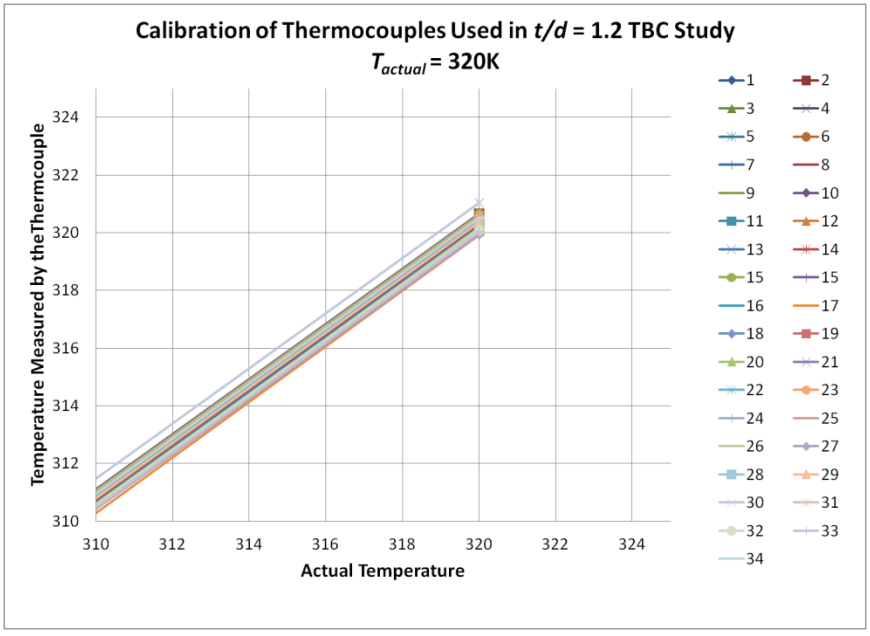

Figure 2.16: Comparison of the calibration curves used for all of the t/d = 1.2 TBC interface thermocouples at T_{actual} = 320K.

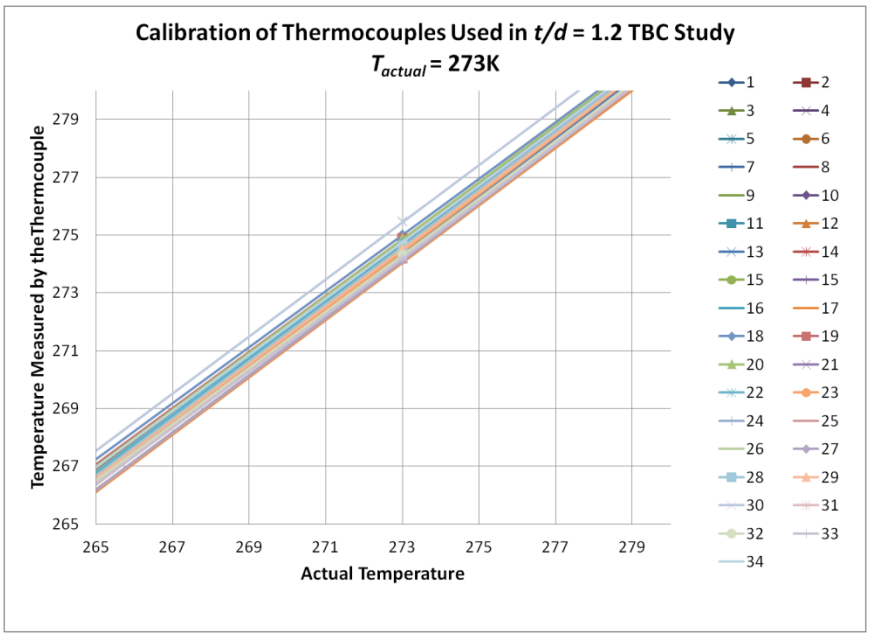

Figure 2.17: Comparison of the calibration curves used for all of the t/d = 1.2 TBC interface thermocouples at T_{actual} = 273K.

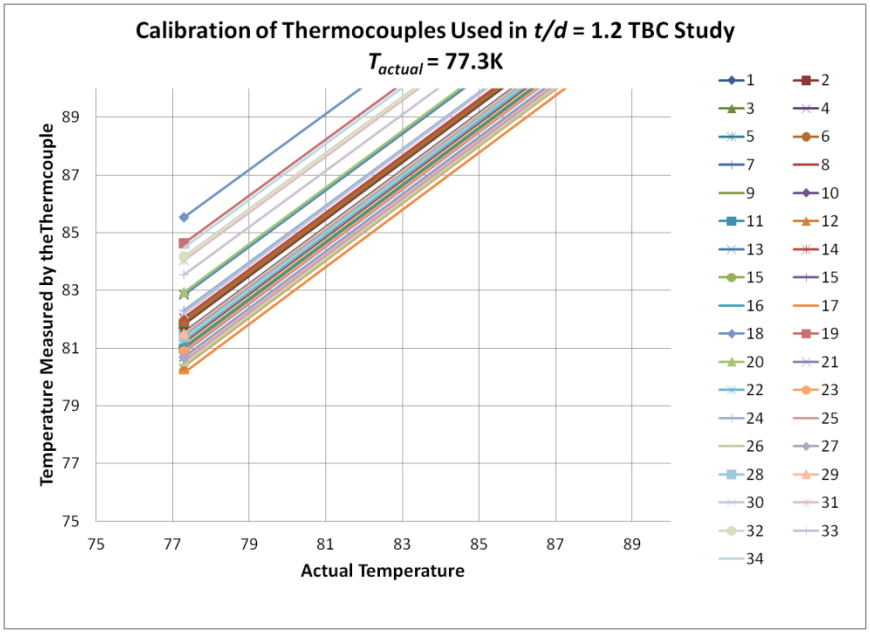

Figure 2.18: Comparison of the calibration curves used for all of the t/d = 1.2 TBC interface thermocouples at T_{actual} = 77.3K.

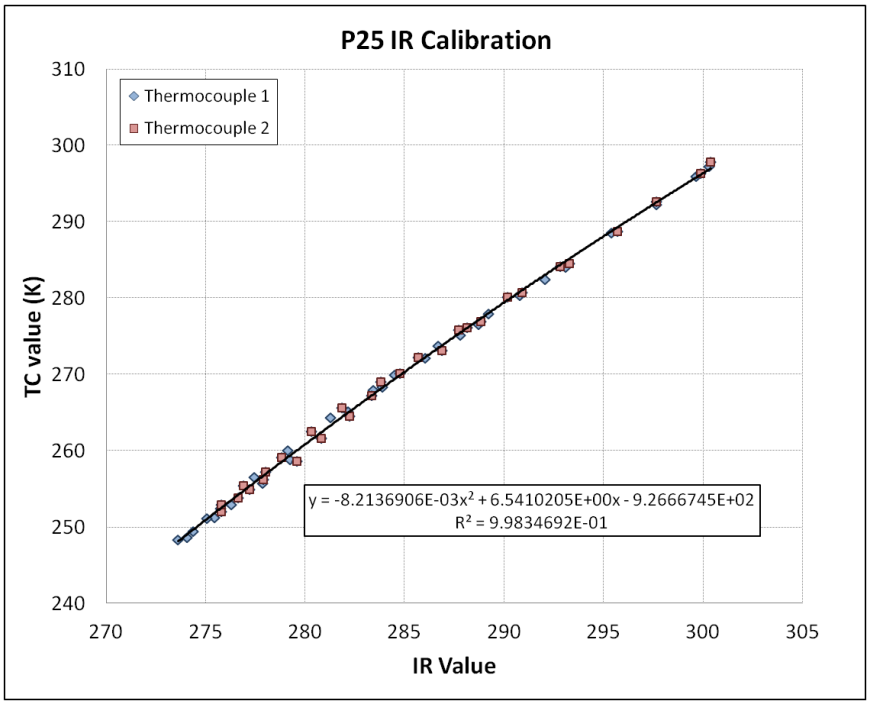

Figure 2.19: Calibration of P25 IR camera using two calibrated surface thermocouples.

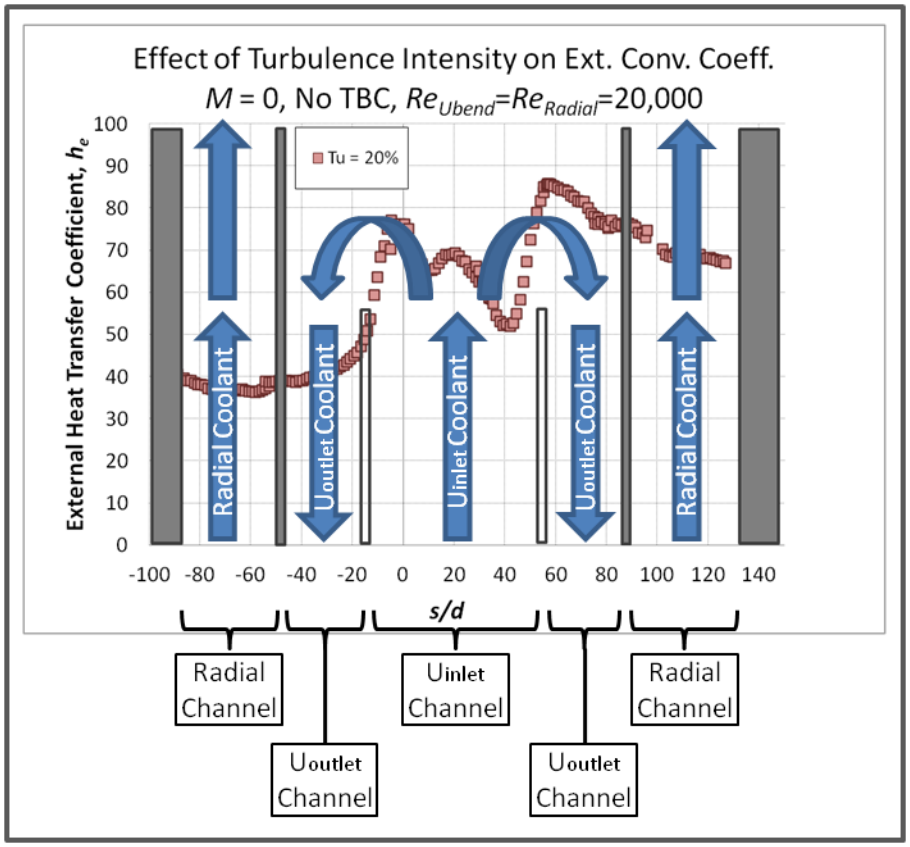

Figure 2.20: Sample plot of data in terms of *s/d* with locations of internal passages identified.

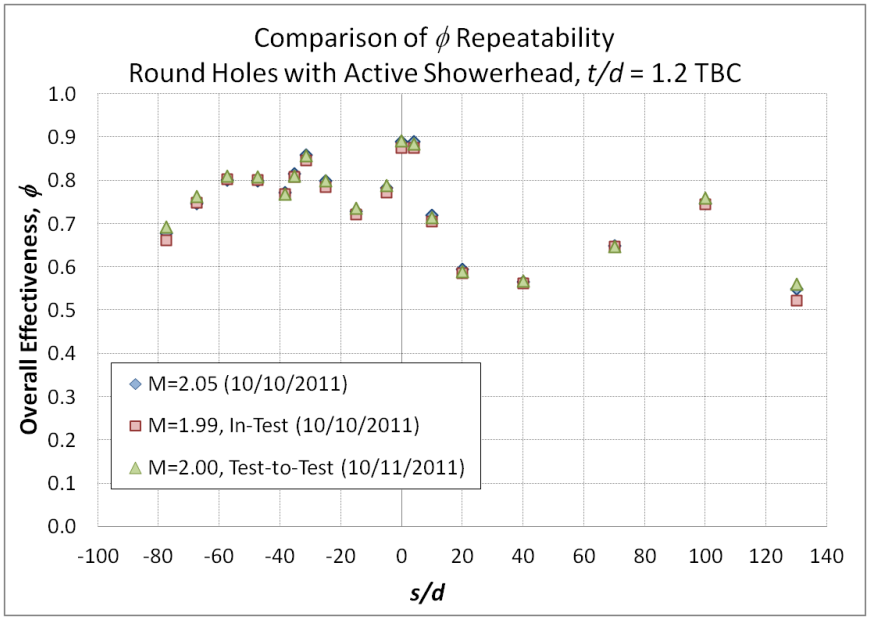

Figure 2.21: Comparison of in-test and test-to-test ϕ repeatability for round holes with an active showerhead at M = 2.0 with t/d = 1.2 TBC and Tu = 20%.

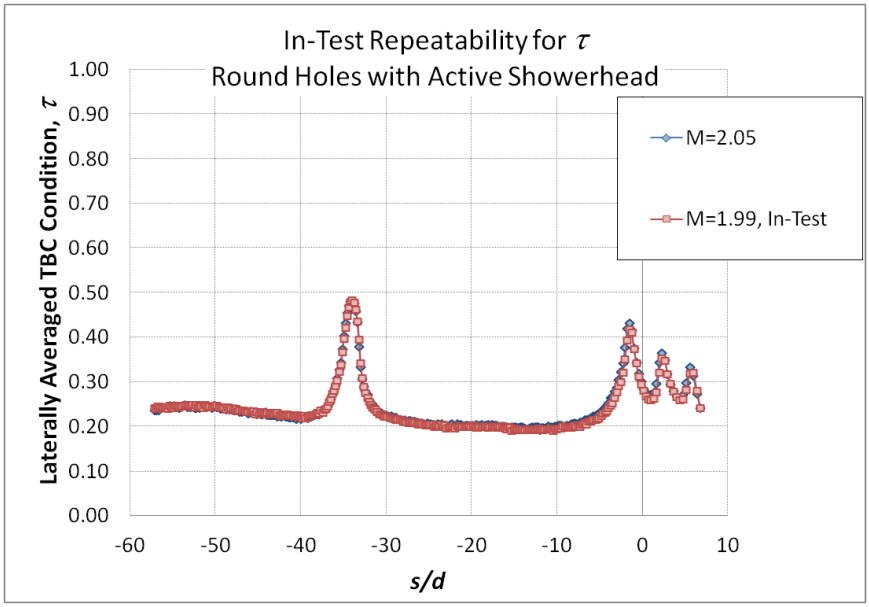

Figure 2.22: In-test repeatability of τ for round holes with an active showerhead at M = 2.0 with t/d = 1.2 TBC and Tu = 20%.

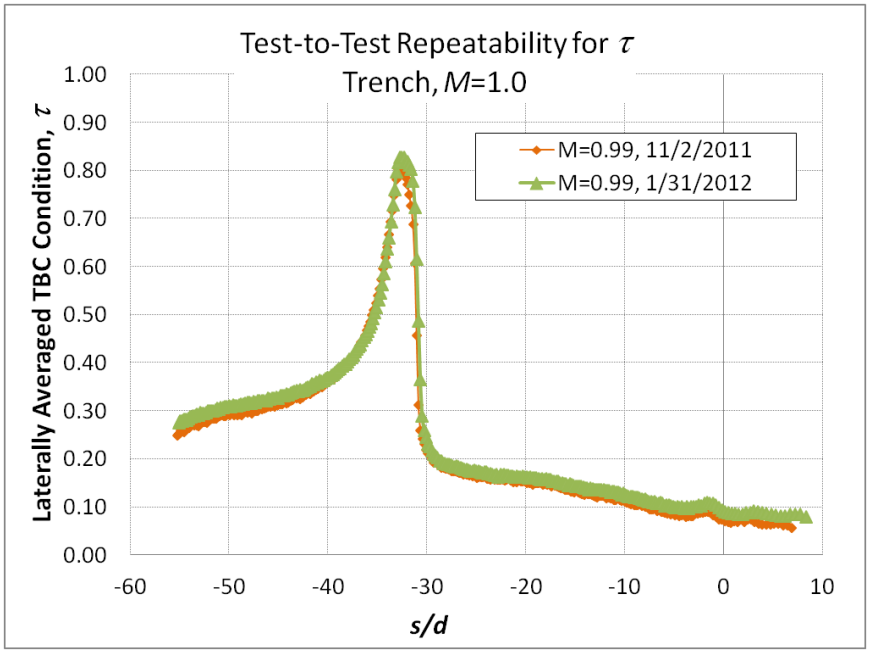

Figure 2.23: Test-to-test repeatability of τ for round holes with an active showerhead at $M = 1.0$ with $t/d = 1.2$ TBC and $Tu = 20\%$.

Chapter 3

3. ANALYTICALLY MODELING TBC

The purpose of this chapter is to provide a thorough derivation of an analytical model of the heat transfer through a turbine vane wall. The resulting analysis will provide an analytical model that predicts overall effectiveness, ϕ, and the external TBC condition, τ, based on a simplified 1-D heat transfer assumption.

3.1. Derivation of Analytical Models

A 1-D model for a system without TBC was presented in Chapter 1 and is defined as

$$\phi = \frac{\left(T_\infty - T_{w,e}\right)}{\left(T_\infty - T_{c,vane\ inlet}\right)} = \frac{(1-\eta)}{1 + Bi_w + {}^{h_e}/_{h_i}} + \eta \tag{1.16}$$

The addition of a TBC to the vane wall will alter the thermal behavior of the system due to the added thermal resistance of the TBC. This added resistance will reduce the heat flux through the wall as well as reducing the temperature of the external surface of the underlying metal wall. Figure 3.1 provides an understanding of the thermal behavior of the vane wall with and without TBC.

The additional thermal resistance of the TBC must be accounted for in order to properly model the thermal behavior of the system with TBC. The heat transfer through the wall may then be expressed as

$$q" = q"_{external} = q"_{TBC-Bond\ Coat} = q"_{wall} = q"_{internal} \tag{3.1}$$

such that

$$q"_{TBC-Bond\ Coat} = \frac{k_{TBC}}{t_{TBC}}\left(T_{TBC,e} - T_{TBC,i}\right) = \frac{1}{R"_{TBC-Bond}}\left(T_{TBC,i} - T_{Bond,e}\right) = \frac{k_{Bond}}{t_{Bond}}\left(T_{Bond,e} - T_{Bond,i}\right) = \frac{1}{R"_{Bond-w}}\left(T_{Bond,i} - T_{w,e}\right) \tag{3.2}$$

where $R"_{TBC\text{-}Bond}$ and $R"_{Bond\text{-}w}$ are the contact resistances between the TBC and bond coat and the bond coat and vane wall, respectively. Equation (3.1) can be rewritten as

$$q" = \frac{\left(T_{e,conv} - T_{i,conv}\right)}{{}^{1}/_{h_e} + {}^{t}/_{k}\Big|_{TBC} + R"_{TBC-Bond} + {}^{t}/_{k}\Big|_{Bond} + R"_{Bond-w} + {}^{t}/_{k}\Big|_{w} + {}^{1}/_{h_i}} \tag{3.3}$$

and

$$q" = \frac{\left(T_{e,conv} - T_{w,e}\right)}{{}^{1}/_{h_e} + {}^{t}/_{k}\Big|_{TBC} + R"_{TBC-Bond} + {}^{t}/_{k}\Big|_{Bond} + R"_{Bond-w}} \tag{3.4}$$

For the purposes of this analysis the parameters h_e and h_i account only for convective heat transfer. However, these terms can also represent the combination of both convective and radiative heat transfer on the external and internal surface, respectively. The effect of radiation will be discussed in greater detail in Section 3.2. Combining Equations (3.3) and (3.4) and multiplying through by $1/h_e$ results in

$$\frac{\left(T_{e,conv} - T_{w,e}\right)}{1 + Bi_{TBC} + Bi_{Bond} + h_e\left(R"_{TBC-Bond} + R"_{Bond-w}\right)} = \frac{\left(T_{e,conv} - T_{i,conv}\right)}{1 + Bi_{TBC} + Bi_{Bond} + h_e\left(R"_{TBC-Bond} + R"_{Bond-w}\right) + Bi_w + {}^{h_e}/_{h_i}} \tag{3.5}$$

In order to simplify this expression let

$$\beta = 1 + Bi_{TBC} + Bi_{Bond} + h_e\left(R"_{TBC-Bond} + R"_{Bond-w}\right) \tag{3.6}$$

Equation (3.5) can now be simplified to

$$\frac{\left(T_{e,conv} - T_{w,e}\right)}{\beta} = \frac{\left(T_{e,conv} - T_{i,conv}\right)}{\beta + Bi_w + {}^{h_e}/_{h_i}} \tag{3.7}$$

Specification of the driving temperature for external convective heat transfer will allow for simplification of this problem. In the case without film cooling, the driving temperature for the external convective heat transfer is assumed to be T_∞. The driving temperature is assumed to be T_{aw} when film cooling is present. For the case with film cooling, the equation can be modified to be

$$T_{aw} - T_{w,e} = \frac{\beta\left(T_{aw} - T_{i,conv}\right)}{\beta + Bi_w + {}^{h_e}/_{h_i}} \tag{3.8}$$

The differential ($T_{aw} - T_{i,conv}$) can be determined with the use of the definition for adiabatic effectiveness. From Chapter 1, η can be defined as

$$\eta = \frac{T_\infty - T_{aw}}{T_\infty - T_{c,hole\ exit}} \tag{1.4}$$

It should be recognized that the coolant temperature for adiabatic and overall effectiveness is defined differently. For adiabatic effectiveness, the coolant temperature is defined as the temperature at the exit of the film cooling holes. For overall effectiveness, the coolant temperature is defined at the inlet of the vane. The parameter χ is used to account for this difference. It is described as a "warming factor" because it accounts for the amount of warming that occurs between the inlet of the vane and the exit of the coolant holes. The warming factor is defined as

$$\chi = \frac{T_\infty - T_{c,hole\ exit}}{T_\infty - T_{c,vane\ inlet}} \tag{3.9}$$

Multiplying both sides of Equation (1.4) by χ yields

$$\chi\eta = \frac{T_\infty - T_{aw}}{T_\infty - T_{c,vane\ inlet}} \tag{3.10}$$

which accounts for the difference in reference coolant temperatures.

It is also necessary to account for the difference in temperature between the inlet of the vane and the driving temperature for internal convective heat transfer. This can be accomplished by establishing the parameter, α, which is defined as

$$\alpha = \frac{T_\infty - T_{i,conv}}{T_\infty - T_{c,vane\ inlet}} \tag{3.11}$$

It should be recognized that this term will vary depending on the vane configuration of interest. For instance, if a TBC is incorporated, the heat flux into a vane will be reduced. Consequently, the coolant temperature within the internal coolant passages may not increase as quickly as compared to a vane that does not utilize a TBC. Subtracting α by $\chi\eta$ results in the differential

$$\alpha - \chi\eta = \frac{T_\infty - T_{i,conv}}{T_\infty - T_{c,vane\ inlet}} - \frac{T_\infty - T_{aw}}{T_\infty - T_{c,vane\ inlet}} \tag{3.12}$$

This equation can then be simplified to

$$T_{aw} - T_{i,conv} = \left(T_\infty - T_{c,vane\ inlet}\right)(\alpha - \chi\eta) \tag{3.13}$$

Using Equation (3.13) the differential ($T_{aw} - T_{i,conv}$) in Equation (3.8) can be substituted for, resulting in the equality

$$T_{aw} - T_{w,e} = \frac{\beta\left(T_\infty - T_{c,vane\ inlet}\right)(\alpha - \chi\eta)}{\beta + Bi_w + {}^{h_e}/_{h_i}} \tag{3.14}$$

Solving for T_{aw} in Equation (3.10) yields

$$T_{aw} = T_\infty - \chi\eta\left(T_\infty - T_{c,vane\ inlet}\right) \tag{3.15}$$

Substituting for T_{aw} in Equation (3.14) provides

$$T_\infty - \chi\eta\left(T_\infty - T_{c,vane\ inlet}\right) - T_{w,e} = \frac{\beta\left(T_\infty - T_{c,vane\ inlet}\right)(\alpha - \chi\eta)}{\beta + Bi_w + {h_e}/{h_i}} \tag{3.16}$$

Dividing by ($T_\infty - T_{c,vane\ inlet}$) and adding the term $\chi\eta$ simplifies the equation to

$$\phi_{pred} = \frac{T_\infty - T_{w,e,pred}}{T_\infty - T_{c,vane\ inlet}} = \frac{\beta(\alpha - \chi\eta)}{\beta + Bi_w + {h_e}/{h_i}} + \chi\eta \tag{3.17}$$

The term for the external wall temperature has been modified to be $T_{w,e,pred}$ in order to recognize that the 1-D heat transfer assumption may predict a different temperature as compared to the values of $T_{w,e}$ that were measured experimentally in determining ϕ, as expressed in Equation (1.6). The utility of Equation (3.17) is that it can conform to various situations depending on the desired constraints. For example, a model with no TBC and no film cooling will simplify to

$$\phi_{pred} = \frac{T_\infty - T_{w,e,pred}}{T_\infty - T_{c,vane\ inlet}} = \frac{\alpha}{1 + Bi_w + {h_e}/{h_i}} \tag{3.18}$$

which is nearly identical to the predictive model presented in Equation (1.16) where η = 0. The only difference is the presence of the parameter α which has been added to account for the fact that the coolant temperature used in Equation (1.16) (i.e. the temperature at the inlet of the vane) is not necessarily the driving temperature for convective heat transfer. The parameter α could be eliminated if the internal heat transfer coefficient, h_i, was defined with the vane inlet temperature, however this method

provides a less clear picture of the 1-D heat transfer that is being modeled. Equation (3.17) can now be used to predict the non-dimensional temperature of the vane wall, or "metal temperature" with or without TBC and film cooling.

The above analysis can also be extended to determine the external surface temperature of a TBC, in the case that it is incorporated. The only difference is to use the equation

$$q" = \frac{\left(T_{e,conv} - T_{TBC,e}\right)}{{}^{1}/_{h_e}} \tag{3.19}$$

instead of Equation (3.4). Following the same analytical steps as above will then yield a predictive model for the external TBC condition, τ, such that

$$\tau_{pred} = \frac{T_\infty - T_{TBC,e,pred}}{T_\infty - T_{c,vane\ inlet}} = \frac{\alpha - \chi\eta}{\beta + Bi_w + {}^{h_e}/_{h_i}} + \chi\eta \tag{3.20}$$

The ratio of the heat transfer coefficients can also be solved for based on a 1-D heat transfer assumption. This can be accomplished by setting the internal convective heat transfer equal to either the local conduction through the vane wall or the local external convective heat transfer. The heat flux using these two methods must first be solved for. Based on conduction through the wall, the heat flux is

$$q"_{cond} = \left.\frac{k}{t}\right|_w \left(T_{w,e} - T_{w,i}\right) \tag{3.21}$$

The difference between the external and internal wall temperature can be determined with the differential of the external and internal overall effectiveness, ϕ_e and ϕ_i, respectively. This results in

$$\phi_e - \phi_i = \frac{T_\infty - T_{w,e}}{T_\infty - T_{c,vane\ inlet}} - \frac{T_\infty - T_{w,i}}{T_\infty - T_{c,vane\ inlet}} \tag{3.22}$$

This expression can be simplified to

$$T_{w,e} - T_{w,i} = \left(T_\infty - T_{c,vane\ inlet}\right)\left(\phi_i - \phi_e\right) \tag{3.23}$$

Equation (3.21) can now be updated to be

$$q"_{cond} = \left.\frac{k}{t}\right|_w \left(T_\infty - T_{c,vane\ inlet}\right)\left(\phi_i - \phi_e\right) \tag{3.24}$$

A similar process can be followed for the convective heat flux

$$q"_{conv} = h_e\left(T_\infty - T_{w,e}\right) \tag{3.25}$$

resulting in the equation

$$q"_{conv} = h_e\left(T_\infty - T_{c,vane\ inlet}\right)\phi_e \tag{3.26}$$

Equations (3.24) and (3.26) can now be used to derive expressions for the internal convective heat transfer coefficients. Starting with the conduction expression yields

$$q"_{cond} = \left.\frac{k}{t}\right|_w \left(T_\infty - T_{c,vane\ inlet}\right)\left(\phi_i - \phi_e\right) = h_{i,cond}\left(T_{w,i} - T_{i,conv}\right) \tag{3.27}$$

It is now necessary to determine the differential between the internal wall temperature and the driving temperature for convective heat transfer. This can be determined with the use of the term, α, as defined by Equation (3.11) starting with the differential

$$\phi_i - \alpha = \frac{T_\infty - T_{w,i}}{T_\infty - T_{c,vane\ inlet}} - \frac{T_\infty - T_{i,conv}}{T_\infty - T_{c,vane\ inlet}} \tag{3.28}$$

which can be simplified to

$$T_{w,i} - T_{i,conv} = \left(T_\infty - T_{c,vane\ inlet}\right)\left(\alpha - \phi_i\right) \tag{3.29}$$

Solving for h_i in Equation (3.27) results in

$$h_{i,cond} = \frac{k}{t}\Big|_w \frac{\left(T_\infty - T_{c,vane\ inlet}\right)}{\left(T_{w,i} - T_{i,conv}\right)}\left(\phi_i - \phi_e\right) \tag{3.30}$$

Substituting in Equation (3.29) yields

$$h_{i,cond} = \frac{k}{t}\Big|_w \frac{1}{\left(\alpha - \phi_i\right)}\left(\phi_i - \phi_e\right) \tag{3.31}$$

The ratio of convective heat transfer coefficients is then

$$h_e \Big/ h_{i,cond} = \frac{h_e}{\frac{k}{t}\Big|_w \frac{1}{\left(\alpha - \phi_i\right)}\left(\phi_i - \phi_e\right)} \tag{3.32}$$

which can be simplified to

$$h_e \Big/ h_{i,cond} = Bi_w \frac{\alpha - \phi_i}{\phi_i - \phi_e} \tag{3.33}$$

A similar process can be used in order to derive the ratio of convective heat transfer coefficients based upon the external convection as compared to the conduction through the wall for the case with no TBC. In this case Equation (3.27) is modified to be

$$q''_{conv} = h_e\left(T_\infty - T_{c,vane\ inlet}\right)\phi_e = h_{i,conv}\left(T_{w,i} - T_{i,conv}\right) \tag{3.34}$$

Solving for h_i and substituting Equation (3.29)

$$h_{i,conv} = h_{e,h_i} \frac{1}{(\alpha - \phi_i)} \phi_e \tag{3.35}$$

The ratio of convective heat transfer coefficients is then

$$h_e \Big/ h_{i,conv} = \frac{h_e(\alpha - \phi_i)}{h_{e,h_i} \phi_e} \tag{3.36}$$

In practice, the h_e term in Equation (3.35) may not be the same as the h_e term in the ratio of heat transfer coefficients. For example, $h_{i,conv}$ may be calculated with the use of measurements from a low mainstream turbulence intensity test while the goal is to determine the ratio of heat transfer coefficients for a high mainstream turbulence intensity test. Consequently, the h_e terms may not cancel in Equation (3.36) and the difference should be accounted for. Equations (3.33) and (3.36) provide two means of calculating the internal heat transfer coefficients based on a 1-D heat transfer analysis.

All of the parameters in the predictive equations for ϕ or τ are now constrained to be functions of ϕ_e, ϕ_i, h_e, T_∞, $T_{c,vane\ inlet}$, $T_{c,hole\ exit}$, and $T_{i,conv}$, all of which can be directly measured in the experimental facilities at the University of Texas at Austin. From the previous sentence, it shows that $\phi_{pred} = f(\phi_e, \phi_i)$ suggesting that in order to predict the overall effectiveness one would already need to know the answer. This is not the case. The inputs for predicting overall effectiveness (e.g. ϕ_e, ϕ_i, h_e, T_∞, $T_{c,vane\ inlet}$, $T_{c,hole\ exit}$, and $T_{i,conv}$) can be obtained from a relatively simple test and utilized to predict a more complicated system. For instance, by testing a conducting vane with no TBC and no film cooling it is possible to obtain all of the necessary information to estimate the performance of a conducting vane with a variety of TBC's and no film cooling. It is then

also possible to predict the performance of a film cooled conducting component with different TBC's if a variety of adiabatic tests are performed in order to determine, η, for various film cooling configurations at different blowing ratios.

3.2. Effect of Radiation on Analytical Models

The aforementioned analytical models did not explicitly address the effect of radiation. Radiation can have a large effect on the total heat transfer, particularly at elevated temperatures and thus it's necessary to quantify this effect. The predictive models for ϕ and τ based on a 1-D heat transfer assumption can be expressed as

$$\phi_{pred} = \frac{T_\infty - T_{w,e,pred}}{T_\infty - T_{c,vane\ inlet}} = \frac{\beta(\alpha - \chi\eta)}{\beta + Bi_w + {h_e}/{h_i}} + \chi\eta \tag{3.17}$$

and

$$\tau_{pred} = \frac{T_\infty - T_{TBC,e,pred}}{T_\infty - T_{c,vane\ linet}} = \frac{\alpha - \chi\eta}{\beta + Bi_w + {h_e}/{h_i}} + \chi\eta \tag{3.20}$$

As previously mentioned, the parameters h_e and h_i can be used to account for both the convective and radiative heat transfer. This can be done by acknowledging that the radiative heat flux can be expressed as

$$q"_{rad} = h_{e,rad}\left(T_\infty - T_{w,e}\right) \tag{3.37}$$

where $h_{e,rad}$ is the equivalent of an external radiative coefficient such that the resistance due to radiation is equal to

$$\frac{1}{h_{e,rad}} = R''_{rad} = \frac{1}{\varepsilon\sigma\left(T_\infty + T_{w,e}\right)\left(T_\infty{}^2 + T_{w,e}{}^2\right)} \tag{3.38}$$

The analysis for radiative heat transfer herein assumes that the surface of the vane is exposed to a large volume with surfaces treated as black-bodies at the same temperature as the hot gas bath, T_∞. The surface of the vane was also treated as a black-body despite. This was done to provide an understanding of the limiting case for radiation. The external coefficient, h_e, can then be expressed as

$$h_e = h_{e,conv} + h_{e,rad} \tag{3.39}$$

Until now the term h_e/h_i in Equations (3.17) and (3.20) only accounted for external and internal convection. The contribution of radiation can be determined by perturbing h_e and h_i to determine what effect radiation has on the predictive models. This can be done to understand how radiation affects a real engine component as compared to the model vane tested herein. The percentage difference in radiation effects is equal to

$$\frac{\phi_{pred,rad}\Big/\phi_{pred,no\ rad}\Big|_{model}}{\phi_{pred,rad}\Big/\phi_{pred,no\ rad}\Big|_{engine}} = \frac{\beta + Bi_w + \left(h_{e,conv} + h_{e,rad}\right)\Big/h_i\Big|_{model}}{\beta + Bi_w + \left(h_{e,conv} + h_{e,rad}\right)\Big/h_i\Big|_{engine}} \tag{3.40}$$

The prediction for overall effectiveness with no radiation was assumed to be equivalent between the model and engine and thus these terms cancelled. This expression was simplified to its final state by also assuming that film cooling was not utilized. Equation (3.40) can be utilized by first determining how much radiation alters h_e. Table 3.1

provides a comparison of the radiation effects on h_e for both a real engine component and the model vane. The addition of radiation increases h_e by approximately 21% and 16% in the engine for the case of $\phi = 0.3$ and $\phi = 0.6$, respectively. This is in contrast to an increase in h_e of approximately 11% with the model for both $\phi = 0.3$ and $\phi = 0.6$. Table 3.2 provides values for the parameters that will be used to solve Equation (3.40). The ratios for h_e / h_i presented in this table are based on the conduction and convection methods for determining h_i and have not yet accounted for radiation effects. Equation (3.40) can then be solved by increasing the values of h_e / h_i by the aforementioned changes due to radiation (e.g. increase h_e / h_i by 20% to predict the effects on the engine component at $\phi = 0.3$). The results of this analysis are shown in Table 3.3 for the conduction and convection methods. It is apparent that the model vane overpredicts the overall effectiveness of a real engine by approximately 1-6% depending on location and whether or not TBC is used. This is a result of radiation having a greater contribution to the total heat transfer in an engine that reduces the cooling performance in comparison to the results that are obtained with the modeled vane. The variation becomes exacerbated when comparing the model vane to the most advanced engines with hotter combustor temperatures. A similar analysis can be completed using $\tau = 0.3$ and $\tau = 0.6$ that will yield identical results.

Table 3.1: Approximated engine and model operating conditions for estimating $h_{e,rad}$.

	Engine vs. Model Conditions			
Parameter	**Engine**	**Model**	**Units**	**Notes**
T_∞	1800	300	K	
$T_{c,vane\ inlet}$	800	250	K	
$T_{w,e,\phi=0.3}$	1500	285	K	Based on $\phi = 0.3$
$T_{w,e,\phi=0.6}$	1200	270	K	Based on $\phi = 0.6$
$h_{e,conv}$	5000	50	W/m^2-K	
$h_{e,rad,\phi=0.3}$	1030	5.7	W/m^2-K	Based on $\phi = 0.3$
$h_{e,rad,\phi=0.6}$	800	5.3	W/m^2-K	Based on $\phi = 0.6$

Table 3.2: Inputs for Equation (3.40) based on experimental data and 1-D heat transfer predictions with Tu = 20%.

	β			Bi_w	h_e/h_i, no radiation	
s/d	No TBC	t/d=0.55 TBC	t/d=1.2 TBC		Cond. Method	Conv. method
-31.5465	1	2.45	4.16	0.51	1.32	1.30
36.76471	1	3.12	5.60	0.73	3.30	5.13

Table 3.3: Results of Equation (3.40) for various conditions showing that the model vane overpredicts the overall effectiveness of a real engine component by 1-6% due to the effect of radiation.

Conduction Method	$\phi = 0.3$			$\phi = 0.6$		
s/d	No TBC	t/d=0.55 TBC	t/d=1.2 TBC	No TBC	t/d=0.55 TBC	t/d=1.2 TBC
-31.5	1.041	1.027	1.020	1.024	1.016	1.012
36.8	1.056	1.040	1.030	1.033	1.024	1.018
Convection Method	$\phi = 0.3$			$\phi = 0.6$		
s/d	No TBC	t/d=0.55 TBC	t/d=1.2 TBC	No TBC	t/d=0.55	t/d=1.2
-31.5	1.040	1.027	1.020	1.024	1.016	1.011
36.8	1.063	1.049	1.039	1.037	1.029	1.023

3.3. Uncertainty of Analytical Models

The uncertainty of the models was determined with the use of the sequential perturbation method proposed by Moffat (1985). This uncertainty was in addition to the bias due to radiation that was previously discussed. The analytical models for ϕ and τ, Equations (3.17) and (3.20), respectively, were expanded to be functions of the parameters that were directly measured. The equations were first modified to reflect the conduction method and then simplified to

$$\phi_{pred,cond} = \frac{\left[q" + \frac{h_e t_{TBC}(T_1 - T_2)_{TBC,k}}{t_{TBC,k}}\right]\left[T_\infty - T_{i,conv} - (T_\infty - T_{c,he,\phi})\left(\frac{T_\infty - T_{aw}}{T_\infty - T_{c,he,\eta}}\right)\right]}{(T_\infty - T_{c,vi})\left[q" + \frac{h_e t_{TBC}(T_1 - T_2)_{TBC,k}}{t_{TBC,k}} + \frac{h_e t_w (T_1 - T_2)_{w,k}}{t_{w,k}}\left(1 + \frac{T_{w,i} - T_{i,conv}}{T_{w,e} - T_{w,i}}\right)\right]} + \left(\frac{T_\infty - T_{c,he,\phi}}{T_\infty - T_{c,vi}}\right)\left(\frac{T_\infty - T_{aw}}{T_\infty - T_{c,he,\eta}}\right) \tag{3.41}$$

and

$$\tau_{pred,cond} = \frac{q"\left[T_\infty - T_{i,conv} - (T_\infty - T_{c,he,\phi})\left(\frac{T_\infty - T_{aw}}{T_\infty - T_{c,he,\eta}}\right)\right]}{(T_\infty - T_{c,vi})\left[q" + \frac{h_e t_{TBC}(T_1 - T_2)_{TBC,k}}{t_{TBC,k}} + \frac{h_e t_w (T_1 - T_2)_{w,k}}{t_{w,k}}\left(1 + \frac{T_{w,i} - T_{i,conv}}{T_{w,e} - T_{w,i}}\right)\right]} + \left(\frac{T_\infty - T_{c,he,\phi}}{T_\infty - T_{c,vi}}\right)\left(\frac{T_\infty - T_{aw}}{T_\infty - T_{c,he,\eta}}\right) \tag{3.42}$$

The analytical equations can also be modified for the convection method, resulting in

$$\phi_{pred,conv} = \frac{\left[q" + \frac{h_e t_{TBC}(T_1 - T_2)_{TBC,k}}{t_{TBC,k}}\right]\left[T_\infty - T_{i,conv} - (T_\infty - T_{c,he,\phi})\left(\frac{T_\infty - T_{aw}}{T_\infty - T_{c,he,\eta}}\right)\right]}{(T_\infty - T_{c,vi})\left[q" + \frac{h_e t_{TBC}(T_1 - T_2)_{TBC,k}}{t_{TBC,k}} + \frac{h_e t_w (T_1 - T_2)_{w,k}}{t_{w,k}} + q"\left(\frac{h_e}{h_{e,h_i}}\right)\left(\frac{T_{w,i} - T_{i,conv}}{T_{w,e} - T_{w,i}}\right)\right]} + \left(\frac{T_\infty - T_{c,he,\phi}}{T_\infty - T_{c,vi}}\right)\left(\frac{T_\infty - T_{aw}}{T_\infty - T_{c,he,\eta}}\right) \tag{3.43}$$

and

$$\tau_{pred,conv} = \frac{q"\left[T_\infty - T_{i,conv} - (T_\infty - T_{c,he,\phi})\left(\frac{T_\infty - T_{aw}}{T_\infty - T_{c,he,\eta}}\right)\right]}{(T_\infty - T_{c,vi})\left[q" + \frac{h_e t_{TBC}(T_1 - T_2)_{TBC,k}}{t_{TBC,k}} + \frac{h_e t_w (T_1 - T_2)_{w,k}}{t_{w,k}} + q"\left(\frac{h_e}{h_{e,h_i}}\right)\left(\frac{T_{w,i} - T_{i,conv}}{T_{w,e} - T_{w,i}}\right)\right]} + \left(\frac{T_\infty - T_{c,he,\phi}}{T_\infty - T_{c,vi}}\right)\left(\frac{T_\infty - T_{aw}}{T_\infty - T_{c,he,\eta}}\right) \tag{3.44}$$

The thickness of the Corian® used for the conductivity measurement was assumed to be the same as the thickness of the vane wall. Consequently, the thickness terms, t_w and $t_{w,k}$, cancelled.

The conductivities of the vane wall and TBC were determined by measuring the temperature drop across a known thickness of material with a constant heat flux boundary condition. The conductivity could then be determined with

$$k = \frac{q"t}{(T_1 - T_2)} \tag{3.45}$$

The heat flux was calculated by measuring the voltage drop, V_{foil}, across a heat flux foil of known area, A, for a current, I. The current was determined by measuring the voltage drop, V_{res}, across a known resistance, R. This can be expressed as

$$q" = \frac{IV_{foil}}{A} = \frac{V_{res}V_{foil}}{RA} \tag{3.46}$$

The uncertainty of the heat flux was determined with the use of the propagation of error method proposed by Kline and McClintock (1953) and was found to be $\delta q"$ = ±13 W/m^2 for a total heat flux of $q"$ = 530 W/m^2. The uncertainty of the convective heat transfer coefficient was set to δh_e = ±2.8 W/m^2-K, as reported by Dees (2010). The uncertainty in thickness was set to δt = ±0.2 mm, which is 20x the resolution of the calibers used to measure the thickness. This was done due to the tolerances of the materials being measured and the likelihood that they were not spatially uniform. The rest of the uncertainty was based on temperature measurements. The uncertainty varied for these measurements dependent on whether the thermocouple was calibrated, an IR camera was used, or the value had to be approximated without a direct measure. Table

3.4 details the uncertainty of the analytical models in predicting ϕ with the conduction and convection methods for no TBC and no film cooling.

The uncertainty of predicting results with a TBC can also be determined. Table 3.5 provides a comparison of the elemental uncertainties that result in the root-sum-square uncertainty for ϕ and τ. The uncertainties of the different TBC thicknesses are also detailed. The t/d = 0.55 TBC was used to determine the conductivity of the cork. Therefore, uncertainties in the thickness of the t/d = 0.55 TBC do not factor into the predictions of ϕ and τ when using the conduction method. This can be seen in Equations (3.41) and (3.43) in which the thickness of the TBC will cancel if it is the same thickness used for determining the conductivity. However, this is not the case when predicting results for the t/d = 1.2 TBC. The increased uncertainty for the t/d = 1.2 TBC case can be seen in Table 3.5. Finally, Table 3.6 provides the uncertainty of the analytical models for a few cases with film cooling.

Table 3.4: Uncertainty of analytical models in predicting ϕ based on the conduction and convection methods for a vane with no TBC and no film cooling.

	No TBC, No Film, ϕ_{pred}					
	Measurement Uncertainty		**Elemental Uncertainty**			
			Conduction Method		**Convection Method**	
Measurement	**δ =**	**Units**	**LTu**	**HTu**	**LTu**	**HTu**
Heat Flux, q''	± 0.185	W/m^2	0.004	0.004	0.001	0.001
Ext. Conv. Coeff., h_e	± 2.8	W/m^2-K	0.015	0.008	0.004	0.003
t/d = 1.2 TBC Thickness, t	± 0.0002	m	N/A	N/A	N/A	N/A
t/d = 0.55 TBC Thickness, t	± 0.0002	m	N/A	N/A	N/A	N/A
TC1 for TBC k Measurement	± 0.5	K	N/A	N/A	N/A	N/A
TC2 for TBC k Measurement	± 0.5	K	N/A	N/A	N/A	N/A
TC1 for Vane Wall k Measurement	± 0.5	K	0.013	0.011	0.003	0.002
TC2 for Vane Wall k Measurement	± 0.5	K	0.013	0.011	0.003	0.002
Coolant Temp. at Hole Exit with Adiabatic Wall	± 1	K	N/A	N/A	N/A	N/A
Coolant Temp. at Hole Exit with Conducting Wall	± 2	K	N/A	N/A	N/A	N/A
Mainstream Temperature	± 0.5	K	0.007	0.008	0.013	0.013
Internal Conv. Temp., $T_{i,conv}$	± 2	K	0.001	0.001	0.000	0.002
Adiabatic Wall Temperature, T_{aw}	± 1	K	N/A	N/A	N/A	N/A
Coolant Temp. at Inlet of Vane, $T_{c,vi}$	± 0.5	K	0.003	0.002	0.003	0.002
Internal Wall Temp. of Conducting Vane, $T_{w,i}$	± 0.5	K	0.014	0.011	0.003	0.002
External Wall Temp. of Conducting Vane, $T_{w,e}$	± 0.5	K	0.011	0.009	0.006	0.005
		$\delta\phi_{pred}$ = ±	**0.031**	**0.024**	**0.016**	**0.015**

Table 3.5: Uncertainty of analytical models in predicting ϕ and τ based on the conduction method for a vane with TBC and no film cooling.

	TBC, No Film					
	Measurement Uncertainty		Elemental Uncertainty			
			ϕ_{pred}			τ_{pred}
			t/d=0.55 TBC		*t/d*=1.2	*t/d*=0.55
Measurement	δ =	**Units**	**LTu**	**HTu**	**HTu**	**HTu**
Heat Flux, q''	± 0.185	W/m^2	0.002	0.002	0.001	0.003
Ext. Conv. Coeff., h_e	± 2.8	W/m^2-K	0.008	0.004	0.002	0.006
t/d = 1.2 TBC Thickness, *t*	± 0.0002	m	0	0	0.007	0
t/d = 0.55 TBC Thickness, *t*	± 0.0002	m	N/A	N/A	0.016	N/A
TC1 for TBC *k* Measurement	± 0.5	K	0.004	0.004	0.005	0.001
TC2 for TBC *k* Measurement	± 0.5	K	0.004	0.004	0.005	0.001
TC1 for Vane Wall *k* Measurement	± 0.5	K	0.017	0.017	0.017	0.005
TC2 for Vane Wall *k* Measurement	± 0.5	K	0.017	0.017	0.017	0.005
Coolant Temp. at Hole Exit with Adiabatic Wall	± 1	K	N/A	N/A	N/A	N/A
Coolant Temp. at Hole Exit with Conducting Wall	± 2	K	N/A	N/A	N/A	N/A
Mainstream Temperature	± 0.5	K	0.005	0.006	0.004	0.008
Internal Conv. Temp., $T_{i,conv}$	± 2	K	0.006	0.005	0.010	0.001
Adiabatic Wall Temperature, T_{aw}	± 1	K	N/A	N/A	N/A	N/A
Coolant Temp. at Inlet of Vane, $T_{c,vi}$	± 0.5	K	0.004	0.004	0.005	0.001
Internal Wall Temp. of Conducting Vane, $T_{w,i}$	± 0.5	K	0.018	0.018	0.019	0.006
External Wall Temp. of Conducting Vane, $T_{w,e}$	± 0.5	K	0.015	0.015	0.016	0.005
	$\delta\phi_{pred}$ or $\delta\tau_{pred}$ = ±		**0.036**	**0.035**	**0.041**	**0.015**

Table 3.6: Uncertainty of analytical models in predicting ϕ and τ based on the conduction method for a vane with TBC and active film cooling.

	TBC, Active Film Cooling				
	Measurement Uncertainty		Elemental Uncertainty		
			ϕ_{pred}		τ_{pred}
			***t/d*=0.55**	***t/d*=1.2**	***t/d*=0.55**
			***M*=0.64**	***M*=2.0**	***M*=0.64**
Measurement	**δ =**	**Units**	**LTu**	**HTu**	**HTu**
Heat Flux, q''	± 0.185	W/m^2	0.001	0.001	0.002
Ext. Conv. Coeff., h_e	± 2.8	W/m^2-K	0.004	0.002	0.004
t/d = 1.2 TBC Thickness, *t*	± 0.0002	m	0	0.006	0
t/d = 0.55 TBC Thickness, *t*	± 0.0002	m	N/A	0.014	N/A
TC1 for TBC *k* Measurement	± 0.5	K	0.003	0.004	0.001
TC2 for TBC *k* Measurement	± 0.5	K	0.003	0.004	0.001
TC1 for Vane Wall *k* Measurement	± 0.5	K	0.013	0.015	0.004
TC2 for Vane Wall *k* Measurement	± 0.5	K	0.013	0.015	0.004
Coolant Temp. at Hole Exit with Adiabatic Wall	± 1	K	0.003	0.001	0.004
Coolant Temp. at Hole Exit with Conducting Wall	± 2	K	0.006	0.002	0.008
Mainstream Temperature	± 0.5	K	0.004	0.004	0.007
Internal Conv. Temp., $T_{i,conv}$	± 2	K	0.010	0.011	0.003
Adiabatic Wall Temperature, T_{aw}	± 1	K	0.010	0.007	0.016
Coolant Temp. at Inlet of Vane, $T_{c,vi}$	± 0.5	K	0.006	0.006	0.003
Internal Wall Temp. of Conducting Vane, $T_{w,i}$	± 0.5	K	0.011	0.017	0.003
External Wall Temp. of Conducting Vane, $T_{w,e}$	± 0.5	K	0.009	0.014	0.003
	$\delta\phi_{pred}$ or $\delta\tau_{pred}$ = ±		**0.03**	**0.038**	**0.022**

It should be recognized that the uncertainty in the analytical models will vary with changes in *s/d*. This is a result of the changing boundary conditions that make the measurement uncertainties a larger or smaller percentage of the total. For instance, the uncertainty in the external convective heat transfer coefficient, h_e, is ±2.8 W/m^2-K. When the external convective heat transfer coefficient drops to around 20 W/m^2-K on the pressure side of the vane the uncertainty exceeds 10% of the measurement. However, on the suction side the convective heat transfer coefficient rises above 70 W/m^2-K in some places which lessens the effect of uncertainty on a percentage basis. Consequently, all of the uncertainties presented in Table 3.4 – Table 3.6 are representative of an average uncertainty over the surface of the vane. Figure 3.2 – Figure 3.4 provide an understanding of how the uncertainty in the analytical models varies with changes in *s/d*, turbulence intensity, and TBC thickness, amongst other variables. As discussed in Chapter 2, the gray rectangles present in these figures indicate the location of the internal coolant passage walls. The use of the uncertainty as a function of *s/d* can be rather cumbersome and thus the averages provided in Table 3.4 – Table 3.6 will generally be used to determine the accuracy of the models.

3.4. Utilization of Analytical Models

The predictive capabilities of the analytical models presented in Section 3.1 will now be compared to the actual measurements obtained via experimentation at the TTCRL at the University of Texas at Austin. A couple assumptions were made in order to simplify the calculations. The first assumption was to ignore the presence of the bond coat. This was done after recognizing that the bond coat is relatively thin, often less than

100 μm. Furthermore, the thermal conductivity of the bond coat, approximately 10 W/m-K, is on the same order of magnitude as the thermal conductivity of the vane wall, which is approximately 20 W/m-K in a real engine. Consequently, the thermal resistance of the bond coat is approximately 1/10 of that for a 2 mm thick vane wall. In fact, since the thermal conductivity of the bond coat is relatively close to that of the vane wall, in comparison to the much lower thermal conductivity of the TBC (~1 W/m-K), the bond coat could simply be considered an extension of the wall thickness. By removing the bond coat from the 1-D analysis there is now only one location for contact resistance, the interface between the TBC and the vane wall. As previously discussed, the thermal conductivity of the TBC used in this study was determined by establishing a known heat flux across a sample piece of the simulated TBC while measuring the temperature drop. The setup for this measurement was done in the same manner as how the simulated TBC was attached to the surface of the model vane. Consequently, the thermal conductivity that was calculated based on Fourier's Law was actually a composite conductivity based on the resistance of the TBC itself as well as the contact resistance. For this reason, use of a separate calculation for the contact resistance was not used is the predictive models for ϕ and τ. Consequently, the thermal resistance of the predictive model may be simplified by setting

$$\beta = 1 + Bi_{TBC} \tag{3.47}$$

Consequently, the predictions of ϕ and τ will be dependent solely on k_{TBC}, k_w, t_{TBC}, t_w, h_e, h_i, and η.

Various experimental cases were used as a basis of comparison to determine the predictive capability of these models. Table 3.7 outlines the various experimental tests that were used as the primary conditions to assess the performance of the predictive models. Various parameters were changed in order to determine whether or not the models were capable of responding to each change. For instance, both high and low mainstream turbulence tests were used to compare to the models. Different TBC thicknesses were also used. Finally, various film cooling configurations at different blowing ratios were used to assess the performance of the models.

Table 3.7: Experiments used to assess the performance of the predictive models.

				Suction Side Holes		Pressure Side Holes	
M		0		0.64		1.0	2.0
Turbulence Level		LTu	HTu	LTu	HTu	HTu	HTu
No TBC	ϕ	✓*	✓*	✓*		✓**	✓**
t/d = 0.55 TBC	ϕ	✓	✓	✓	✓		
	τ	✓	✓		✓		
t/d = 1.2 TBC	ϕ		✓			✓	✓
	τ		✓			✓	✓

* Data collected by Dees (2010)
** Data collected by Albert (2011)

A variety of experimental data from different studies was needed in order to use the analytical models. The additional data came from the work of Dees (2010) and Albert (2011). Dees (2010) and Albert (2011) obtained overall and adiabatic effectiveness measurements for film cooling configurations that were identical to the

ones studied herein. However, TBC was not incorporated in the work of Dees (2010) and Albert (2011). The data from these two researchers was often used as the inputs for the variables in the analytical models, such as η. Figure 3.5 - Figure 3.10 provides a synopsis of the majority of data that was used to implement the analytical models. Detail concerning overall effectiveness without film cooling at high turbulence levels of Tu = 20% can be found in Dees (2010).

It is important to recognize that the study completed by Albert (2011) was at a density ratio of DR = 1.4. The work completed herein, as well as Dees (2010), was completed at DR = 1.2. Consequently, for a given blowing ratio, M, the data of this study is more prone to show signs of separation in comparison to the results presented by Albert (2011). This can be better understood by recognizing that for a given blowing ratio a system operating at a higher density ratio will have coolant jets with less momentum. This will result in coolant jets that a more easily turned onto the surface of the component and thus remain attached. Bogard and Thole (2006) discussed the fact that a momentum flux ratio of $I > 0.8$ will result in a separated jet despite changes in density ratio (surface curvature, cooling configuration, and other variables may change this value). Table 3.8 provides a comparison of the momentum flux ratio for given blowing ratios using two different density ratios, DR = 1.2 and 1.4, which correspond to the work completed for this study and Albert (2011), respectively. The momentum flux ratio is above I = 0.8 for both cases when the blowing ratios is above M = 1.1. Consequently, the results for the study presented herein are expected to produce greater separation at a blowing ratio of M = 1.0 as compared to the results from Albert (2011).

Table 3.8: Comparison of momentum flux ratio, *I*, for this study and Albert (2011) for given blowing ratios.

		M			
	DR	**1**	**1.5**	**2**	**3**
This Study	**1.20**	0.83	1.88	3.33	7.50
Albert (2011)	**1.40**	0.71	1.61	2.86	6.43

The use of various experimental cases as a basis of comparison for the predictive models required that additional assumptions be made due to a lack of sufficient baseline data. For instance, internal overall effectiveness data, ϕ_i, was only collected for the case with no film cooling. Consequently, the computations for the internal heat transfer coefficient with no film cooling had to be extended to cases with film cooling. It is possible that the presence of active film cooling holes may have altered the internal flow behavior changing the internal heat transfer coefficient distribution. This was not accounted for. However, in most cases, the mass flow rate of the film coolant was less than 20% of the overall mass flow rate of the internal coolant passing through the U-bend passage. Consequently, it was assumed that the film cooling did little to alter the internal heat transfer coefficients. Another assumption was made by setting T_{aw} as the driving temperature for external convective cooling in the cases with film cooling. As discussed by Dees (2010), the adiabatic wall temperature assumption fails under certain conditions. Consequently, the results of the predictive models should be viewed with a discerning eye recognizing that the underlying assumptions may not be valid under all conditions.

Additional approximations were made in order to quantify various coolant temperatures. This was necessary since not every temperature of interest was directly

measured during the baseline tests. The first of these was to approximate the appropriate driving temperature for internal convection. The temperature of the coolant at the mid-span of the vane was assumed to be the most appropriate driving temperature for convective cooling for the purposes of the 1-D heat transfer analysis. Alternate temperatures could be used to define the internal convective heat transfer, such as the temperature at the inlet of the vane. However, if the temperature at the inlet of the vane were used the predictions of h_i may artificially appear to vary between the cases with and without TBC since the internal coolant would warm at different rates. Therefore, the coolant temperature at the mid-span of the vane was used to define the internal convective heat transfer. The temperature at the mid-span was estimated using linear interpolation based on the temperature measurements at the inlet and exit of the vane. The temperature difference between the inlet and exit of the vane was at most 10 K for models without TBC. The difference was approximately 3-5 K for the models with TBC. A different driving temperature was used dependent upon whether the external surface of the vane was being cooled by either the fore or aft passage of the U-bend. It is possible that in some cases linear interpolation may not be the most accurate representation of how the coolant warms within the vane. To account for this the uncertainty of the internal convective driving temperature was set to $\delta T_{i,conv} = \pm 2$ K, as shown in Table 3.4 – Table 3.6. As previously alluded to, an additional coolant temperature approximation was made. This was done in order to determine the temperature of the film coolant at the exit of the film cooling holes for the various conducting model cases. This temperature was directly measured for only one case, a conducting vane model with round holes at *s/d*

= 30 operating at various blowing ratios. It was found that, on average, the film coolant exiting the holes was approximately 6 K higher than the temperature at the mid-span of the vane for a model with no TBC. This means that the coolant increased by 6 K due to heating as it passed through the round holes in the wall of the vane. It is expected that this level of warming would be less for the cases with TBC. The uncertainty for the temperature at the exit of the holes was set to $\delta T_{c,hole\ exit} = \pm 2$ K which should encompass the expected variations in this temperature.

3.4.1. Comparison to Cases with No Film Cooling

The models for predicting ϕ and τ will now be compared to experimental results for various vane configurations (e.g. with and without film cooling for varying TBC thicknesses). The results from the predictive models are presented with the use of both the conduction and convection methods for determining the internal convection coefficients. This was done since the two different methods resulted in noticeably different predictions for the internal coefficients at certain *s/d* locations that were outside of the expected levels of uncertainty. Consequently, both methods were used for comparison since there is no clear argument as to why one method would be superior to the other. The first comparison made was to determine how well the analytical models performed for a relatively simple system. In particular, this meant starting with a vane model with no TBC and no film cooling. Figure 3.11 shows this comparison for a condition with low mainstream turbulence intensity, *Tu* = 0.5%. In general the two different methods for determining the internal heat transfer coefficient perform quite well in predicting the overall effectiveness of the vane. This is expected though considering

that the simplest experiments for overall effectiveness, ϕ, were used to derive the internal heat transfer coefficients. However, the conduction method does not perform as well as the convection method, particularly at $30 < s/d < 50$. This is also the case for the high mainstream turbulence condition, Tu = 20% shown in Figure 3.12. However, the deviation between the two models is reduced in comparison to the lower turbulence condition. This is a result of the fact that the higher external convection coefficient for the high mainstream turbulence condition suppresses the differences in estimating the internal convection coefficient based on the two different methods. The results presented for the high turbulence case of Tu = 20% shown in Figure 3.12 are arguably more "predictive" since the internal heat transfer coefficient, h_i, was determined using the Tu = 0.5% data.

Insight into why the two different methods for estimating the internal convection coefficient differ can be gained by investigating the behavior of the external heat transfer coefficient and the 1-D heat flux through the wall based on the two methods. Figure 3.13 plots the external heat transfer coefficient for a Tu = 0.5% test along with the heat flux through the wall based on the conduction and convection methods. It can be seen that the external convection coefficient decreases by over 50% between $30 < s/d < 50$ resulting in a similar reduction in heat flux based on the convection method. The transition of the external boundary layer is not being captured in a similar manner between the conduction and convection methods. This may be due to the fact that rapid changes in boundary conditions may result in a more 3-D system, rather than the 1-D assumption that the system is being modeled as. The result is that the convection method predicts a lower

internal heat transfer coefficient due to the reduced prediction of heat flux. However, the conduction method predicts an increase in 1-D heat flux due to an increasing temperature differential between the exterior and interior vane surface from s/d = 30 to s/d = 50. Internal and external wall temperatures are shown in Figure 3.14 for T_∞ = 301 K and $T_{c,vane\ inlet}$ = 252 K. The temperature difference between the external and internal surface of the vane remains relatively constant over the region of 30 < s/d < 50. Referring back to Figure 3.13, it is evident that the conduction method predicts an increase in the heat flux for the same region on the suction side of the vane. On the other hand, the convection method predicts a decreasing heat flux for 30 < s/d < 50. Utilizing the information from both figures, the conduction method predicts an increasing internal convective heat transfer coefficient over the same region. The convection method predicts a decreasing internal coefficient.

The convection method for determining the internal convective heat transfer coefficient is dependent on knowing the external convection heat transfer coefficient. Consequently, determining the ratio of *he/hi* based on the convection method is a circular argument. Therefore, for the simplest case with no TBC and no film cooling, it seems most appropriate to use the conduction method when considering the predictive capability of the models. Unfortunately, using the conduction method results in less agreement between the prediction and the actual results over the range of 30 < s/d < 50.

As previously discussed, the analytical models can be used to predict the performance of a vane with or without a TBC. The only necessity is to alter the resistive model of the system by adjusting the term β to account for the additional thermal

resistance of the TBC. Figure 3.15 provides a comparison of the overall effectiveness for a matched Biot number vane with a TBC with thickness of t/d =0.55 and no film cooling with low mainstream turbulence, Tu = 0.5%. The analytical models do not do well in predicting the actual results. This is also the case for the high mainstream turbulence case shown in Figure 3.16.

One possible explanation for why the models do not perform well for the t/d = 0.55 TBC is that there may have been additional thermal resistance that has not been accounted for. The additional thermal resistance could manifest itself due to delamination of the TBC from the surface, incorrect measurement of the TBC thickness, or under-estimation of the contact resistance. A "phantom" resistance was added to β to determine whether or not this could explain the discrepancy between the model predictions and the actual results. Figure 3.17 and Figure 3.18 provide a comparison of the analytical models with a modified thermal resistance for the conduction and convection methods, respectively. The predictive models perform well with the additional thermal resistance. The additional resistance is equivalent to a 1.3 mm increase in the thickness of the cork and adhesive layer (which is also equivalent to a 0.5 mm gap of air). Delamination seems to be the only thing that could cause such a large increase in thermal resistance. If delamination did occur it likely was present on the pressure side of the vane. It was observed that the cork was resistant to adhering to the concave surface of the pressure side during the application process of the simulated TBC. Retrospectively, it is thought that the layer of double sided tape (t_{tape} = 0.2 mm) and the additional thickness of paint and primer were not included in the t/d = 0.55 TBC

thickness. The thickness of the paint and primer may have been greater than 0.1 mm depending on how many coatings were used. Unfortunately, since the model has been disassembled it is only speculation to estimate what additional thermal resistances may have existed. However, an error in the thickness reported for the t/d = 0.55 TBC could not account for the apparent additional thermal resistance. This is due to the fact that the cork with paint and double sided tape was used to measure the thermal conductivity of the simulated TBC. Therefore, the effect of the additional thickness that may not have been recorded would have been captured in the calculation of the thermal conductivity. Considering the behavior of the predictive models, it appears likely that additional thermal resistance existed. The most likely answer is imperfect contact between the adhesive layer and the cork and vane wall. It is possible that the layer of cork began to delaminate over the duration of the 5 months of testing the t/d = 0.55 TBC model. If this were the case, the apparent thermal resistance of the simulated TBC would increase which is consistent with the predictions of the analytical models.

The cooling performance on the external surface of the TBC, τ, can be predicted based on Equation (3.20). The predictive results for the case with no film cooling and high mainstream turbulence, Tu = 20%, is shown in Figure 3.19. The model works relatively well in this case as compared to the previous predictions of ϕ. This can be explained by the fact that the exterior temperature of the TBC will asymptotically approach the mainstream temperature as more thermal resistance is added. Consequently, relatively large changes in the thermal resistance would be required to

make a significant change in the external surface temperature considering that it is already near $\tau = 0.1$.

The performance of overall effectiveness, ϕ, and TBC condition, τ, were also predicted for the t/d = 1.2 thick TBC vane model. Figure 3.20 - Figure 3.21 show the predicted performance for the overall effectiveness and TBC condition for a vane model with no film cooling, t/d = 1.2 TBC, and Tu = 20%. In both cases the predictive models perform well. The only discrepancy is at the location of s/d = 46, which as previously discussed is a result of the conduction and convection methods overpredicting and underpredicting the internal convective heat transfer coefficient, respectively.

3.4.2. Comparison to Cases with Film Cooling

The predictions of ϕ and τ can be extended to systems will film cooling by incorporating the use of adiabatic effectiveness results. This entails making the assumption that the appropriate driving temperature for external convective heat transfer is the adiabatic wall temperature. Inevitably, the cooling performance of a film cooled system will be strongly affected by 3-dimensional heat transfer near the film cooling holes. Consequently, it is expected that the predictive models may not perform as well with film cooling due to the adiabatic wall temperature assumption and the 1-D heat transfer simplification.

Two unique film cooled models were tested during this study. The first of these models incorporated a single row of round holes at s/d = 31. The second model incorporated a single row of round holes at s/d = -32 and three rows of round holes in the

stagnation region. Greater detail concerning these configurations is provided in Chapter 2. The cooling performance of each of these configurations will now be compared to the predictive models for select blowing ratios. Figure 3.22 shows the performance of the analytical models in predicting the overall effectiveness for a vane with no TBC, Tu = 0.5% and round holes operating at M = 0.64 on the suction side of the vane. The predictive models do not capture the actual performance of the system immediately upstream of the suction side holes. Film cooling should have no effect upstream of the holes for a 1-D heat transfer system since the adiabatic effectiveness in this region is zero. Therefore, the upstream cooling is clearly a result of convective cooling within the cooling holes that is producing 3-D heat transfer that is not being captured by the models. The models perform well downstream of the holes, other than at a location of s/d = 46 for the conduction method. As previously discussed, the conduction method seems to over predict the internal convective heat transfer coefficient as compared to the convective method, resulting in higher predicted cooling performance in this region.

The performance of the pressure side film cooling configuration with no TBC was also predicted. Figure 3.23 and Figure 3.24 shows the performance of the predictive models at a blowing ratio of M = 1.0 and 2.0, respectively, for a high mainstream turbulence intensity condition of Tu = 20%. The models do not perform well for these cases. This is likely due to the fact that the analytical models under-predict the 3-D nature of the heat transfer. This is particularly evident at the pressure side holes and near the showerhead region in which the cooling of the wall is dominated by the in-hole convective cooling. It is also possible that the expected 6 K warming of the coolant as it

passed through the film cooling holes was overpredicted; however, the uncertainty in this temperature cannot account for the differences seen in Figure 3.23 and Figure 3.24. For example, if the exit hole temperature were set to be equal to the temperature at the inlet of the vane, the most extreme case, the predicted performance of ϕ improves by at most $\Delta\phi$ = 0.02 for the conduction method results shown in Figure 3.24. This conclusion emphasizes how the convective cooling through the holes and on the inside of the vane dominates the cooling performance of the vane wall. This is particularly true when a TBC is added due to the additional insulation from the effects of film cooling on the exterior surface. In the cases of Figure 3.23 and Figure 3.24 the inability of the analytical models to predict the overall effectiveness must be attributed to the 3-D nature of the heat transfer.

The effects of TBC with film cooling will now be considered for the predictive models. Figure 3.25 compares overall effectiveness results to the analytical models for the prediction of ϕ with a TBC of t/d = 0.55 thickness, Tu = 20%, and film cooling with round holes at M = 0.64 on the suction side of the vane. The analytical models predict the actual result within 10%, excluding locations near the holes that will be affected by convection through the cooling holes. These results do not account for the possibility that there was an additional thermal resistance for the t/d = 0.55 TBC as previously discussed. The convection method predicts the actual results within 5% if the additional thermal resistance is accounted for. However, accounting for the additional thermal resistance results in the conduction method overpredicting the overall effectiveness by over 17% at s/d = 46. Figure 3.26 provides a direct comparison of measurements and

predictions of overall effectiveness, ϕ, for varying blowing ratios from suction side holes with t/d = 0.55 TBC at Tu = 20% . The conduction method was used to predict the internal heat transfer coefficient in this case. It is clearly evident that the analytical models do not predict the collapse in overall effectiveness that is observed in the measurements at approximately s/d = 37. This is likely due to the analytical models underpredicting 3-D cooling effects near the holes that offset the detrimental effects of separation at higher blowing ratios.

The external TBC condition, τ, can also be predicted for the cases with film cooling. This is shown in Figure 3.27. The models overpredict the performance of τ by over 60% at s/d = 37. This error cannot be explained solely by the inclusion of additional thermal resistance in the model for this only reduces the predictions of TBC condition by approximately $\Delta\tau$ = 0.01 at s/d = 37 for the conduction method. Furthermore, this discrepancy cannot be accounted for by 3-D heat transfer effects since, if anything, the analytical models should underpredict 3-D effects. One possible explanation results from the possibility that the incorrect blowing ratio was used to predict τ. The effect of predicting τ with the use of high blowing ratio adiabatic effectiveness results is shown in Figure 3.28 for the conduction method. It can be seen that the presumed blowing ratio has a large effect on the predicted TBC condition, τ. It appears as if the blowing ratio for the experimental result was somewhere between M = 1.0 and 1.3, rather than the originally presumed M = 0.64. The uncertainty in the blowing ratio, as reported in Chapter 2, was $\delta M = \pm 0.15$, of which over 60% was attributable to the bias uncertainties

of the pressure transducers and orifice meter discharge coefficients. Consequently, this uncertainty could not account for the totality of the difference between the predicted and actual results for τ. Another source of error for the round holes in the TBC was the fact that they were made by hand rather than being machine drilled as they were for the adiabatic effectiveness measurements. It is possible that the film cooling holes for the TBC model were undersized which would have caused a higher than expected blowing ratio. An unexpected increase in the blowing ratio would have encouraged separation of the coolant jets from the wall and a subsequent reduction in adiabatic effectiveness. In order to account for an increase in blowing ratio from $M = 0.64$ to $M = 1.30$, the diameter of handmade holes would have needed to be approximately 30% smaller than the target diameter of $d = 4.2$ mm. A 30% reduction in hole diameter would have been noticed and thus it's unlikely that hand making the TBC holes could account for the entire difference. It is also possible that the surfaces within the hole were not perfectly smooth or that the holes through the TBC were not perfectly angled at 42°. The coolant behavior exiting the hole may have been altered if a bump or other non-uniformity existed within the hole. This may have caused a local acceleration in the film coolant resulting in different behavior as compared to the results for the adiabatic model. An additional source of error was due to the calculation of τ and η based on IR thermography. In both cases the error in the measurement was approximately ± 0.02. The final source of error is based on the assumption used in the predictive models for the coolant temperature at the exit of the film cooling holes. The temperature was assumed to be 6 K higher than the temperature at the mid-span of the internal passage, as previously discussed. This was done based on

temperature measurements at the exit of the hole for a film cooled model with no TBC. The predicted values for ϕ reduce by $\Delta\phi = 0.03$ at a location of $s/d = 37$. Therefore, an error in the exit hole temperature cannot account for the difference seen between the predicted and actual results. None of the above sources of error could solely account for the differences seen between the actual results and the predictions of the analytical models. However, if the TBC holes were undersized by 10 - 20% it is possible that the other sources of error could account for the differences that are seen between the predictive models and the experimental measurements.

The analytical models were also used to predict the overall effectiveness and TBC condition for the $t/d = 1.2$ TBC with film cooling. Figure 3.29 and Figure 3.30 provide comparisons between the actual results of overall effectiveness, ϕ, and the predictions of the analytical models for the pressure side film cooled vane with $t/d = 1.2$ TBC at $Tu =$ 20%. The predictive models do not do very well in these cases. The most likely case for error is the fact that the model is underpredicting the 3-D effects of heat transfer for the pressure side film cooling configurations, as previously discussed. Figure 3.31 provides a direct comparison of measurements and predictions of ϕ for varying blowing ratios on the pressure side of the vane using the conduction method. In this case, it is evident that the predictive models do not do well. An additional explanation for this error, aside from the 3-D issue previously discussed, is the fact that the internal heat transfer coefficient being used is based on a model with no film cooling due to the limitations of available data. The pressure side cooling shown here with an active showerhead can bleed off more than 40% of the internal coolant at higher blowing ratios. This may have a

significant effect on the internal heat transfer coefficient that is not being captured in the analytical models.

The final use of the analytical models was to compare the external TBC condition, τ, of the actual results and predictions for the $M = 2.0$ pressure side film cooled vane with $t/d = 1.2$ TBC at $Tu = 20\%$. The analytical models perform well for both the conduction and convection methods and are shown in Figure 3.32. However, the models do not predict the 3-D conduction effects near the showerhead due to convective cooling through the film cooling holes.

3.5. Supplementing the Analytical Models with Experimental Data

The predictive models for ϕ and τ based on a 1-D heat transfer assumption can be expressed as

$$\phi_{pred} = \frac{T_\infty - T_{w,e,pred}}{T_\infty - T_{c,vane\ inlet}} = \frac{\beta(\alpha - \chi\eta)}{\beta + Bi_w + {}^{h_e}/_{h_i}} + \chi\eta \tag{3.17}$$

and

$$\tau_{pred} = \frac{T_\infty - T_{TBC,e,pred}}{T_\infty - T_{c,vane\ linet}} = \frac{\alpha - \chi\eta}{\beta + Bi_w + {}^{h_e}/_{h_i}} + \chi\eta \tag{3.20}$$

Without film cooling these equations simplify to

$$\phi_{pred,o} = \frac{T_\infty - T_{w,e,pred}}{T_\infty - T_{c,vane\ inlet}} = \frac{\beta\alpha}{\beta + Bi_w + {}^{h_e}/_{h_i}} \tag{3.48}$$

and

$$\tau_{pred,o} = \frac{T_\infty - T_{TBC,e,pred}}{T_\infty - T_{c,vane\ inlet}} = \frac{\alpha}{\beta + Bi_w + {h_e}/{h_i}} \tag{3.49}$$

where the subscript "*o*" denotes no film cooling. Equations (3.17) and (3.20) can then be written as

$$\phi_{pred} = \frac{T_\infty - T_{w,e,pred}}{T_\infty - T_{c,vane\ inlet}} = \phi_o \left(1 - \frac{\chi\eta}{\alpha}\right) + \chi\eta \tag{3.50}$$

and

$$\tau_{pred} = \frac{T_\infty - T_{TBC,e,pred}}{T_\infty - T_{c,vane\ inlet}} = \tau_o \left(1 - \frac{\chi\eta}{\alpha}\right) + \chi\eta \tag{3.51}$$

where ϕ_o and τ_o describe either the overall effectiveness or TBC condition for a vane with no film cooling. The cooling performance of the vane without film cooling can be measured experimentally and then used as an input variable to determine the cooling performance of the vane with film cooling. One of the benefits of using Equations (3.50) and (3.51) is that they are independent of the ratio of heat transfer coefficients. This means that the uncertainty due to the prediction of the internal coefficient, h_i, has been eliminated.

The results from implementing the supplemented analytical models found an improvement in the prediction of film cooling results in comparison to the analytical predictions without the use of ϕ_o or τ_o. However, in general, the use of the supplemented analytical models did not provide results that consistently predicted the performance of a film cooled system. The supplemented analytical predictions will first be compared to

measurements for suction and pressure side film cooled models with no TBC. Figure 3.33 compares predictions with measurements for suction side film cooling at varying blowing ratios. The models perform well in this case, often predicting the measured value for overall effectiveness within 10%. As expected, the predictions of the model do not perform well upstream of the holes due to 3-D heat transfer effects. Figure 3.34 provides a similar comparison except using the pressure side measurements collected by Albert (2011). In this case, the models did not perform as well, regularly underpredicting the overall effectiveness over the region of $0 < s/d < -32$. The models come closer to predicting the ϕ measurements at locations of $s/d = -22$ and -40, likely due to the reduced 3-D effects at these locations as well as further downstream.

The supplemented analytical models were also used to predict film cooling performance with $t/d = 0.55$ and $t/d = 1.2$ TBC. Figure 3.35 and Figure 3.36 provide comparisons of predictions for ϕ and τ for a suction side film cooled vane with $t/d = 0.55$ TBC. Figure 3.37 and Figure 3.38 provide similar comparisons except for a pressure side film cooled vane with $t/d = 1.2$ TBC. The comparisons show that the analytical models were consistently unable to accurately predict the film cooling results for varying blowing ratios near the cooling holes. However, the predictions of τ for the $t/d = 1.2$ TBC in Figure 3.38 were regularly within 10%, excluding locations near the pressure side holes.

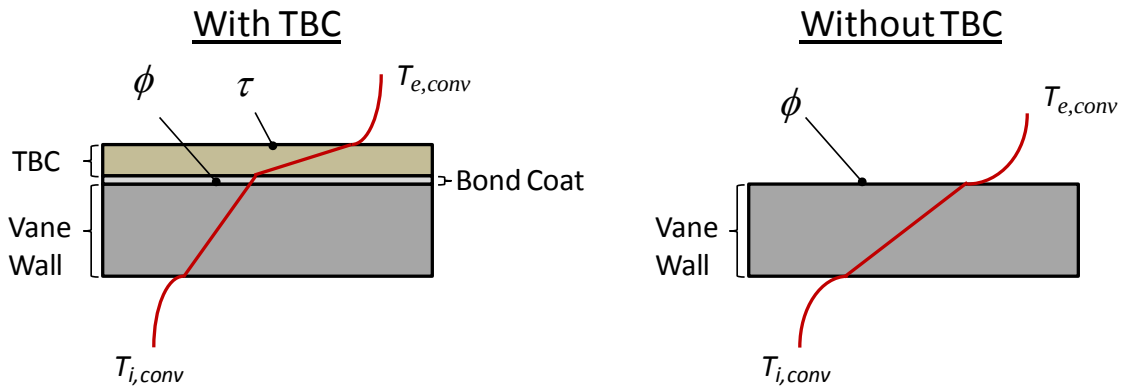

Figure 3.1: Comparison of 1-D heat transfer through turbine vane wall with and without a TBC.

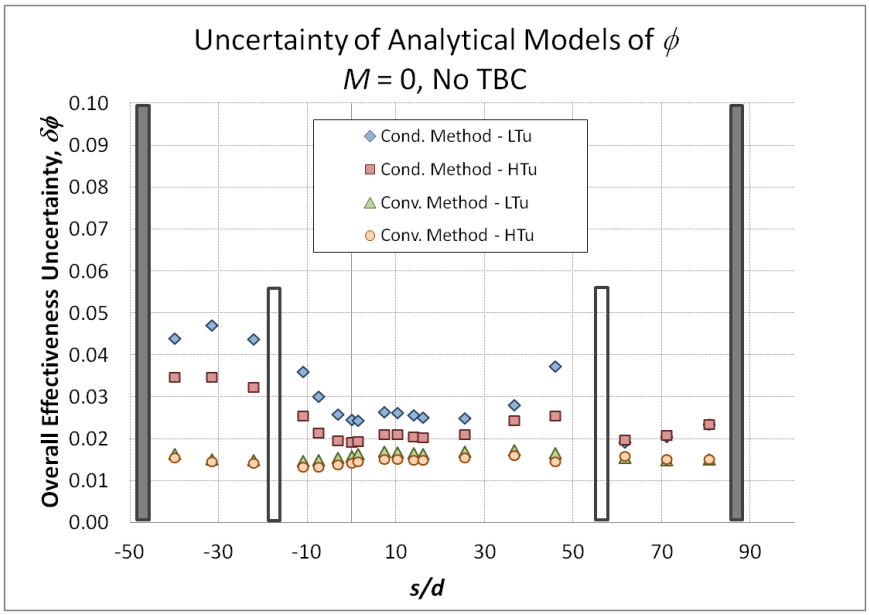

Figure 3.2: Comparison of analytical model uncertainty as f(*s/d*) with changes in 1-D heat transfer method and mainstream turbulence intensity and no film cooling.

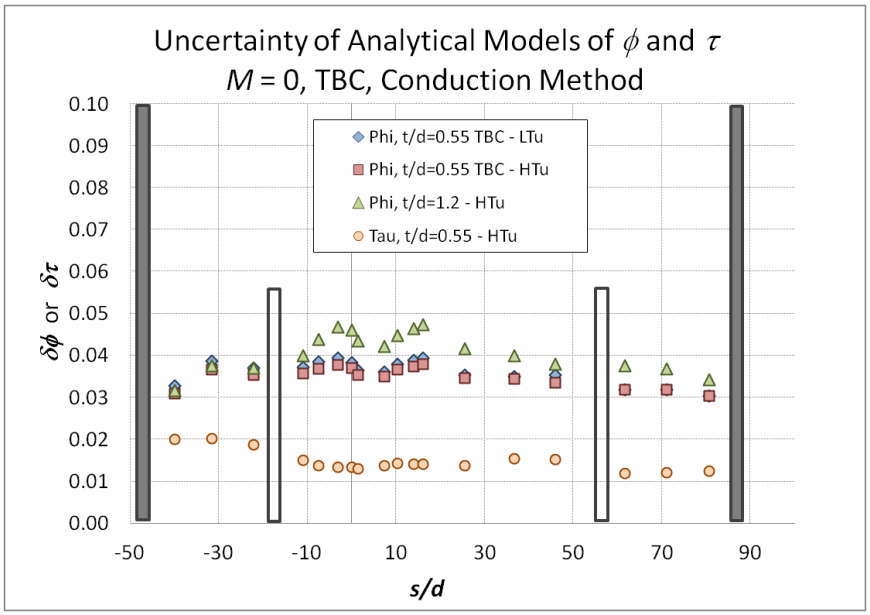

Figure 3.3: Comparison of analytical model uncertainty as f(*s/d*) for either ϕ or τ with changes in TBC thickness and no film cooling.

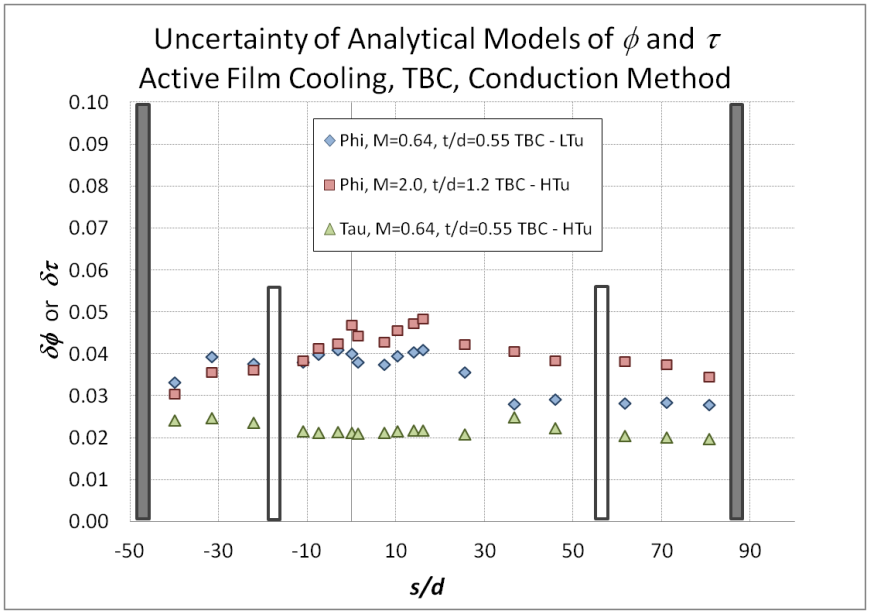

Figure 3.4: Comparison of analytical model uncertainty as f(*s/d*) for either ϕ or τ with active film cooling.

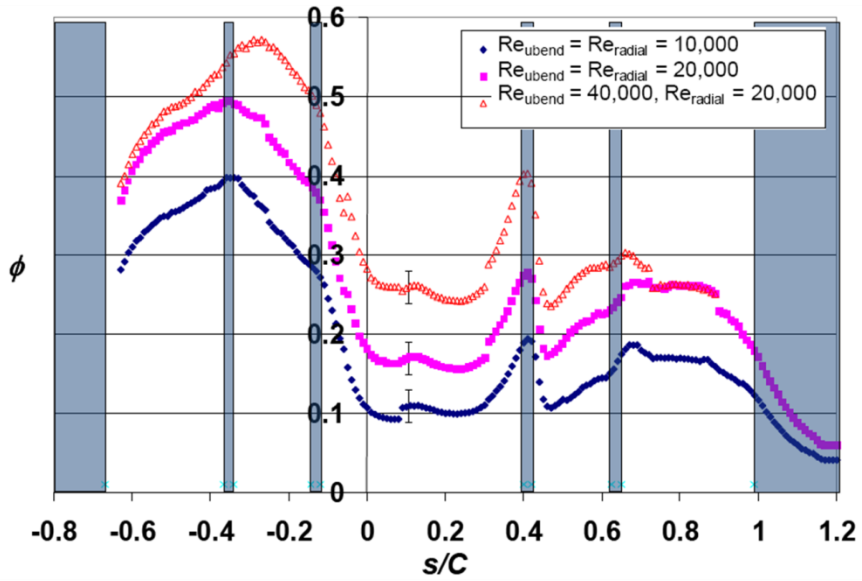

Figure 3.5: Overall effectiveness of matched Biot number vane at various internal Reynolds number conditions with *Tu* = 0.5% (from Dees (2010)).

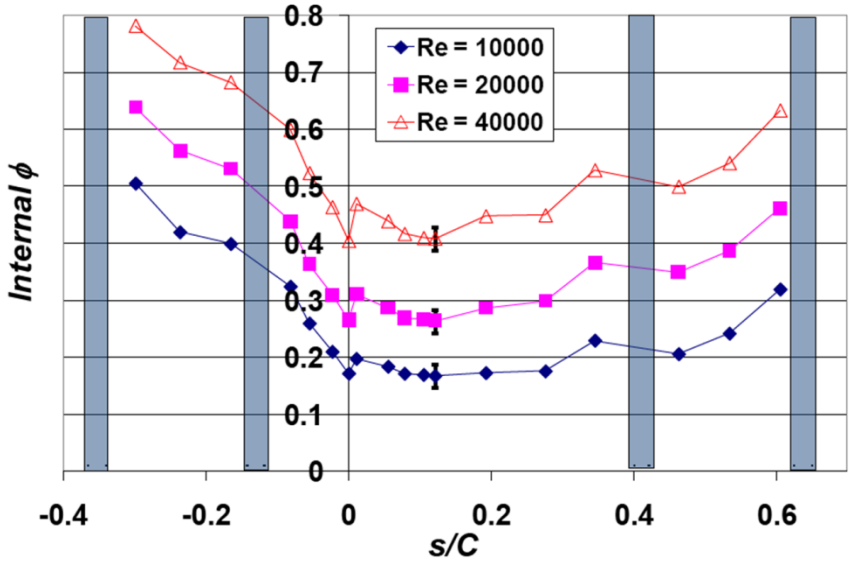

Figure 3.6: Internal effectiveness of matched Biot number vane at various internal Reynolds number conditions with *Tu* = 0.5% (from Dees (2010)).

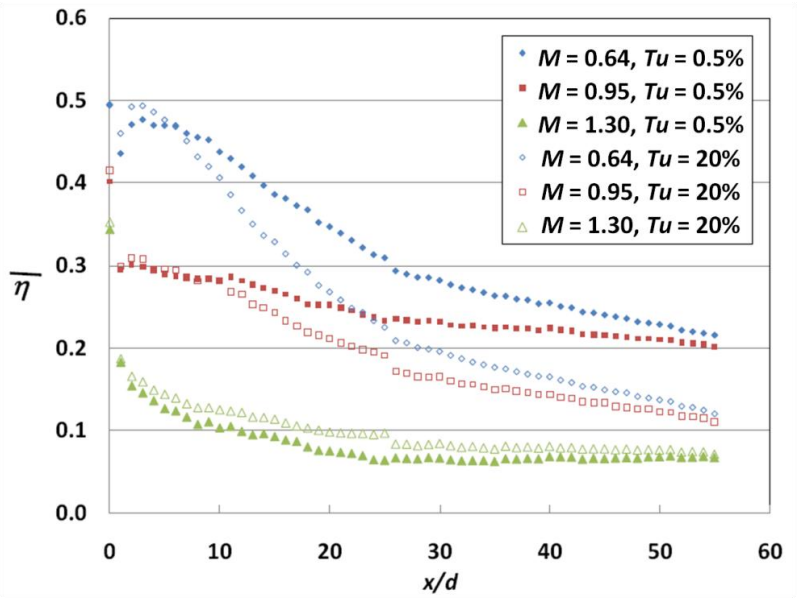

Figure 3.7: Adiabatic effectiveness of suction side round holes at $s/d = 31$ for varying blowing ratios at $Tu = 0.5\%$ and 20% (modified from Dees (2011)).

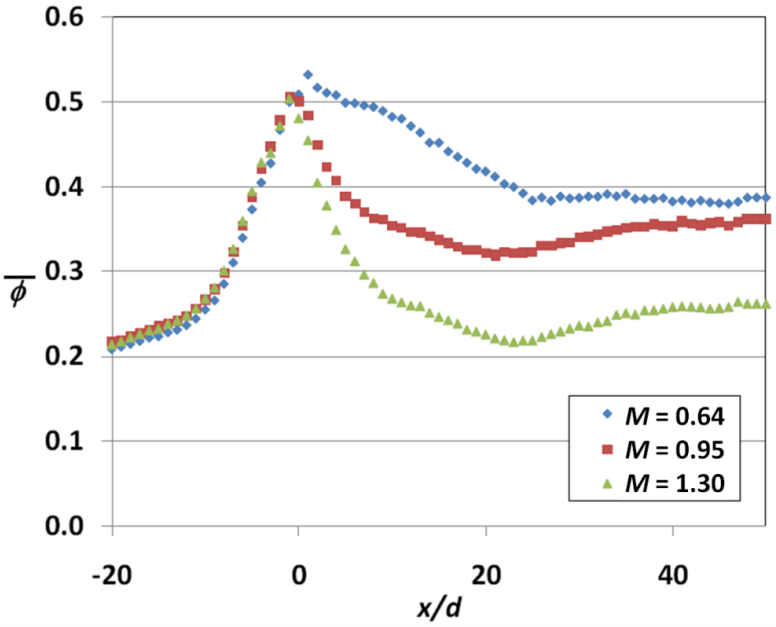

Figure 3.8: Overall effectiveness of suction side round holes at $s/d = 31$ for varying blowing ratios at $Tu = 0.5\%$ (modified from Dees (2011)).

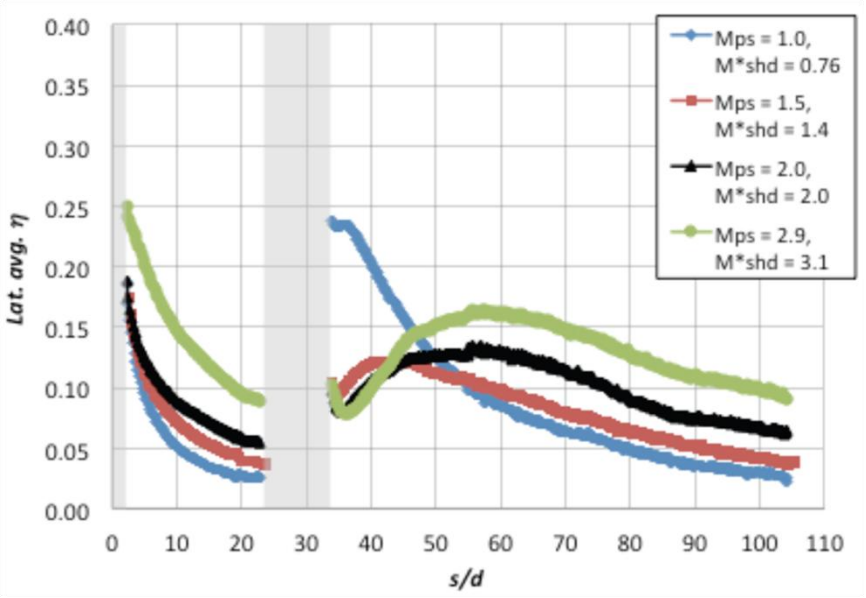

Figure 3.9: Adiabatic effectiveness of pressure side round holes at *s/d* = 32 with an active showerhead for varying blowing ratios with *Tu* = 20% (from Albert (2011)). Albert (2011) defined the pressure side of the vane as being positive *s/d*.

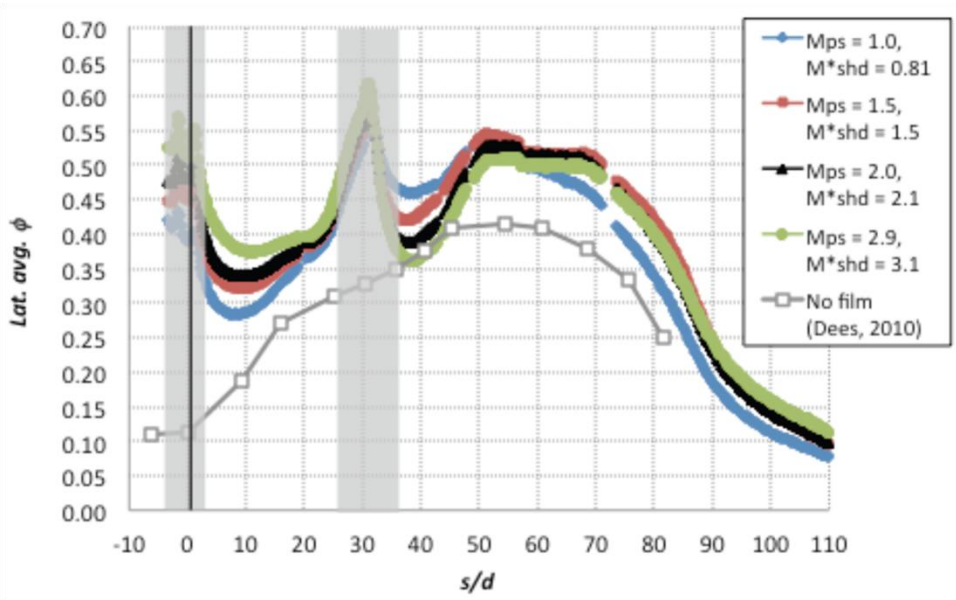

Figure 3.10: Overall effectiveness of pressure side round holes at *s/d* = 32 with an active showerhead for varying blowing ratios with *Tu* = 20% (from Albert (2011)). Albert (2011) defined the pressure side of the vane as being positive *s/d*.

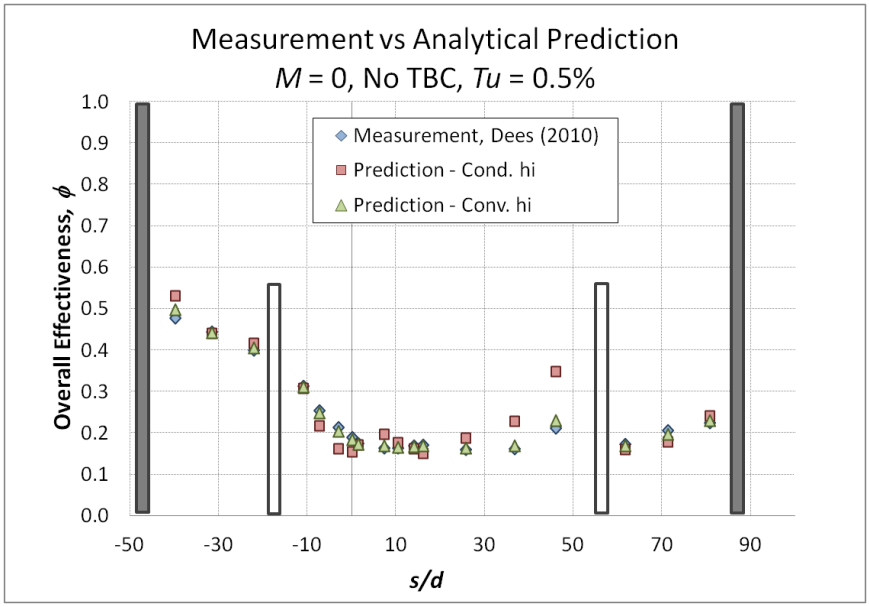

Figure 3.11: Comparison of actual results of ϕ to predictive models for a matched Biot number vane with no film cooling and no TBC at Tu = 0.5%.

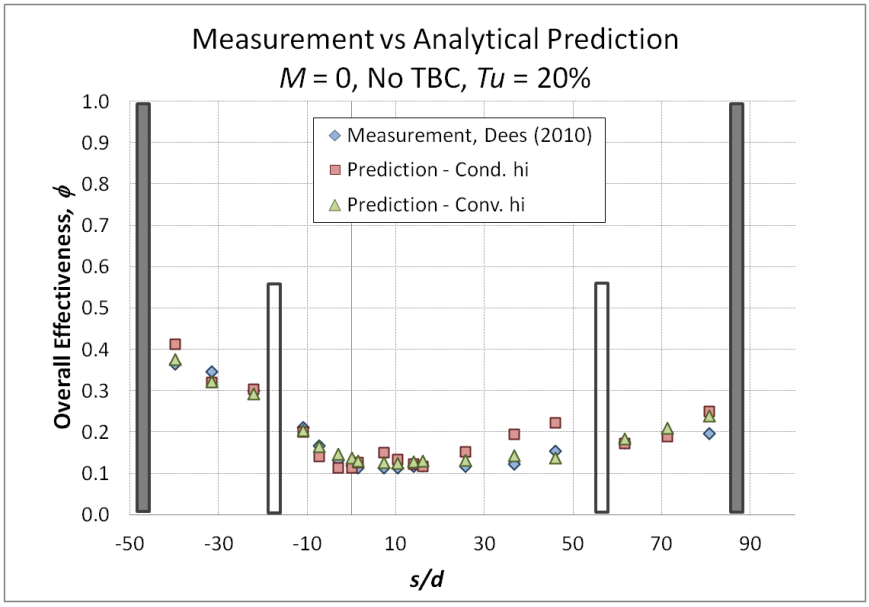

Figure 3.12: Comparison of actual results of ϕ to predictive models for a matched Biot number vane with no film cooling and no TBC at Tu = 20%.

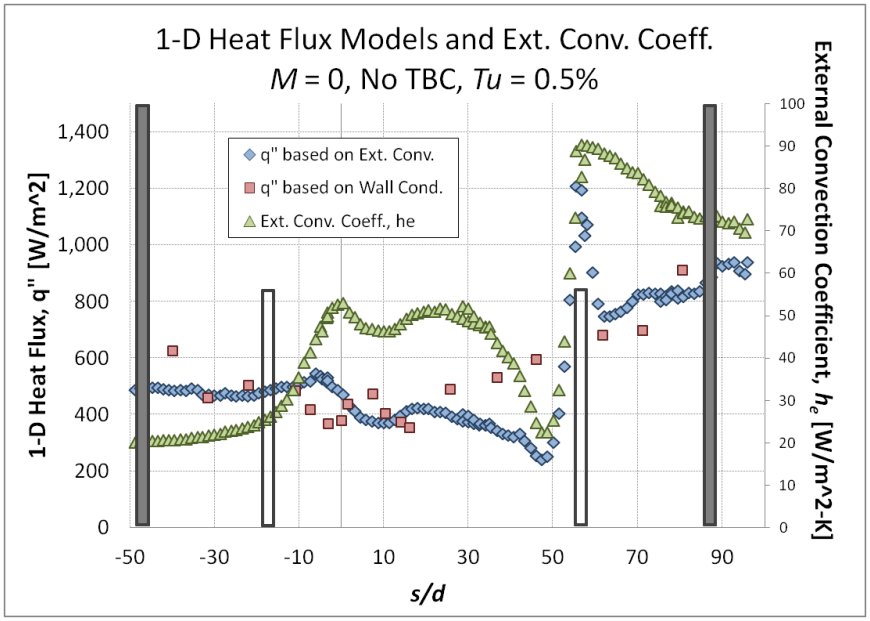

Figure 3.13: Comparison of external convection coefficient and heat flux through the vane wall based on conduction and convection methods.

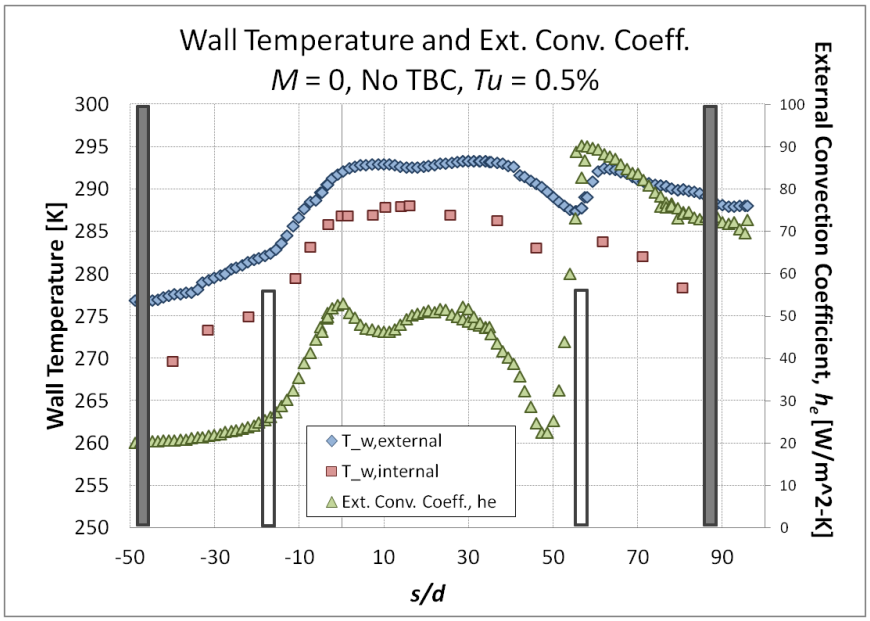

Figure 3.14: Comparison of external convection coefficient and external and internal wall temperature for $T_\infty = 301$, $T_{c,vane\ inlet} = 252$ K, $Tu = 0.5\%$ with no film cooling and no TBC.

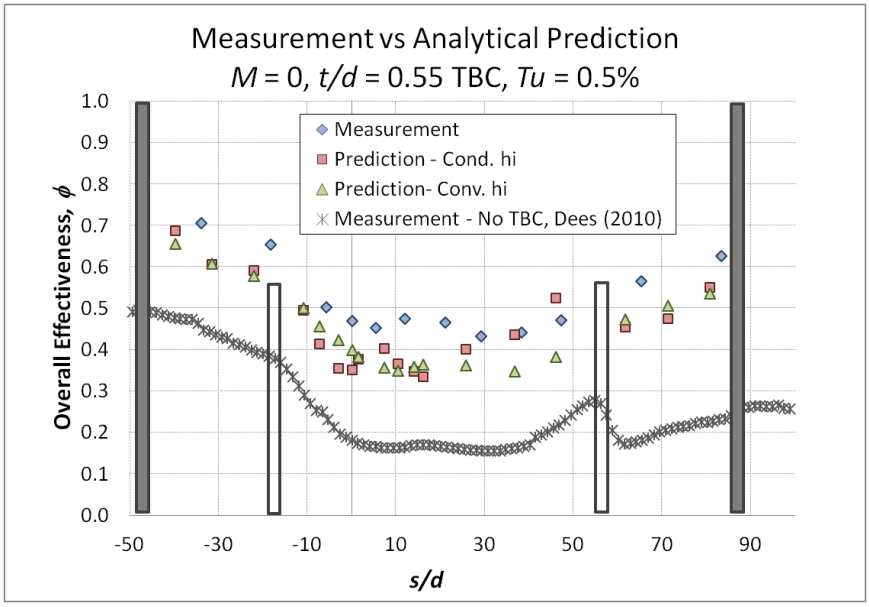

Figure 3.15: Comparison of actual results of ϕ to predictive models for a matched Biot number vane with no film cooling and t/d = 0.55 TBC at Tu = 0.5%.

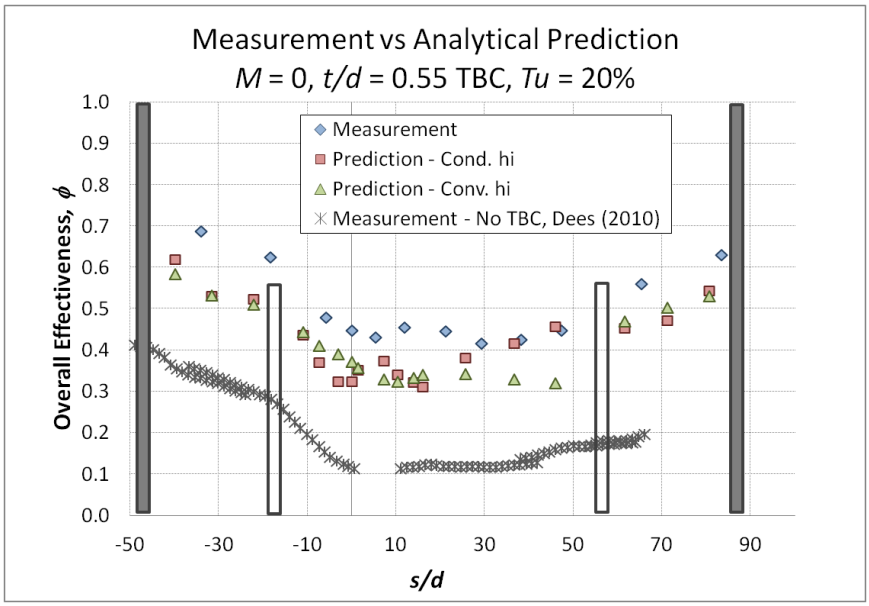

Figure 3.16: Comparison of actual results of ϕ to predictive models for a matched Biot number vane with no film cooling and t/d = 0.55 TBC at Tu = 20%.

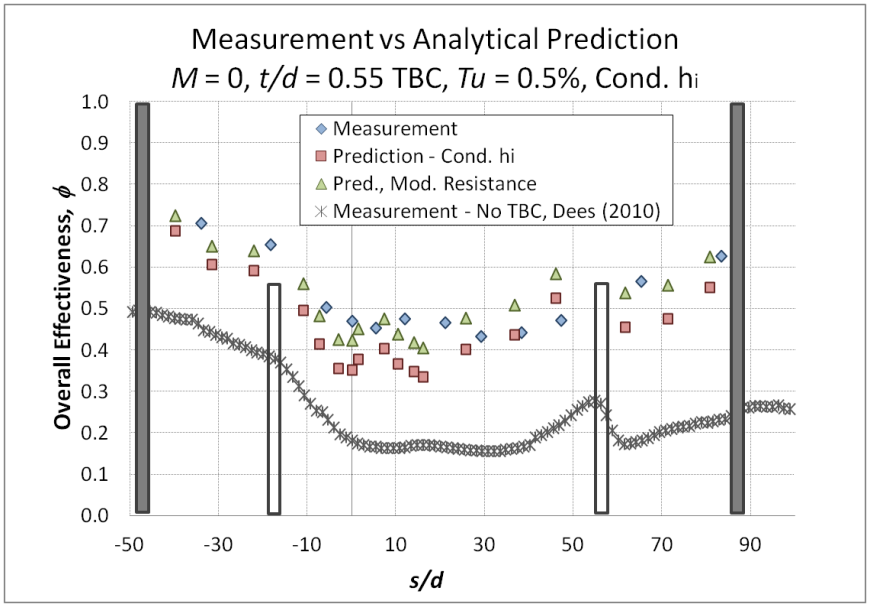

Figure 3.17: Comparison of actual results of ϕ to predictive models with varied resistances using wall conduction for derivation of internal convective coefficients.

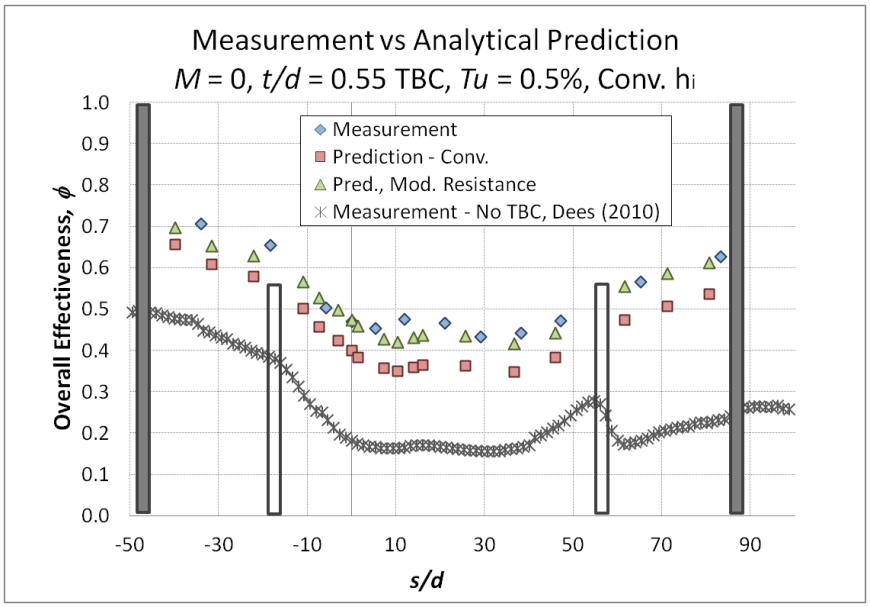

Figure 3.18: Comparison of actual results of ϕ to predictive models with varied resistances using external convection for derivation of internal convective coefficients.

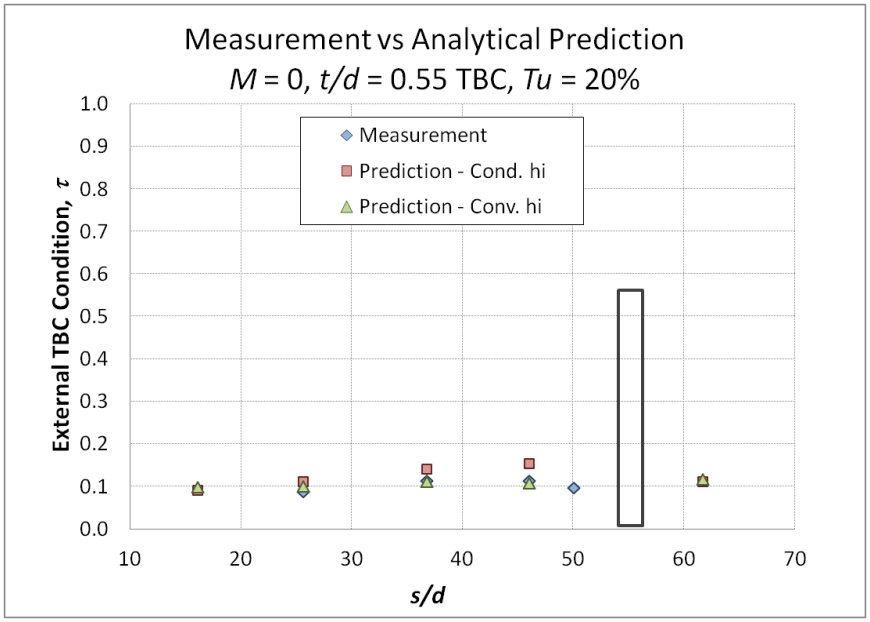

Figure 3.19: Comparison of actual results of τ to predictive models for a matched Biot number vane with no film cooling and t/d = 0.55 TBC at Tu = 20%.

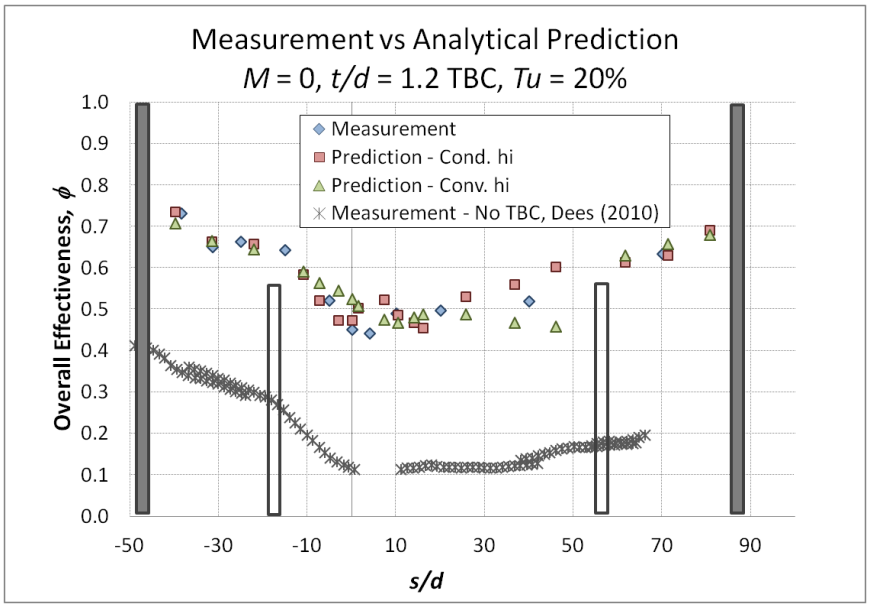

Figure 3.20: Comparison of actual results of ϕ to predictive models for a matched Biot number vane with no film cooling and t/d = 1.2 TBC at Tu = 20%.

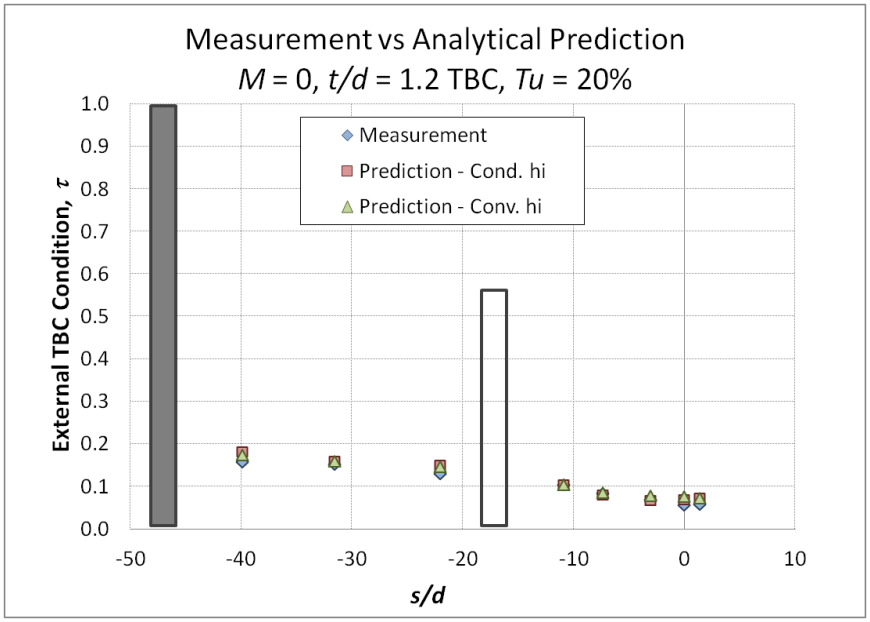

Figure 3.21: Comparison of actual results of τ to predictive models for a matched Biot number vane with no film cooling and t/d = 1.2 TBC at Tu = 20%.

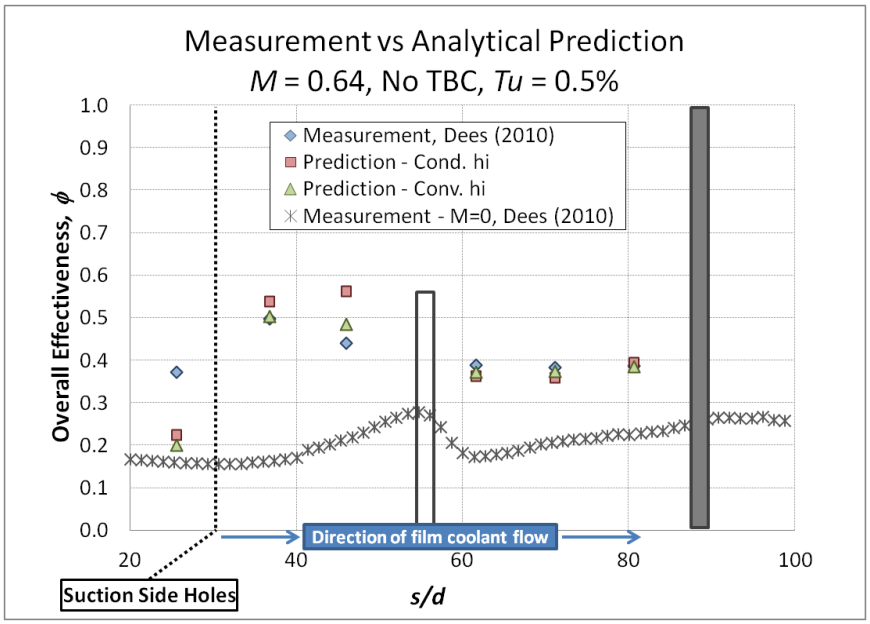

Figure 3.22: Comparison of actual results of ϕ to predictive models for a matched Biot number vane with round holes at M = 0.64 and no TBC at Tu = 0.5%.

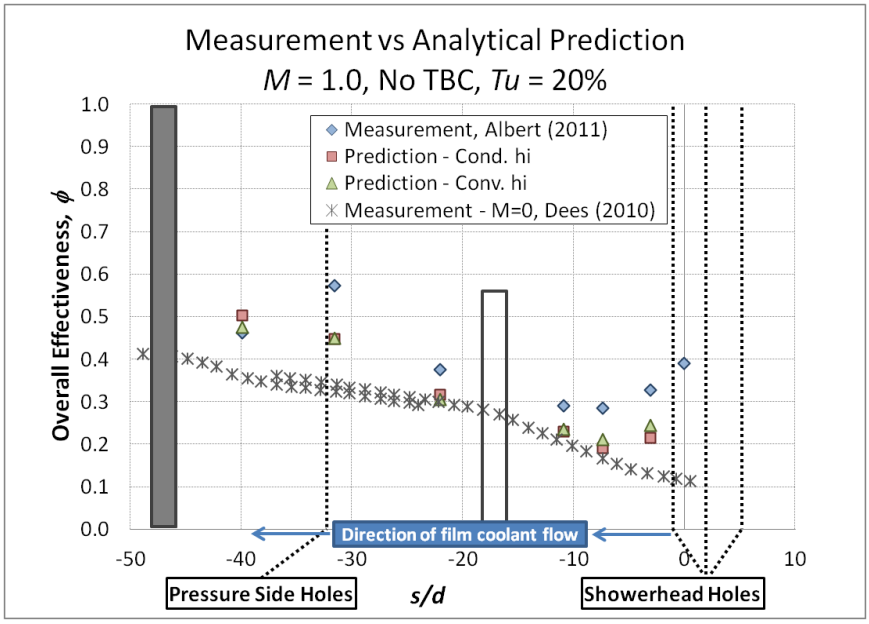

Figure 3.23: Comparison of actual results of ϕ to predictive models for a matched Biot number vane with round holes at $M = 1.0$ and no TBC at $Tu = 20\%$.

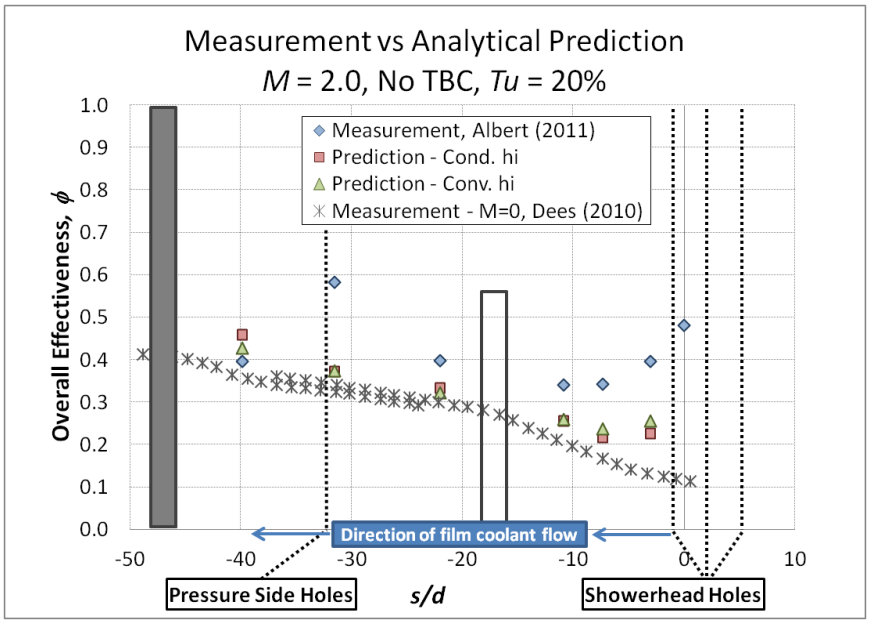

Figure 3.24: Comparison of actual results of ϕ to predictive models for a matched Biot number vane with round holes at $M = 2.0$ and no TBC at $Tu = 20\%$.

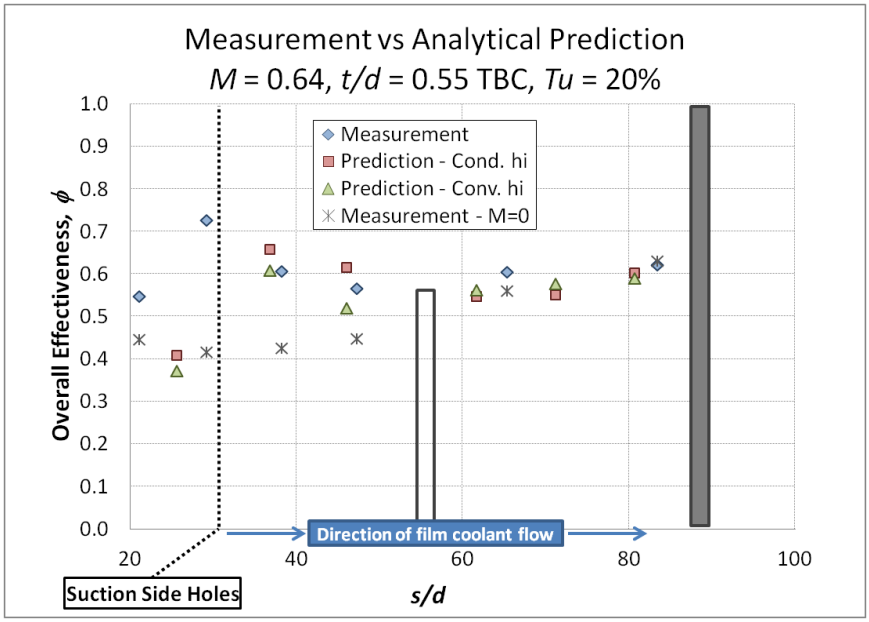

Figure 3.25: Comparison of actual results of ϕ to predictive models for a matched Biot number vane with round holes at $M = 0.64$ and $t/d = 0.55$ TBC at $Tu = 20\%$.

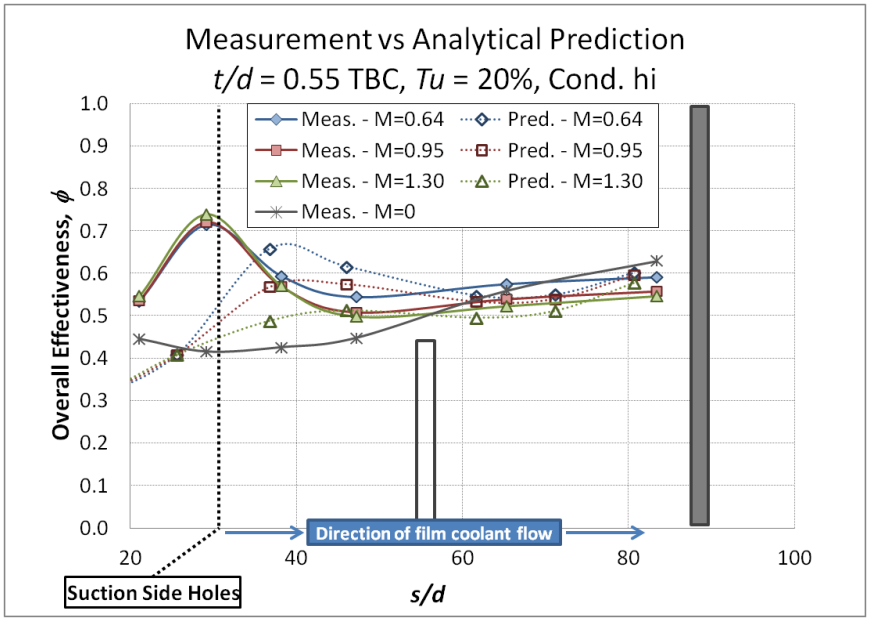

Figure 3.26: Comparison of measurements of ϕ to predictive models for a matched Biot number vane with round holes varying blowing ratios and $t/d = 0.55$ TBC at $Tu = 20\%$.

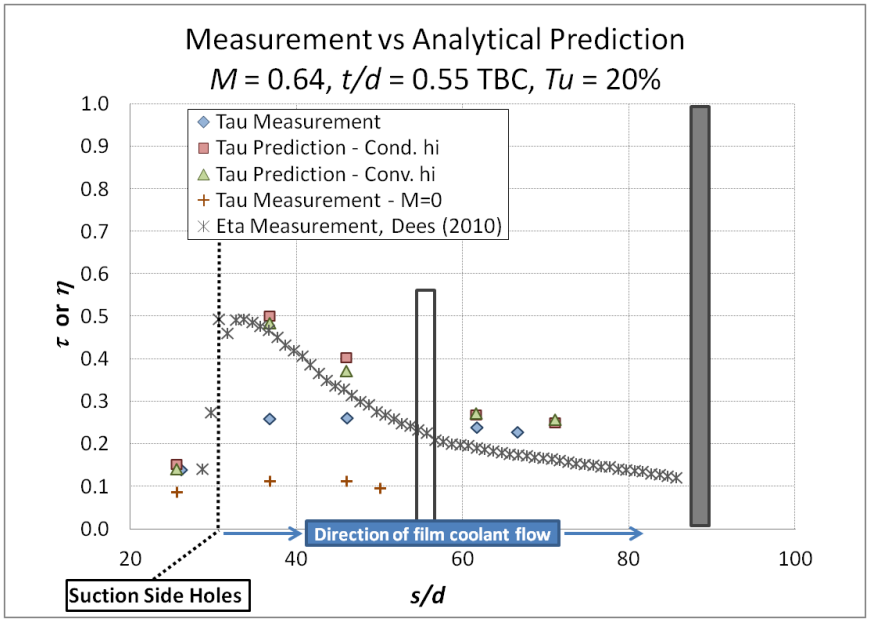

Figure 3.27: Comparison of actual results of τ to predictive models for a matched Biot number vane with round holes at $M = 0.64$ and $t/d = 0.55$ TBC at $Tu = 20\%$.

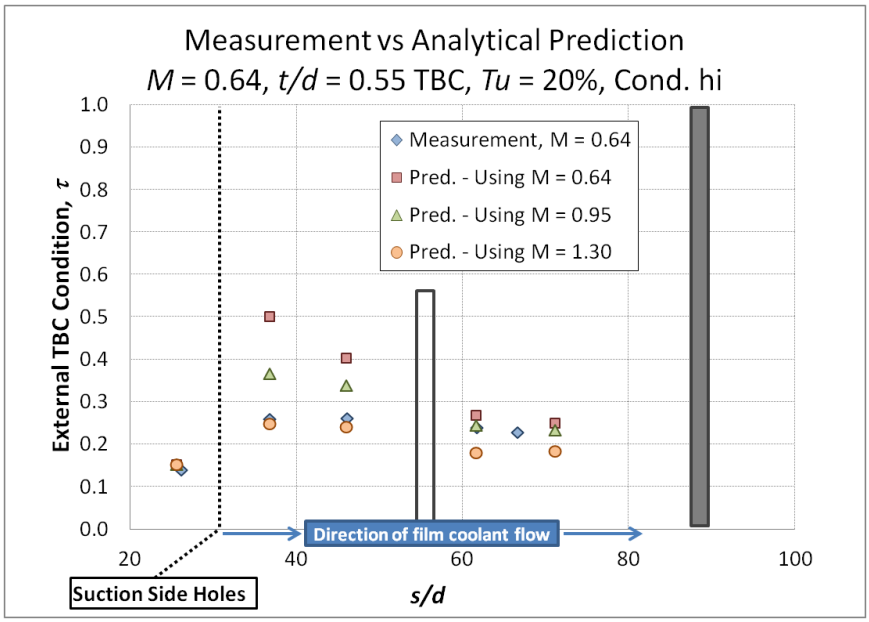

Figure 3.28: Comparison of actual results of τ to analytical models with varying blowing ratios used to estimate the effect of adiabatic effectiveness on τ.

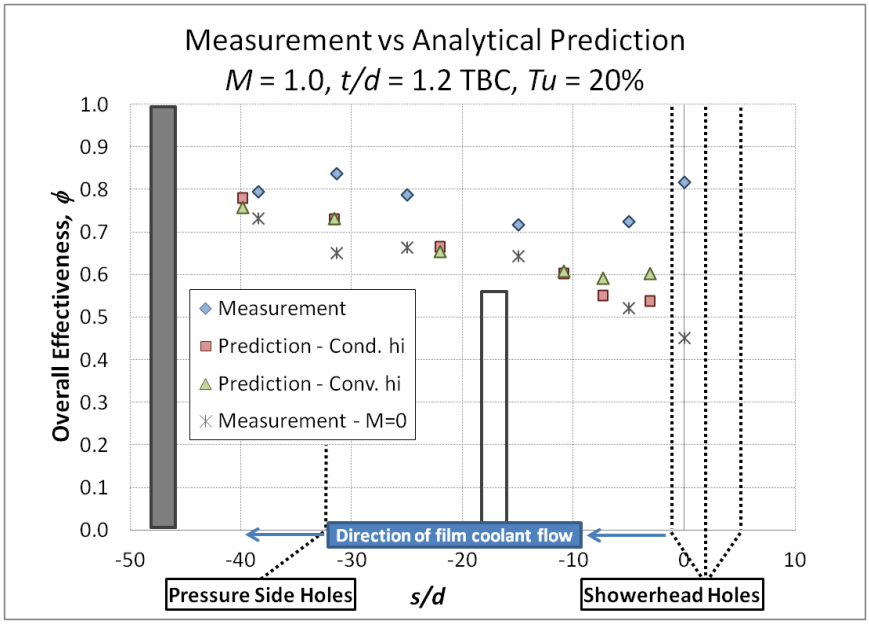

Figure 3.29: Comparison of actual results of ϕ to predictive models for a matched Biot number vane with round holes at $M = 1.0$ and $t/d = 1.2$ TBC at $Tu = 20\%$.

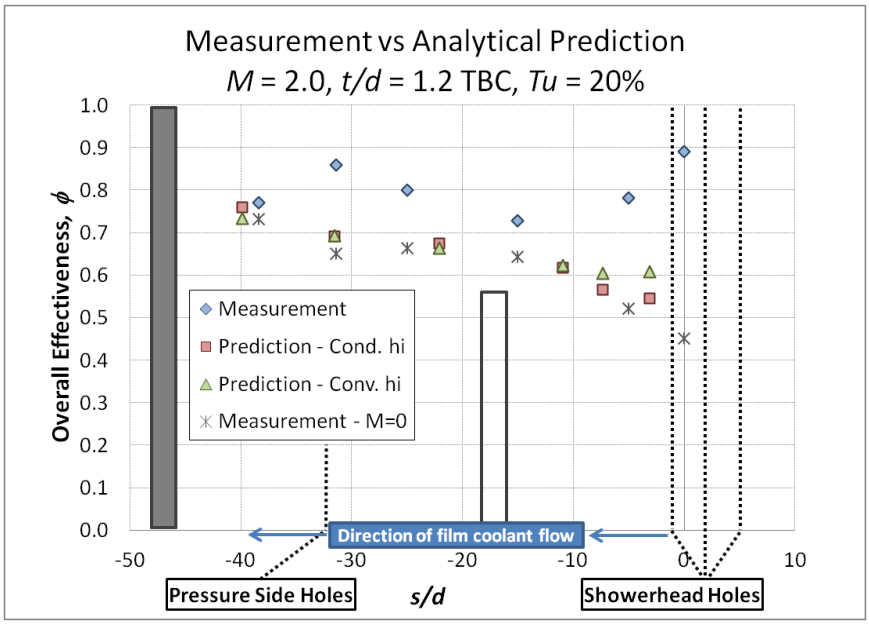

Figure 3.30: Comparison of actual results of ϕ to predictive models for a matched Biot number vane with round holes at $M = 2.0$ and $t/d = 1.2$ TBC at $Tu = 20\%$.

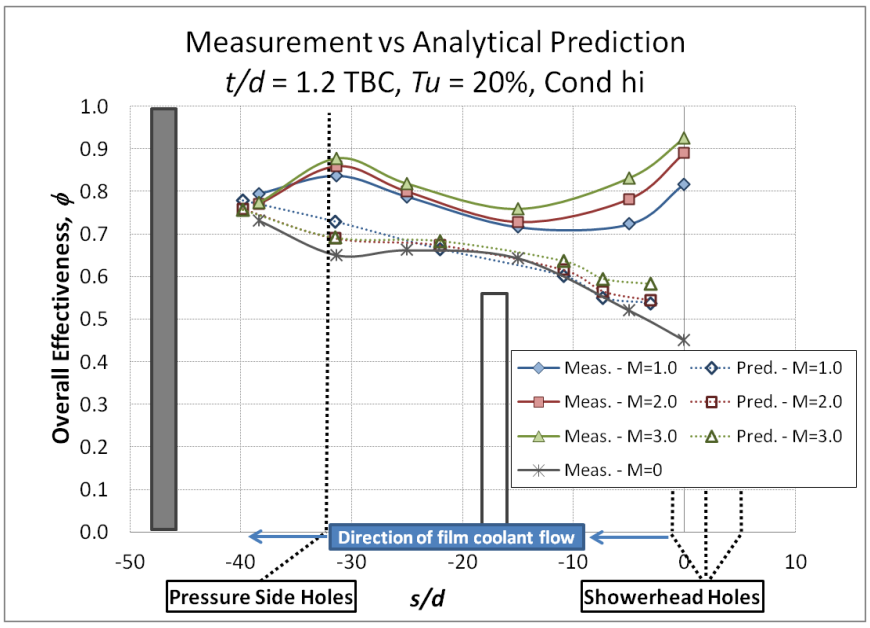

Figure 3.31: Comparison of measurements of ϕ to predictive models for a matched Biot number vane with round holes at varying blowing ratios and t/d = 1.2 TBC at Tu = 20%.

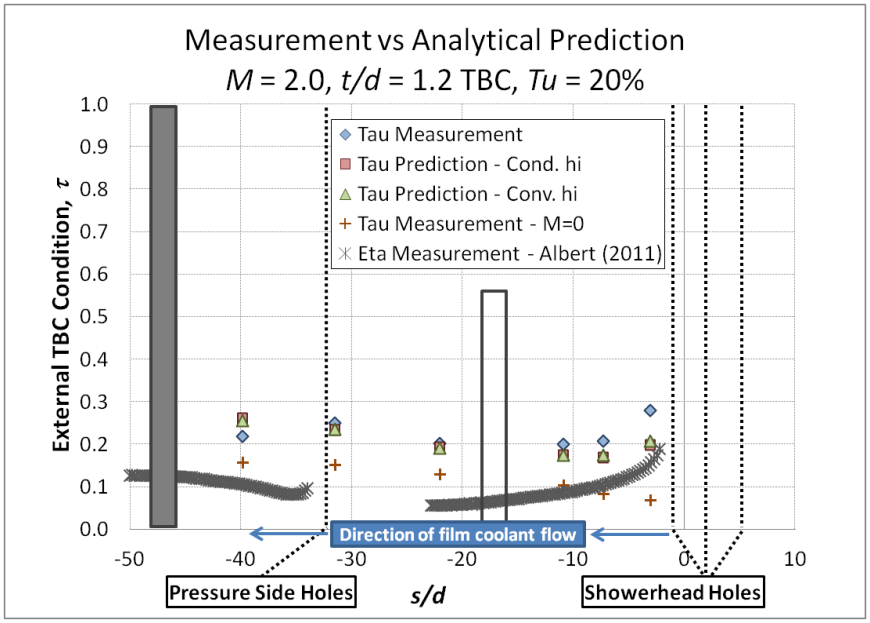

Figure 3.32: Comparison of actual results of ϕ to predictive models for a matched Biot number vane with round holes at M = 2.0 and t/d = 1.2 TBC at Tu = 20%.

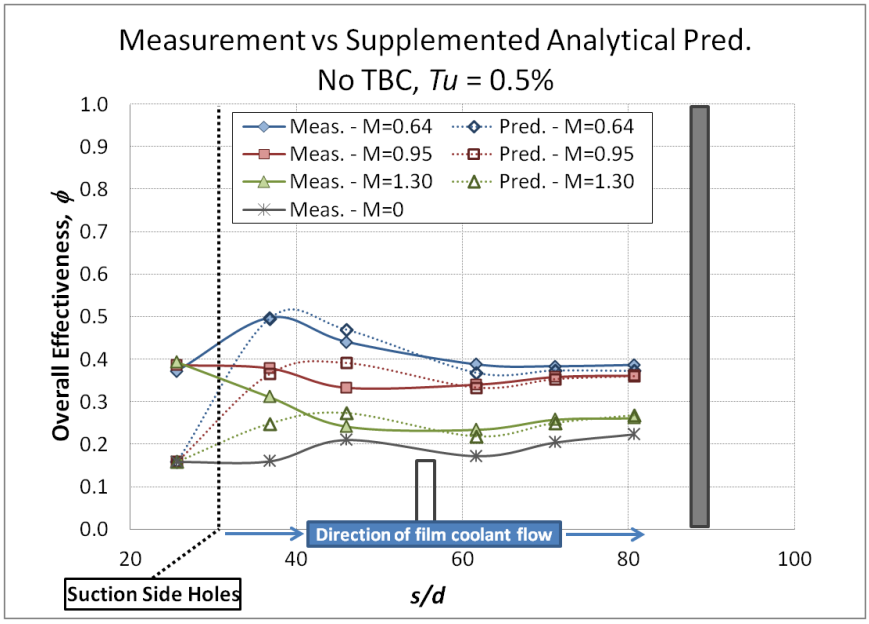

Figure 3.33: Comparison of measurements and supplemented analytical predictions of ϕ for suction side round hole film cooling at varying blowing ratios with no TBC and Tu = 0.5%. Measured data obtained by Dees (2010).

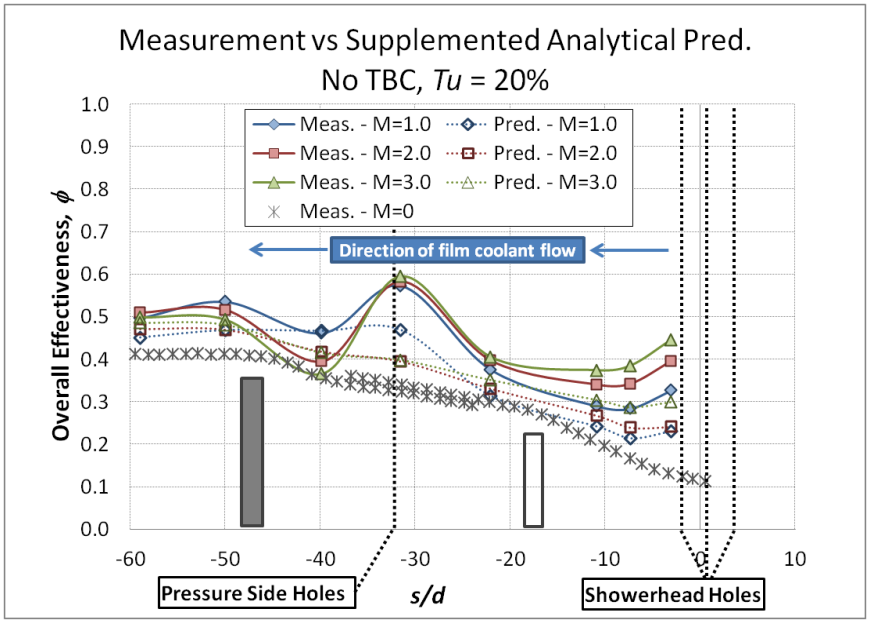

Figure 3.34: Comparison of measurements and supplemented analytical predictions of ϕ for pressure side round hole film cooling at varying blowing ratios with no TBC and Tu = 20%. Measured data obtained by Albert (2011).

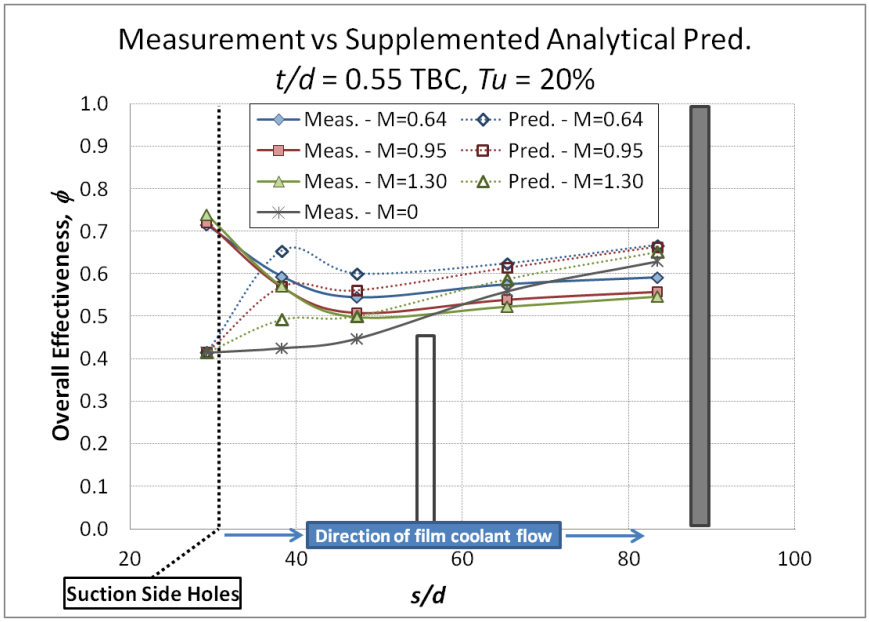

Figure 3.35: Comparison of measurements and supplemented analytical predictions of ϕ for suction side round hole film cooling at varying blowing ratios with t/d = 0.55 TBC and Tu = 20%.

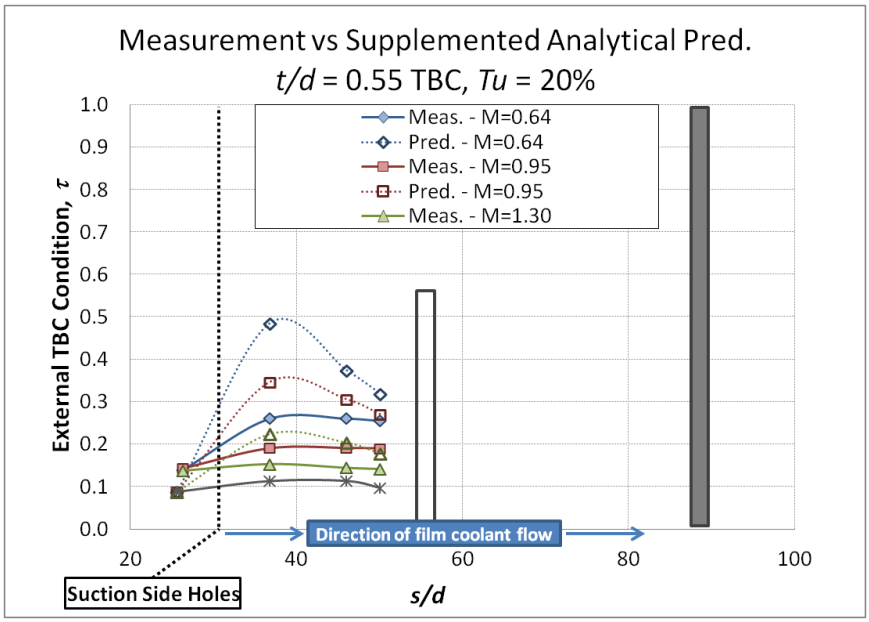

Figure 3.36: Comparison of measurements and supplemented analytical predictions of τ for suction side round hole film cooling at varying blowing ratios with t/d = 0.55 TBC and Tu = 20%.

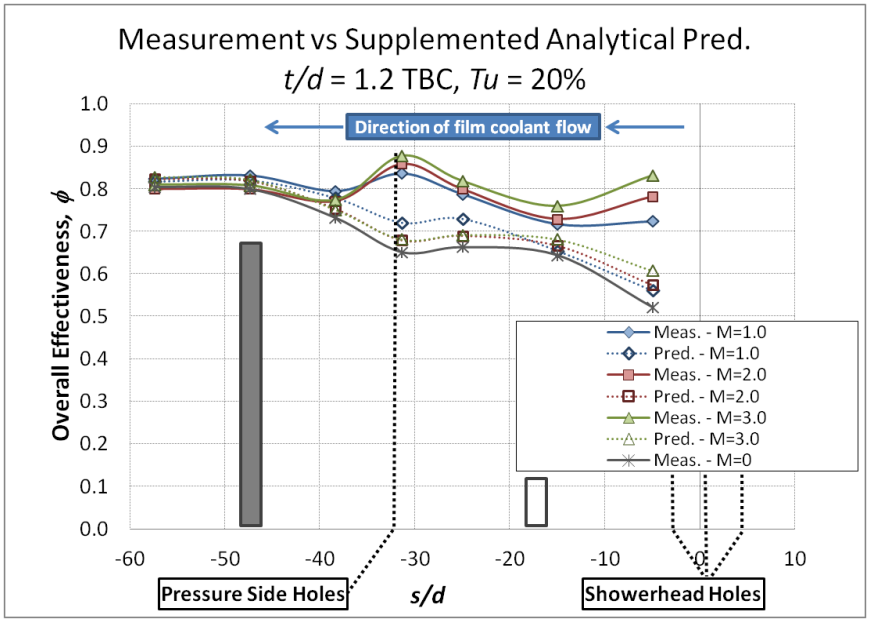

Figure 3.37: Comparison of measurements and supplemented analytical predictions of ϕ for pressure side round hole film cooling at varying blowing ratios with t/d = 1.2 TBC and Tu = 20%.

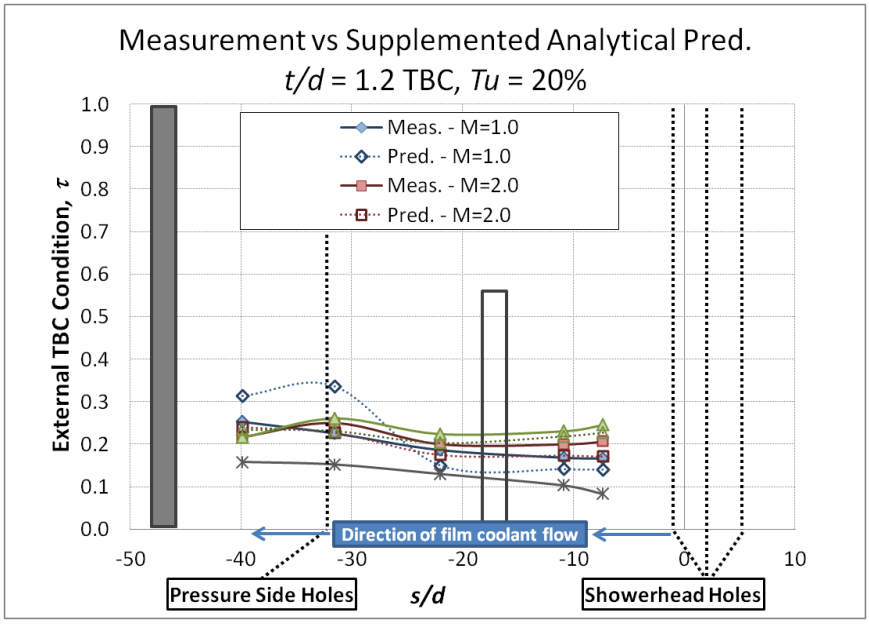

Figure 3.38: Comparison of measurements and supplemented analytical predictions of τ for pressure side round hole film cooling at varying blowing ratios with t/d = 1.2 TBC and Tu = 20%.

Chapter 4

4. THE EFFECT OF THERMAL BARRIER COATINGS

The purpose of this chapter is to provide a detailed understanding of how thermal barrier coatings affect the performance of a realistically cooled turbine vane. This will be accomplished by studying the change in overall effectiveness, ϕ, and TBC condition, τ, for various vane configurations. The different configurations utilized TBC's of varying thickness as well as varying film cooling designs on the suction side and pressure side of the vane. It is shown that thermal barrier coatings significantly improve the cooling performance of a turbine vane, as expected. It was discovered that the overall effectiveness achieved for a film cooled vane nearly collapses despite changes in blowing ratio or cooling configuration when a TBC is utilized. Finally, it was found that trenched film cooling does not provide the advantages that adiabatic effectiveness tests have previously shown, particularly when operated at suboptimal conditions.

4.1. Thinner TBC: $t/d = 0.55$

This section will provide a synopsis of the cooling performance of a vane with a simulated TBC with thickness of $t/d = 0.55$. This configuration was studied with and without film cooling on the suction side of the vane. The baseline cooling configuration consisted of 4.2 mm diameter round holes angled at 42° to the surface of the vane at a location of $s/d = 31$. The film cooling performance of a trench fed by the round holes was also studied at this location.

The analysis presented in Chapter 3 showed that the experimental results for the $t/d = 0.55$ TBC were not predictable over much of the vane surface without modifications

to the analytical model (e.g. increasing the expected thermal resistance of the TBC). This is likely a result of the t/d = 0.55 TBC partially delaminating from the surface of the vane. Delamination would have increased the thermal contact resistance at the interface of the vane wall and TBC layer. This behavior may have been exacerbated on the pressure side of the vane due to the cork's resistance to adhering to the concave surface. This argument is reinforced by comparing the overall effectiveness that was measured for the two TBC cases studied herein, as shown in Figure 4.1. The greater thermal resistance of the t/d = 1.2 TBC ought to allow for higher effectiveness levels at the interface of the TBC and vane wall as compared to the t/d = 0.55 case. This is not the case on the pressure side of the vane. Consequently, the data presented herein for the t/d = 0.55 TBC should only be used to observe trends rather than absolute values of effectiveness.

The t/d = 0.55 TBC was tested at varying internal Reynolds number conditions with no film cooling in order to determine the effect of internal convective cooling. Figure 4.2 provides the comparison of ϕ for varying internal Reynolds number with the t/d = 0.55 TBC at Tu = 0.5%. The Reynolds number was varied by increasing the mass flow rate of coolant through the internal passages of the vane. This was done in order to achieve three separate internal conditions: 1.) $Re_{Ubend} = Re_{Radial}$ = 10,000, 2.) $Re_{Ubend} = Re_{Radial}$ = 20,000, and 3.) Re_{Ubend} = 40,000 and Re_{Radial} = 20,000. The non-TBC results were obtained from previous work completed by Dees (2010). As would be expected, the inclusion of TBC provides a significant increase in the cooling performance of the vane and shows why TBC is so important. This figure also highlights the fact that increasing the internal convection has a significant effect on the temperature of the vane wall at the

interface with the TBC. Over the region of s/d = 50 – 80 the results with and without TBC show a different trend. In the case with TBC the overall effectiveness is increasing in this region. However, ϕ stays relatively constant for the case with no TBC. One explanation for this is that the TBC is isolating the effects of the varying external heat transfer coefficient. It is worth noting that the cooling performance is relatively consistent in the radial channel (s/d > 90 and s/d < -50) for the separate conditions of 2.) and 3.) as outlined above. This should be expected since the radial channel was set to Re_{Radial} = 20,000 in both cases.

The cooling performance improvement due to the presence of the TBC can be determined by calculating the augmentation which is defined as

$$Aug_{TBC} = \frac{\phi_{TBC} - \phi_{No\ TBC}}{1 - \phi_{No\ TBC}} \tag{4.1}$$

This method is used to determine the effect that TBC has on the cooling performance due to the fact that a percentage change does not tell the whole story. This is because as the system approaches the ideal cooling of ϕ = 1 it requires exponentially more thermal resistance to achieve such performance. Due to this, there is a diminishing "return on investment" for increasing the thermal resistance of the vane and thus, using percentage differences as the metric for performance can be deceiving. For example, a system could be described as having a 200% improvement in performance if the overall effectiveness of a vane was ϕ = 0.1 without TBC but increased to ϕ = 0.3 with TBC. However, the performance would have only increased by 25% if the system were at ϕ = 0.8 without TBC and increased to ϕ = 1.0 with TBC. In the latter case the system achieved ideal

performance of $\phi = 1.0$ but on a percentage basis it didn't look as impressive. The augmentation, as described in Equation (4.1), can be thought of as a means to quantify the change in overall effectiveness due to the addition of TBC as a fraction of the available potential for the effectiveness to change. So, from the examples provided above the augmentation would be $Aug_{TBC} = 0.22$ for the case in which the overall effectiveness improved to $\phi = 0.3$ with TBC whereas it would be $Aug_{TBC} = 1.0$ for the case that it improved to $\phi = 1.0$. This method of comparison, as opposed to a simple percentage change, recognizes that it is more difficult to gain additional performance in terms of ϕ as the base level of performance increases. This method could be extended to make comparisons of different vane configurations and film cooling designs amongst other applications. Figure 4.3 provides the augmentation of ϕ for the various Reynolds number conditions presented in Figure 4.2.

The effect of mainstream turbulence on a non-film cooled vane with $t/d = 0.55$ TBC is shown in Figure 4.4 – Figure 4.6. Increasing the mainstream turbulence from $Tu = 0.5 – 20\%$ generated minimal change in the overall effectiveness, ϕ. This conclusion held true regardless of changes to the internal Reynolds number of the vane. Previous results obtained by Dees (2010) showed that the mainstream turbulence intensity had a noticeably effect on the overall effectiveness of a vane with no TBC. This implies that the TBC dampens the effect of the increased heat transfer. Despite the dampening effect, it is not clear as to why the data at different turbulence intensities could agrees so well over much of the vane. It is possible that this could be explained by the behavior of the

external heat transfer coefficient. Figure 4.7 provides a comparison of external heat transfer coefficient for low and high mainstream turbulence intensity conditions. It can be seen that h_e is not altered due to changes in the mainstream turbulence intensity downstream of $s/d = 50$. This is due to the fact that the boundary layer has transitioned and is dominating the heat transfer coefficient locally. The heat transfer coefficient is quite different between the $Tu = 0.5\%$ and $Tu = 20\%$ cases for the showerhead and pressure side regions of the vane. Consequently, it stands to reason that the overall effectiveness should be higher for the $Tu = 0.5\%$ case for $s/d < 50$, despite the dampening effect of the TBC. In fact, that analytical models predict a decrease in ϕ of approximately 20% over much of the vane due to increasing the turbulence intensity from $Tu = 0.5\%$ to $Tu = 20\%$. However, the data shows that the turbulence intensity has minimal effect on ϕ, particularly for the $Re_{Ubend} = Re_{Radial} = 10{,}000$ case shown in Figure 4.4. It is unclear why this is the case, unless it can be completely accounted for by the dampening effects of the TBC.

The vane model with $t/d = 0.55$ TBC was tested with active film cooling from round holes inclined at 42° at a location of $s/d = 31$. The film cooling results were obtained for four different blowing ratios, $M = 0.50$, 0.64, 0.95, and 1.30. Three of these blowing ratios are presented in Figure 4.8 to compare to no TBC results obtained by Dees (2010). The presence of TBC significantly dampens the sensitivity of ϕ to the blowing ratio. As the blowing ratio increases the coolant jets begin to separate from the wall resulting in reduced cooling performance. However, as the blowing ratio increases the convective cooling within the holes will also increase. It appears as though the TBC

allows for the convective cooling within the holes to offset the detrimental effects of jet separation within 5 – 10*d* of the cooling holes. The effect of in-hole convective cooling is particularly evident at a location of s/d = 20, upstream of the cooling holes where no film cooling is present. The difference between the cases with film cooling and the case without film cooling is a result of in-hole convective cooling that is propagating upstream. This suggests that the dominate means for cooling a vane with TBC is convection cooling through the holes and, as previously discussed, the convection within the internal passages. Further downstream, where the effect of convective cooling within the holes has degraded, the performance of ϕ becomes more dominated by the film cooling performance on the external surface of the TBC and changes to the internal heat transfer coefficient. This is similar to the case without TBC. Unless otherwise specified, the results presented immediately downstream of the film cooling holes represent an average of four spanwise thermocouples within the 4x3 array in this region, as discussed in Chapter 2.

Further understanding of the film cooling effect can be gained by comparing the results to the case with no film cooling. Figure 4.8 and Figure 4.9 provide overall effectiveness results, ϕ, for the *t/d* = 0.55 TBC model with and without film cooling and TBC. The results presented in Figure 4.9 focus on the performance of a single blowing ratio, M = 0.64, in order to simplify the discussion. It is evident in both figures that film cooling provides a significant improvement in ϕ over the case without film cooling. This is likely due to the in-hole convective cooling for regions near *s/d* = 30. Film cooling

with a t/d = 0.55 TBC provides a performance increase over the case with no film cooling for up to 30 hole diameters, d, downstream of the round holes at M = 0.64.

The data shown in Figure 4.8 and Figure 4.9 show that there are disagreements in the cooling performance on the pressure side of the vane for the TBC cases with and without film cooling. The cooling performance on the pressure side of the vane is solely driven by the external and internal convective coefficients since there is no film cooling in this region. One reason for this disagreement is based on the fact that the Reynolds number in the aft (i.e. exit) passage of the U-bend channel was actually higher for the non-film cooled case. This was a result of the fact that 15-40% (depending on blowing ratio) of the internal coolant is lost through the suction side holes for the film cooled case and consequently less coolant passes through the exit passage of the U-bend when film cooling is utilized. The reduction in mass flow rate would have decreased the internal heat transfer by reducing the internal Reynolds number in the aft passage of the U-bend from $Re_{U\text{-}bend}$ = 20,000 down to 16,000 – 12,000, depending on blowing ratio. Figure 4.8 provides the cooling performance of the TBC vane with no film cooling for two different internal Reynolds number conditions, $Re_{U\text{-}bend}$ = 10,000 and 20,000. It can be seen that the data on the pressure side of the vane splits the difference between the performance at $Re_{U\text{-}bend}$ = 10,000 and 20,000, which is consistent with the previous concept that the suction side film cooling reduces the internal convection on the pressure side due to reduced mass flow of internal coolant.

Delamination of the simulated t/d = 0.55 TBC may also explain some of the disagreements that are observed. This may be particularly true on the concave curvature

of the pressure side due to the resistance the cork presented in adhering to this specific location. The film cooling data with round holes was obtained before the no film case. It is possible that the TBC began to delaminate between the separate tests. If this were the case, the delamination would have increased the thermal resistance of the system and improved the overall effectiveness, ϕ, as is seen in Figure 4.9.

The internal Reynolds numbers for different blowing ratios are shown in Table 4.1. The inlet Reynolds number for the $t/d = 0.55$ TBC experiments was set to be $Re_{U\text{-}bend} = 20{,}000$ regardless of changes in blowing ratio. This meant that there was less coolant exiting the vane for higher blowing ratios as shown in Table 4.1. The changes in Reynolds number at the exit of the U-bend shown in Table 4.1 would result in a decrease of approximately $\Delta\phi = 0.03$ for the $M = 1.30$ case as compared to the $M = 0.64$ case over the region of $55 < s/d < 85$. This would cause the data for the varying blowing ratios in Figure 4.8 to collapse even more if the internal Reynolds number were identical for the region of $55 < s/d < 85$. This was determined with linear interpolation using the data in Figure 4.2 which provides overall effectiveness for $t/d = 0.55$ TBC with $M = 0$ and varying internal Reynolds numbers. It should be recognized that the data in the radial passage (i.e. $s/d > 90$ and $s/d < -50$) agrees well despite changes in blowing ratio, as expected. This is due to the fact that the radial channel does not feed any of the film cooling holes and thus the internal conditions are not affected by changes in blowing ratio.

Table 4.1: Comparison of Reynolds numbers at the inlet and outlet of the U-bend channel depending on the blowing ratio, *M*, that is set.

M	Re_{Uin}	Re_{Uout}	Avg
0.64	20000	15700	17850
0.95	20000	14000	17000
1.30	20000	12000	16000

Internal wall temperature data was also collected during the tests of the $t/d = 0.55$ TBC. This was accomplished with the use of discrete surface thermocouples placed at the mid-span at various *s/d* locations. Figure 4.10 provides a comparison of the non-dimensional temperature of the internal and external vane wall for a film cooled model with round holes at $M = 0.64$ and $Tu = 20\%$. As would be expected, the internal wall is noticeably colder than the external wall over the majority of the *s/d* locations, with the largest variation being near the stagnation region of $s/d = 0$. However, this is not the case downstream of the film cooling holes at a location of $s/d \sim 35$. At this location the temperature across the wall has nearly collapsed. If the temperature difference across the wall goes to zero it implies that the 1-D heat transfer across the wall also approaches zero. However, if the 1-D heat transfer across the wall approached zero then the internal wall temperature would have to approach the temperature of the internal coolant. This is not the case. Consequently, the location of $s/d = 36$ cannot be represented with a simplified 1-D model. This is similar to the conclusion from Chapter 3 that the 1-D models performed poorly in predicting the cooling performance near active film cooling holes.

A transverse trench with embedded round holes was examined with particular interest due to the promising results that the design has shown historically in terms of adiabatic effectiveness, as shown by Waye and Bogard (2006) and Dorrington *et al.* (2007). The trench tested had a depth of $t/d = 0.55$, due to the thickness of the TBC, and a width of $w = 1.5d$. The width of the trench was such that the walls of the trench were coincident with the upstream and downstream lips of the embedded round holes, as discussed in Chapter 2. The trench also provided a means of determining how a system with TBC would be affected by a change in the film cooling configuration. The performance of the trench in comparison to round holes is shown in Figure 4.11 - Figure 4.13 for varying blowing ratios at $Tu = 20\%$. At a blowing ratio of $M = 0.64$ the trench shows only marginal improvement over the round hole configuration. At the higher blowing ratios of $M = 0.95$ and $M = 1.30$ the trench shows improved performance in comparison to the round holes near $s/d \sim 50$. However, the overall effectiveness within the trench between the embedded round holes at $s/d = 31$ begins to drop off with increasing blowing ratio. In fact, at the highest blowing ratio of M = 1.30 the round holes are far superior to the trench at the location of the suction side holes. It is speculated that the reduced performance of the trench is a result of a suboptimal design. The trench used with the $t/d = 0.55$ TBC only had a depth of $0.55d$ since it was formed by the thickness of the TBC. Previous work by Dorrington *et al.* (2007) showed that an ideal trench has a depth of at least $0.75d$. At the highest blowing ratios the momentum of the jet likely carries the majority of the coolant up and over the trench wall prior to it spreading laterally and filling the trench. This may result in hot mainstream air mixing with the

coolant within the trench and warming the wall locally. This highlights the danger of removing the TBC in order to form a trench. The trench appears to provide improved film cooling performance with the drawback of heating the wall near the cooling holes under suboptimal operation.

The data between the various tests disagree on the pressure side of the vane despite the fact that no film cooling is present in this region. The disagreement over the region of $-50 < s/d < 0$ can be explained by the deficit in internal coolant flow rate within the aft passage of the U-bend due to the utilization of film cooling on the suction side of the vane. The disagreements in the data for $s/d < -50$ cannot be explained by this since the cooling of the vane in this region should be driven by the conditions within the radial passage. One explanation for the disagreement in the data between the round holes and trench configurations at approximately $s/d = -60$ and -85 is that the TBC may have begun to delaminate between testing of the round holes and the trench. These two tests were completed 4 – 5 months apart which may have resulted in a change in the thermal resistance of the cork due to partial delamination.

The limiting case for assessment of cooling performance is to identify how well a cooling configuration reduces hot spots. For instance, some film cooling configurations have more discrete characteristics than others. The discrete nature often results in regions that are much warmer than others which can accelerate material failure in these "hot spots". Round holes, for example, create more discrete film coolant jets on the surface of a vane wall as compared to the coolant that is emitted from a trench. It is important to compare the cooling configurations taking into account the minimum effectiveness that is

observed. Figure 4.14 – Figure 4.16 compare the average overall effectiveness, ϕ_{avg}, as well as the minimum overall effectiveness, $\phi_{min,}$ for the round holes and trench design at varying blowing ratios. This was accomplished with the use of the thermocouple array that was placed downstream of the suction side holes. The array allowed for a lateral average to be approximated as well as measurement of the hottest temperature (i.e. minimum effectiveness). The figures show that the neither of the designs were far superior in improving the minimum effectiveness in relation to the averaged overall effectiveness. This is likely due to the insulating effects of the TBC that allows for a more uniform temperature of the vane wall regardless of the behavior of the film coolant on the exterior surface of the TBC. The data point at $s/d = 31$ for the trench was obtained with the use of IR thermography. The data point is slightly different in format in order to distinguish it from the other data points that were obtained with discrete thermocouple measurements.

The external TBC condition, τ, is a measure of the cooling performance on the exterior surface of the TBC. The TBC condition is often dominated by the film cooling performance, particularly near film cooling configurations. IR thermography can be used to generate detailed temperature maps of the surface of the TBC. These maps can then be converted to contour plots showing the spatial variation in TBC condition providing great insight into the behavior of the film coolant on the surface of the TBC. Figure 4.17 provides a comparison of contour plots for the round holes and trench at varying blowing ratios, M. These results were obtained for the $t/d = 0.55$ TBC at $Tu = 20\%$. The plots distinctly show the separation of the coolant jets for the round hole configuration with

increasing blowing ratio. The contour plots also show how the film cooling performance begins to degrade for the trench configuration as the blowing ratio is increased. This is likely due to the fact that the trench is of suboptimal design with a depth of less than 0.75*d*, as previously discussed. However, Waye and Bogard (2006) showed that a *t/d* = 0.5 deep trench has improving adiabatic effectiveness, η, up to a blowing ratio of M = 1.4. This is not the behavior shown here considering that the film cooling performance in terms of τ begins to degrade for blowing ratios above M = 0.64. The most likely explanation for this is the fact that the embedded holes tested by Waye and Bogard (2006) had an inclination angle of 30° whereas the embedded holes in this study were angled at 42°. The steeper inclination angle would result in coolant jets impinging at a higher point on the downstream wall of the trench. This may have resulted in a behavior in which the majority of the coolant was carried up out of the trench before it had the chance to spread laterally, as compared to the results shown by Waye and Bogard (2006) which had a shallower inclination angle. The contour plots support the theory that the coolant jets begin to separate from the surface of the TBC at the highest blowing ratio of M = 1.30, rather than spreading laterally within the trench. A reference case with no film cooling is also provided. The film cooling holes are visible in the contour plot as the discrete patches of orange. This is a result of the holes being plugged entirely with clay for the non-film cooled case. The clay had a higher thermal conductivity than the cork used to simulate TBC. Consequently, the clay provided less thermal resistance between the interior coolant passages and the exterior surface observable by the IR camera, resulting in a colder temperature at the exterior surface. The change in TBC condition

across the surface of the non-film cooled case is likely a result of changes in the external heat transfer coefficient. For instance, the decrease in τ at the location of x/d = 20 (s/d = 51) corresponds to the point of transition of the boundary layer that results in a significant rise in the external heat transfer coefficient. The rise in h_e increases the heat transfer to the wall and increases the temperature of the TBC surface, resulting in a decrease in τ.

4.2. Thicker TBC: t/d = 1.2

The effect of TBC thickness was studied by measuring the cooling performance of a vane with a TBC thickness of t/d = 1.2. Cork was again used to simulate the layer of TBC. In this case, however, the film cooling was exclusive to the pressure side of the vane. A single row of 24, 4.2 mm diameter round holes inclined at 30° with a pitch of p/d = 3 was located at s/d = -32. Three rows of round holes with d = 4.2 mm inclined at 25° were located in the stagnation region of the vane. The holes in these rows had a 90° compound angle with a pitch of p/d = 5.6. The rows were separated by 3.3d. The three rows in the stagnation region were referred to as the "showerhead holes". This film cooling configuration was also used by Albert (2011) to study the effects of film cooling on ϕ and η with no TBC. Figure 4.18 provides a comparison of ϕ for Albert's data with no TBC and the measurements obtained in this study with t/d = 1.2 TBC. The blowing ratios presented in Figure 4.18 represent the value for the pressure side row at s/d = -32. As discussed in Chapter 2, the blowing ratio of the showerhead and pressure side holes was coupled such that a pressure side blowing ratio of M = 1.0, 1.5, 2.0, and 3.0 resulted in an average showerhead blowing ratio of M_{SH} = 0.8, 1.5, 2.0, and 3.2, respectively. It

should be recognized that IR thermography was utilized with the no TBC case. The results for the no TBC cases are lateral averages over the mid-span region of the vane. This data is represented by lines in Figure 4.18. The discrete data points are discrete measurements of the mid-span temperature at the interface of the TBC and the vane wall. As previously mentioned, a 4x3 array of thermocouples was placed downstream of the pressure side film cooling holes. The discrete points in Figure 4.18 at locations of s/d = -36, -39, and -48 represent an average of four thermocouples in the array. A small spanwise variation of approximately $\delta\phi = \pm 0.015$ was observed between the averaged thermocouples at each of the respective locations of s/d = -36 and -39. Further downstream, at s/d = -48, the variation diminished to less than $\delta\phi = \pm 0.010$. The small spanwise variation in overall effectiveness was a result of the TBC insulating the vane wall from gradients on the external surface of the TBC. The results presented in Figure 4.18 show how the TBC significantly improves the cooling performance of the vane by providing additional thermal protection between the hot mainstream gas and the external surface of the vane wall. The results also show the cooling performance of the vane with t/d = 1.2 TBC nearly collapses downstream of the pressure side holes despite large changes in the blowing ratio. This is in stark contrast to the vane with no TBC that shows relatively large changes in overall effectiveness with variations in blowing ratio. This is particularly true for the data immediately downstream of the cooling holes with no TBC that shows a decrease in performance due to the separation of the coolant jets. The collapse in performance for the TBC data, despite changes in blowing ratio, may imply that the dominant factor for locally cooling the vane wall is the presence of the TBC.

Furthermore, it appears as though improved convective cooling through the holes with increasing blowing ratio helps to mitigate the detrimental effect of jet separation. The showerhead region of the vane shows improvement in overall effectiveness with increasing blowing ratio. This is true with and without TBC. The cooling performance of the showerhead region is heavily dependent on convective cooling through the holes due to the relatively dense nature of the holes perforating the wall of the vane. Furthermore, the showerhead cooling holes are oriented radially, 90º to the streamwise direction. This allows for the coolant to accumulate in the stagnation region and improve cooling despite jet separation at higher blowing ratios as shown by the adiabatic effectiveness measurements obtained by Albert (2011).

The measurements for the t/d = 1.2 TBC were consistent with the 1-D analytical models presented in Chapter 3 giving confidence in the accuracy of the data. Consequently, the results should be a direct measure of the overall effectiveness of a real engine component for the given cooling geometry. All of the data collected with the t/d = 1.2 TBC were at a high turbulence intensity approach flow condition of Tu = 20%.

In order to increase the blowing ratio for the vane model, a greater amount of coolant must be fed into the vane. This results in an altered internal Reynolds number that could affect internal convective heat transfer. As previously discussed, the internal Reynolds number for the t/d = 1.2 experiments was established by averaging the entrance and exit Reynolds numbers. This average was set to be Re = 20,000±500. Table 4.2 provides a comparison of typical inlet and outlet Reynolds numbers for the U-bend passage with varying blowing ratio. The variation in internal Reynolds number through

the U-bend was greater with the showerhead running due to the increased coolant loss out of the additional holes. This resulted in a difference in internal Reynolds number, ΔRe, at the mid-span of the showerhead of approximately ΔRe = 1,000 for the M = 2.98 case when compared to the M = 0.96 case. Consequently, the change in ϕ near the showerhead shown in Figure 4.18 was primarily due to increased convective cooling through the holes considering that the change in internal Re was relatively minimal, at worst ΔRe = 1,000. However, the difference was significantly larger, approaching ΔRe = 5,000 at the mid-span of the pressure side holes. As previously mentioned, the difference in Re at the inlet and exit of the U-bend is increased with increasing blowing ratio. This means that the pressure side Re decreases as the blowing ratio increases. Consequently, ϕ at high blowing ratios might be expected to decrease due to reduced internal Re and increased separation of the coolant jets. However, referring again to Figure 4.18, it is seen that ϕ increases slightly at the location of the pressure side holes as the blowing ratio is increased. This further supports the claim that the dominant mode of cooling the vane locally is convective cooling through the holes. In fact, it seems the increased convective cooling through the holes, due to increased blowing ratio, is offsetting the detrimental effects of reduced internal Re and increased jet separation.

Table 4.2: Comparison of typical inlet and outlet U-bend Reynolds numbers for the *t/d* = 1.2 TBC experiments with varying blowing ratio, *M*.

No Showerhead					Active Showerhead			
M	**Re_{Uin}**	**Re_{Uout}**	**Avg**		**M**	**Re_{Uin}**	**Re_{Uout}**	**Avg**
0.5	20700	19300	20000		**0.5**	Not Tested		
1.0	21500	18500	20000		**1.0**	22500	17500	20000
2.0	22000	18000	20000		**2.0**	25800	14200	20000
3.0	22900	17100	20000		**3.0**	28500	11500	20000
5.0	24300	15700	20000		**5.0**	Not Tested		

The exterior surface of the TBC was imaged with IR thermography in order to measure the TBC condition, τ. The laterally averaged results for τ with round hole film cooling with an active showerhead, *t/d* = 1.2 TBC, and *Tu* = 20% are presented in Figure 4.19. As the blowing ratio increases the performance of τ near the showerhead improves despite the increased separation of the coolant jets. As previously mentioned, this is a result of the fact that the coolant jets are oriented at 90º to the streamwise direction, meaning that coolant travels radially up the vane as the mainstream flow in the stagnation region turns the coolant jets back onto the vane. Albert (2011) provides further discussion concerning this behavior based on adiabatic effectiveness measurements. The large number of holes in the showerhead means that changes in coolant flow rate can have substantial effects on the convective cooling within the coolant holes. Conversely, the performance of τ decreases as blowing ratio increases for the pressure side row of holes due to the separation of the jets.

Detailed contour plots of the cooling performance on the exterior surface of the TBC may be seen in Figure 4.20. The separation of the coolant jets from the pressure

side holes is shown as the blowing ratio increases above $M = 1.0$. This can be determined by the fact that the cooling performance downstream of the holes degrades despite the fact that a greater amount of film coolant is coming out of the holes. The accumulation of coolant in the showerhead region with increasing blowing ratio is also observable. Above $M_{SH} = 3.0$ the coolant from the showerhead appears to improve the cooling performance of the entire region between $s/d = 0$ to $s/d = -32$. Ideally, the showerhead would be operated at $M_{SH} = 3.0$ and the pressure side holes would be set to $M = 1.0$. This would allow for optimal coolant coverage of the vane surface. A contour plot of the TBC surface with no film cooling is also provided in Figure 4.20. This was achieved by completely filling the film cooling holes with clay to ensure that no film coolant emitted on to the surface of the TBC. The clay plugs are particularly evident for the pressure side row of cooling holes at $s/d = -34$ since they appear as periodic spots of lower temperature. This is a result of the higher thermal conductivity of the clay as compared to the cork making the clay plugs appear as local cold spots. It is important to recognize that the TBC condition was greater than zero with no film cooling. This was a result of conduction through the vane wall and the TBC. The increase in τ from $s/d = -5$ to -35 is a result of the external convective heat transfer coefficient decreasing in this region as shown in Figure 4.7.

The vane with $t/d = 1.2$ TBC was tested with and without an active showerhead. The results presented in Figure 4.21 provide a comparison of ϕ with and without an active showerhead at two different blowing ratio conditions for the pressure side holes, $M = 1.0$ and $M = 2.0$. The presence of film cooling in the stagnation region of the vane

significantly improves the cooling performance of the system from $-10 < s/d < 15$. This is likely dominated by the convective cooling within the holes, as previously discussed. However, further downstream on the pressure side (i.e. $s/d < -25$) the showerhead provides no significant change in the overall effectiveness, ϕ. Albert (2011) showed that the adiabatic effectiveness falls below $\eta = 0.05$ in the region of $s/d = -25$. This likely explains why the showerhead is providing no additional thermal protection at this location for the blowing ratios shown herein. It's possible that the showerhead could begin to have an effect on the overall effectiveness downstream of the pressure side holes if it were operated at a significantly higher blowing ratio, maybe $M_{SH} > 4.0$.

Figure 4.22 – Figure 4.26 provide comparisons of the overall effectiveness with changes in blowing ratio for the round holes, craters, ideal trench, modified trench, and realistic trench, respectively. All of the configurations were tested with the $t/d = 1.2$ TBC at a location of $s/d = -32$ on the pressure side of the vane. None of the configurations shown in these figures had an active showerhead. The results in Figure 4.22 show that the performance of the round holes essentially collapses downstream of the coolant holes despite changes in blowing ratio. This is the same result that was obtained when the pressure side round hole configuration had an active showerhead. The round hole configuration without a showerhead was operated down to a blowing ratio of $M = 0.5$ in order to see if increased jet attachment would improve the cooling performance. For instance, Albert (2011) showed that the adiabatic effectiveness of pressure side film cooling with round holes improved from $\eta < .1$ for $M = 2.0$ to $\eta > 0.2$ for $M = 1.0$ due to increased attachment. Minimal improvement was observed due to the increased jet

attachment which may be a result of reduced convective cooling through the holes offsetting the improvement in surface cooling. Figure 4.23 – Figure 4.26 show the performance of ϕ for the craters and trench designs. In each case the performance improves marginally with increased blowing ratio. However, it should be recognized that the blowing ratio was increased substantially, from $M = 0.5$ up to $M = 5.0$. Consequently, the fractional improvement in ϕ comes at the expense of using significantly more coolant. In all cases the overall effectiveness of a model with no film cooling is included in the figures as a basis of comparison. It's evident that the film cooling provides a distinct improvement to the cooling performance of the vane, in particular near the exit of the cooling configurations. However, a major part of the increased cooling appears to be due to convective cooling in the holes as is evident with the improved performance upstream of the holes. Consequently, the convective cooling within the holes improves the cooling performance of the vane even in a region where the film cooling provides no additional thermal protection on the external surface of the TBC.

In most of the figures, a noticeable improvement in ϕ is observable far upstream of the film cooling holes with increasing blowing ratio. For instance, at a location of $s/d = -5$ the performance of ϕ increases by more than $\Delta\phi = 0.05$ for some of the cooling configurations when the blowing ratio is increased from $M = 0.5$ to $M = 5.0$. This increase can be explained by changes in the internal Reynolds number since increased internal coolant flow rate is required to achieve higher blowing ratios. For the configurations without an active showerhead the difference in Reynolds number at the mid-span of the inlet U-bend passage can be as great as $\Delta Re = 4{,}000$ when comparing the

conditions for the M = 0.5 and M = 5.0 cases. This is why the performance of ϕ is improved upstream of the pressure side coolant holes when the blowing ratio is increased. The higher mass flow rate would increase the heat transfer rates for internal coolant flow and thus improve the overall effectiveness. This effect is significantly less downstream of the pressure side cooling holes since the internal Reynolds number in this region varies by only ΔRe = 200. Consequently, any change in ϕ downstream of the pressure side holes is only a result of the change in convective cooling through the holes and the behavior of the coolant on the exterior surface of the TBC.

Directly comparing the overall effectiveness achieved by the different film cooling configurations at a set blowing ratio can provide more insight into the relative performance. Figure 4.27 – Figure 4.30 provide direct comparisons of the performance of ϕ for the varying film cooling designs. It may be seen that at low blowing ratios none of the designs are superior in improving cooling at the interface of the TBC and the vane wall. However, the realistic trench performs poorly in comparison to the other configurations at the lowest blowing ratio of M = 0.5. This is likely due to the fact that at the lowest blowing ratio the film coolant does not fill out the wider realistic trench. Consequently, hot mainstream gas may have mixed with the local film coolant and warmed the exposed vane wall within the realistic trench. As the blowing ratio increases, the crater and trench designs begin to show a relative improvement as opposed to the round holes which suffer from jet separation. Of particular interest is the trend that is observed at blowing ratios of $M \geq 2.0$. It may be seen in Figure 4.29 and Figure 4.30 that the performance of the trenches begins to fall off at higher blowing ratios based on the

measurement of the thermocouple located at s/d = -32. This thermocouple was placed mid-pitch, in line with the pressure side row of holes. This also means that the thermocouple was at the bottom of the trench designs. The local decrease in ϕ at the location of the holes for M = 5.0 may suggest that suboptimal operation of a trench can result in local heating due to the absence of TBC. This is a similar conclusion for why the realistic trench performed so poorly at low blowing ratios as well as why the t/d = 0.55 TBC trench performed poorly in comparison to round holes. The higher performance of the craters, at the same location of s/d = -32 at M = 5.0 may highlight how retaining more of the TBC near the cooling holes improves the thermal protection of the vane wall. It is also of particular interest to determine whether or not the trench design is more susceptible to spallation due to the increased exposure of the underlying TBC structure.

As previously mentioned, an array of thermocouples was placed at the interface of the TBC and vane wall downstream of the pressure side coolant holes. This was done in order to provide better insight into the lateral average of ϕ in a region that was expected to have greater temperature gradients due to the periodic nature of some of the film cooling designs. Figure 4.31 compares results for laterally averaging ϕ as compared to the minimum ϕ measured by four different thermocouples at a given s/d location. This is an important factor in order to identify hot spots which could lead to local failure of the system over time. Focusing at a location of approximately s/d = -39 in Figure 4.31(b), due to the fact that the greatest variations are at this location, it may be seen that the round holes and craters both exhibit a difference between average and minimum ϕ of

approximately $\Delta\phi = 0.02$. The trench designs consistently have a differential of approximately $\Delta\phi = 0.01$. This helps to illuminate the advantage of having a more uniform distribution of coolant across the surface of the TBC that minimizes local hot spots. However, it should be recognized that for different blowing ratios or different *s/d* locations there is minimal performance difference observed between the various configurations in terms of comparing ϕ_{avg} and ϕ_{min}. Dees (2010) showed the discrete nature of round hole film cooling without a TBC can cause variations approaching $\Delta\phi = 0.5$ between the coldest and warmest regions within $5d$ downstream of the exit of the suction side holes operating at $M = 0.64$. Albert (2011) showed less variation on the pressure side of the vane when measuring ϕ with no TBC; however, Albert (2011) operated the round holes at higher blowing ratios which would have promoted separation thus reducing the discrete nature of the coolant jet footprint on the surface of the vane.

The film cooling performance of the $t/d = 1.2$ TBC configurations was also quantified by measuring the TBC condition, τ, with the use of IR thermography. Figure 4.32 – Figure 4.36 compare the laterally averaged values of τ for each of the respective film cooling configurations at varying blowing ratios. These figures are plotted with respect to *x/d*, where $x/d = 0$ is defined as the downstream edge of the round holes feeding the different configurations. Figure 4.32 clearly shows decreased τ with increasing blowing ratio which can be attributed to jet separation. The results for the other designs show that increasing blowing ratio leads to substantial improvements in the cooling performance on the exterior surface of the TBC. All of the designs, other than

the round holes, begin to plateau in performance at around $M = 2.0$. The realistic trench shows a much broader increase in τ immediately adjacent to the pressure side holes. This is a result of the wider trench that is exposing the cold underlying vane wall to the view of the IR camera.

Direct comparisons of τ for the various designs at blowing ratios of $M = 0.5$, 1.0, 2.0 and 5.0 are provided in Figure 4.37 – Figure 4.40, respectively. At the lowest blowing ratio of $M = 0.5$, the round holes perform on par with the ideal and modified trench designs for $x/d > 5$. The realistic trench performs poorly at $M = 0.5$. This is likely due to the mainstream air warming the coolant within the wider trench before it spills over the downstream lip of the trench, as previously discussed. Figure 4.38 and Figure 4.39 show that the showerhead does little to alter the film cooling performance downstream of the round holes at $M = 1.0$ and 2.0. The three trench designs have very similar film cooling performance for $M \geq 2.0$. The performance of the craters is fractionally less than the ideal and modified trench designs for $x/d < 5$ at $M = 1.0$. At $M = 2.0$, the trench designs have a noticeable advantage over the craters. This may be a result of the trenches nearing their optimal operating conditions in which the majority of the coolant spreads laterally within the trench without separating from the surface as it spills over the TBC lip and onto the exterior surface. At the highest blowing ratio of $M = 5.0$ the crater and trench configurations have near identical performance for cooling the exterior surface of the TBC.

Greater insight into the coolant behavior on the TBC surface may be gained from the contour plots shown in Figure 4.41 and Figure 4.42. These contour plots provide a

distribution of τ on the surface of the TBC for all of the various designs at blowing ratios of M = 0.5, 1.0, 2.0 and 5.0. The periodic nature of the coolant emitted from discrete round holes is clearly shown in Figure 4.41. This behavior leads to local hot streaks on the surface of the TBC. In comparison, the other designs create a more uniform layer of coolant on the surface of the TBC. This is advantageous for it reduces the amount of mixing with the hot mainstream thus sustaining the cold core of the coolant as it progresses downstream. The contour plots of the realistic trench show how the temperature within the trench is warmer than the results obtained for the ideal and modified trenches, particularly at M = 0.5. Furthermore, the realistic trench provides less uniform coverage of the TBC surface as compared to the craters and other trench designs. This may be a result of the film coolant not spreading laterally in the same manner as the other trenches due to the fact that the downstream wall of the realistic trench is spaced further from the exits of the embedded round holes. Results were not obtained for the round holes at M = 5.0 or for the craters at M = 0.5.

The contour plots shown in Figure 4.41 and Figure 4.42 provide a means for understanding the magnitude of temperature variation within the trenches. This is important information because some of the previous conclusions concerning the performance of the trench configurations in term of ϕ were based on a single thermocouple measurement at the location of the pressure side holes. It's possible that the thermocouple was placed in a location that would slightly under-predict or over-predict the laterally averaged temperature within the trench. However, the contour plots shown in Figure 4.41 and Figure 4.42 show that the temperature in the mid-pitch region

between the coolant holes within the trench is relatively consistent. Consequently, the single thermocouple measurement at the location of the pressure side holes should be considered a good representation of the average mid-pitch temperature within the trench. Lateral variations in metal temperature are not thought to be as much of an issue for the round holes and craters because the presence of the overlying TBC should produce a more uniform distribution of temperature near the holes.

4.3. Comparison of TBC Results with Engine Requirements

It should be recognized that the necessary cooling performance of a component in a real engine is dictated by the temperature requirements for the vane wall and the TBC. Neither material, the metal of the vane wall or the TBC, can be allowed to exceed specific temperatures that keep the engine operating within a specified margin of safety. The design process for a real engine turbine component involves determining the maximum allowable operating temperatures of the vane wall and TBC surface in order to maintain the necessary margins of safety. This information is critical in determining the relative performance of a design. Unfortunately, this information is not readily available from the primary engine manufacturers due to the competitive environment surrounding gas turbine engine production. However, piecing together various open literature sources can begin to provide an understanding of the material requirements for a component in a real engine. With that in mind, let us assume that the maximum operating temperatures for the vane metal and TBC are 1250°C and 1400°C, respectively. These temperatures are based on the author's assumptions of the operating conditions of a modern engine as well as open-literature studies such as Perepezko (2009) and Padture *et al.* (2002). The

Sulzer (2011) material data sheet for 8% yttria stabilized zirconia was also used to refine the assumed operating temperature for a typical TBC. It should be recognized that the melting point of ceramic based TBC's is significantly higher than the proposed maximum operating temperatures for TBC's. This is due to the fact that additional factors are at play such as sintering of the TBC which will detrimentally increase the thermal conductivity. Furthermore, higher temperatures can results in accelerated erosion and corrosion of the TBC which may promote spallation. Consequently, it is likely that the TBC must be operated at temperatures well below its melting point. This is in contrast to the proposed operating conditions of the vane metal which is close to $9/10^{th}$'s of the melting temperature of a nickel based superalloy.

The minimum allowable values of ϕ and τ in order to satisfy the aforementioned maximum material temperatures can be described as design requirements for the engine. The minimum requirements will be labeled as ϕ_{req} and τ_{req}. These requirements can be determined if the temperature of the hot gas path and coolant are known for realistic engine conditions. Table 4.3 provides the minimum requirements for a modern engine operating at various temperature conditions. The table also provides the requirements for a future engine in which the maximum allowable operating temperatures for the vane metal and TBC were assumed to have increased. It should be remembered that the numbers used herein for determining ϕ_{req} and τ_{req} are assumed values and were not supplied by any of the manufacturing companies. Instead, the numbers were based upon available open literature sources. Consequently, it is possible that the numbers are in slight error for what is expected in a real engine. The temperatures used for the

mainstream hot gas path were based on a typical engine (T_∞ = 1500°C) and an advanced engine (T_∞ = 2000°C). The maximum material temperatures for the future engine were set based on assumptions of future research and development that improves the thermal behavior of the materials under higher temperature environments. As expected, the necessary cooling performance of the vane increases with increasing temperature of the hot gas path. It is worth noting that the requirement for external TBC condition, τ_{req}, is negative for the future engine operating with T_∞ = 1500°C. This represents a case in which advancement in the material properties of TBC could lead to a design relying solely on TBC for thermal protection while film cooling is no longer needed.

Table 4.3: Engine requirements, ϕ_{req} and τ_{req}, for varying engine conditions and material temperature thresholds.

Modern Engine					**Future Engine**			
Max Metal Temp (°C)		1250			**Max Metal Temp (°C)**		1300	
Max TBC Temp (°C)		1400			**Max TBC Temp (°C)**		1600	
T_∞ **(°C)**	$T_{c,vane\ inlet}$ **(°C)**	ϕ_{req}	τ_{req}		T_∞ **(°C)**	$T_{c,vane\ inlet}$ **(°C)**	ϕ_{req}	τ_{req}
1500	600	0.28	0.11		1500	600	0.22	-0.11
1800	800	0.55	0.40		1800	800	0.50	0.20
2000	900	0.68	0.55		2000	900	0.64	0.36

The performance of the *t/d* = 1.2 TBC model presented earlier in this chapter performs relatively well in comparison to the requirements shown in Table 4.3. In most cases the overall effectiveness achieved by the *t/d* = 1.2 TBC satisfied the requirements for both the modern and future engine. It performs particularly well in terms of the future engine due to the assumptions that the maximum allowable material temperatures will increase. However, the *t/d* = 1.2 TBC model did not satisfy τ_{req} for the modern engine

case with T_∞ = 1800°C and 2000°C. The performance of the *t/d* = 1.2 TBC may be a result of the TBC being relatively thick. In general, the overall effectiveness of the *t/d* = 1.2 TBC model often exceeded the requirements shown in Table 4.3, particularly when film cooling was utilized. Consequently, the thickness of the *t/d* = 1.2 TBC could be reduced in order to improve the performance of the external TBC condition, τ, while still satisfying the requirement for overall effectiveness, ϕ. This may then bring the system closer to satisfying the requirement for the external TBC condition, τ_{req}.

The performance of the *t/d* = 1.2 TBC model can be summarized with the following information in order to support the preceding claims and make conclusions concerning how it performs in comparison to the requirements presented in Table 4.3. The crater and trench film cooling configurations with *t/d* = 1.2 TBC operating at *M* = 2.0 provide overall effectiveness levels of $\phi > 0.8$ within 30*d* downstream of the pressure side holes based on the results presented in Figure 4.29. The round holes perform slightly worse at the same blowing ratio. The overall effectiveness of the system without film cooling varies significantly due to changes in the external and internal convective heat transfer coefficient. For instance, the overall effectiveness with *t/d* = 1.2 TBC decreases to approximately $\phi = 0.45$ at the stagnation point as compared to approximately $\phi = 0.75$ at *s/d* = -67 for a turbulence intensity of *Tu* = 20%, as shown in Figure 4.29. With an active showerhead of round holes operating at *M* = 2.0 the overall effectiveness near the stagnation region improves to $\phi > 0.8$ as shown in Figure 4.21. The cooling performance of craters and trenches provides $\tau > 0.3$ at *M* = 2.0 within 20*d* downstream of the film

cooling holes with t/d = 1.2 TBC based on the results presented in Figure 4.39. The round holes for the same case provide τ = 0.2 - 0.25 for 20d downstream of the holes. The external TBC condition is approximately τ = 0.2 over the region of -32 < s/d < -5 with an active showerhead at M = 2.0 based on the results presented in Figure 4.19 for a t/d = 1.2 TBC.

As discussed in Chapter 3, the thermal resistance of the t/d = 0.55 TBC appears to be higher than expected. Therefore, the results for the thinner TBC are not used here as a basis for how a t/d = 0.55 TBC would perform in comparison to the requirements expected in a real engine.

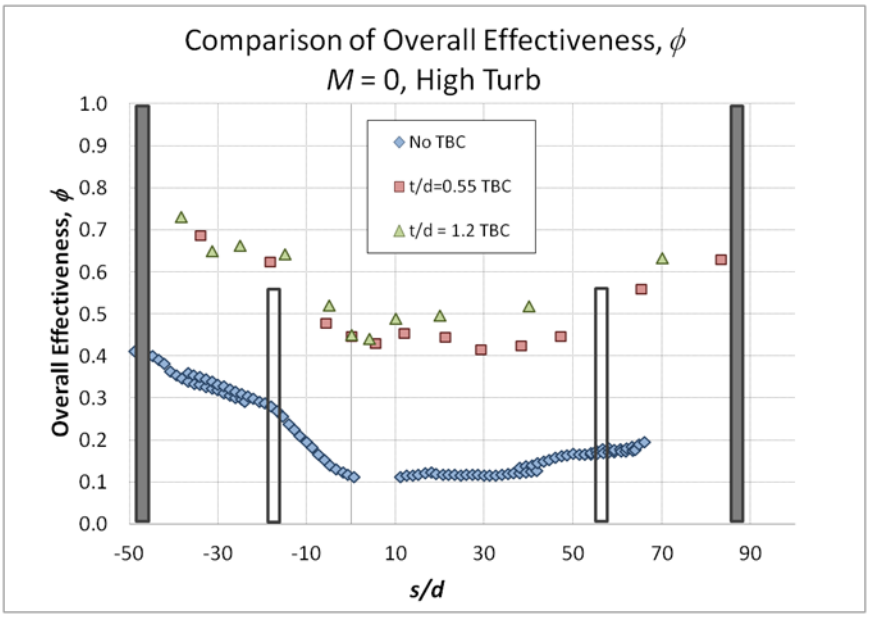

Figure 4.1: Comparison of t/d = 0.55 and t/d = 1.2 TBC at M = 0 and Tu = 20%.

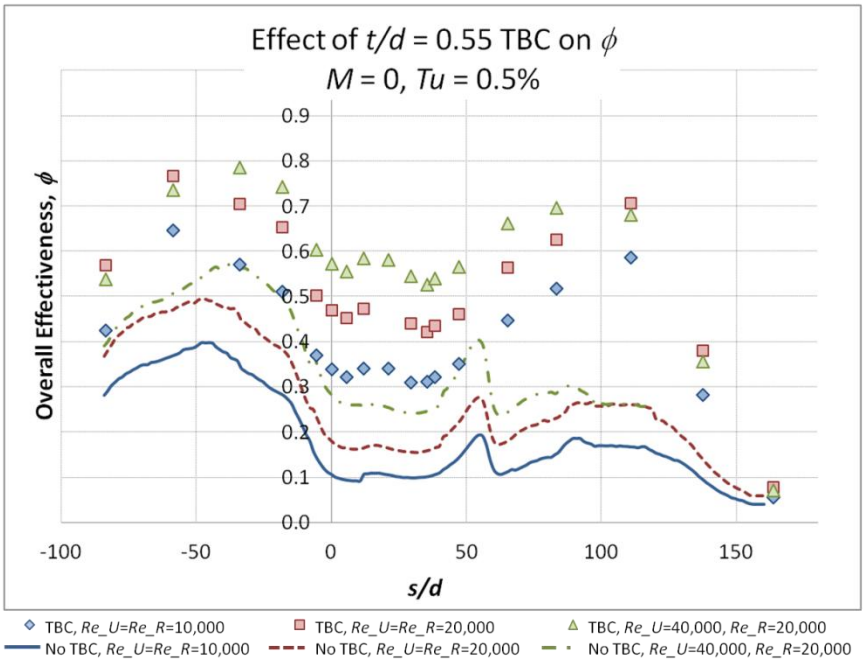

Figure 4.2: Comparison of overall effectiveness, ϕ, with and without t/d = 0.55 TBC for varying internal Re with M = 0 and Tu = 0.5%.

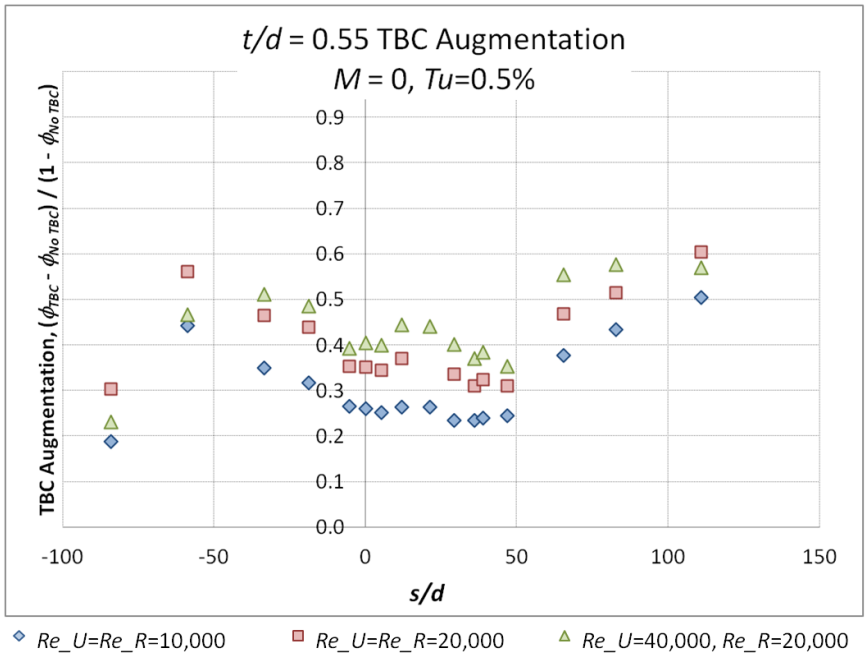

Figure 4.3: Comparison of $t/d = 0.55$ TBC augmentation for varying internal Re conditions with $M = 0$ and $Tu = 0.5\%$.

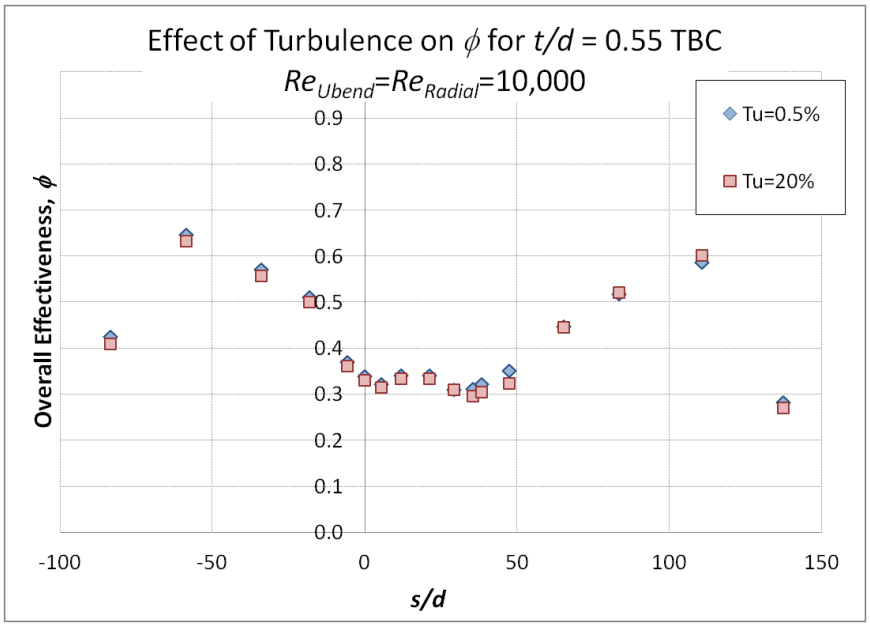

Figure 4.4: Effect of turbulence intensity on ϕ for $t/d = 0.55$ TBC with $M = 0$ and internal conditions set to $Re_{Ubend} = Re_{Radial} = 10{,}000$.

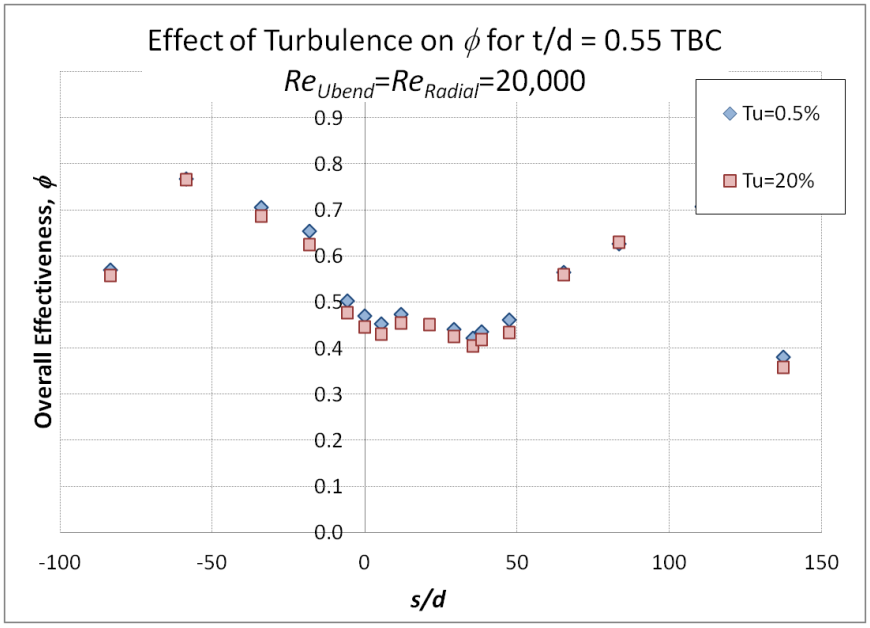

Figure 4.5: Effect of turbulence intensity on ϕ for t/d = 0.55 TBC with M = 0 and internal conditions set to Re_{Ubend} = Re_{Radial} = 20,000.

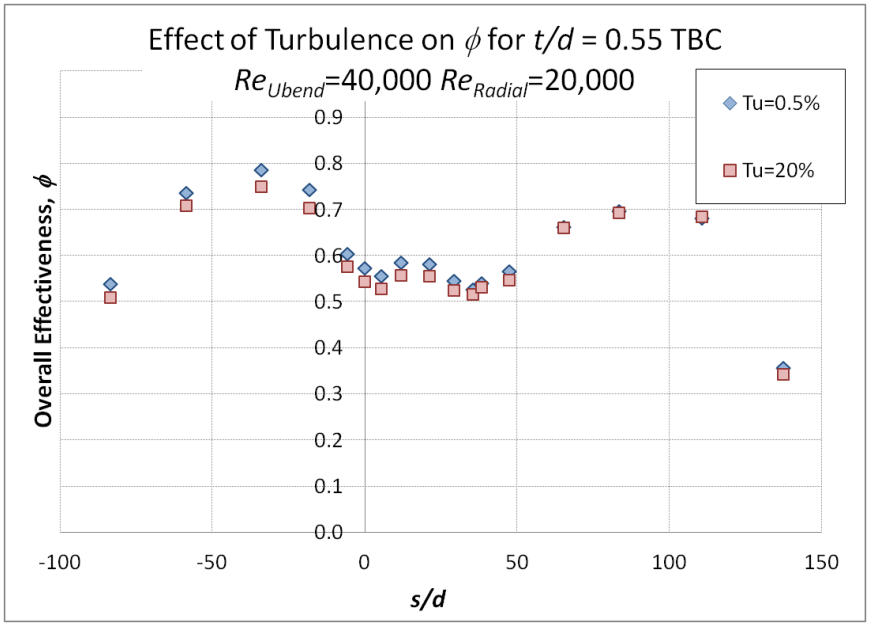

Figure 4.6: Effect of turbulence intensity on ϕ for t/d = 0.55 TBC with M = 0 and internal conditions set to Re_{Ubend} = 40,000 and Re_{Radial} = 20,000.

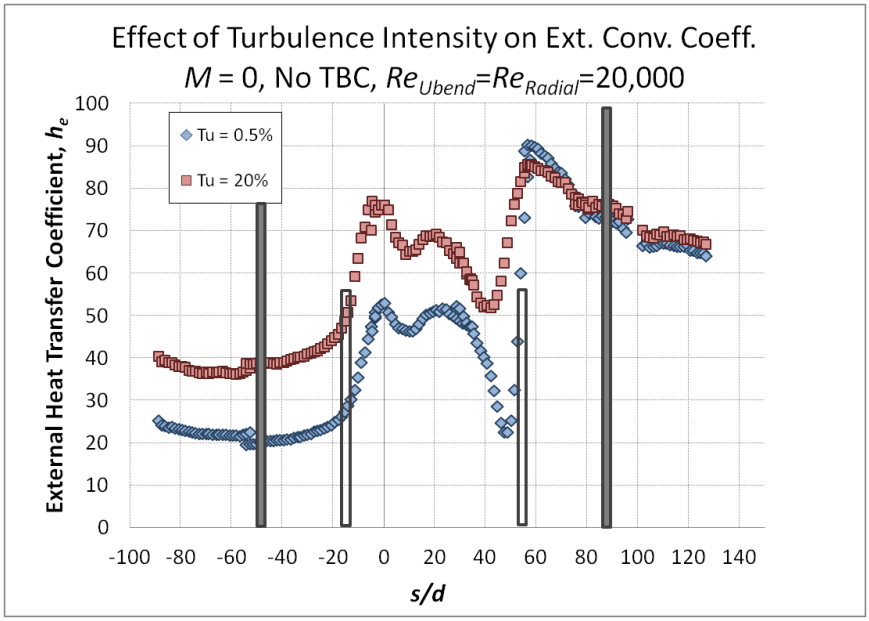

Figure 4.7: Effect of turbulence intensity on external heat transfer coefficient for a vane with no TBC, $M = 0$, and $Re_{Ubend} = Re_{Radial} = 20{,}000$ (modified from Dees (2010)).

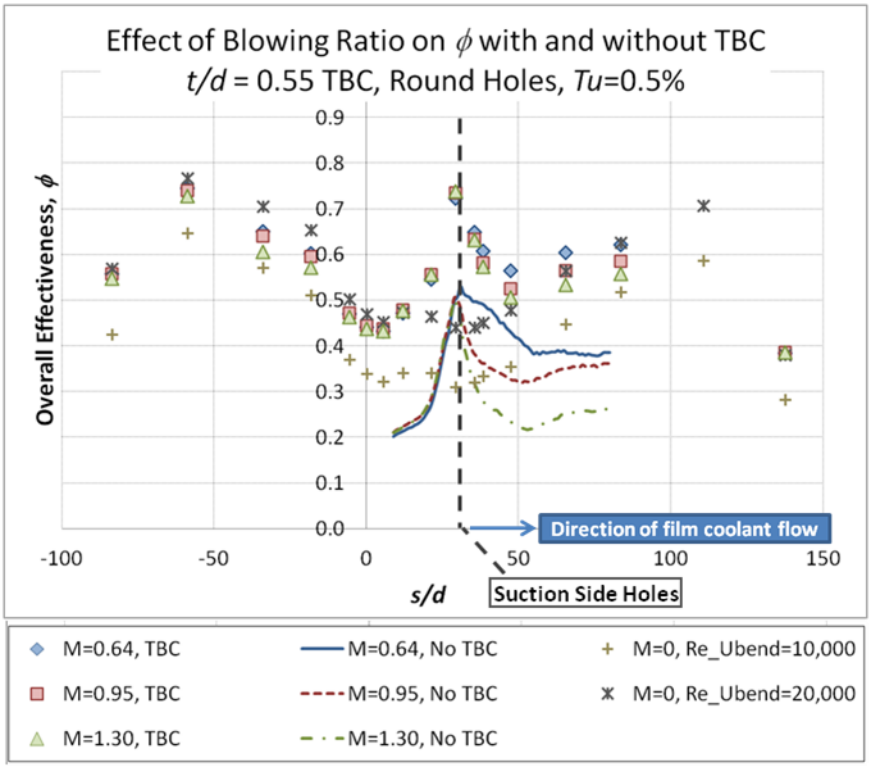

Figure 4.8: Effect of blowing ratio on ϕ with and without t/d = 0.55 TBC for round holes with internal conditions set to $Re_{Ubend} = Re_{Radial}$ = 20,000 (No TBC data obtained by Dees (2010)). M = 0 data also included for $Re_{Ubend} = Re_{Radial}$ = 10,000 and $Re_{Ubend} = Re_{Radial}$ = 20,000.

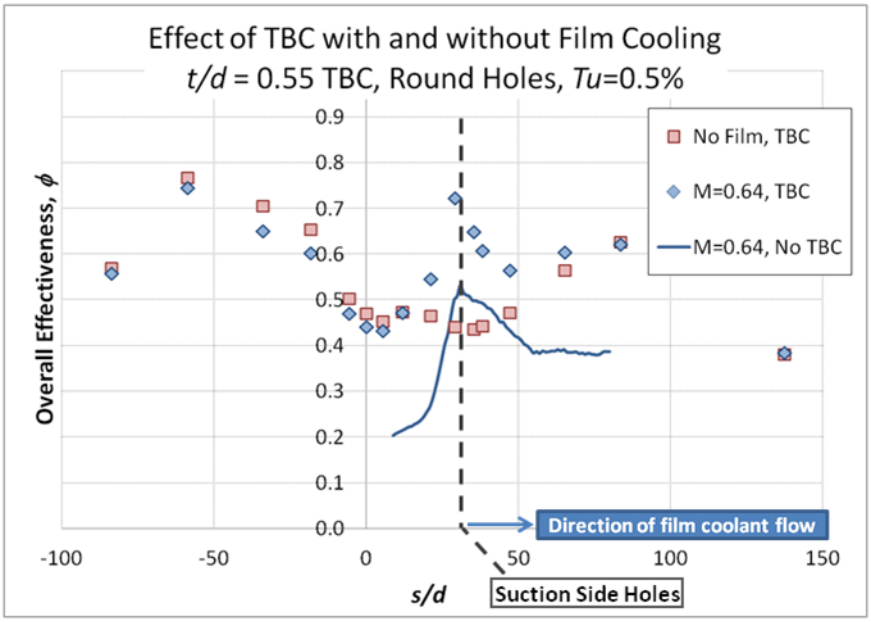

Figure 4.9: Effect of t/d = 0.55 TBC on ϕ with and without round hole film cooling with internal conditions set to $Re_{Ubend} = Re_{Radial}$ = 20,000.

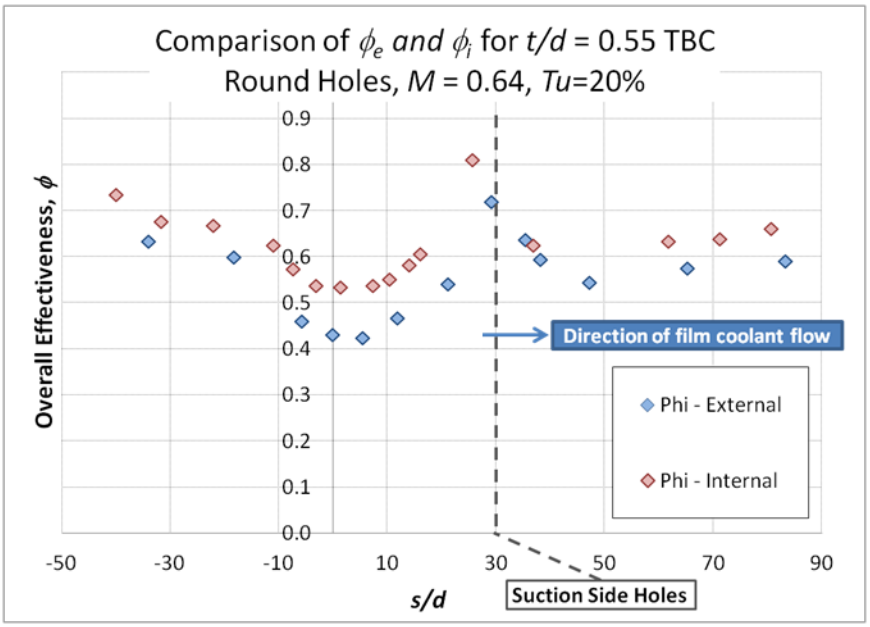

Figure 4.10: Comparison of internal and external (interface) overall effectiveness for a film cooled vane with round holes at M = 0.64, t/d = 0.55 TBC, and Tu = 20%.

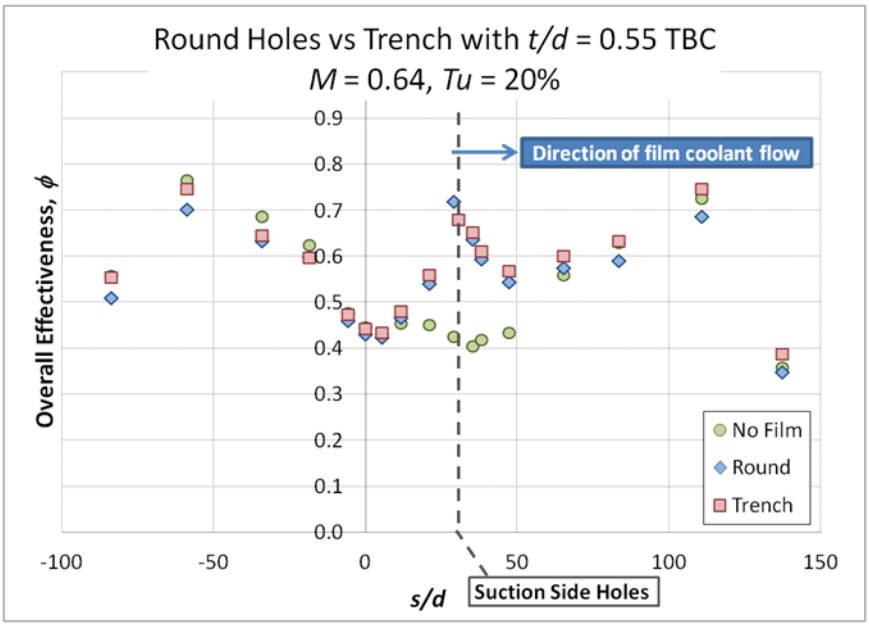

Figure 4.11: Comparison of ϕ for round holes and a trench at $M = 0.64$ with $t/d = 0.55$ TBC at $Tu = 20\%$.

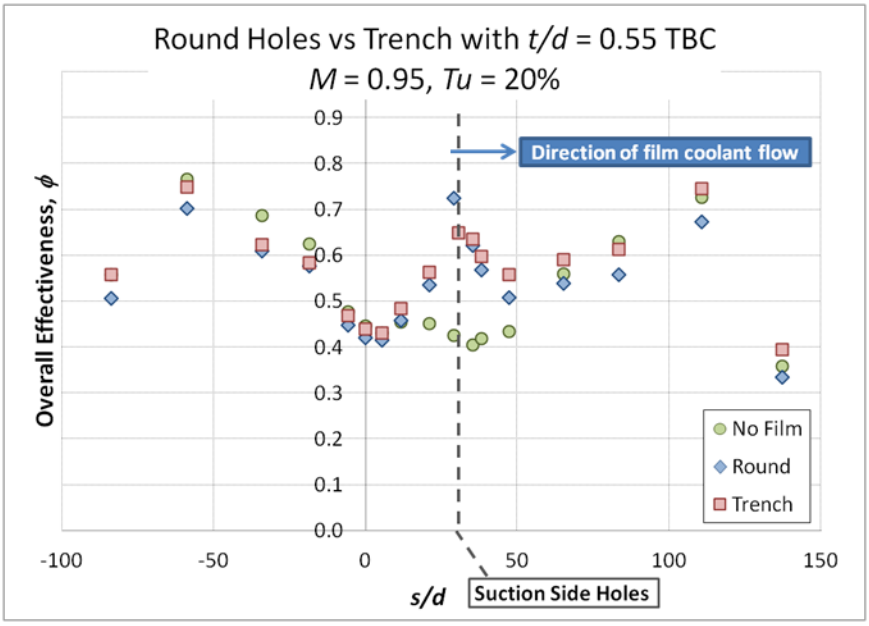

Figure 4.12: Comparison of ϕ for round holes and a trench at $M = 0.95$ with $t/d = 0.55$ TBC at $Tu = 20\%$.

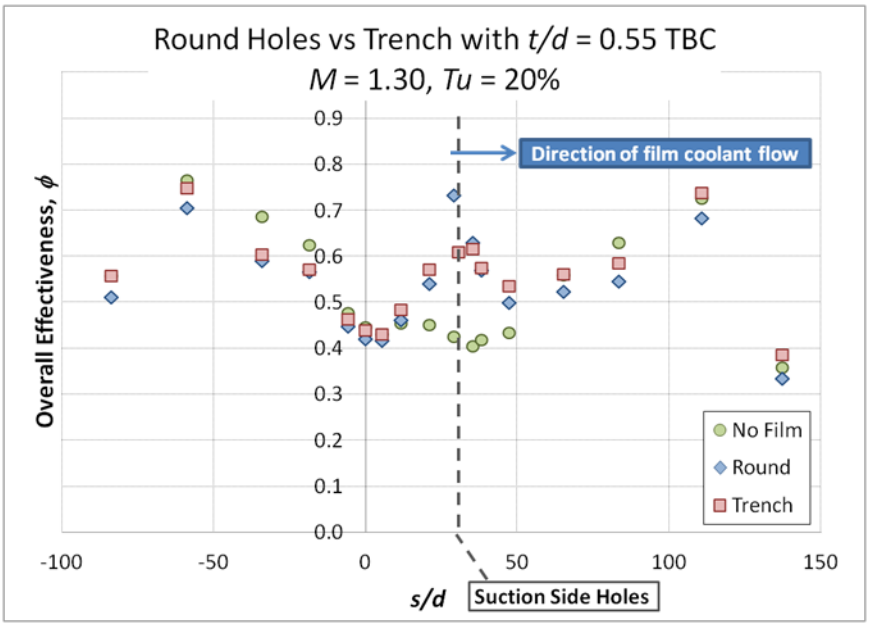

Figure 4.13: Comparison of ϕ for round holes and a trench at $M = 1.30$ with $t/d = 0.55$ TBC at $Tu = 20\%$.

Figure 4.14: Comparison of ϕ_{min} and ϕ_{avg} for round holes and a trench at $M = 0.64$ with $t/d = 0.55$ TBC at $Tu = 20\%$.

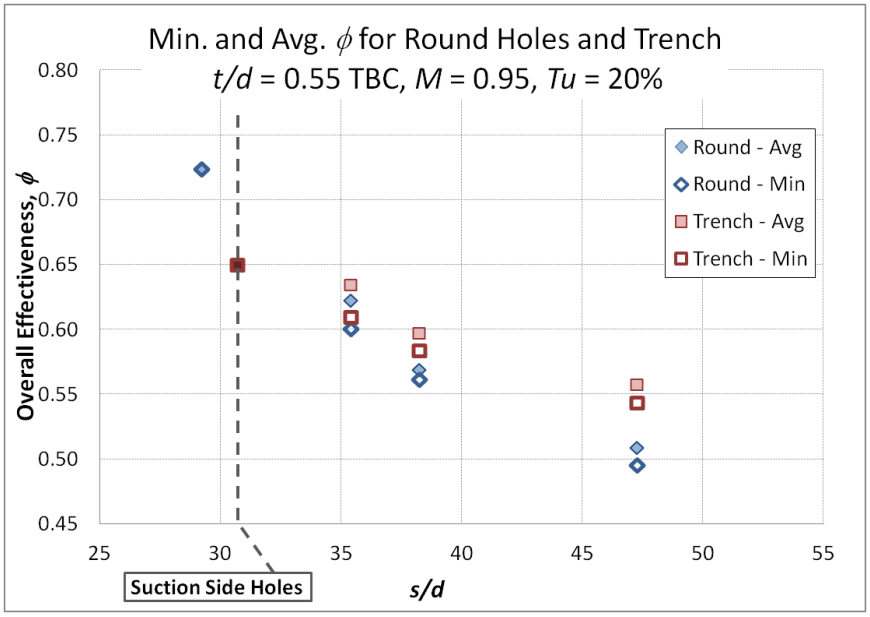

Figure 4.15: Comparison of ϕ_{min} and ϕ_{avg} for round holes and a trench at M = 0.95 with t/d = 0.55 TBC at Tu = 20%.

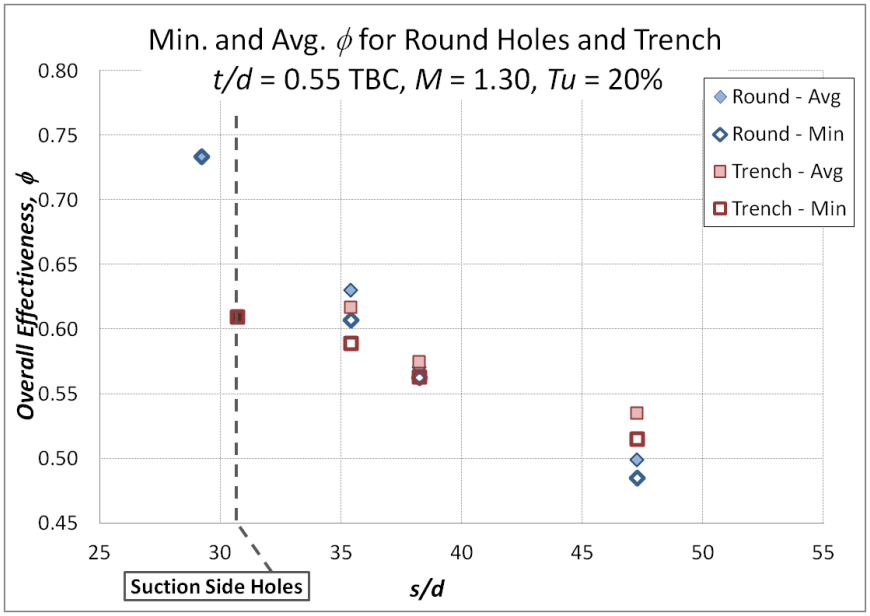

Figure 4.16: Comparison of ϕ_{min} and ϕ_{avg} for round holes and a trench at M = 1.30 with t/d = 0.55 TBC at Tu = 20%.

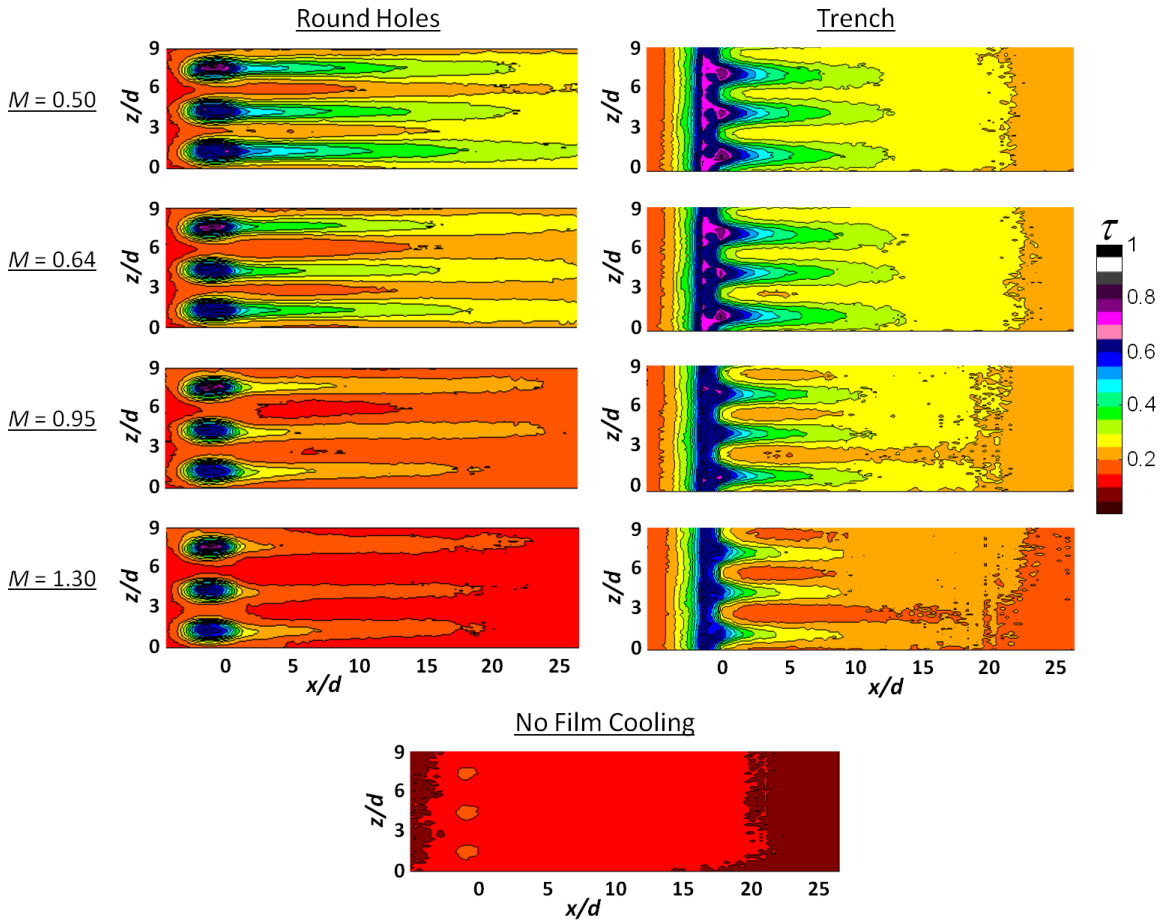

Figure 4.17: Comparison of external TBC condition, τ, for the t/d = 0.55 TBC for round holes and trench at varying blowing ratios with Tu = 20%.

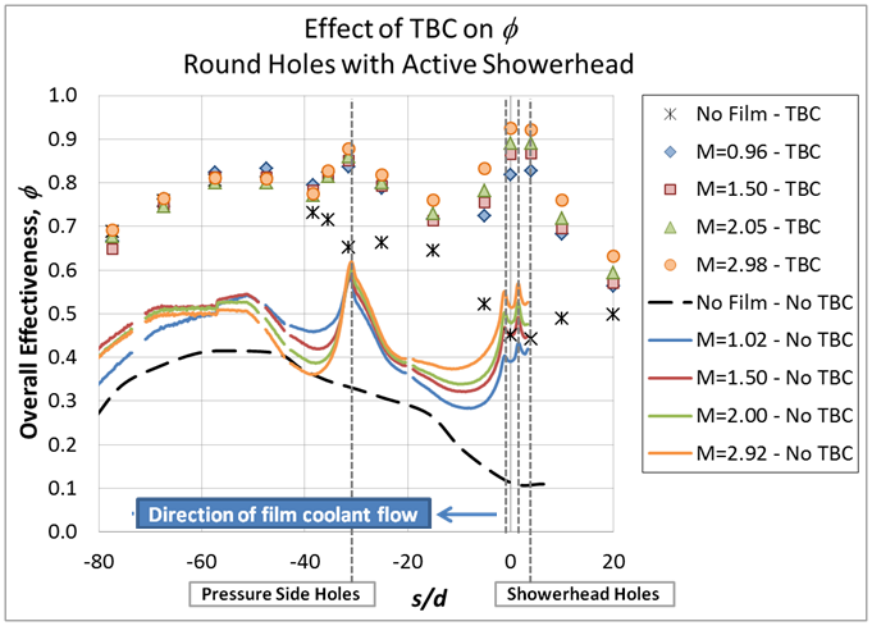

Figure 4.18: Comparison of ϕ with and without t/d = 1.2 TBC for round holes with an active showerhead (M listed here is for only the pressure side holes) at Tu = 20%. No TBC data collected by Albert (2011).

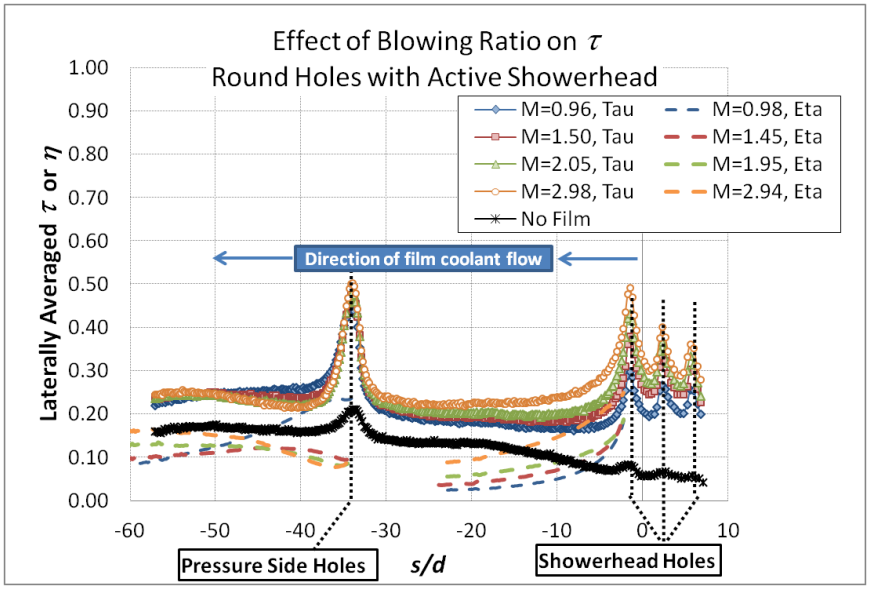

Figure 4.19: Comparison of laterally averaged τ for round holes with an active showerhead at varying blowing ratios with Tu = 20% and t/d = 1.2 TBC (M listed here is for only the pressure side holes). Albert (2011) collected adiabatic effectiveness results.

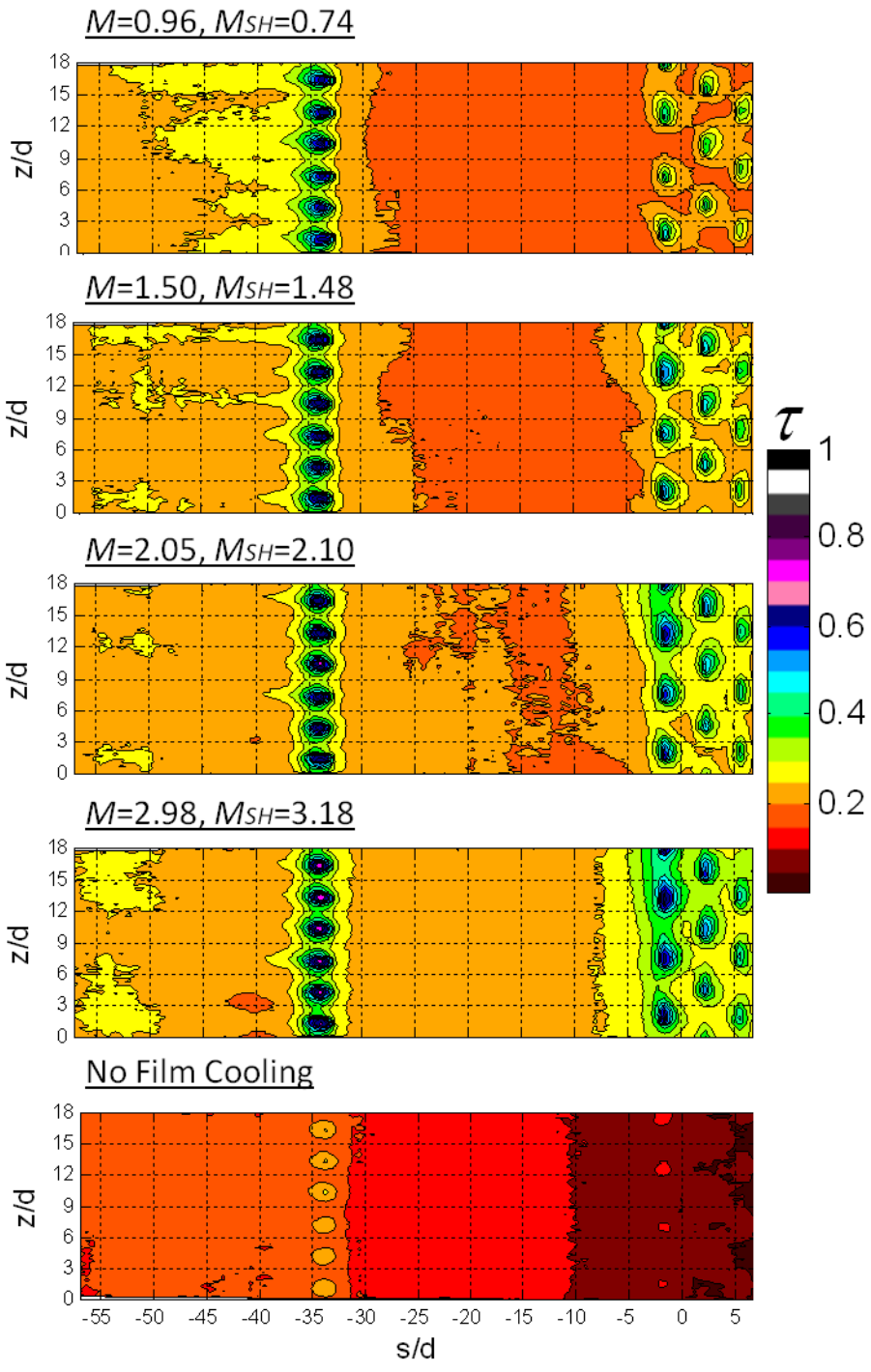

Figure 4.20: Contour plots of τ for round holes with an active showerhead with t/d = 1.2 TBC at Tu = 20%.

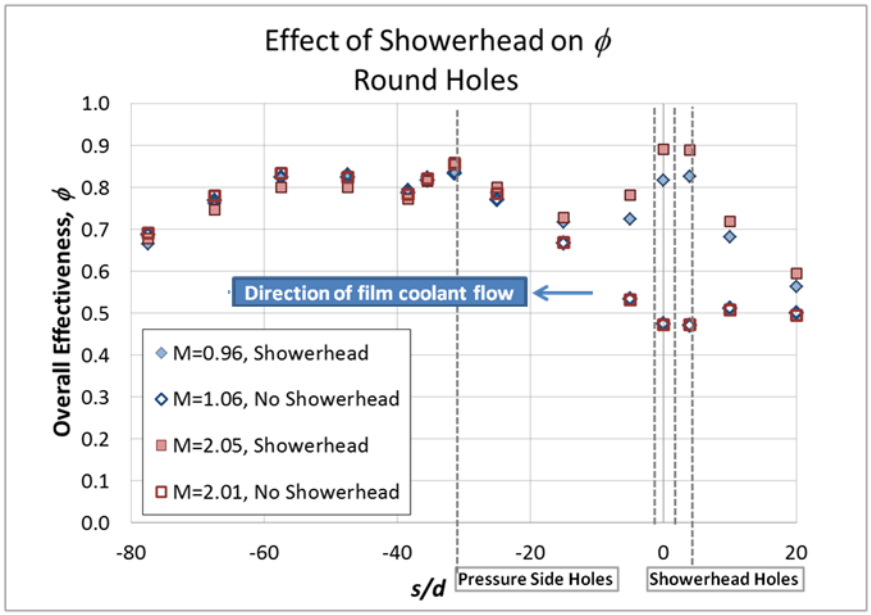

Figure 4.21: Comparison of ϕ for round holes with and without showerhead film cooling at Tu = 20% with t/d = 1.2 TBC (M listed here is for only the pressure side holes).

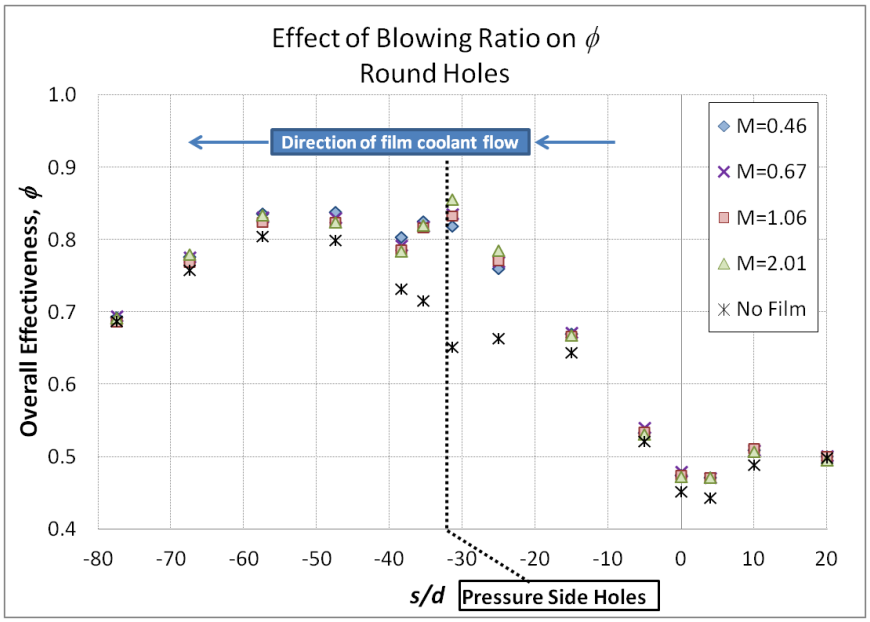

Figure 4.22: Effect of blowing ratio on ϕ for round holes with a plugged showerhead and t/d = 1.2 TBC at Tu = 20%.

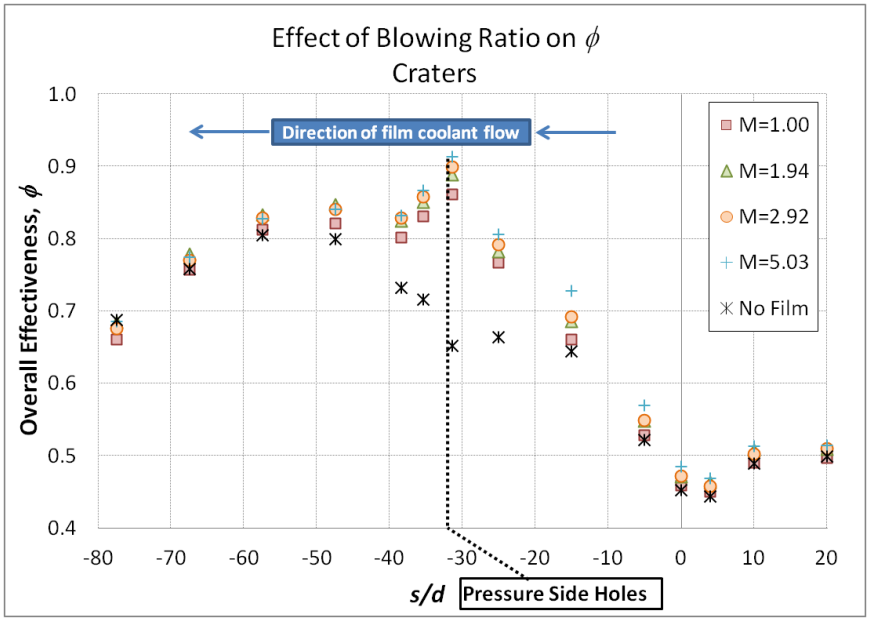

Figure 4.23: Effect of blowing ratio on ϕ for craters with a plugged showerhead and t/d = 1.2 TBC at Tu = 20%.

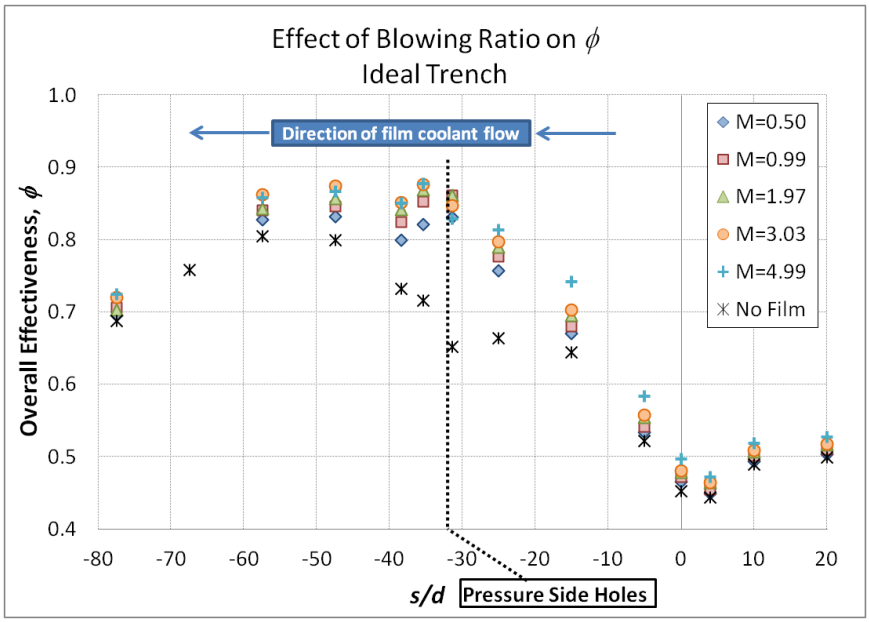

Figure 4.24: Effect of blowing ratio on ϕ for an ideal trench with a plugged showerhead and t/d = 1.2 TBC at Tu = 20%.

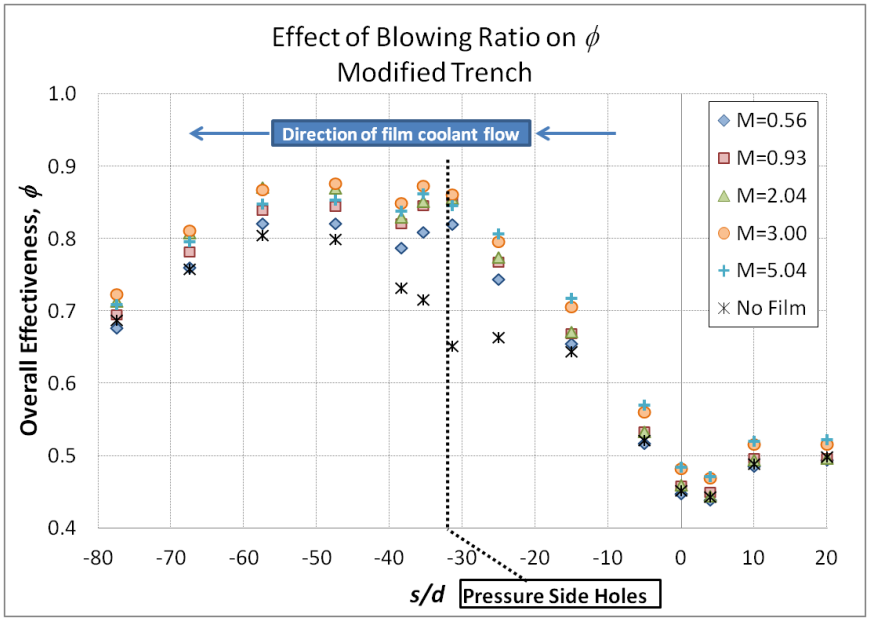

Figure 4.25: Effect of blowing ratio on ϕ for a modified trench with a plugged showerhead and t/d = 1.2 TBC at Tu = 20%.

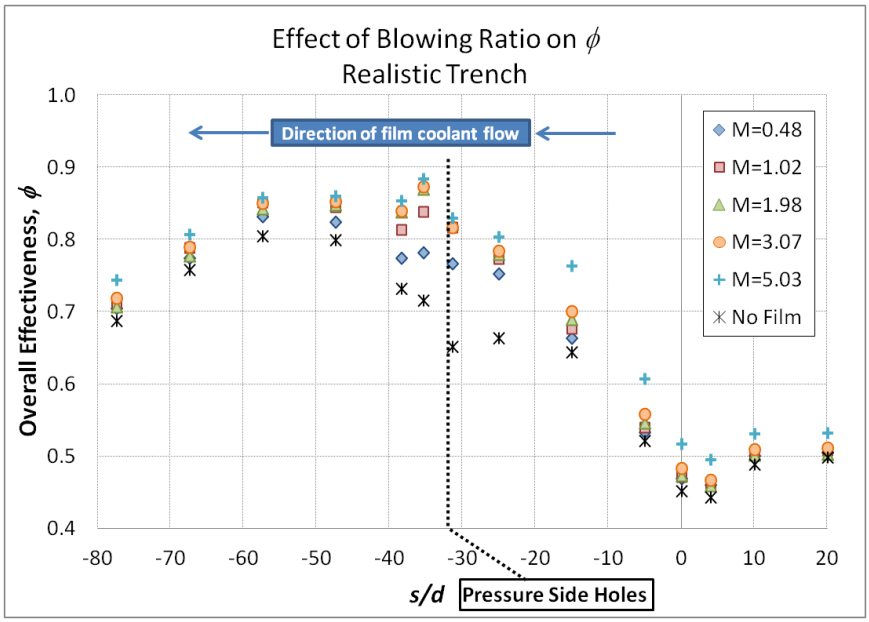

Figure 4.26: Effect of blowing ratio on ϕ for a realistic trench with a plugged showerhead and t/d = 1.2 TBC at Tu = 20%.

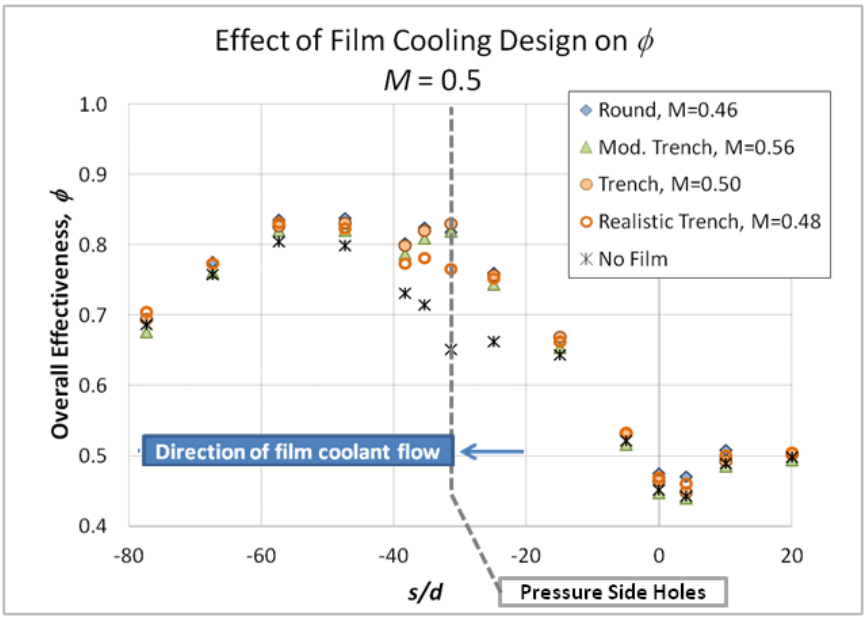

Figure 4.27: Effect of film cooling design on ϕ for $M = 0.5$ at $Tu = 20\%$ with $t/d = 1.2$ TBC.

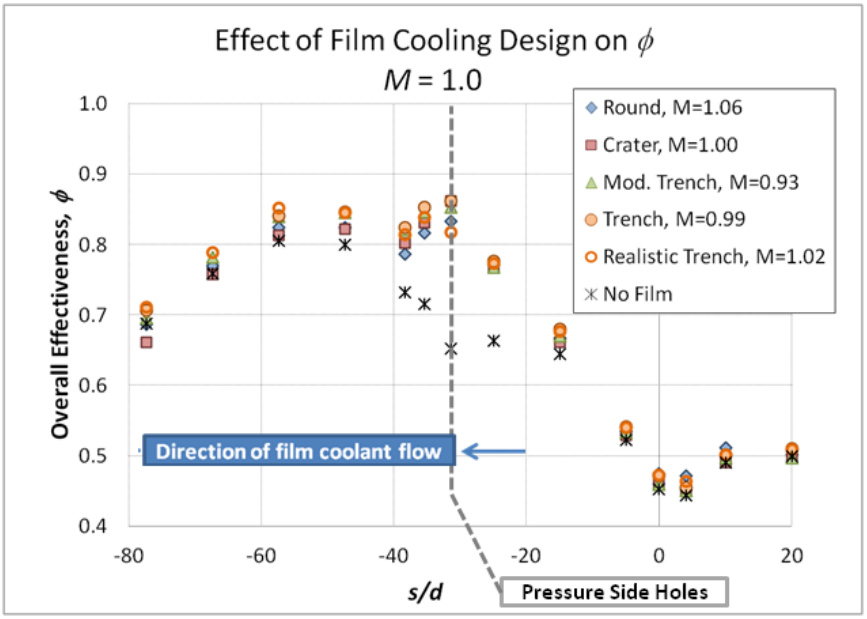

Figure 4.28: Effect of film cooling design on ϕ for $M = 1.0$ at $Tu = 20\%$ with $t/d = 1.2$ TBC.

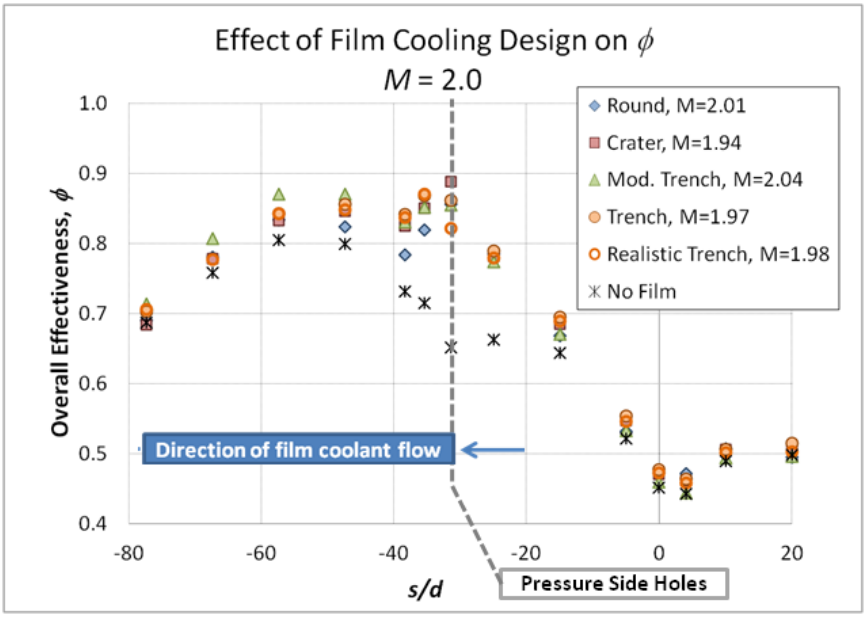

Figure 4.29: Effect of film cooling design on ϕ for M = 2.0 at Tu = 20% with t/d = 1.2 TBC.

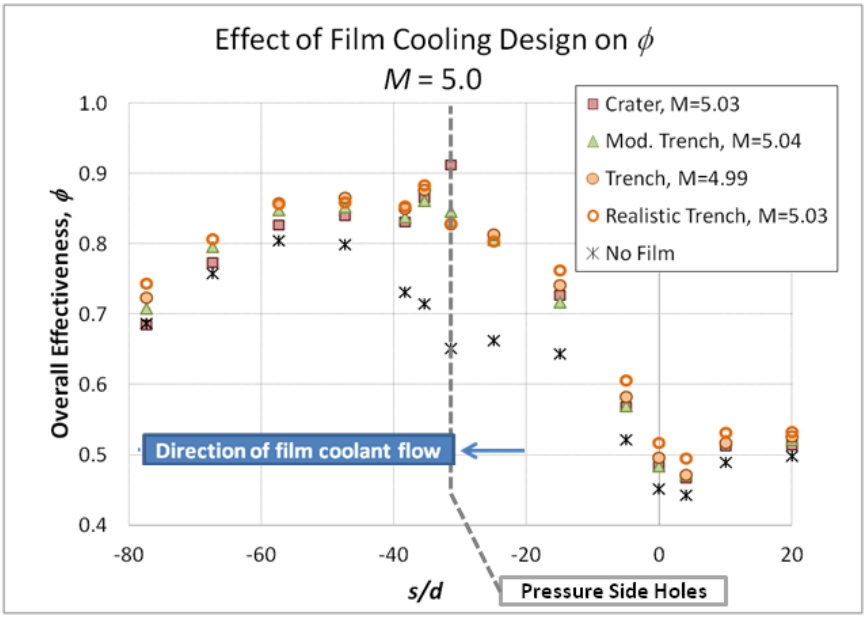

Figure 4.30: Effect of film cooling design on ϕ for M = 5.0 at Tu = 20% with t/d = 1.2 TBC.

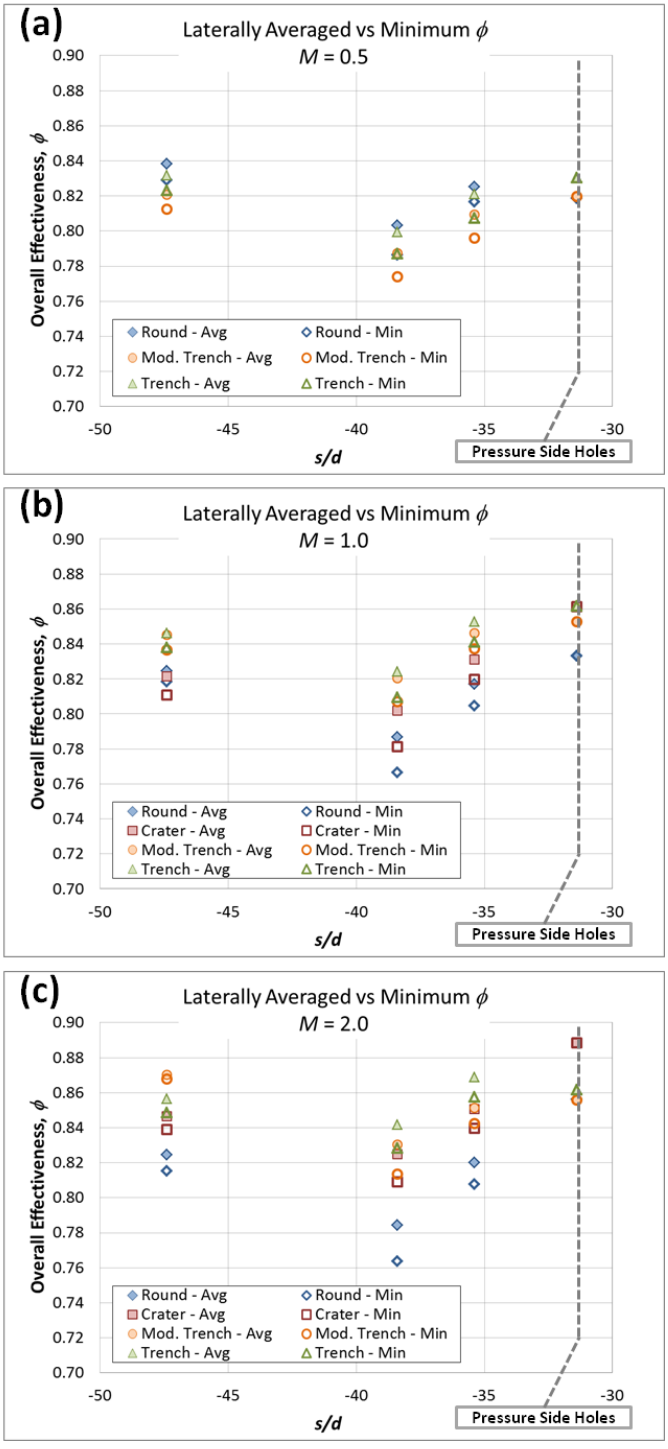

Figure 4.31: Comparison of ϕ_{avg} and ϕ_{min} for varying film cooling designs with t/d = 1.2 TBC and Tu = 20% at different blowing ratios of: (a) M = 0.5, (b) M = 1.0, and (c) M = 2.0.

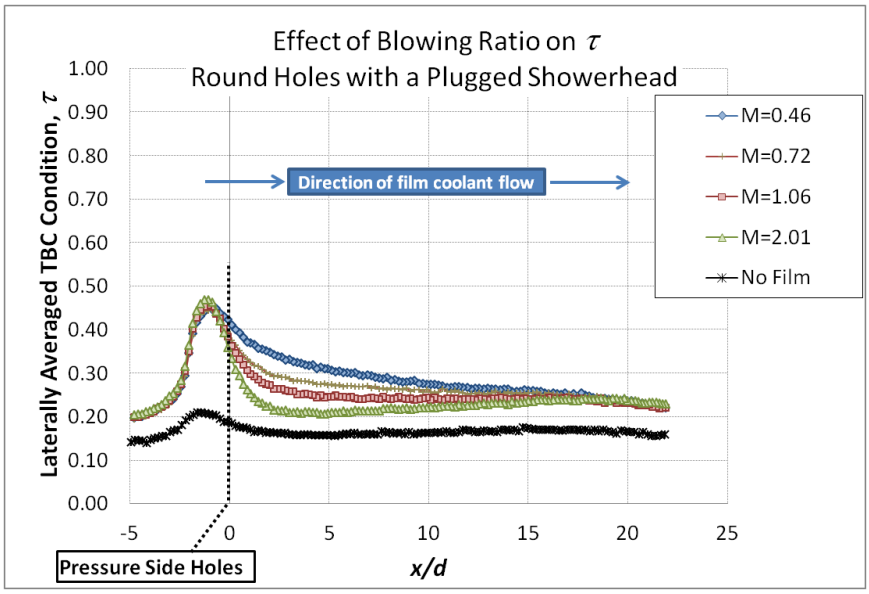

Figure 4.32: Effect of blowing ratio on τ for round holes with a plugged showerhead and t/d = 1.2 TBC at Tu = 20%.

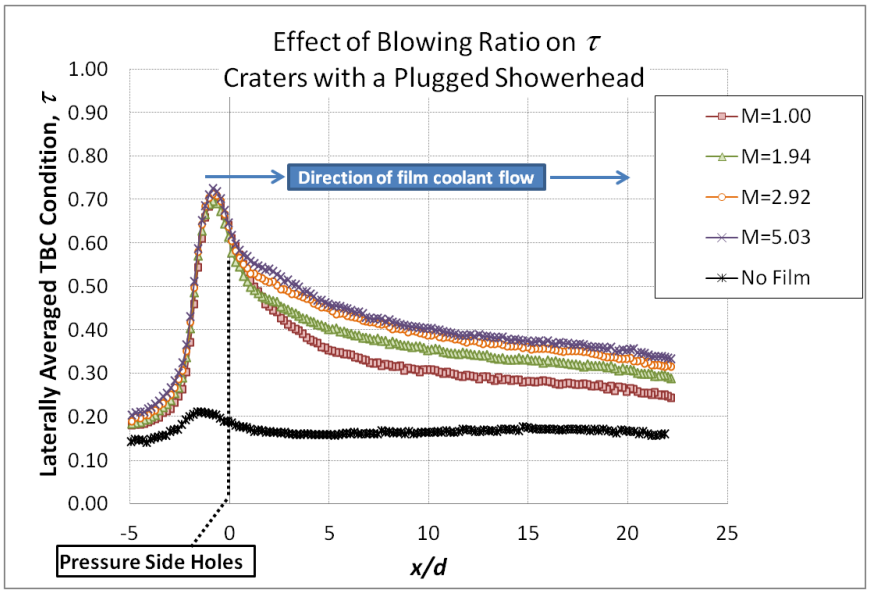

Figure 4.33: Effect of blowing ratio on τ for craters with a plugged showerhead and t/d = 1.2 TBC at Tu = 20%.

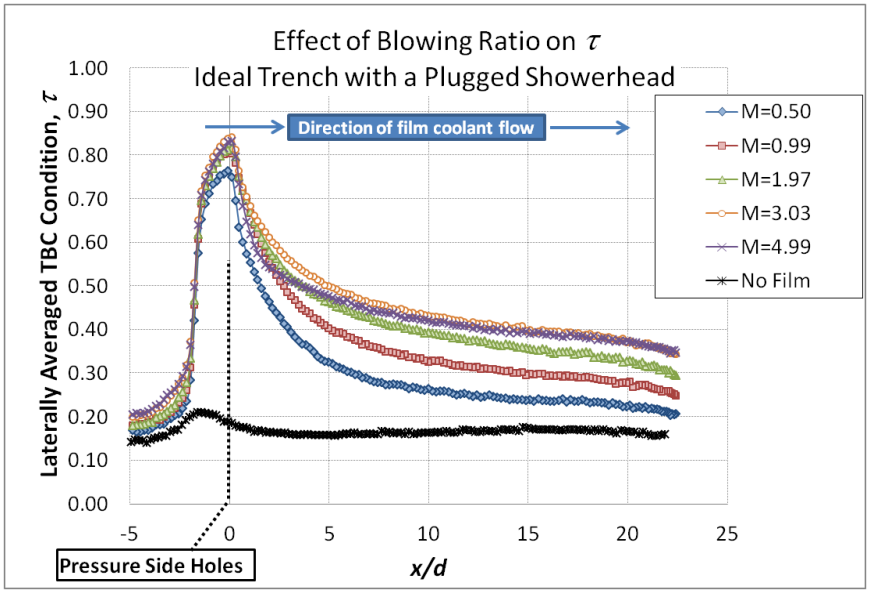

Figure 4.34: Effect of blowing ratio on τ for an ideal trench with a plugged showerhead and t/d = 1.2 TBC at Tu = 20%.

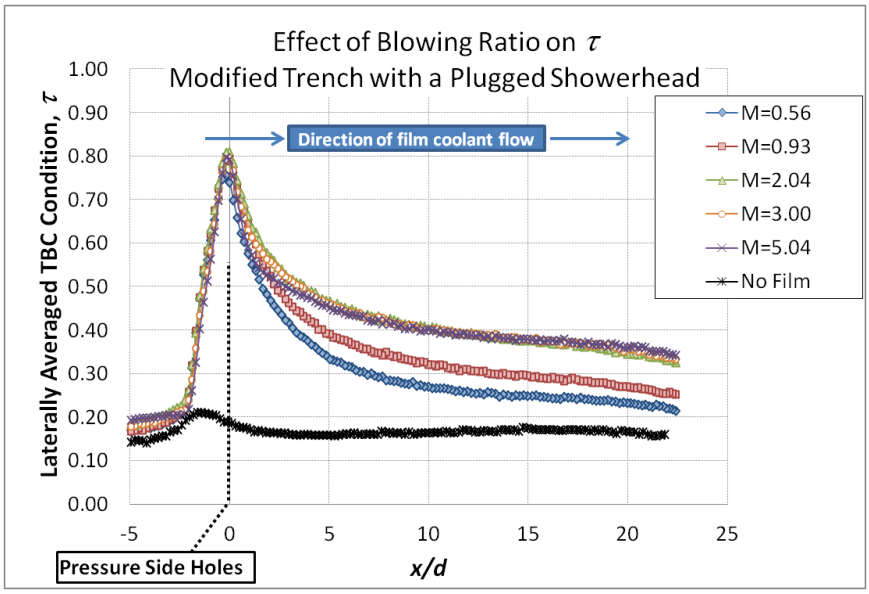

Figure 4.35: Effect of blowing ratio on τ for a modified trench with a plugged showerhead and t/d = 1.2 TBC at Tu = 20%.

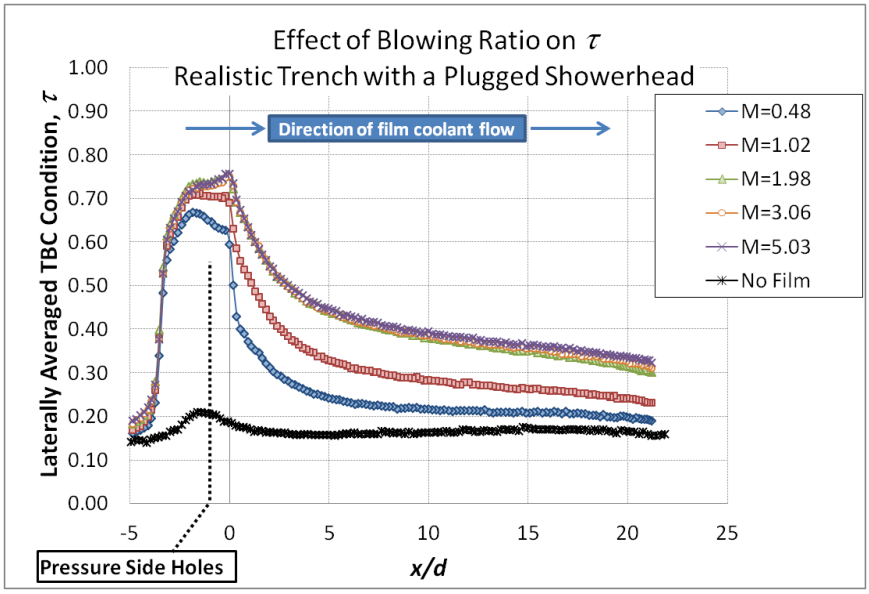

Figure 4.36: Effect of blowing ratio on τ for a realistic trench with a plugged showerhead and $t/d = 1.2$ TBC at $Tu = 20\%$.

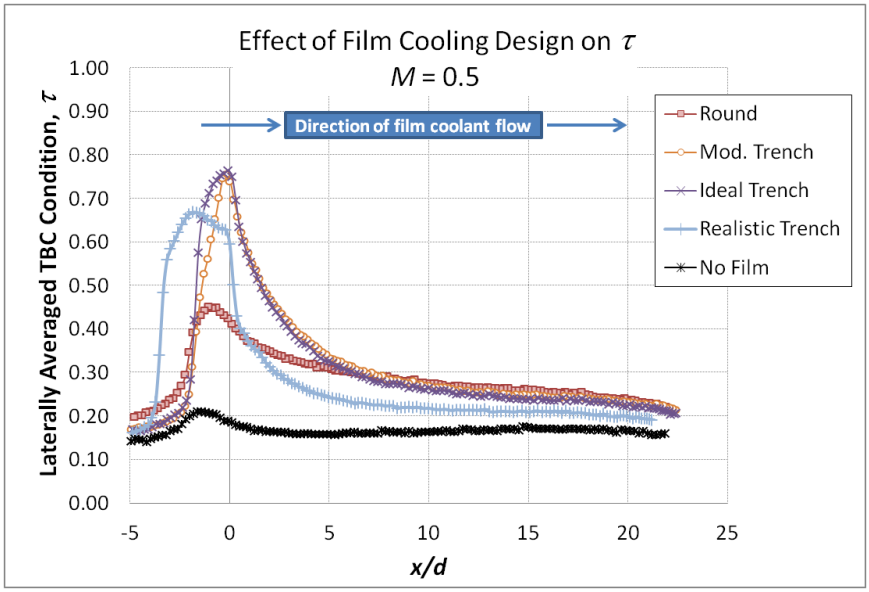

Figure 4.37: Effect of film cooling design on τ for $M = 0.5$ at $Tu = 20\%$ with $t/d = 1.2$ TBC.

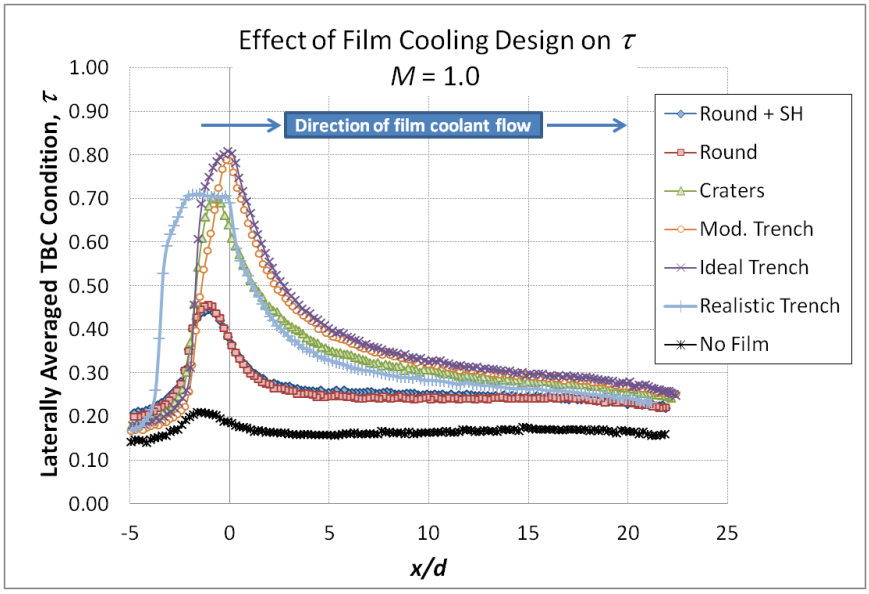

Figure 4.38: Effect of film cooling design on τ for $M = 1.0$ at $Tu = 20\%$ with $t/d = 1.2$ TBC.

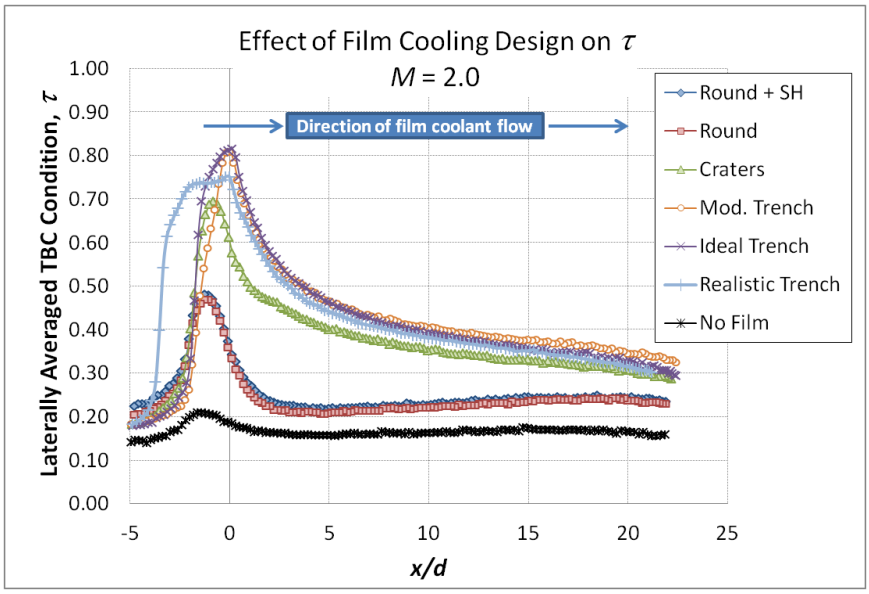

Figure 4.39: Effect of film cooling design on τ for $M = 2.0$ at $Tu = 20\%$ with $t/d = 1.2$ TBC.

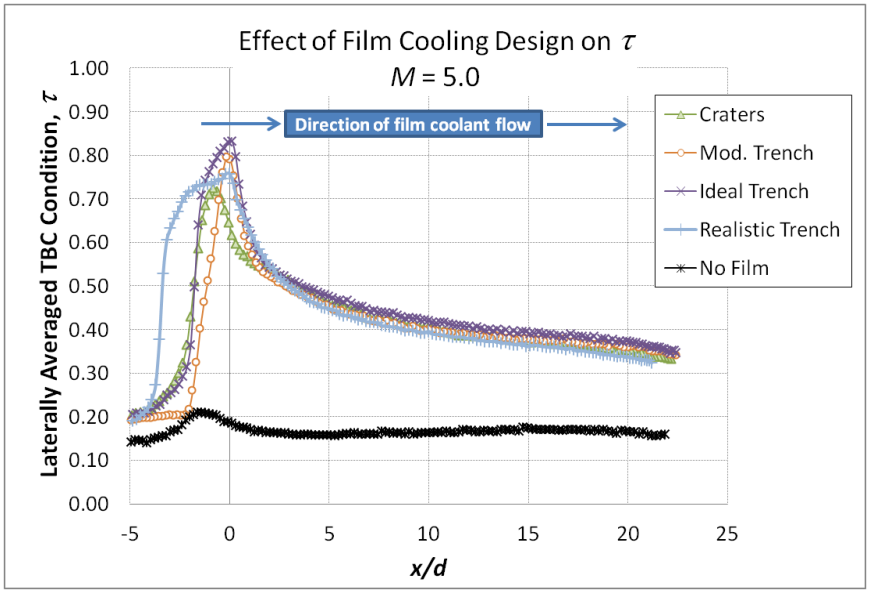

Figure 4.40: Effect of film cooling design on τ for $M = 5.0$ at $Tu = 20\%$ with $t/d = 1.2$ TBC.

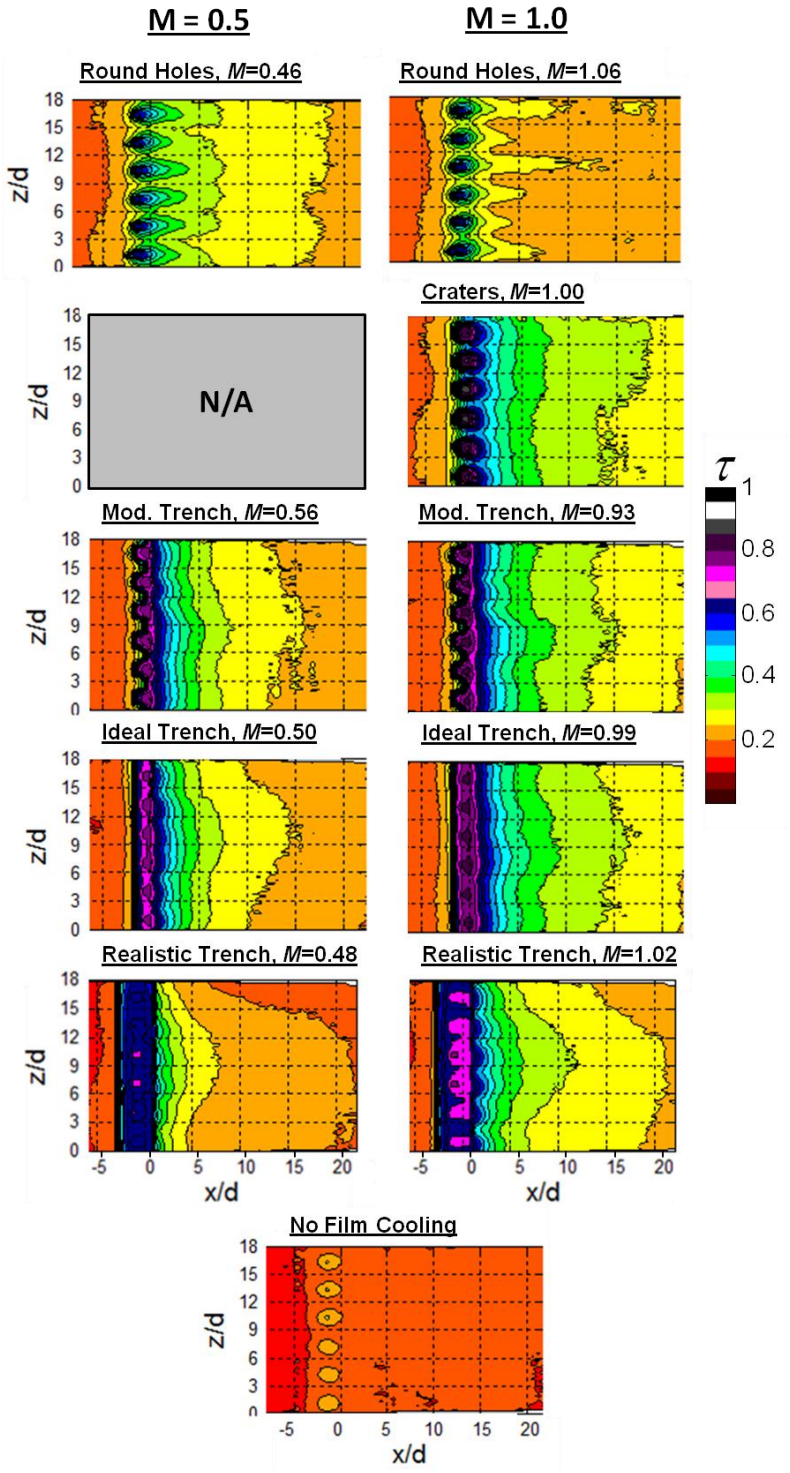

Figure 4.41: Contour plots of τ for varying film cooling designs at $M = 0.5$ and $M = 1.0$ with $t/d = 1.2$ TBC at $Tu = 20\%$.

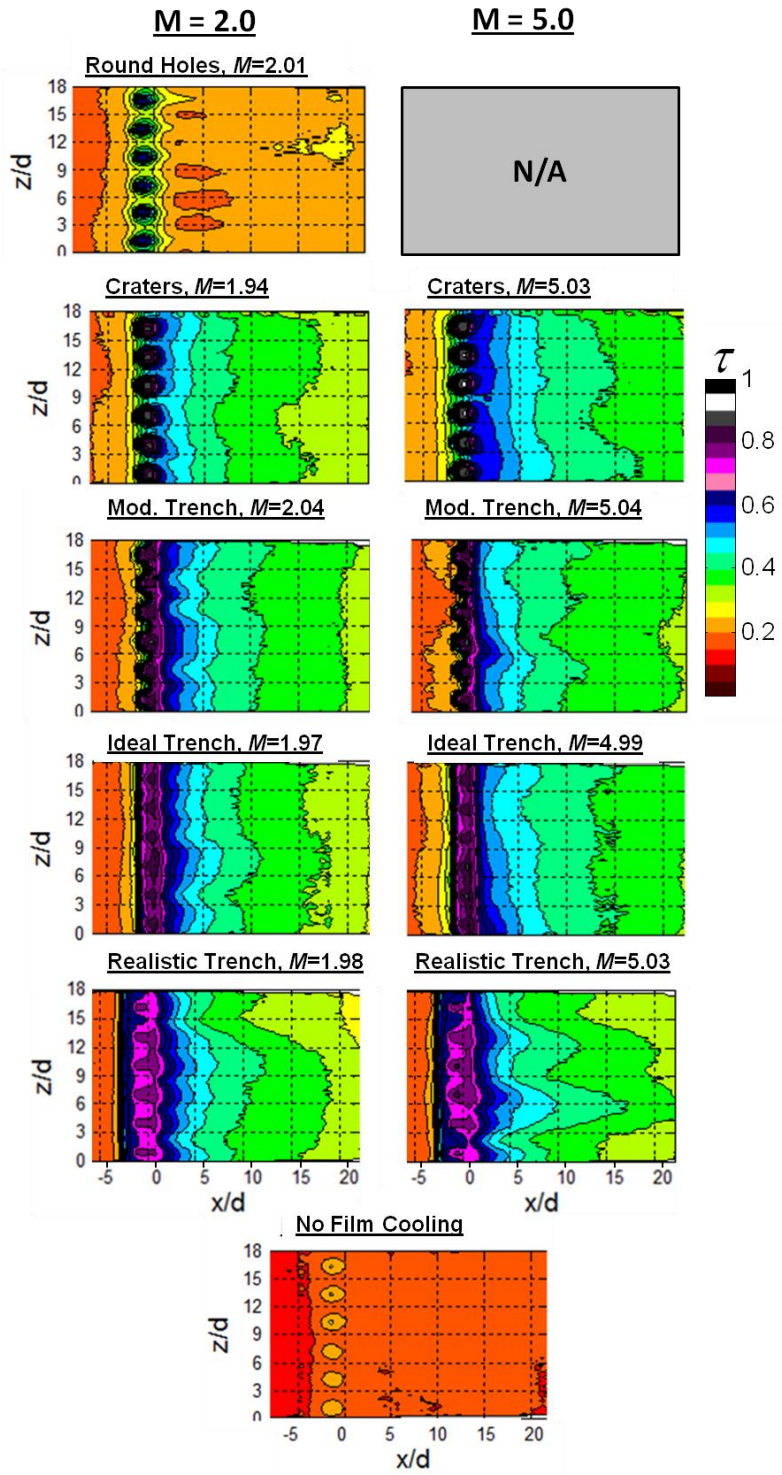

Figure 4.42: Contour plots of τ for varying film cooling designs at $M = 2.0$ and $M = 5.0$ with $t/d = 1.2$ TBC at $Tu = 20\%$.

Chapter 5

5. CONTAMINANT DEPOSITION WITH A THERMAL BARRIER COATING

This chapter will provide a detailed understanding of deposition behavior on a film cooled vane with a thermal barrier coating of thickness t/d = 1.2. The deposition was simulated with the use of molten wax particles that were scaled to match the behavior of coal ash particles in a real engine. Five different film cooling configurations were studied on the pressure side of the vane at a location of s/d = -32. The various configurations were round holes, craters, and three different trenches. The affect of active showerhead film cooling was also studied with the round hole configuration. This work found that the trenches mitigated the growth of deposits more so than any of the other designs. It was also found that heavy depositions accumulated around the discrete film cooling configurations (e.g. round holes) that significantly altered the local surface conditions. However, the depositions were found to improve the film cooling performance of round holes operating at relatively high blowing ratios. This was a result of the depositions accumulating over the top of the round hole exits forcing the coolant jet back to the surface of the vane and promoting jet attachment. Finally, the depositions were shown to improve the cooling performance at the interface of the TBC and vane wall by increasing the thermal resistance between the vane wall and the hot mainstream gas.

5.1. Deposition Results

The cooling performance of a gas turbine component can be detrimentally affected by deposition of contaminants in the hot gas path. The contaminants are often

byproducts of incomplete combustion or debris such as ingested sand or volcanic ash particles. Deposition can accelerate the material degradation of a turbine component by reducing the film cooling performance, increasing the external heat transfer coefficient, promoting chemical attack on the component materials and encouraging spallation of the TBC. Consequently, mitigation of contaminant deposition can greatly improve the life and performance of an engine.

This study investigated the effects of deposition by modeling the molten nature of contaminants in a hot gas path. This was accomplished by spraying molten wax particles into the mainstream flow of the wind tunnel as discussed in Chapter 2. This practice provided contaminant particles that simulated the "stickiness" of contaminants in a real engine. The wax used was Rubitherm RT31, with a relatively low melting temperature of 31°C that allowed for the particles to remain partially molten in the mainstream flow. The size of the wax particles was set in order to properly model the trajectory of real contaminant particles by matching the appropriate range of Stokes number. The focus of the deposition results was on the pressure side of the vane due to the fact that minimal deposition accumulated on the suction side which is consistent with observations of deposition behavior in real engines. Various film cooling configurations including round holes, craters, and the three different trench designs discussed in Chapter 4 were used to assess the effect of altering the film cooling geometry on the behavior of the deposition. All deposition results were obtained at the high turbulence intensity condition of Tu = 20% with an integral length scale of Λ_f = 4 cm. Albert (2011) used the same molten wax technique to simulate deposition on a first stage turbine vane with round hole and trench

film cooling on the pressure side of the vane model. However, Albert's work utilized a wax with a higher melting point of 42°C that yielded lower deposition thicknesses. Albert also did not study the effects of TBC on the resulting deposition behavior.

Figure 5.1 provides a direct comparison of τ and ϕ for an identical vane with and without TBC, respectively. The data with no TBC was collected by Albert (2011). For both cases, the data was obtained by imaging the surface with an IR camera. The difference is that for τ the camera views the surface of the TBC whereas for ϕ with no TBC the camera views the exposed vane wall. It can be easily seen that the addition of TBC results in significantly warmer temperatures on the external surface as compared to when no TBC is present. Albert and Bogard (2011) showed that the deposition behavior on a vane is strongly dependent on the temperature distribution that the simulated contaminant particles encounter. Consequently, it is vital that the surface of the model vane be covered with a simulated TBC in order to accurately model deposition behavior.

The deposition results on the exterior surface of the TBC were recorded with visual and IR cameras. Figure 5.2 and Figure 5.3 show the visual and IR results, respectively, before and after deposition for the non-film cooled model. To obtain the non-film cooled results the coolant holes were plugged with clay. The plugs are not shown in the pre-deposition images of the surface in Figure 5.2. The silver tick marks in the top two panes of Figure 5.2 were separated by 10 mm. The visual pictures show how the deposition characteristics change with variations in *s/d*. The deposition thickness for the case with no film cooling amounted to approximately $t/d = 0.6$ at $s/d = 0$ and $t/d = 1.2$ at $s/d = -34$. The deposition accumulated in a relatively uniform manner in the stagnation

region of the vane. However, near s/d = -34 the deposition began to form individual structures that varied in height by more than 2 mm from peak-to-valley. The deposition characteristics will be discussed in greater detail later in this chapter, including an approximation of the deposition roughness.

Figure 5.3 provides contour plots of τ over the vane surface before and after deposition. These plots represent the non-dimensional surface temperatures between the two lines of silver tick marks shown in Figure 5.2. This provides a means for understanding how the presence of deposition affects the cooling behavior of the vane. For the pre-deposition case, the plugged cooling holes can be seen in these contours. They appear as periodic spots of lower temperature due to the difference in thermal conductivity of the clay in comparison to the cork. Note that the increase in τ values with increasing distance downstream from s/d = -5 to -35 was due to decreasing h_e, as shown by Dees (2010) for a geometrically identical model with no TBC. The behavior of the external heat transfer coefficient was presented in Figure 4.7. After deposition the temperature observed by the IR camera increases, as would be expected. This is due to two factors, the additional insulation provided by the deposition and the increase in h_e caused by increased surface roughness. The relatively random pattern in the post-deposition contour shown in Figure 5.3 is a result of the increased surface roughness.

It should be recognized that the emissivity of the vane coated with wax will be different than when no deposition is present. Consequently, all results for τ post-deposition must be observed with the recognition that the measurement of temperature has greater uncertainty. To understand this effect, IR images were obtained for a constant

temperature body with and without wax deposition. It was found that the presence of the wax increased the perceived temperature by less than 1ºC when the reference temperature of a flat black body was at approximately 12ºC. This was accomplished by cold soaking a cork coupon that was painted flat black and partially covered with wax deposition. The observed variation was used to calculate an expected difference in perceived values for τ on the surface of the TBC. It was found that the presence of wax would decrease τ by approximately $\Delta\tau = 0.03$ at a condition of $\tau = 0.3$. This difference increases the uncertainty in the IR thermography of the TBC surface with deposition. However, the difference is small enough that reasonable comparisons can still be made to determine the effect of deposition on the film cooling performance of the various cooling designs.

Figure 5.4 shows photographs of the vane surface before and after deposition when both the pressure side holes and showerhead were operational at a blowing ratio of $M = 2.0$. The presence of film cooling promoted greater accumulation of deposition on the surface in comparison to the non-film cooled case presented in Figure 5.2. This is true in both the showerhead region as well as near the pressure side row of holes. The deposition thickness for the round holes with an active showerhead measured approximately $t/d = 1.1$ at $s/d = 0$ and $t/d = 3.0$ at $s/d = -32$ as compared to $t/d = 0.6$ and 1.2 for the respective locations with no film cooling. The deposition behavior in the showerhead region shows that the coolant streaks seem to form shallow channels through the surrounding build-up of deposition.

Contour plots of τ before and after deposition for round holes at $M = 2.0$ with an active showerhead at $M_{SH} = 2.0$ are provided in Figure 5.5. Post-deposition, the cooling

performance on the surface of the TBC appears to actually improve immediately downstream of the pressure side cooling holes. At a blowing ratio of $M = 2.0$ the coolant emitting from the pressure side row of round holes is separated from the surface of the vane when no deposition is present. It is suspected that the presence of the deposition arching over the exit of the holes reduces the jet separation and promotes attachment of the coolant, improving the local cooling. The performance of the showerhead, however, dropped off significantly. This is thought to be a result of the coolant no longer spreading easily in the lateral direction and thus not accumulating in the stagnation region.

It's possible that as the wax particles accumulate on the surface they act as an obstruction to the coolant emitting from the various cooling designs. This may reduce the coolant flow rate locally which would divert the coolant to other holes that have not been obstructed as severely. The sprayer in this system directs the majority of the wax particles to accumulate over the middle two-thirds of the vane span. This means that for all film cooling configurations there were holes at either end of the row that were not as severely obstructed by the wax deposits. This may lead to the blowing ratio decreasing locally through holes subjected to heavier deposition while the increasing through holes that were not obstructed. This may produce a negative feedback loop as the cooling configuration gets more and more buried by deposition.

Table 5.1 provides a comparison of point measurements of the deposition thickness at various locations on the pressure side of the vane for all of the different film cooling configurations. The results are expressed in terms relative to the hole diameter,

d. The table shows that the presence of film cooling increased the magnitude of deposition. This is particularly evident at a location of *s/d* = -34 when comparing the no film case to the round hole configurations. However, some of the configurations reduced the deposition growth at *s/d* = -34. The deposition thickness varied from 0.5*d* to 2.0*d* over the majority of the pressure side of the vane for most configurations. This is consistent with deposition thicknesses observed in previous studies for high-temperature engine conditions such as the work completed by Lewis *et al.* (2011). In some instances the deposition thickness exceeded 3*d*. The realistic trench yielded the lowest level of deposition at a location of *s/d* = -44. This is likely a result of altered deposition behavior due to the large structure that accumulated on the downstream lip of the realistic trench. A detailed discussion concerning this behavior for the realistic trench will be provided below.

Table 5.1: Deposition thickness at different locations on the pressure side of the *t/d* = 1.2 TBC vane for varying cooling configurations.

Deposition Thickness (*t*/d)					
s/d	**0**	**-17**	**-34**	**-44**	**M**
No Film (Plugged)	0.6	0.9	1.2	1.2	**0**
Round + SH	1.1	N/A	3.0	N/A	**2.0**
Round + SH, Repeat	1.1	1.2	3.1	1.5	**2.0**
Round	0.6	0.9	2.4	1.2	**0.7**
Craters	0.5	0.9	0.3	1.8	**2.0**
Mod. Trench	0.6	0.9	2.1	2.4	**2.0**
Ideal Trench	0.6	0.9	0.3	1.2	**2.0**
Realistic Trench*	0.4	0.6	0.9	0.6	**2.0**

*Large wax formation at *s/d* = -34 broke away before measurement.

Table 5.1 also shows that the deposition method used in this study had good repeatability in terms of thickness. This may be concluded by looking at the thickness results at s/d = 0 and s/d = -17 for the cases without showerhead holes (SH). From test-to-test, the deposition thickness remained very consistent upstream of the pressure side cooling holes.

Due to the relatively fragile nature of the wax deposits it was not possible to do detailed roughness measurements with a contact profilometer. However, an approximation of the deposition roughness was made at s/d = -17 and s/d = -44 by comparing the point measurements of thickness to the average thickness of adjacent peaks. Given the average separation of the peaks and approximating the rest of the surface as being equal to the point measurements, the centerline average roughness was approximated as $Ra = 0.1d$ at s/d = -17. The average roughness at s/d = -44 was approximated as $Ra = 0.4d$ with variations of $\pm 0.1d$ depending on the configuration. The roughness of the deposits in this study was similar to the high-temperature findings of Lewis *et al.* (2011), albeit slightly rougher.

Figure 5.6 provides photographs before and after deposition for the round holes with no showerhead cooling. In this case the blowing ratio was set to M = 0.7. This blowing ratio was selected in order to assess the behavior of deposition when encountering an attached jet from a round hole. The results were similar to those obtained for the round holes with an active showerhead in which significant accumulation was observed at the location of the pressure side holes, albeit slightly less thick. The deposition thicknesses at s/d = 0 and s/d = -17 were consistent with the non-film cooled

case which is expected since these locations are upstream of the pressure side film cooling holes. Table 5.1 provides greater detail concerning the deposition thicknesses for the round holes configuration.

A comparison of the surface effectiveness, τ, for the round holes at $M = 0.7$ is shown in Figure 5.7. In this case the cooling performance on the surface of the vane is reduced due to the presence of deposition. Unlike the results presented in Figure 5.5, the coolant jets at $M = 0.7$ are attached. Consequently, no film cooling benefit is obtained if the deposition promotes attachment as was the case when the pressure side holes were operated at a blowing ratio of $M = 2.0$. Instead, the obstructions, due to the deposition accumulation, appear to promote mixing of the coolant with the hot mainstream which degrades the performance of τ.

The crater configuration was also studied to determine how well it performed under active deposition. Figure 5.8 shows photographs of the craters before and after deposition. The craters were operated at a blowing ratio of $M = 2.0$ while the deposition accumulated on the surface of the TBC. The post-deposition images show that the craters reduce the tendency for deposition to accumulate immediately downstream of the cooling holes. However, heavy accumulation, with thicknesses approaching $t/d = 2$ was seen within a few diameters downstream of the holes. The deposition also built up in a small ramp immediately upstream of the craters. The effect of these characteristics may be seen in Figure 5.9 which shows that the cooling performance was degraded due to the presence of the deposits. This is likely due to a similar reason for why the performance degraded for the round holes with an attached jet. However, what is different for the

craters is that their discrete nature can still be observed in the contour images post-deposition. This implies that their exit area is relatively clear in comparison to the round holes which were essentially buried by the deposition and lost in the post-deposition contour images.

Photographs of the modified trench before and after deposition at a blowing ratio of $M = 2.0$ are provided in Figure 5.10. Significant accumulation was again observed at the location of the pressure side cooling holes, reaching thicknesses of greater than $t/d = 2$. In this case, the deposition appeared to grow upstream from the downstream lip of the modified trench. However, due to the periodic nature of the modified trench the accumulation was not consistent across the trench lip but rather periodic as well. The deposits accumulated in-line with the round coolant holes feeding the modified trench. The periodic openings in deposition shown in the post-deposition image of Figure 5.10 are in-line with the mid-pitch "tongues" of TBC within the modified trench. This is thought to occur because the coolant emitted from the modified trench tends to peak in cooling performance in-line with the TBC tongues. This may be seen in the pre-deposition contour of Figure 5.11 within a couple holes diameters of the downstream lip of the modified trench. This may imply that a greater amount of coolant tends to emit from these sections of the modified trench and that it has sufficient momentum to keep the mid-pitch regions clear of deposition. Figure 5.11 shows that the accumulation of deposits detrimentally effects the cooling performance in terms of τ for the modified trench.

Figure 5.12 and Figure 5.13 provide the results for the ideal trench. The total accumulation of deposits was noticeably less within 10*d* downstream of the ideal trench as compared to the previously discussed film cooling configurations. Similar to the modified trench, deposition accumulated on the downstream lip of the ideal trench and grew upstream crowding over the opening of the trench. Deposits also accumulated near the upstream lip which led to further blockage over the opening of the trench. This behavior may have promoted greater lateral spreading of the coolant within the trench. This is suggested by the behavior of the deposition shown in the post-deposition image of the full pressure side of the vane in Figure 5.12. A large crescent shape opening to the left is observable in this figure downstream of the ideal trench. The bottom portion of the crescent is coincident with the thermocouple wire that may be seen in the pre-deposition image. The thermocouple wire may have promoted accumulation of deposits on the surface locally. Consequently, the presence of the lower portion of the crescent should be ignored. However, the upper portion of the crescent is not coincident with a wire or any other physical feature on the TBC surface. It is thought that the increased obstruction, due to the accumulation of deposits crowding the exit of the trench, forced more coolant to move laterally. This may have resulted in a spanwise component to the coolant once it emitted from the ideal trench. The crescent shape in the surface deposits may have been a result of this spanwise component. Figure 5.13 shows that the accumulation of deposits reduces the cooling performance downstream of the ideal trench in a similar manner as the other configurations.

The realistic trench was also tested to determine how it would perform under active deposition. The realistic trench was different from the ideal trench due to the increased width, w/d = 3.8 as opposed to w/d = 2, and the rounding of the trench lip. Figure 5.14 provides photographs of the realistic trench before and after deposition. Unfortunately, only a few pictures were taken of the realistic trench without deposition. Consequently, the pictures used in Figure 5.14 are not the ideal perspectives in order to compare the TBC surface before and after deposition. The deposition behavior of the realistic trench was characterized by significant accumulation of deposits on the downstream lip of the trench. This accumulation likely measured over 4d growing at an angle over the trench as the structure increased in thickness. The rounded lip of the realistic trench may have provided greater area upon which a wax structure could build allowing for larger accumulations in comparison to the sharp lips of the other trench designs. The large wax structure broke off of the realistic trench lip before still photographs could be captured. Similar spallation behavior has been observed under real engine conditions such as the work of Webb *et al.* (2011). The IR camera captured evidence of this large accumulation since it was taken prior to stopping the tunnel at which point the visual photographs are obtained. Figure 5.15 shows evidence of the large accumulation nearly covering the opening of the realistic trench for $0 < z/d < 6$. The accumulation did not grow parallel to the surface but rather at an angle off the surface; consequently, the IR images cannot be used as a direct measure of the total size of the structure. It is likely that the presence of this structure affected the behavior of the deposition further downstream. The photographs in Figure 5.14 show that much of the

surface downstream of the realistic trench was relatively clear of deposits. It is possible that this was a result of the large structure that accumulated on the downstream lip of the trench. Looking again at Figure 5.15 it is evident that the coolant was directed into a single region, much more so than any of the other configurations. The increased amount of coolant within a relatively small area may have reduced the ability for contaminants to adhere to the surface. The reduced accumulation may have also been a result of the large structure altering the streamlines of the local flow in such a way that the contaminants did not make contact with the vane wall. Finally, a small amount of deposition was observed to have accumulated within the realistic trench. The ideal trench had negligible growth of depositions within the trench. This difference is likely a result of the increased width of the realistic trench.

Figure 5.16 – Figure 5.21 provide laterally averaged surface temperatures on the exterior surface of the TBC, normalized as τ, for varying film cooling designs before and after deposition. The results are also compared to the cooling performance of the non-film cooled model with a TBC and no deposition present. The results quantify the difference in film cooling performance before and after deposition. Figure 5.16 emphasizes how the deposition increases the cooling performance of the round holes at a blowing ratio of $M = 2.0$. Again, this is thought to be a result of the deposition forcing the coolant jets to remain attached to the TBC surface. In most other cases, the laterally averaged effectiveness declined to a similar level due to the accumulation of deposits on the surface, while the realistic trench performed the worst. This fact, that the laterally averaged performance nearly collapses despite cooling configuration, suggests that the

difference in deposition behavior seen for most of the designs has only a minimal effect on the final performance. This is not necessarily true for the realistic trench whose performance was dominated by the accumulation of a significantly larger wax structure as compared to the deposition growth observed for any of the other designs. It should be remembered that the measurement of τ after deposition has greater uncertainty due to the altered emissivity of the surface, as previously discussed.

It should be recognized that the data presented for the round holes in Figure 5.16 have an active showerhead. This results in a slight increase of τ upstream of the coolant holes; at s/d = -25, τ = 0.20 as compared to τ = 0.16 for cases without an active showerhead. This is not the case for the other configurations. Comparisons of effectiveness results for the round holes found that the presence of the showerhead did little to change cooling performance behavior at the location of the pressure side holes over a wide range of blowing ratios. This may suggest that the deposition behavior would be the same despite operation of the showerhead and thus allow for direct comparison of Figure 5.16 – Figure 5.21. The weakness in this argument is that the streamlines upstream of the pressure side row of holes will be affected by the presence of showerhead film cooling. This may alter the trajectory of the wax particles and yield different deposition behavior with and without showerhead cooling. It should also be recognized that the location of the pressure side cooling holes appears to be different for the round holes in comparison to the other configurations. This is a result of the round holes maintaining their angular path through the entire layer of TBC. This may be clearly

seen in Figure 2.8 which shows that the centerline of the round holes at the point of break out is further to the left in comparison to the other configurations.

Figure 5.22 – Figure 5.26 provide comparisons of the cooling performance, ϕ, at the interface of the TBC and vane wall before and after deposition. In all cases, the accumulation of deposits on the surface of the TBC led to an increase in ϕ over the region of $-32 < s/d < 0$, i.e. a decrease in the metal temperature at the TBC interface. This was a result of the deposits increasing the thermal resistance on top of the vane wall surface. This affect was muted downstream of the film cooling holes for most of the cooling configurations likely due to the detrimental effects deposition has on external film cooling performance and heat transfer coefficient. The trench configurations appeared to mitigate the growth of deposits downstream of $s/d = -32$ which would have limited the amount of increase in thermal resistance that the deposits could provide. This may have been another factor in why the trenches had minimal change in ϕ before and after deposition. The presence of deposition resulted in a significant improvement in overall effectiveness, ϕ, for the round holes with an active showerhead. This is due to the fact that the deposition promoted jet attachment downstream of the pressure side round holes. Furthermore, the active showerhead encouraged additional contaminant deposition that increased the thermal resistance of the vane over the region of $-32 < s/d < 0$.

The above conclusions concerning ϕ before and after deposition hinge on whether or not the wax thermally scales to the properties of the contaminants in a real engine. This can be studied by determining whether or not the ratio of the thermal conductivities

of the deposition and vane are the same between the engine and experimental model. The TBC conductivity can also be used as the reference, instead of the vane. These ratios can be expressed as

$$\left.\frac{k_{deposit}}{k_{vane\ wall}}\right|_{model} = \left.\frac{k_{deposit}}{k_{vane\ wall}}\right|_{engine} \tag{5.1}$$

or

$$\left.\frac{k_{deposit}}{k_{TBC}}\right|_{model} = \left.\frac{k_{deposit}}{k_{TBC}}\right|_{engine} \tag{5.2}$$

The thermal conductivity of the deposit for the model and engine will of course be different. The deposits for the experimental model were assumed to be wax structures with 60% volumetric porosity comprised of air, as discussed by Albert (2011). The effective thermal conductivity, k_{eff}, of the wax structures can be estimated by

$$k_{eff} = Pk_{gas} + (1 - P)k_{solid} \tag{5.3}$$

where P is the porosity of the two phase material. The conductivity of the wax in solid state is k_{solid} = 2 W/m-K according to the RT-31 data sheet provided by Rubitherm® (2009). The pores within the wax structure were assumed to be filled with air at 273 K yielding a gaseous thermal conductivity of k_{gas} = 0.024 W/m-K. The effective thermal conductivity of the wax structures, as defined by Equation (5.3), was then calculated to be k_{eff} = 0.09 W/m-K. Zbogar *et al.* (2005) provide a detailed discussion concerning various models that can be used to estimate the thermal conductivity of multiphase materials.

The deposits in the engine were assumed to be primarily coal ash. Rezaei *et al.* (2000) reported the thermal conductivity of coal ash under a variety of conditions. The results showed that the thermal conductivity of coal ash can vary from k_{ash} = 0.5 – 2.3 W/m-K depending on temperature, chemical constituents, and porosity. For the purpose of this analysis the thermal conductivity of coal ash was assumed to be k_{ash} = 1.5 W/m-K at a temperature of 1200°C. Equations (5.1) and (5.2) can then be solved yielding

$$\left.\frac{k_{deposit}}{k_{vane\ wall}}\right|_{model} = \left.\frac{0.09}{1}\right|_{model} = 0.09\ , \qquad \left.\frac{k_{deposit}}{k_{vane\ wall}}\right|_{engine} = \left.\frac{1.5}{20}\right|_{engine} = 0.08 \tag{5.4}$$

and

$$\left.\frac{k_{deposit}}{k_{TBC}}\right|_{model} = \left.\frac{0.09}{0.064}\right|_{model} = 1.5\ , \qquad \left.\frac{k_{deposit}}{k_{TBC}}\right|_{engine} = \left.\frac{1.5}{1}\right|_{engine} = 1.5 \tag{5.5}$$

The thermal conductivities for the vane wall and TBC were taken as nominal values from the more detailed discussion provided in Chapter 2. The resulting ratios show that the wax deposits in the experimental setup should accurately model the thermal behavior of deposits in a real engine. Consequently, the post-deposition results for overall effectiveness, ϕ, should be representative of the performance in a real engine.

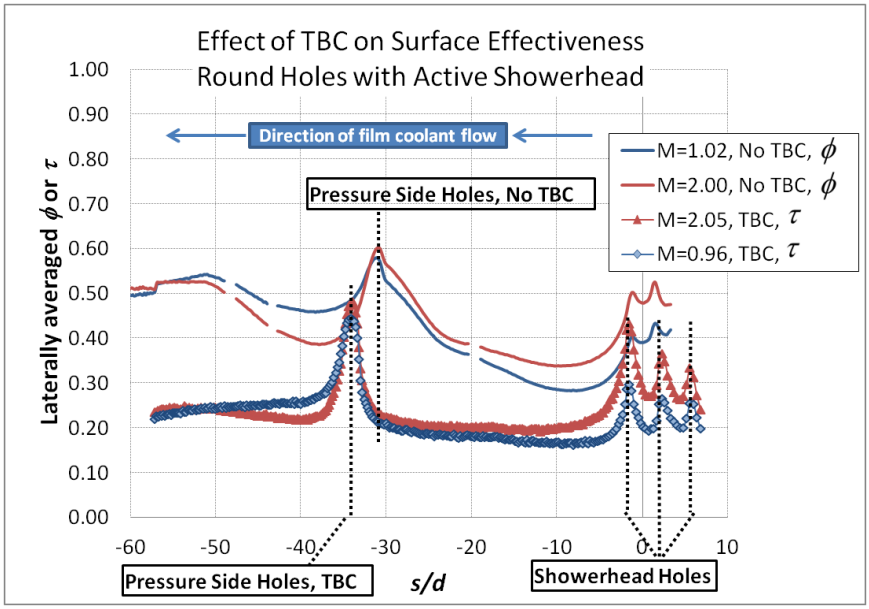

Figure 5.1: Comparison of laterally averaged surface effectiveness with and without TBC, τ and ϕ, respectively.

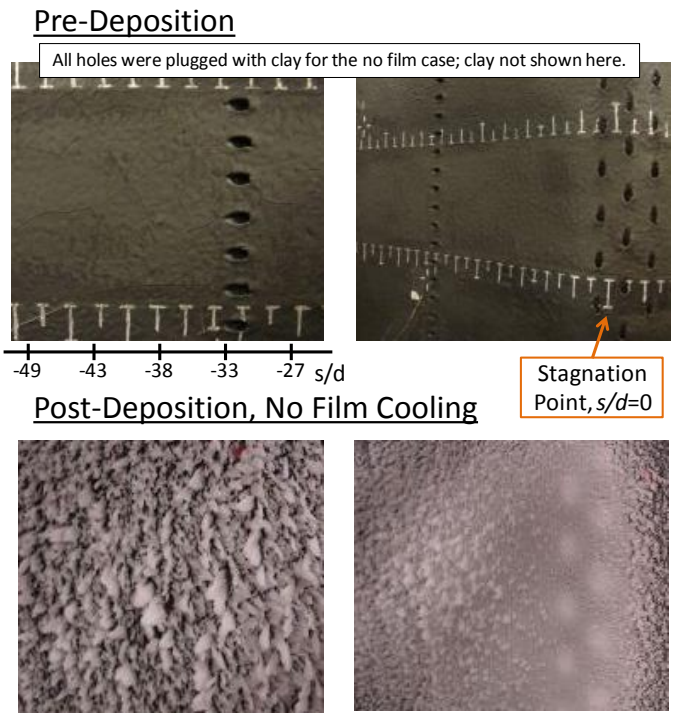

Figure 5.2: Photographs of vane surface before and after deposition with no film cooling.

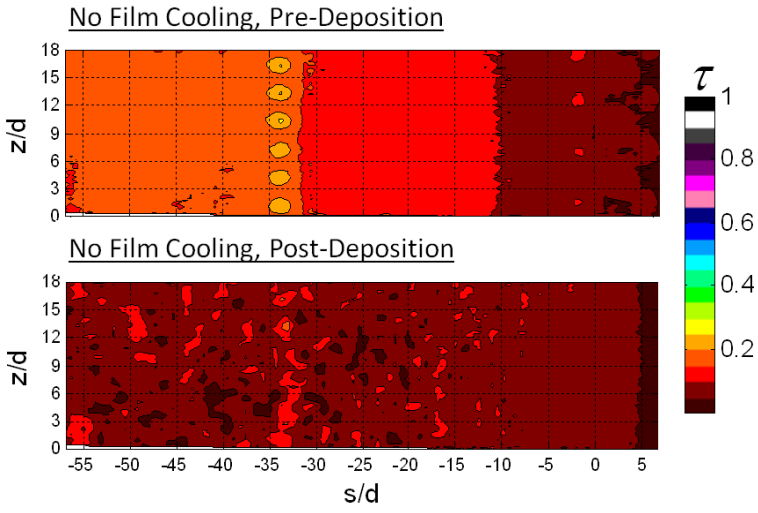

Figure 5.3: Contour plots of τ for vane with no film cooling before and after deposition.

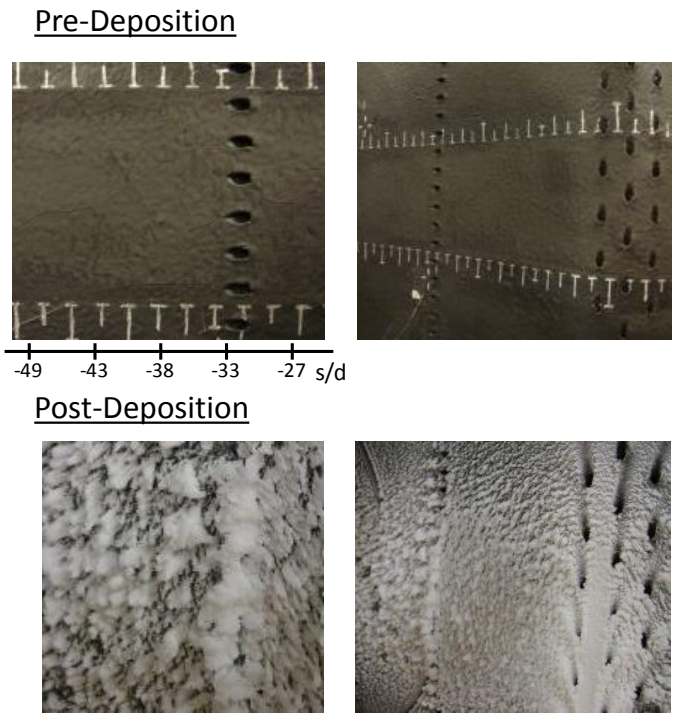

Figure 5.4: Photographs of vane surface before and after deposition for round holes at M = 2.0 and M_{SH} = 2.0.

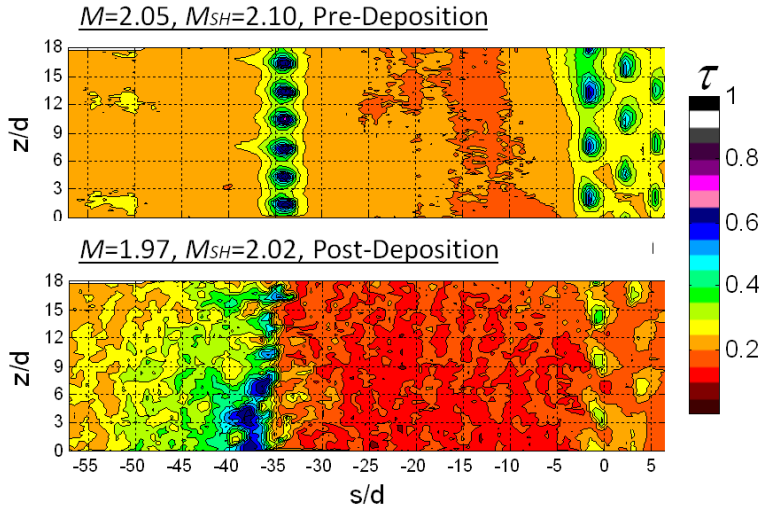

Figure 5.5: Contour plots of τ for round holes at M = 2.0 and M_{SH} = 2.0 before and after deposition.

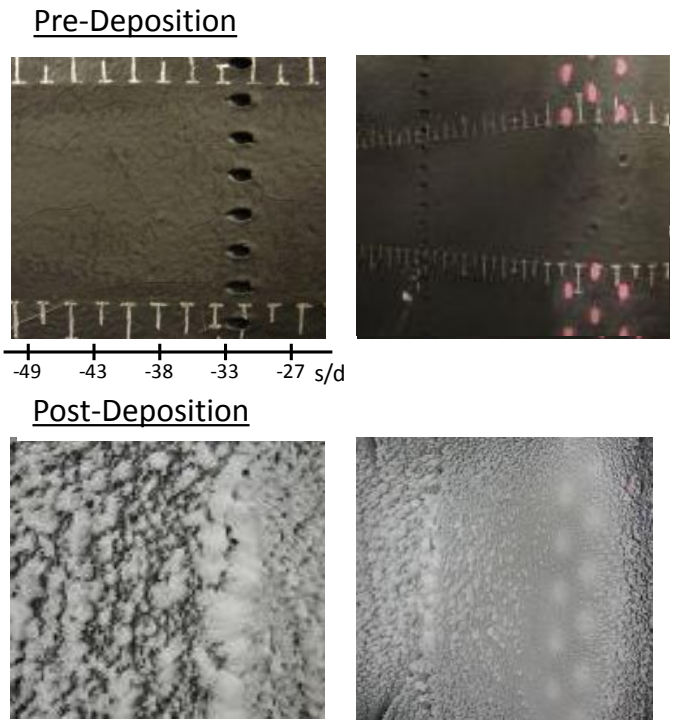

Figure 5.6: Photographs of vane surface before and after deposition for round holes at M = 0.7 with no showerhead cooling.

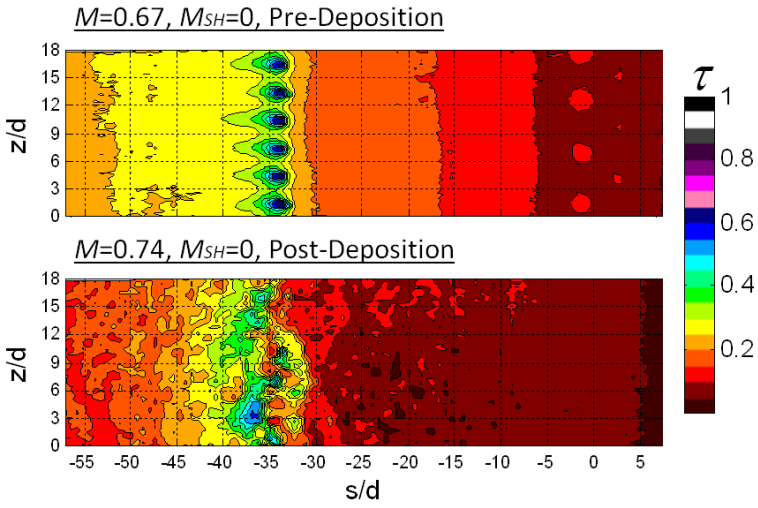

Figure 5.7: Contour plots of τ for round holes at M = 0.7 before and after deposition with no showerhead cooling.

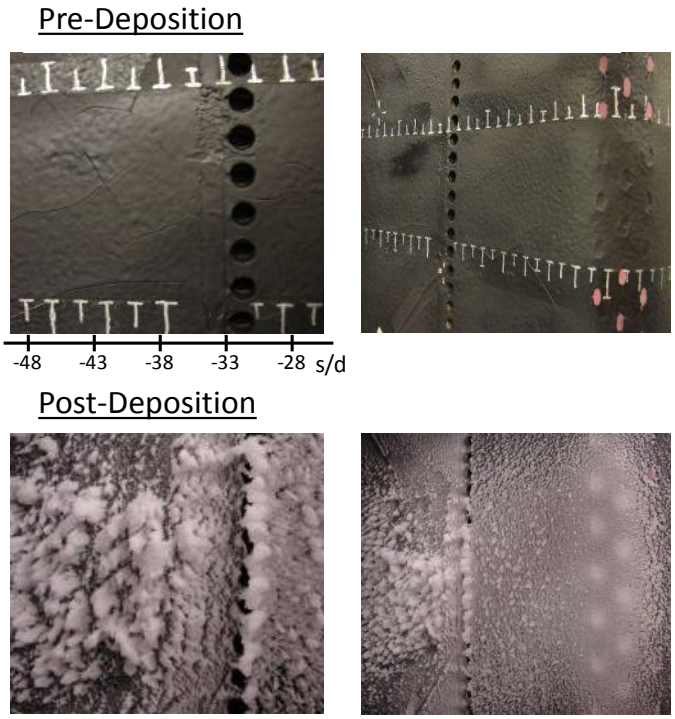

Figure 5.8: Photographs of vane surface before and after deposition for craters at $M = 2.0$ with no showerhead cooling.

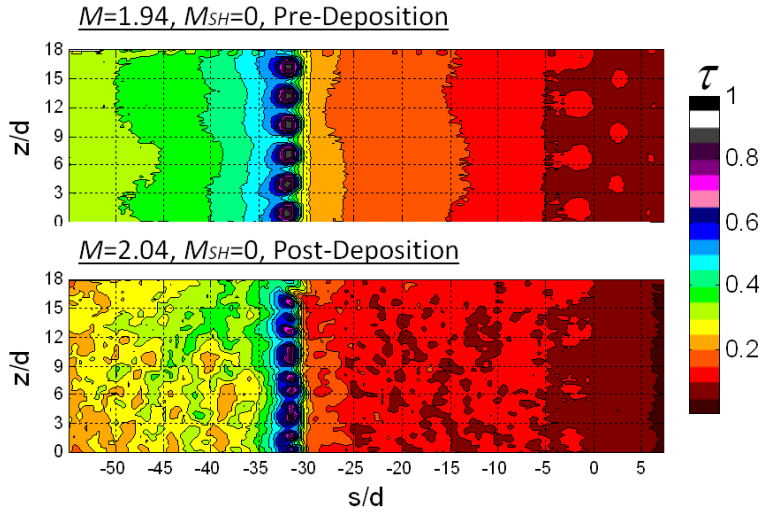

Figure 5.9: Contour plots of τ for craters at $M = 2.0$ before and after deposition with no showerhead cooling.

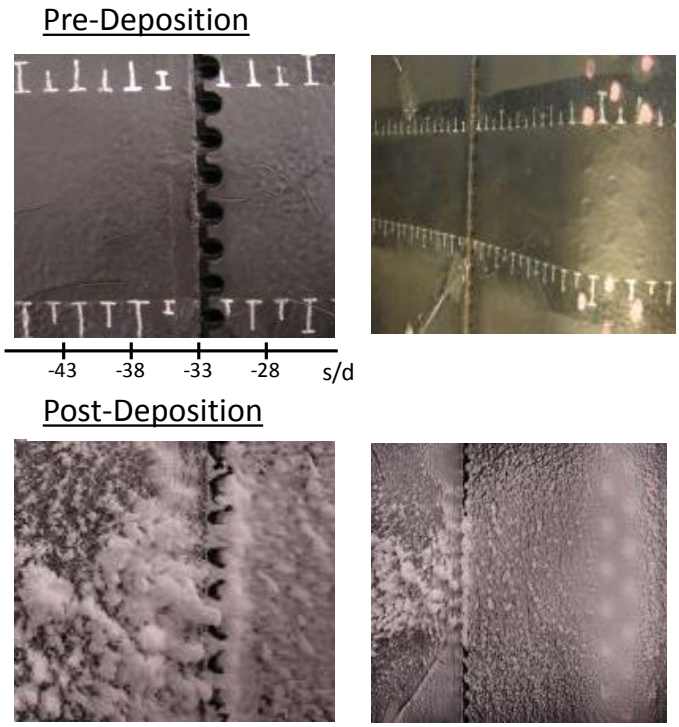

Figure 5.10: Photographs of vane surface before and after deposition for a modified trench at $M = 2.0$ with no showerhead cooling.

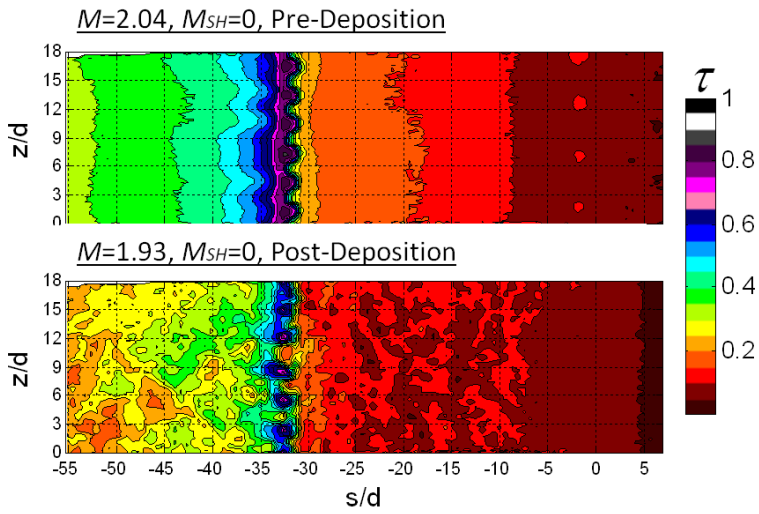

Figure 5.11: Contour plots of τ for a modified trench at $M = 2.0$ before and after deposition with no showerhead cooling.

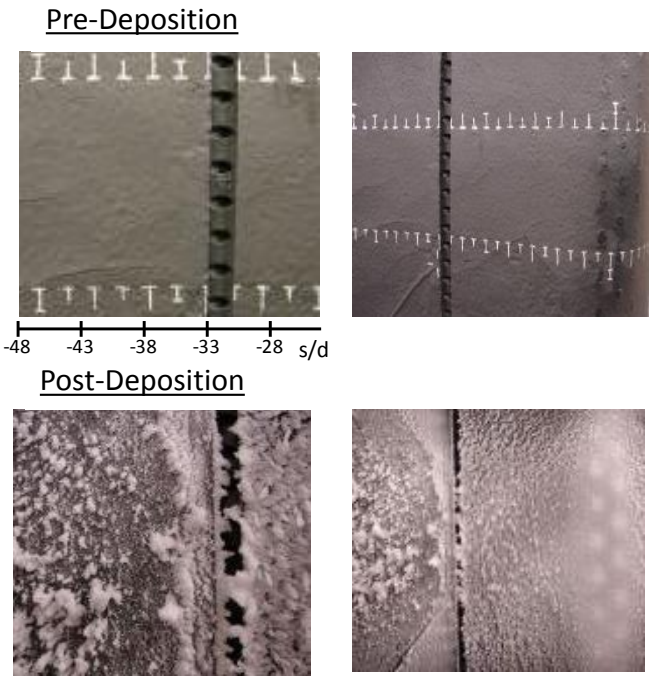

Figure 5.12: Photographs of vane surface before and after deposition for an ideal trench at $M = 2.0$ with no showerhead cooling.

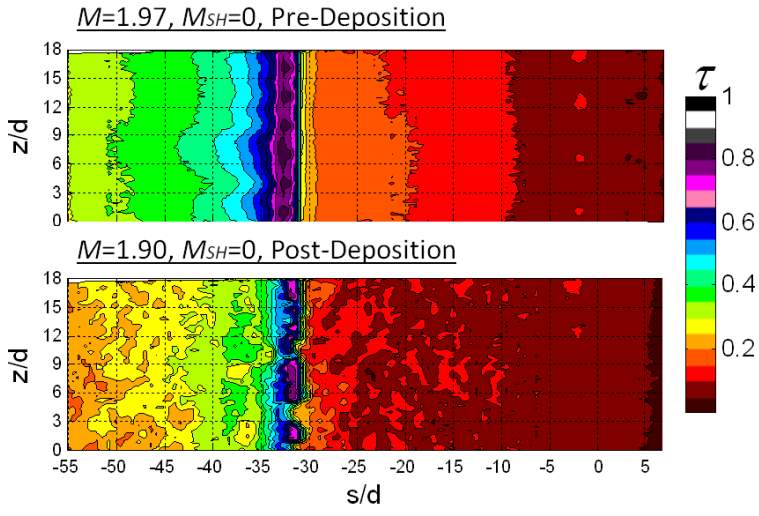

Figure 5.13: Contour plots of τ for an ideal trench at $M = 2.0$ before and after deposition with no showerhead cooling.

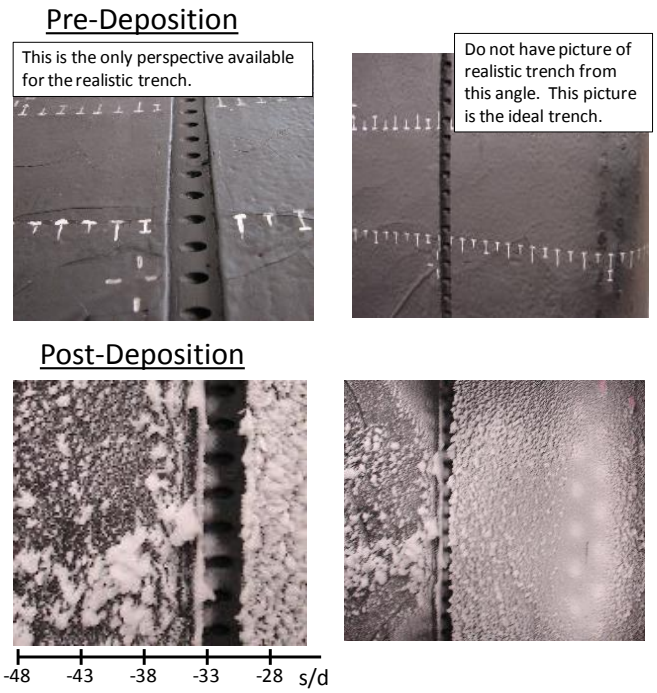

Figure 5.14: Photographs of vane surface before and after deposition for a realistic trench at $M = 2.0$ with no showerhead cooling.

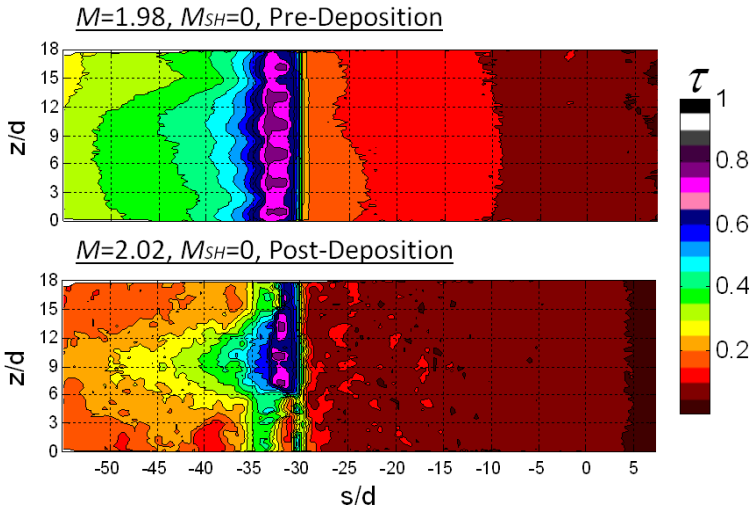

Figure 5.15: Contour plots of τ for a realistic trench at $M = 2.0$ before and after deposition with no showerhead cooling.

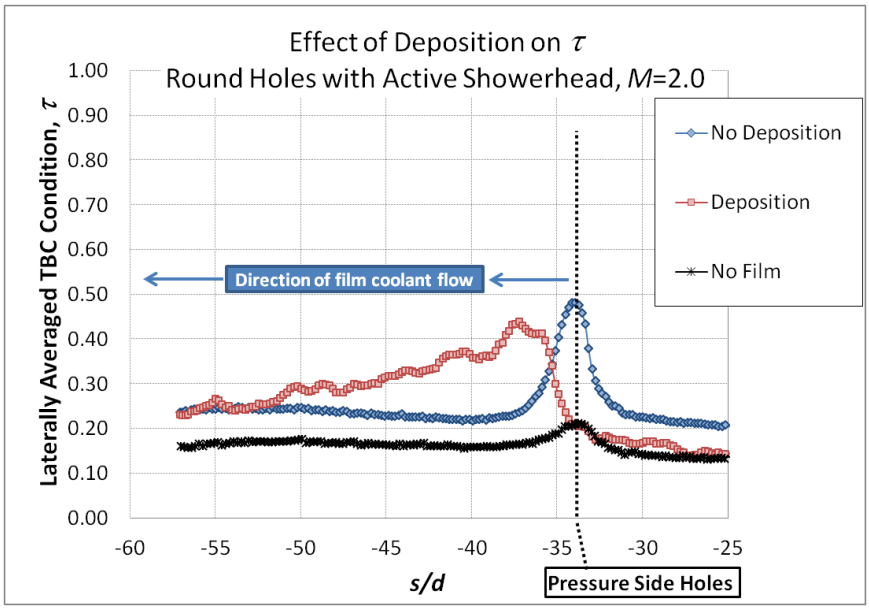

Figure 5.16: Effect of deposition on τ for round holes with an active showerhead at M = 2.0 and t/d = 1.2 TBC.

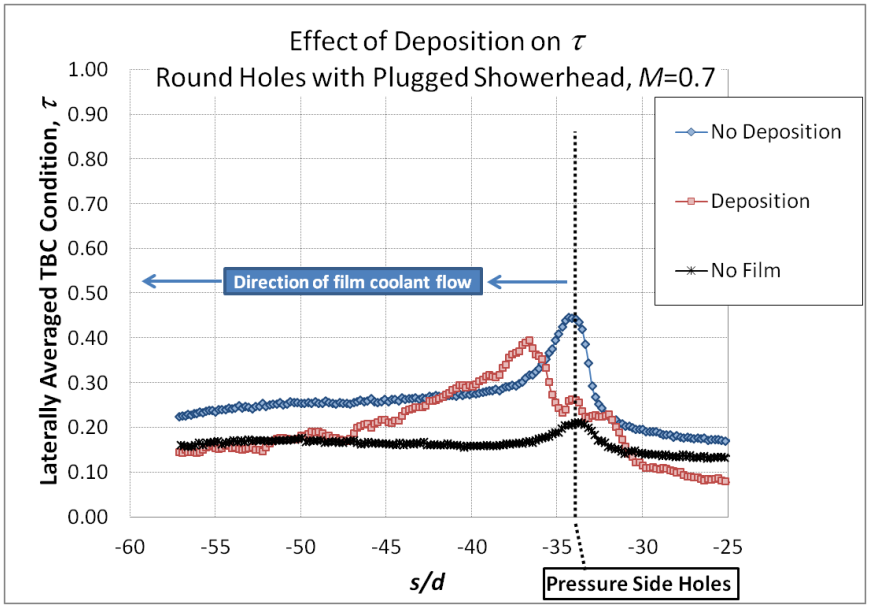

Figure 5.17: Effect of deposition on τ for round holes at M = 0.7 with no showerhead cooling and t/d = 1.2 TBC.

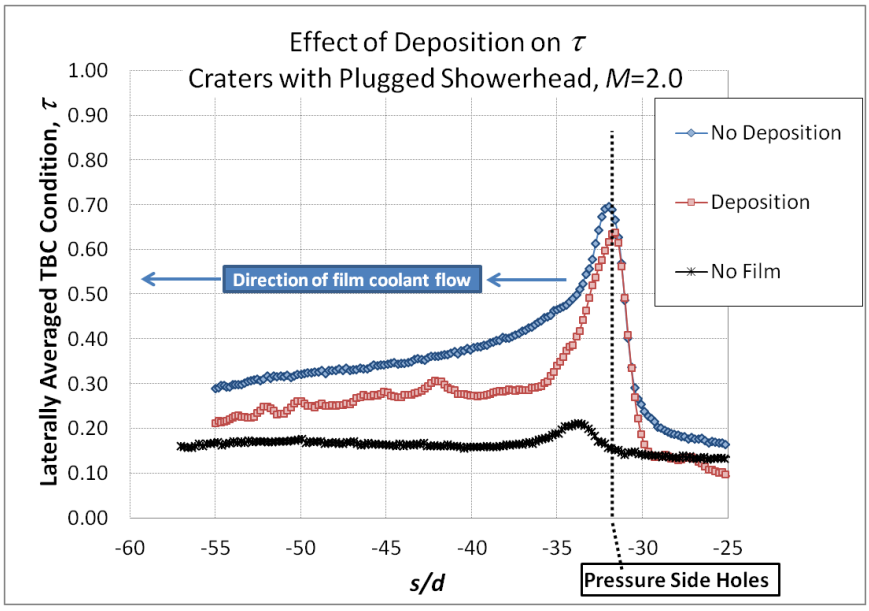

Figure 5.18: Effect of deposition on τ for craters at $M = 2.0$ with no showerhead cooling and $t/d = 1.2$ TBC.

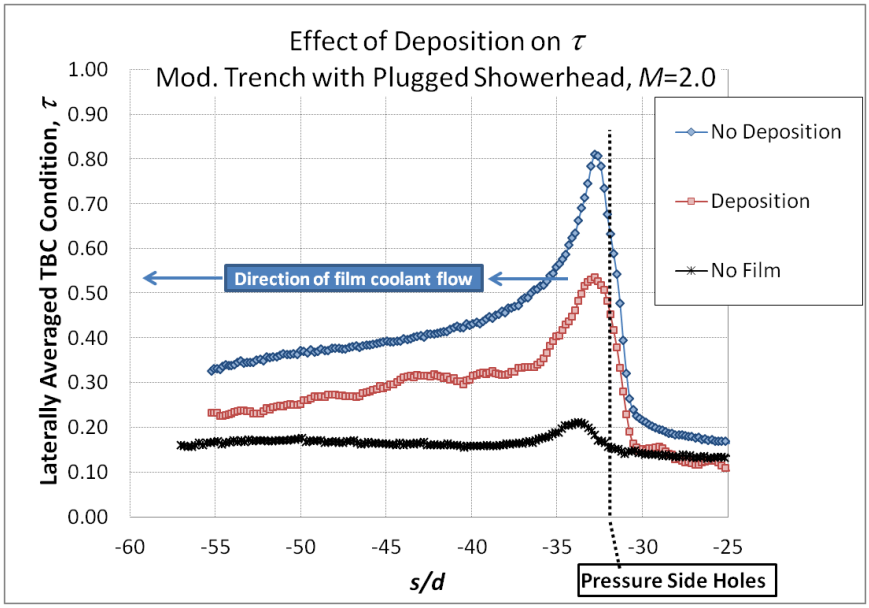

Figure 5.19: Effect of deposition on τ for a modified trench at $M = 2.0$ with no showerhead cooling and $t/d = 1.2$ TBC.

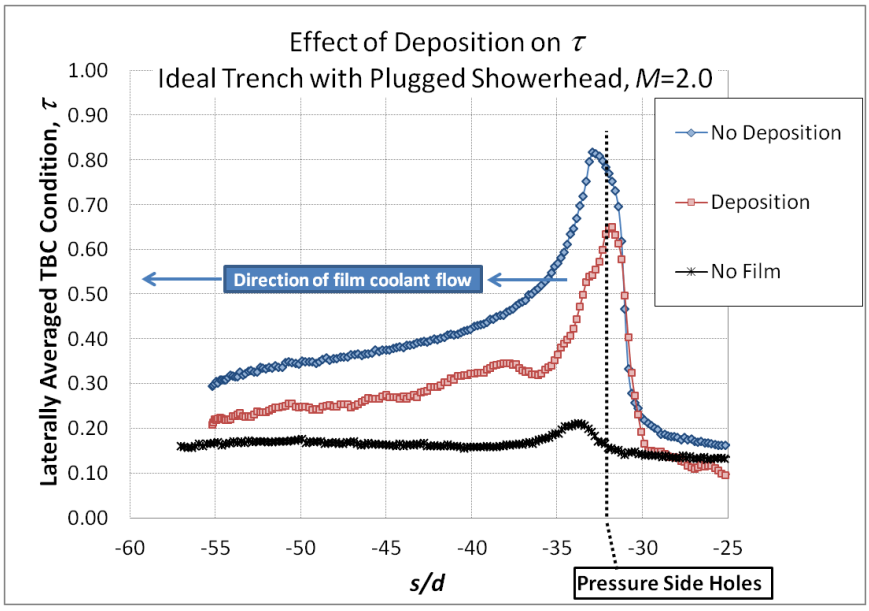

Figure 5.20: Effect of deposition on τ for an ideal trench at $M = 2.0$ with no showerhead cooling and $t/d = 1.2$ TBC.

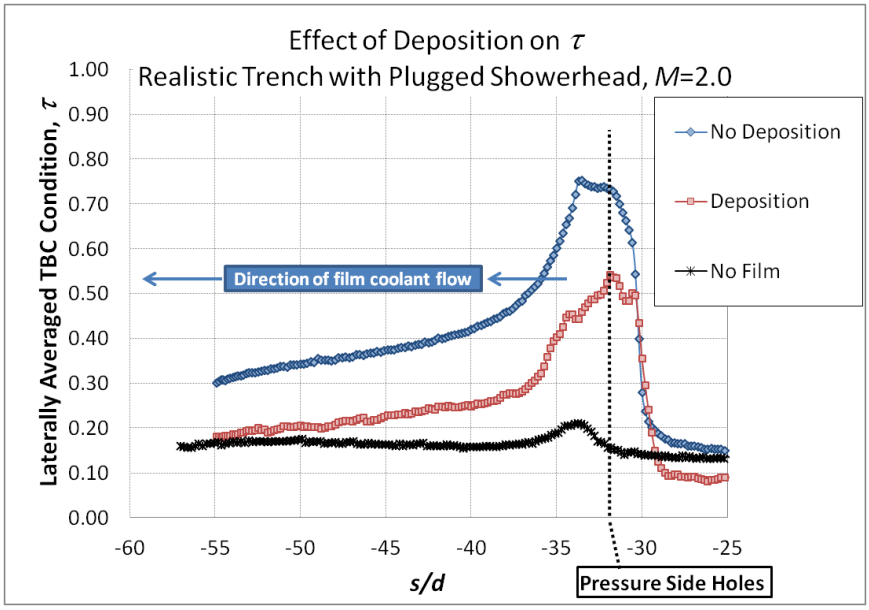

Figure 5.21: Effect of deposition on τ for a realistic trench at $M = 2.0$ with no showerhead cooling and $t/d = 1.2$ TBC.

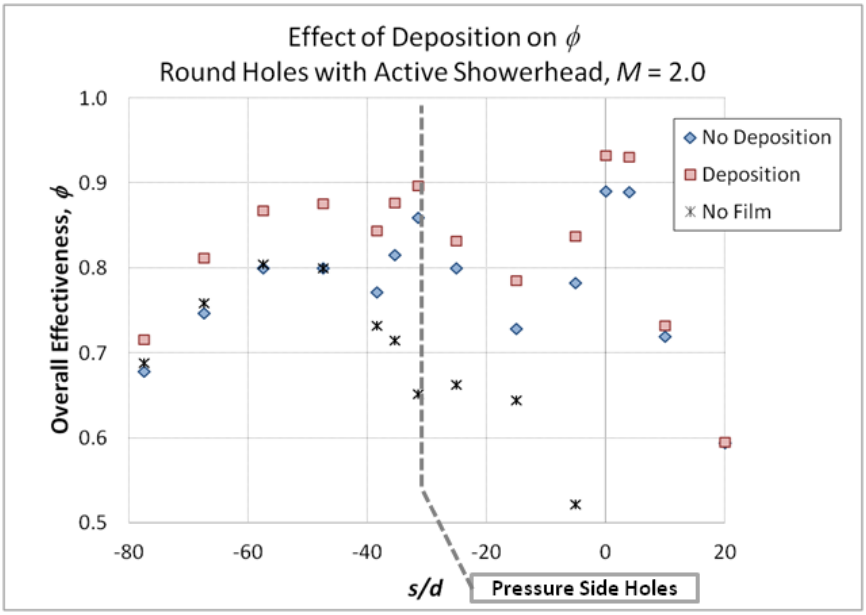

Figure 5.22: Effect of deposition on ϕ for round holes with an active showerhead.

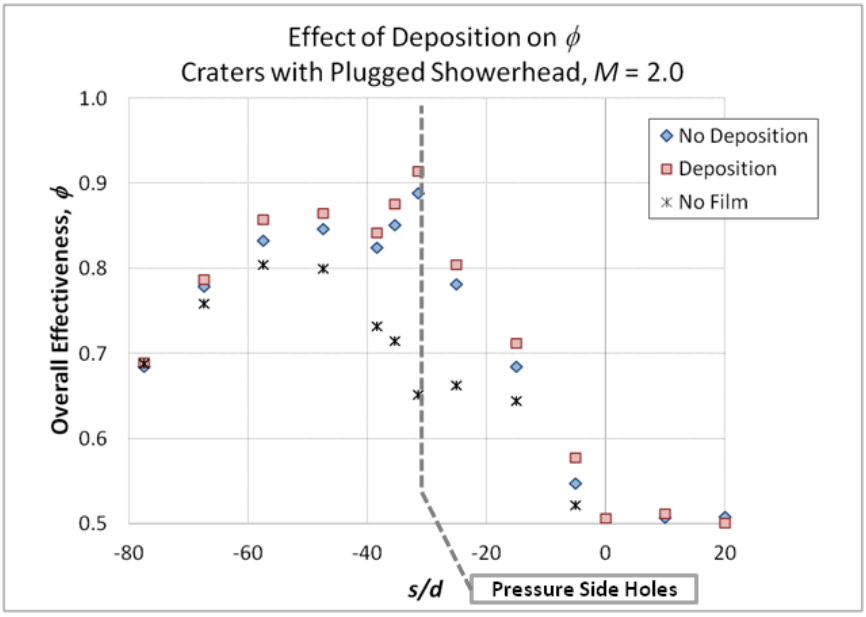

Figure 5.23: Effect of deposition on ϕ for craters with no showerhead cooling.

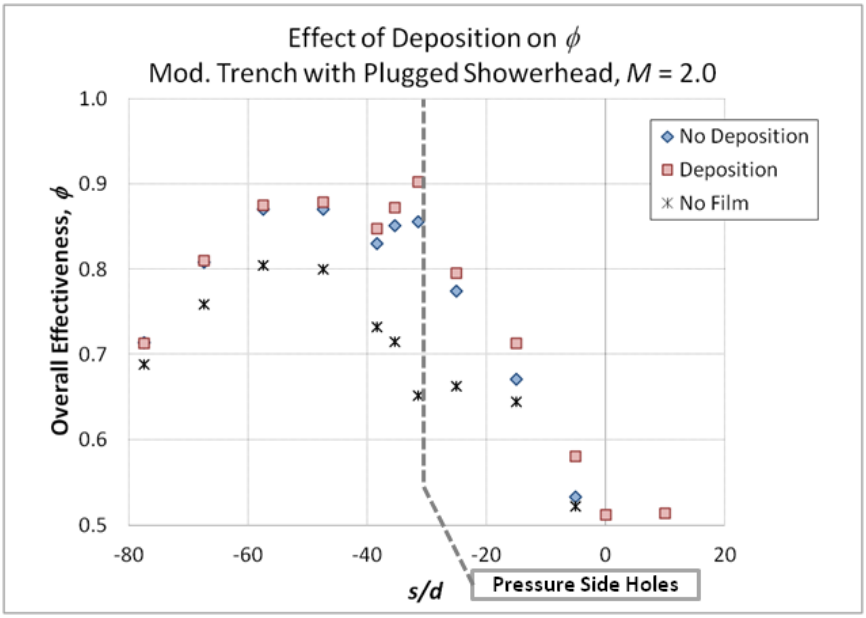

Figure 5.24: Effect of deposition on ϕ for a modified trench with no showerhead cooling.

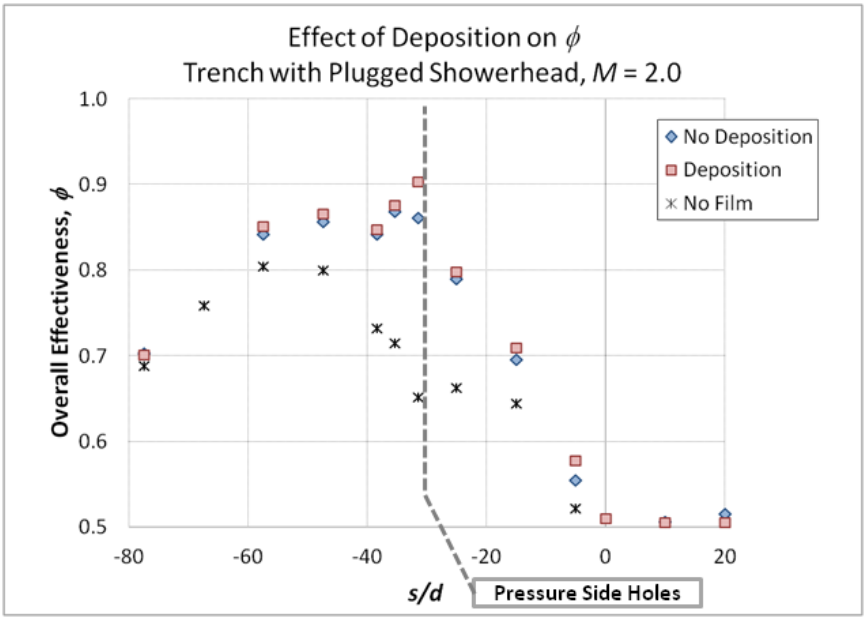

Figure 5.25: Effect of deposition on ϕ for an ideal trench with no showerhead cooling.

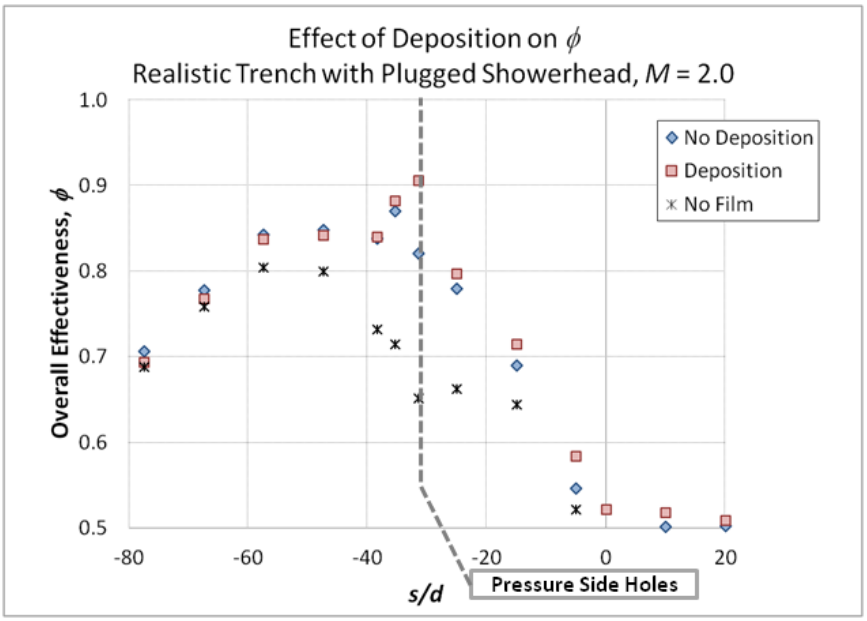

Figure 5.26: Effect of deposition on ϕ for a realistic trench with no showerhead cooling.

Chapter 6

6. CONCLUSIONS

The purpose of this chapter is to provide an overview of the important conclusions that can be drawn from this study. In summary, the work presented herein has provided measurements of cooling performance for a realistic first-stage vane with a thermal barrier coating. This work studied the thermal behavior of a vane with TBC and film cooling with various configurations in great detail. A novel modified trench design has also been proposed. The thermal behavior of the vane was observed with active contaminant deposition resulting in post-deposition measurements of vane metal temperatures with a TBC. Various film cooling configurations were studied with active deposition. This provided an understanding of whether or not trench film cooling can mitigate the growth of deposits on a turbine vane with a TBC. Much of this data is the first of its kind to be reported in the open literature.

The collection of this data has allowed for improved understanding of the thermal behavior of a first-stage vane employing realistic thermal protection techniques. The impact of this can be realized by recognizing that minor improvements in our understanding of the thermal behavior in a real engine can lead to substantial cost savings. For instance, a 1% improvement in domestic gas turbine efficiency would save over 5 million barrels of oil used for jet fuel annually. Furthermore, it would save over 70 billion cubic feet of natural gas per year used for electricity generation. This would result in annual savings approaching $1 billion dollars. The numbers expressed here are a reflection of the data presented in the 2010 U.S. Energy Information Administration's

Annual Energy Review. A small increase in combustor temperature of 30 - 50°C would be sufficient to increase engine efficiency by 1%, assuming a typical engine operating under ideal conditions. Consequently, minor improvements in our understanding of the thermal behavior of an engine can have dramatic results. The conclusions from this study should facilitate improved engine designs that may rely heavily on TBC's in order to safely operate while pushing combustor temperatures ever higher in the pursuit of increased efficiency.

6.1. Summary of Objectives and Conclusions

A summary of the objective and conclusions for this study are presented here:

1.) Determine how round hole film cooling and internal convective cooling affect the cooling performance of a vane with a thermal barrier coating.

- Convective cooling, both internal convection and in-hole convection, is the dominant factor for cooling a vane wall with a TBC.
- Overall effectiveness nearly collapses despite changes in blowing ratio.
- TBC significantly improves thermal protection.

2.) Determine how the cooling performance of a vane with a TBC is altered due to changes in the film cooling configuration.

- Changing the film cooling configuration does little to alter overall effectiveness.
    - Simple cooling designs may be advantageous in order to reduce cost.

3.) *Compare the cooling performance of an ideal and realistic trench.*

- Trenches improve cooling performance on the exterior surface of the TBC.
- The trench design discussed in this study is susceptible to heating within the trench due to the removal of TBC (this emphasizes the negative impact of TBC spallation).
- The realistic trench does poorly at low blowing ratios.

4.) *Provide detailed temperature measurements at the interface of the TBC and vane wall as well as on the external surface of the TBC.*

- Temperature behavior at the interface of the TBC and vane wall was observed and provided the insight for the conclusions above.

5.) *Develop an analytical model for predicting the thermal behavior of a film cooled vane with a TBC.*

- A simplified analytical model was derived for both overall effectiveness and TBC condition.
- The models perform well for two cases, no film cooling and away from the holes when active film cooling is utilized.
    - The models do not predict the 3-D nature of heat transfer near the film cooling holes.

6.) *Develop a molten wax deposition method that simulates heavy loading of contaminants in the hot gas path of an engine.*

- A low cost method for simulating heavy contaminant deposition was developed.

7.) *Determine how active contaminant deposition alters the thermal behavior of a film cooled vane with a TBC.*

- The presence of contaminant deposition detrimentally effected film cooling performance, in most cases.
- The contaminant deposition increased the thermal resistance of the vane and resulted in improved cooling performance at the interface of the TBC and vane wall.

8.) *Identify a film cooling configuration that is capable of mitigating the growth of deposition on the surface of the turbine component.*

- Trenches mitigate contaminant growth more so than the other configurations examined in this study.

6.2. Effect of TBC

This study has provided the only experimental data available in the open literature that quantifies the overall effectiveness of a film cooled conducting vane with a TBC. This was accomplished by testing a matched Biot number vane with a modeled TBC while measuring the temperature at the interface of the vane wall and TBC layer with discrete thermocouples. Two different TBC thicknesses were investigated, $t/d = 0.55$ and

1.2. A variety of film cooling geometries were tested during this study. The large majority of previous film cooling studies have implemented an adiabatic wall condition. The adiabatic wall method makes it impossible to understand the conjugate heat transfer effects of a film cooled vane with a TBC. Consequently, the use of the matched Biot number model has made it possible to study the effect of TBC's. A baseline configuration of round holes was tested on both the suction side and the pressure side of the vane. A t/d = 0.55 deep trench was tested on the suction side of the vane. The pressure side round holes were tested with and without active cooling from a dense array of film cooling holes in the stagnation region of the vane (i.e. showerhead film cooling). Craters, an ideal trench, a modified trench, and a realistic trench were tested on the pressure side of the vane with a t/d = 1.2 TBC. It was found that the thermal protection provided by the TBC often overshadowed the effect of changing film cooling configurations or altering blowing ratio. This behavior was not predictable based on a simplified 1-D heat transfer analysis of the system, as will be discussed later. The experiments showed that the overall effectiveness, ϕ, was nearly independent of blowing ratio for round hole film cooling. This is in stark contrast to results obtained by Albert (2011) who showed the overall effectiveness with no TBC decreased by 20% when the blowing ratio was increased from M = 1 to 3 for round hole film cooling. Albert (2011) also showed that the adiabatic effectiveness varied significantly with changes in the blowing ratio. Dees (2010) showed similar behavior. Albert's and Dees' results may lead an individual to concluding that the blowing ratio would have a strong effect on the overall effectiveness of a vane with a TBC when, in reality, this effect is significantly

dampened. It was also observed that the cooling performance of the vane appeared to be strongly affected by in-hole convection and internal convection. The fact that the overall effectiveness was nearly independent from changes in blowing ratio for the round holes may be a result of the increased in-hole convection offsetting the detrimental effect of jet separation at higher blowing ratios.

All of the cooling designs showed very similar performance in terms of overall effectiveness at $M = 1.0$. This is the only study available in the open literature that has been able to make this measurement. The craters, ideal trench, and modified trench designs all showed higher external TBC conditions, τ (i.e. colder external TBC surface temperatures), in comparison to the round holes. It should be recognized that increasing τ is not necessarily advantageous. For instance, one could improve τ by decreasing the thickness of the TBC. However, this would result in increased vane wall metal temperatures which could be very detrimental to the long-term life of the turbine component. Increasing τ with improved film cooling performance is advantageous if the engine is operated at a temperature significantly above the maximum allowable operating temperature of the TBC. This will allow the TBC to protect the metal of the vane wall while utilizing film cooling to protect the external surface of the TBC. These effects are, of course, not entirely independent of one another. The realistic trench performed worse than the other trench designs within and immediately near the wider, more exposed trench. This was likely a result of the increased exposure of the vane wall that allowed for additional heating of the local coolant from the hot mainstream gas. Furthermore, the realistic trench was not as effective in lateral distribution of the film coolant due to the

fact that the downstream edge of the trench was not coincident with the exit of the film cooling holes. The film cooling performance of the craters and trench designs with t/d = 1.2 TBC began to plateau at a blowing ratio of approximately M = 2.0. Additional mass flux of film coolant provided little improvement in the performance of ϕ and τ. It is recommended that the blowing ratio for such designs be targeted between M = 1.0 – 2.0 in order to use the minimum amount of film coolant while still maximizing cooling performance. The showerhead implemented in this study provided noticeably improved film coolant coverage on the exterior surface of the TBC over the region of s/d = 0 to -32 when operated at a blowing ratio of M_{SH} = 3.0. However, it may be preferable to operate at $M_{SH} \leq 2.0$ in order to minimize the amount of film coolant used depending on whether the performance of τ is within safe operating conditions as to not exceed the maximum allowable temperature of the TBC. Round holes on the pressure side of the vane performed the best at blowing ratios below M = 1.0 due to separation of the coolant jets. If multiple rows of round holes are utilized in a vane with TBC, they should be spaced at no more than 30d apart in order to maximize the effect of the external film cooling. Future engines should target these conditions if operating with a similar film cooling configuration in order to maximize the cooling performance of the engine.

Estimations were made concerning the design requirements for the maximum allowable material temperature of the vane wall and TBC. The results showed that the t/d = 1.2 TBC model exceeded the performance metrics in terms of minimum requirements for overall effectiveness, ϕ. However, the model did not meet the minimum requirement for τ for the more advanced combustor temperature conditions. This means that the

current TBC and film cooling design would not cool the external surface of the TBC below the maximum allowable temperature. One solution to this problem would be to reduce the thickness of the TBC. This will improve the cooling on the external surface of the TBC by reducing the thermal resistance to internal convective cooling. However, it will also increase the temperature at the vane wall interface. This is not thought to be a problem though since the performance of the system outperformed the necessary requirements in terms of ϕ. The proper balance will need to be found. Additional rows of film cooling holes could also improve the performance of the system.

A dramatic difference was observed in comparing the film cooling performance of round holes and trenches depending on whether or not TBC was incorporated. Albert (2011) showed that the trench design with no TBC was far superior to round holes in terms of overall and adiabatic effectiveness. This was to be expected since all previous studies of the trench showed a similar result (Waye and Bogard (2006) and Dorrington *et al.* (2007)). However, the current study with TBC showed that the trench provided only minimal improvement in terms of overall effectiveness over the performance of round holes on the pressure side at blowing ratios of $M > 1.0$. At a blowing ratio of $M = 0.5$, the performance of the two designs was equivalent on the pressure side of the vane. Prior to this result, the trench was considered one of the best film cooling designs, far outpacing the performance of round holes. It is apparent that the TBC significantly dampens the effect of external film cooling on the temperature behavior at the interface of the vane wall and TBC. This result is not predictable based on a simplified 1-D analysis.

A trench design with depth of $t/d < 0.75$ made from TBC resulted in reduced overall effectiveness between the film cooling holes (i.e. within the trench) in comparison to the performance achieved at the same location for round holes. This is in stark contrast to previous adiabatic studies showing significant improvement in film cooling performance over that of round holes. This is likely due to the fact that the inherent nature of the trench design exposes the vane wall to the hot mainstream gas by removing some of the TBC locally. The round holes, on the other hand, retain the TBC between each of the cooling holes which appears to improve the local thermal protection. It is possible that the trench design could be altered to correct for this issue. For instance, the trench could be machined into the vane wall prior to being coated with TBC. However, this presents certain challenges with respect to machining since line-of-sight is required to cut the film cooling holes. Furthermore, it would result in trench walls that were noticeably rounded in comparison to the sharp edges tested herein. It is possible that the trench could be cut into the vane wall after the holes are already formed; however, if this is done it would not be possible to form an ideal trench in which the edge of the holes is coincident with the downstream edge of the trench wall.

The design of the trench is a balance between making the trench have a depth of $t/d > 0.75$ while maintaining the requirements for the vane wall and TBC. For example, the trench depth can be increased by increasing the thickness of the TBC. However, in doing this the thickness of the TBC may result in a structurally unsound coating that is more likely to spall off the vane surface. Instead, the trench could be machined into the vane wall, as previously suggested. However, it is likely that the vane wall in real

engines is already close to its minimal thickness in order to reduce component weight and thermal resistance through the vane wall. Therefore, it stands to reason that machining the trench into the wall would jeopardize the structural integrity of the component. Additional wall thickness could be added to the vane to allow for the trench to be machined into the metal while still maintaining its structural integrity. Unfortunately, this may result in additional component weight, material costs, and thermal resistance through the thicker wall producing a sub-optimal design.

The warming of the vane wall within the trench highlights the danger of TBC spallation. It is quite evident that the TBC is vital in providing the maximum amount of thermal protection near the cooling holes. This was shown to be the case with the superior interface cooling performance near the cooling holes for the round holes and crater designs which had minimal TBC removed for the purpose of film cooling. If any of the trench designs are implemented in a real engine it will be critical to determine how susceptible such designs are to spallation. For instance, the trench designs proposed within this study expose the underlying TBC structure within the trench, including what would be the bond coat on a real component. This may increase the likelihood that the TBC structure would begin to spall. Spallation of the TBC forming the trench would not only further expose the vane wall but would also break down the very reason the trench has been studied with such great interest since the coolant would no longer be forced to spread laterally. Given this concern, trenches are only recommended if additional improvement in the external TBC condition, τ, is required via improved film cooling performance for higher blowing ratios. Otherwise, configurations such as round holes are

recommended since their design does not expose the underlying TBC structure and thus reduces the likelihood of component failure due to spallation.

The novel modified trench presented herein showed no significant improvement over the other trench designs in terms of protecting the vane wall within the trench. This may be a result of limited measurement resolution. Additional measurement resolution may provide enough detail to clearly delineate the performance of the various trench designs. Of particular interest, is to determine whether the design of the modified trench provides improved thermal protection between the coolant holes within the trench. Further study of the modified trench with greater measurement resolution as well as additional optimization of the design may yield improved results.

Optimization of film cooling appears to have minimal effect on the underlying cooling performance at the interface of the TBC and vane wall. Consequently, it may be advantageous to choose more cost effective designs, while maximizing the in-hole convective cooling. This may lead to implementation of simple round holes over other more complicated designs. However, film cooling performance does have a large effect on the external TBC condition, τ. Improved film cooling may prolong the life of the TBC and thus, indirectly, the life of the turbine component. These conclusions may result in the generality that TBC and convection protect the vane wall while film cooling protects the TBC.

Future engine designs should maximize in-hole convection by decreasing the inclination angle as much as possible to increase the surface area within the hole. For the t/d = 0.55 TBC case the convective cooling within the holes appeared to dominate the

cooling performance within 5-10*d* of the cooling holes. It may then be advantageous to place holes according to a pattern of tangent circles with radiuses of 5-10*d*. There are of course limits due to manufacturing constraints and structural requirements that may not allow for minimum inclination angles to be implemented in a real engine.

TBC has a dramatic effect on the thermal behavior of a turbine vane as shown herein. It is strongly recommended that future studies of turbine durability should incorporate the matched Biot number method with an appropriately scaled thermal barrier coating.

6.3. Effect of Deposition

This work modeled active contaminant deposition by modeling the molten nature of coal ash particles in the hot gas path of a real engine and provided the first open literature results detailing how heavy deposition affects the cooling performance of a vane with a TBC. This was accomplished with the use of molten paraffin wax particles that were used to seed the mainstream flow of the wind tunnel facility. The sizes of the particles were set to model the dynamic behavior of contaminants in a real engine by matching a range of expected Stokes numbers. This ensured that the wax particles reacted properly to changes in the flow field that governed whether or not the particles would impact and adhere to the model vane. The effect of deposition was quantified in terms of ϕ, τ, and physical characteristics, such as roughness. Deposition results were obtained for various pressure side film cooling configurations including round holes, craters, an ideal trench, a modified trench, and a realistic trench, all with t/d = 1.2 TBC. The resulting physical characteristics of the deposition were found to be in good

agreement with the limited results that are available for real engine conditions. Discussions with various industry partners and contacts also confirmed that the deposition characteristics appeared to be realistic and representative of conditions in a real engine. Detailed comparison between the deposition results obtained herein and results from actual hardware is made difficult due to the proprietary nature of the hardware in a real engine. The deposition thicknesses achieved in this study were significantly thicker than the results obtained by Albert (2011). Albert (2011) reported thicknesses that were very thin, nearly unmeasurable. The results obtained herein are representative of an engine under extreme operating conditions, either due to extended operating life or an event such as ingestion of volcanic ash.

The presence of deposition on the surface of the vane reduced film cooling performance in terms of the external TBC condition, τ, for most cases that were tested. This was likely due to the increased surface roughness that promoted mixing of the film coolant with the hot mainstream gas. Of particular interest is the fact that the presence of deposition actually improved the film cooling performance of the round hole configuration when it was operated at M = 2.0. This was a result of the deposition accumulating over the exits of the holes and forcing the coolant to remain attached to the surface rather than separating. The presence of film cooling in the showerhead region resulted in wax accumulations at s/d = 0 and -17 that were between 30-100% greater than the thickness of accumulations with no film cooling. The exact cause for this increase in deposition accumulations is currently unknown. The operation of the showerhead would intuitively seem to push the particles away from the surface which would reduce the rate

of accumulation. However, the presence of the showerhead may create local vortical structures that capture mainstream particles and move them towards the vane surface. Additional study is needed to identify the root cause for why the showerhead increases the deposition rate.

The trench designs showed marginal improvement over the craters and round holes in terms of mitigating the growth of deposition downstream of the pressure side holes. The physical understanding for why this is the case is currently unknown. However, it may be a result of the more uniform layer of attached coolant that the trenches create. The relatively uniform layer of coolant may be acting as a barrier that is sweeping away impinging particles. It is also possible that the improved film cooling performance with the trench designs accelerates the solidification of the exterior surface of the wax particles. If this is the case, the particles would become less sticky and thus more likely to rebound from the surface rather than adhere.

The deposits improved the overall effectiveness, ϕ, of the vane wall over the region of $-32 < s/d < 0$. This is the first open literature study to obtain this measurement. The improved overall effectiveness was likely due to the increased thermal resistance due to the addition of wax on the surface of the vane that essentially acted as additional TBC thickness. The presence of deposits on the surface likely increased the external convective heat transfer coefficient due to the additional roughness. Consequently, the increased thermal resistance of the deposits must have more than offset the increased convective heat transfer coefficient in order for the overall effectiveness to improve. The overall effectiveness was nearly unchanged downstream of the trench configurations.

This was likely a result of the reduced deposition accumulation for these cases and the decrease in film cooling performance that was observed due to the increased mixing with the mainstream. The overall effectiveness improved significantly downstream of the pressure side round hole configuration. This was a result of the substantial accumulations observed for this configuration and the fact that the external film cooling performance was improved for the round holes. The deposition managed to improve the film cooling performance of the round holes by forcing the detached jet back towards the surface of the vane.

The deposition method presented in this study provides a simple cost effective means of studying how ingested contaminants will affect the thermal behavior of a turbine vane. This study is the most detailed open literature assessment to date of how heavy deposition affects the film cooling performance of a first stage turbine vane with a TBC.

6.4. Utility of Analytical Model

An analytical model was developed with the goal of determining whether or not it could predict the cooling performance of a film cooled vane with a TBC. The model was based on a 1-D heat transfer assumption despite the fact that 3-D heat transfer behavior is expected in certain parts of a film cooled vane. The motivation behind this simplification was the goal of identifying a simplified analytical model that could quickly provide the engineer with an understanding of how the thermal behavior of a system might change, without having to complete a detailed numerical solution. The model was an improvement to a similar model discussed by Dees (2010) and Albert (2011); however,

the model discussed by the earlier researchers did not incorporate the effects of a TBC. The analytical models for ϕ and τ are

$$\phi_{pred} = \frac{\beta(\alpha - \chi\eta)}{\beta + Bi_w + {}^{h_e}/_{h_i}} + \chi\eta \tag{3.17}$$

and

$$\tau_{pred} = \frac{\alpha - \chi\eta}{\beta + Bi_w + {}^{h_e}/_{h_i}} + \chi\eta \tag{3.20}$$

Each of the above variables could be measured experimentally to provide a prediction of the overall effectiveness or TBC condition. However, the utility of these models was hindered by the fact that a direct measure of h_i was not available. Consequently, the internal convective heat transfer coefficient was estimated based on a 1-D assumption of the heat transfer through the wall knowing the external convective heat transfer as well as the conduction through the wall. The use of the external convection and the wall conduction to determine heat flux were described as the convection and conduction methods for calculating h_i. In general, minor variations in the predictions were observed due to the two different methods that were used to determine the distribution of internal convective heat transfer coefficient. The results from utilizing these models showed that the predictive accuracy varied depending upon the cooling configuration being studied. For instance, the models performed relatively well in predicting overall effectiveness for a vane with no TBC and no film cooling. The models also performed well in predicting ϕ and τ for a vane with t/d = 1.2 TBC and no film cooling. The models performed well in

predicting the thermal behavior of a suction side film cooled model with no TBC beyond 30*d* from the exit of the film cooling holes. This was also true for predicting the overall effectiveness of a suction side film cooled model with a t/d = 0.55 TBC. The models failed to predict the cooling performance near the exit of film cooling holes with active blowing. This is likely due to the in-hole convection that is causing local 3-D heat transfer that the models do not account for.

The analytical models could be supplemented with the use of experimental data with no film cooling, ϕ_o and τ_o. One of the benefits of using the supplemented method is that it eliminates the dependency on knowing h_i. The use of ϕ_o and τ_o to predict film cooling performance improved the results of the analytical models. However, the models still failed to predict the film cooling performance near the cooling holes, likely due to 3-D effects.

6.5. Recommendations for Future Work

6.5.1. "Thin" TBC

The TBC's that were tested in this study scaled such that they were on the relatively thick side of the expected thickness range for TBC's in a real engine. It is recommended that a "thin" TBC be tested to understand how the conclusions herein might be affected if the TBC were not as thick. It is likely that the reduced thermal resistance of a thinner TBC would result in the film cooling performance having a greater effect on the underlying temperature behavior at the interface of the TBC and vane wall.

6.5.2. Spallation

Detailed measurement of cooling performance with an eroded or spalled TBC would be very valuable. TBC in real engines invariably undergoes wear that alters the surface condition of the materials. In the extreme case, pieces of the TBC may break away from the surface. When this happens the underlying metal is directly exposed to the harsh environment of the hot gas path. The difficulty in implementing this on the model system is that it would likely require a selection of a specific spallation pattern that may in the end be arbitrary. This arbitrary nature of the spallation pattern may be decreased if industry partners were involved in detailed discussions identifying typical erosion and spallation patterns that are observed on real engine components.

6.5.3. Shaped Holes

It would be very useful to complete a TBC study with shaped holes. This is primarily due to the fact that advanced engines are often using shaped holes as the standard hole design. Consequently, shaped holes, rather than round holes, ought to be used as the baseline for comparison to other designs.

6.5.4. Thermal and Velocity Field Measurements

Detailed measurements of the thermal and velocity fields around a vane with a TBC may provide improved physical understanding of the thermal behavior that has been observed. These measurements may provide greater insight into understanding how the trench designs affect the aerodynamic performance of the vane. These results may extend to a better understanding of how the contaminants deposit on the vane.

6.5.5. Improving Analytical Models

Additional measurements to determine the internal heat transfer coefficient distribution would significantly improve the models. This is primarily due to the fact that the current models use the convection and conduction methods described in Chapter 3 to determine the internal heat transfer coefficients. These methods result in disagreement for the predicted internal convective coefficients at certain *s/d* locations. Placement of heat flux gauges on the internal and external walls of the vane could significantly improve the predictions based on a 1-D heat transfer model. A computational solution for the 3-D heat transfer behavior of the vane with a TBC could also provide good insight into the limitations of the 1-D analytical models that were proposed.

6.5.6. Using the Analytical Models to Improve Engine Design

With improvements the analytical models presented herein may provide the capability to augment design methods for future engines. For instance, if the underlying metal of the vane has a specific threshold temperature that it cannot exceed then the models may provide a means of determining where additional film cooling is required or where the TBC thickness should be increased. At this time the models do not predict film cooling well; however, they do predict overall effectiveness well for a vane with a TBC and no film cooling. In this case, the analytical models could be used to determine how thick the TBC would need to be to thermally protect a component with no film cooling for a given operating environment. This thickness could then be used as a target for future material development and TBC research. These statements imply that the engine would be designed without the use of film cooling. Not utilizing film cooling has

the benefit of reduced complexity in the engine. This may result in efficiency and cost savings due to the fact that all ingested air would be available for combustion and components would be easier to machine. However, protecting turbine components by thickening the layer of TBC may result in surface temperatures that exceed the requirements of the TBC. Consequently, film cooling may still be required for the most advanced engines with firing temperatures above the temperature requirement for TBC. It may be possible to depend solely on thicker TBC's without film cooling in engines with lower firing temperatures or on latter stage turbine components.

References

Ai, W., Murray, N., Fletcher, T.H., Harding, S., Lewis, S., and Bons, J.P., 2008, "Deposition Near Film Cooling Holes on a High Pressure Turbine Vane," ASME Paper No. GT2008-50901.

Albert, J.E., Keefe, K.J., and Bogard, D.G., 2009, "Experimental Simulation of Contaminant Deposition on a Film Cooled Turbine Airfoil Leading Edge," ASME Paper No. IMECE2009-11582

Albert, J.E., "Experimental Simulation and Mitigation of Contaminant Deposition on Film Cooled Gas Turbine Airfoils" Ph.D. Dissertation, University of Texas at Austin, 2011.

Albert, J.E. and Bogard, D.G., 2011, "Experimental Simulation of Contaminant Deposition on a Film Cooled Turbine Vane Pressure Side with a Trench," GT2011-46709, ASME Turbo Expo, Vancouver, Canada.

Annual Energy Review 2009; U.S. Energy Information Administration, August 2010, DOE/EIA-0384(2009).

Annual Energy Review 2010; U.S. Energy Information Administration, October 2011, DOE/EIA-0384(2010).

Bittlinger, G., Schulz, A., and Wittig, S., "Film Cooling Effectiveness and Heat Transfer Coefficients for Slot Injection at High Blowing Ratios," American Society of Mechanical Engineers, ASME Paper 94-GT-182, 1994.

Blair, M.F., "An Experimental Study of Heat Transfer and Film Cooling on Large-Scale Turbine Endwalls", *Journal of Heat Transfer*, Nov. 1974, pp. 524-529.

Bogard, D.G., Schmidt, D.L., and Tabbita, M., 1996, "Characterization and Laboratory Simulation of Turbine Airfoil Surface Roughness and Associated Heat Transfer," ASME Paper No. 96-GT-386.

Bogard, D.G. and Thole, K.A., "Gas Turbine Film Cooling", *Journal of Propulsion and Power*, Vol. 22, 2006, pp. 249-270.

Bons, J. P., Crosby, J., Wammack, J. E., Bentley, B. I., and Fletcher, T. H., 2005, "High Pressure Turbine Deposition in Land Based Gas Turbines from Various Synfuels," ASME Paper No. GT2005-68479.

Bose, S., DeMasi-Marcin, J., 1997, “Thermal Barrier Coating Experience in Gas Turbine Engines at Pratt & Whitney”, *Journal of Thermal Spray Technology*, Vol. 6(1), pp. 99-104.

Boyle, R.J., 2006, “Effects of Thermal Barrier Coatings on Approaches to Turbine Blade Cooling”, Paper No. GT2006-91202, ASME Turbo Expo, Barcelona, Spain.

Bunker, R.S., 2002, “Film Cooling Effectiveness due to Discrete Holes Within a Transverse Surface Slot”, Paper No. GT-2002-30178, IGTI Turbo Expo, Amsterdam, Netherlands.

Bunker, R.S., “A Review of Shaped Hole Turbine Film-Cooling Technology,” *Journal of Heat Transfer*, Vol. 127(4), 2005, pp. 441-453.

Bunker, R.S., 2009, “The Effects of Manufacturing Tolerances on Gas Turbine Cooling”, *Journal of Turbomachinery*, Vol. 131.

Crosby, J.M., Lewis, S., Bons, J.P., Ai, W., and Fletcher, T.H., 2008, “Effects of Temperature and Particle Size on Deposition in Land Based Turbines,” *Journal of Engineering for Gas Turbines and Power*, Vol. 130.

Davidson, F.T., Dees, J.E., and Bogard, D.G., 2011 “An Experimental Study of Thermal Barrier Coatings and Film Cooling on an Internally Cooled Simulated Turbine Vane”, Paper No. GT2011-46604, ASME Turbo Expo, Vancouver, Canada.

Davidson, F.T., Kistenmacher, D.A., Bogard, D.G., 2012, “Film Cooling with a Thermal Barrier Coating: Round Holes, Craters, and Trenches”, Paper No. GT2012-70029, ASME Turbo Expo, Copenhagen, Denmark.

Davidson, F.T., Kistenmacher, D.A., Bogard, D.G., 2012, “A Study of Deposition on a Turbine Vane with a Thermal Barrier Coating and Various Film Cooling Geometries”, Paper No. GT2012-70033, ASME Turbo Expo, Copenhagen, Denmark..

Dees, J.E., Ledezma, G.A., Bogard, D.G., Laskowski, G.M., Tolpadi, A.K., 2009, “Experimental Measurements and Computational Predictions for an Internally Cooled Simulated Turbine Vane,” ASME paper IMECE2009-11622.

Dees, J.E., “Experimental Measurements of Conjugate Heat Transfer on a Scaled-up Gas Turbine Airfoil with Realistic Cooling Configuration” Ph.D. Dissertation, University of Texas at Austin, 2010.

Dees, J.E., Ledezma, G.A., Bogard, D.G., Laskowski, G.M., 2011, "Overall and Adiabatic Effectiveness Values on a Scaled Up, Simulated Gas Turbine Vane: Part I – Experimental Measurements", ASME paper GT2011-46612.

Dees, J.E., Ledezma, G.A., Bogard, D.G., Laskowski, G.M., "The Effects of Conjugate Heat Transfer on The Thermal Field Above a Film Cooled Wall: Part I – Experimental Measurements", ASME paper GT2011-46617.

Dorrington, J.R., Bogard, D.G., Bunker, R.S., "Film Effectiveness Performance for Coolant Holes Embedded in Various Shallow Trench and Crater Depressions", ASME Paper No. GT2007-27992.

Dusinberre, G.M., Lester, J.C., 1962, Gas Turbine Power, International Textbook Company, Scranton, PA

Ethridge, M.I., Cutbirth, J.M., Bogard, D.G., 2000, "Effects of Showerhead Cooling on Turbine Vane Suction Side Film Cooling Effectiveness", 2000, ASME IMECE Conference, Orlando, FL.

Feuerstein, A. *et al.*, 2008, "Technical and Economical Aspects of Current Thermal Barrier Coating Systems for Gas Turbine Engines by Thermal Spray and EBPVD: A Review", *Journal of Thermal Spray Technology*, Vol. 17(2), pp. 199-21.

Fric, T.F. and Campbell, R.P, 2002, "Method for improving the cooling effectiveness of a gaseous coolant stream which flows through a substrate, and related articles of manufacture", U.S. patent No. 6,383,602.

Gritsch, M., Schulz, A., and Wittig, S., 2001, "Effect of Crossflows on the Discharge Coefficient of Film Cooling Holes with Varying Angles of Inclination and Orientation", *Journal of Turbomachinery*, Vol. 123, pp. 781-787.

Hamed, A., Tabakoff, W., and Wenglarz, R., 2006, "Erosion and Deposition in Turbomachinery," *Journal of Propulsion and Power*, Vol. 22, No. 2, pp. 350-360.

Han, J., Dutta, S., and Ekkad, S., 2000, Gas Turbine Heat Transfer and Cooling Technology, Taylor & Francis, New York, NY.

Harrison, K.L., and Bogard, D.G., 2008, "Use of the Adiabatic Wall Temperature in Film Cooling to Predict Wall Heat Flux and Temperature," ASME paper GT2008-51424.

Hinds, W. C., 1999, Aerosol Technology: Properties, Behavior, and Measurement of Airborne Particles, 2nd edition, Wiley-Interscience, New York, NY.

Hylton, L.D., Milhec, M.S., Turner, E.R., Nealy, D.A., and York, R.E., 1983, "Analytical and Experimental Evaluation of the Heat Transfer Distribution Over the Surface of Turbine Vanes," NASA CR 168015.

Hylton, L.D., Nirmalan, V., Sultanian, B.K., and Kaufman, R.M., 1988, "The Effects of Leading Edge and Downstream Film Cooling on Turbine Vane Heat Transfer," NASA CR 182133.

Inconel® alloy X-750 Data Sheet, Publication No. SMC-067, Sept. 2004, Special Metals Corporation, www.specialmetals.com.

Kline, S.J., McClintock, F.A., "Describing Uncertainties in Single Sample Experiments." *Mechanical Engineering*, 3-8, January 1953.

Langston, L.S., "Fahrenheit 3600", *Mechanical Engineering*, 2007, Vol. 129, pp. 34-37.

Lawson, S.A., and Thole, K.A., 2010, "Simulations of Multi-phase Particle Deposition on Endwall Film-Cooling," ASME Paper No. GT2010-22376.

Lewis, S., Barker, B., Bons, J.P., Ai, W.., Fletcher, T.H., 2011, "Film Cooling Effectiveness and Heat Transfer Near Deposit-Laden Film Holes", *Journal of Turbomachinery*, Vol. 133.

Maikell, J., Bogard, D., Piggush, J., Kohli, A., 2009, "Experimental Simulation of a Film Cooled Turbine Blade Leading Edge Including Thermal Barrier Coating Effects", Paper No. GT2009-60286, ASME Turbo Expo, Orlando, Florida, USA.

Meier, S.M., Gupta, D.K., 1994, "The Evolution of Thermal Barrier Coatings in Gas Turbine Engine Applications", *Journal of Engineering for Gas Turbines and Power*, Vol. 116, pp. 250 – 257.

Moffat, R.J., "Using Uncertainty Analysis in the Planning of an Experiment", *Journal of Fluids Engineering*, 107:173-178, June 1985.

Moffat, R.J., 1988, "Describing the Uncertainties in Experimental Results", *Journal of Thermal and Fluid Science*, Vol. 1, pp. 3-17.

Munson, B.R., Young, D.F., Okiishi, T.H., Fundamentals of Fluid Mechanics, 5th Ed., 2006, John Wiley & Sons, Inc.

Na, S., Williams, B., Dennis, R.A., Bryden, K.M., Shih, T.I-P., "Internal and Film Cooling of a Flat Plate with Conjugate Heat Transfer", Paper No. GT2007-27599, ASME Turbo Expo, Montreal, Canada.

Nathan, M.L., Dyson, T.E, Bradshaw, S.E., Bogard, D.G., "Adiabatic and Overall Effectiveness for the Showerhead Film Cooling of a Turbine Vane", Paper No. GT2012-69109, ASME Turbo Expo, Copenhagen, Denmark.

Padture, N.P., Gell, M., Jordan, E.H., 2002, "Thermal Barrier Coatings for Gas-Turbine Engine Applications", *Science*, Vol. 296, pp.280-284.

Perepezko, J.H., 2009, "The Hotter the Engine, the Better", *Science*, Vol. 326, pp. 1068-1069.

Rastogi, A. K., and Whitelaw, J. H., "The Effectiveness of Three-Dimensional Film-Cooling Slots – I. Measurements," *Journal of Heat Transfer*, Vol. 16, 1973, pp. 1665-1681.

Rezaei, H.R., Gupta, R.P., Bryant G.W., Hart, J.T., Liu, G.S., Bailey, C.W., Wall, T.F., Miyamae, S., Makino, K., Endo, Y., "Thermal Conductivity of Coal Ash and Slags and Models Used", *Fuel*, 2000, pp. 1697 – 1710.

Rigney, D.V., Viguie, R., Wortman, D.J., Skelly, D.W., 1997 "PVD Thermal Barrier Coating Applications and Process Development for Aircraft Engines", *Journal of Thermal Spray Technologies*, Vol. 6(2), pp. 167-175.

Rubitherm® RT-31 data sheet, Version 20.08.2009, Rubitherm Technologies GmbH, www.rubitherm.com.

Saumweber, C., Schulz, A., Wittig, S., "Free-Stream Turbulence Effects on Film Cooling with Shaped Holes," *Journal of Turbomachinery*, Vol. 125(1), pp. 65-73.

Schlichting, K.W., Padture, N.P., Jordan, E.H., Gell, M., 2003, "Failure Modes in Plasma-Sprayed Thermal Barrier Coatings", *Materials Science and Engineering*, pp. 120-130.

Shih, T., Chi, K., Ramachandran, P., Ames, R., Dennis, R., "The Role of the Biot Number in Turbine-Cooling Design and Analysis", 2010 UTSR Workshop, Oct. 2010.

Soechting, F.O., 1999, "A Design Perspective on Thermal Barrier Coatings", *Journal of Thermal Spray Technology*, Vol. 8(4), pp. 505-511.

Somawardhana, R.P., and Bogard, D.G., 2007, "Effects of Obstructions and Surface Roughness on Film Cooling Effectiveness With and Without a Transverse Trench," ASME Paper No. GT-2007-28003.

Sulzer Metco Inc., 2011, Material Product Data Sheet: 8% Yttria Stabilized Zirconia Agglomerated and HOSP™ Thermal Spray Powders, DSMTS-0001.2, www.sulzermetco.com.

Tan, Y., Longtin, J.P., Sampath, S., Zhu, D., 2010, "Temperature-Gradient Effects in Thermal Barrier Coatings: An Investigation Through Modeling, High Heat Flux Test, and Embedded Sensor", *Journal of the American Ceramic Society*.

Turner, E.R., Wilson, M.D., Hylton, L.D., and Kaufman, R.M., 1985, "Analytical and Experimental Heat Transfer Distributions with Leading Edge Showerhead Film Cooling," NASA CR 174827.

Waye, S.K., Bogard, D.G., 2006, "High Resolution Film Cooling Effectiveness Measurements of Axial Holes Embedded in a Transverse Trench with Various Trench Configurations", Paper No. GT-2006-90226, IGTI Turbo Expo, Barcelona, Spain.

Walsh, P. M., Sayre, A. N., Loehden, D. O., Monroe, L. S., Beér, J. M., and Sarofim, A. F., 1990, "Deposition of Bituminuous Coal Ash on an Isolated Heat Exchanger Tube: Effects of Coal Properties on Deposit Growth," *Progress in Energy and Combustion Science*, Vol. 16, pp. 327-346.

Webb, J., Casaday, B., Barker, B., Bons, J.P., Gledhill, A.D., Padture, N.P., 2011, "Coal Ash Deposition on Nozzle Guide Vanes: Part I – Experimental Characteristics of Four Coal Ash Types", Paper No. GT2011-45894, IGTI Turbo Expo, Vancouver, British Columbia, Canada.

Wenglarz, R.A. and Fox, R. G., 1990, "Physical Aspects of Deposition From Coal-Water Fuels Under Gas Turbine Conditions," *Journal of Engineering for Gas Turbines and Power*, Vol. 112, pp. 9-14.

Wenglarz, R.A., "Materials and Syngas Turbine Flow Path Degradation – Part 2", United States Department of Energy 3-Day Short Course: *Impact of Coal Derived Synthesis and Hydrogen Gas (SHG) Fuels Relevant to Gas Turbines*, Aug. 3-5, 2004, West Virginia University, National Research Center for Coal and Energy.

Zbogar, A., Flemming, J.F., Jensen, P.A., Glarborg, P., 2005, "Heat Transfer in Ash Deposits: A Modeling Tool-Box", *Progress in Energy and Combustion Science*, Vol. 31, pp. 317-421.

Vita

Frederick Todd Davidson was born and raised in Tucson, Arizona. He earned a B.S. in engineering science from Trinity University in San Antonio in 2005. After college, Todd went to work with Raytheon Company in Tucson, Arizona as a Systems Engineer. Todd enrolled at the University of Texas at Austin in 2006 and earned the degree of Master of Science in mechanical engineering in May 2008.

Permanent e-mail: davidsonft@gmail.com

This dissertation was typed by the author.